Unstructured MEL modelling of non linear 3D Ship Hydrodynamics

Alberto Cerello Chapchap

Faculty of Engineering and the Environment

School of Engineering Sciences, University of Southampton

A thesis submitted for the degree of

Doctor of Philosophy

Spring 2015

To my wife Georgia and in the memory of my grandfather.

Abstract

In the present work the investigations of non linear effects, in the context of potential flow theory, are investigated. These effects are caused by three main reasons, namely: the changes of the wetted geometry of the floating body, the water line dynamics and the fully non linear nature of the free surface boundary conditions. In order to understand the importance of tackling the non linear effects, a three dimensional frequency study of the S175 conteinership is carried out, at different Froude numbers, using linear frequency domain methods and a partly non linear time domain method.

A time domain analysis, with the aid of an unstructured mixed Eulerian Lagrangian (MEL) description of the fluid flow, is implemented aiming in exploring potential flow non linear effects. In this framework, the mixed boundary value problem of the Eulerian phase of the MEL scheme is tackled by means of a Boundary Element Method using constant elements (or a direct Rankine panel method). At given time step, on Neumann boundaries the impervious boundary condition is specified whereas, on Dirichlet boundaries, the potential on the free surface is prescribed. The solution of the Boundary Value problem yields the potential on the Neumann boundaries and its normal derivative on Dirichlet boundaries. In the Lagrangian phase, the free surface boundary conditions are then integrated in time. This method was used to solve the linear time domain radiation, i.e by applying linearized free surface boundary conditions on the exact free surface and solving the mixed boundary value problem on the mean undisturbed free surface, for the case of forced motions of a hemisphere and a Wigley hull. In addition, the linear time domain method is

also extended to the unified hydroelastic analysis in time domain for the cases of 2 and 3 nodes bending. Results are presented for the the Wigley hull, undergoing prescribed forced oscillations for both rigid and flexible mode shapes.

The extension of the MEL scheme to a numerical tool capable of addressing several degrees of non linearities (from body nonlinear to fully nonlinear) is also discussed. In this context, two numerical formulations to calculate the time derivative of the velocity potential are implemented, namely: a backward finite scheme and an exact calculation based in the time harmonic property of the velocity potential. In latter case, a second boundary value problem is constructed and solved for the time derivative of the potential on Neumann boundaries and for the normal acceleration on Dirichlet boundaries. Results of both approaches are compared for the case of a sphere undergoing force oscillations in heave are compared to results obtained by other time domain methods. Moreover, after the boundary value problem is solved, a radial basis function representation of the velocity potential and free surface elevation is constructed, this approach allows for the estimation of the gradient of the velocity potential (body nonlinear and fully nonlinear simulations) and free surface steepness (fully nonlinear simulations). The results of the body non linear analysis, for large amplitude of oscillation in heave, are presented for the both the sphere and Wigley hull. For the latter, body non linear results of the coupling between heave into the first distortion mode (2-node) are also presented. The results of the fully non linear simulations are presented for the case of a sphere.

An investigation of the suitability of two unstructured meshing libraries is also performed in the context of the MEL simulation scheme. Practical issues related to (re)meshing at each time step, the representation of ship like geometries, free surface evolution and numerical stability are highlighted for both libraries.

Acknowledgements

I would like to thank my supervisor, Professor Pandeli Temarel, who managed to guide me through this research and has also tolerated a great deal of what he would call "unusual" behaviour. In addition, I am also indebted to Professor Alexandre Simos, of the University of Sao Paulo, who has motivated me to pursue this degree to its fullest extent. The financial support of Lloyds Register strategic research group is also acknowledged.

Declaration Of Authorship

I, Alberto Cerello Chapchap, declare that the thesis entitled **Unstructured MEL modelling of non linear 3D Ship Hydrodynamics** and the work presented in the thesis are both my own, and have been generated by me as the result of my own original research. I confirm that:

- this work was done wholly or mainly while in candidature for a research degree at this University;
- where any part of this thesis has previously been submitted for a degree or any other qualification at this University or any other institution, this has been clearly stated;
- where I have consulted the published work of others, this is always clearly attributed;
- where I have quoted from the work of others, the source is always given. With the exception of such quotations, this thesis is entirely my own work;
- I have acknowledged all main sources of help;
- where the thesis is based on work done by myself jointly with others, I have made clear exactly what was done by others and what I have contributed myself;
- parts of this work have been published as:

    1. Chapchap, A., Hudson, D.A., Temarel, P., Ahmed, T.M. and Hirdaris, S.E, 2011, "The influence of forward speed and nonlinearities on the dynamic behaviour of a containership in regular waves". Transaction

of the Royal Institution of Naval Architects, Int. Journal of Maritime Engineering, 153, 137-148.

2. Chapchap, A. C., Chen, Y., Temarel, P. and Hirdaris, S, 2011, "Investigation of geometric nonlinear potential flow effects on free surface flows" , 26 th International Workshop on Water Waves and Floating Bodies, Athens, Greece.

3. Chapchap, A.C., Miao S. H., Temarel P. and Hirdaris S. E., 2012, "Time Domain Hidroelasticity Analysis: The Three Dimensional Linear Problem", 6 th International Conference on Hydroelasticity in Marine Technology, Tokyo, Japan.

4. Chapchap; A.C and Temarel P.: "Unstructured MEL Scheme for 3D body non linear ship Hydrodynamics", 5th International Conference on Marine Structures, March 2015, Southampton, UK.

Signed: . . . . . .

Date: . . . . . .

Contents

List of Figures

List of Tables

List of Algorithms

Chapter 1

Introduction

1.1 Problem Motivation

The present work addresses hydrodynamic problems based on potential flow theory in which the effects of lift can be neglected. This formulation has been used since the 70's on a wide range of ship hydrodynamic problems, e.g seakeeping analysis, wave resistance prediction, hydroelasticity, impact problems and so on. More specifically, efforts focused in developing tools that allow for the analysis of effects that cannot be addressed by the so called linear frequency domain analysis, these effects are usually called "potential flow non linear effects" or "geometric non linearities".

There are, basically, three sources of non linear effects when it comes to potential flow analysis, namely: the submerged geometry of the floating body, the water line dynamics and the exact free surface boundary conditions.

In order to gain some intuition on how the submerged geometry can create non linear effects in the hydrodynamic context, a parallel with the hydrostatic case can be made. For instance, when a cylindrical column oscillates on a flat free surface, the hydrostatic force it experiences is proportional to its submerged depth, z, and its cross sectional area A_s, i.e: $F = -zgA_s$, which is in fact proportional to the vertical coordinate. On the other hand, if the cross sectional area of the geometry is not constant, then even in the context of a constant pressure field (hydrostatic pressure field is $p = -gz$) the hydrostatic force will actually have a non linear

behaviour with respect to the vertical coordinate. The question that naturally rises here is what sort of influence does the body geometry has when it comes to more complex pressure fields, say the hydrodynamic pressure field ? Moreover, of particular interest to the hydrodynamic analysis is how the components of the hydrodynamic force proportional to velocity and acceleration vary as the body submerged geometry is taken into account exactly. The effect of change in the submerged body surface has led to formulations of the partly non linear methods and body non linear methods, as discussed in chapters 3 and 7, respectively.

One of the main consequences of the assumptions made in the linear potential flow theory is that the free surface boundary conditions can be linearized. If the time domain perspective is taken, the linearization assumes a simpler dynamic for the evolution of the free surface and, hence, the potential field in time. In particular, the linearized free surface avoids problems of wave breaking that have been causing numerical issues and limitations on the applications of the exact free surface conditions (Beck et al. [1994]). From an implementation point of view, the linearized free surface assumption is handy, to the extent that the computational mesh on the free surface does not need to be deformed and hence the domain does not change in time. That said, since the boundary value problem is coupled by the free surface evolution and the potential on the floating body, it can be the case that using the exact free surface boundary conditions, a different hydrodynamic pressure field can arise, and, therefore, change the hydrodynamic force.

The effect of water line dynamic is somewhat more challenging to describe since it seems to be a combination of both the geometry of the body and the velocity field surrounding the intersection of the body and the free surface. The velocity field is intimately associated with the free surface boundary conditions, so that a linearized free surface formulation will probably yield a smaller potential gradient on the free surface body intersection, hence, contribute less to changes on the wetted surface. Note that this effect is enhanced in the case of incident wave potential and diffraction. Furthermore, the intersection of the free surface and body is a region where there is discontinuity of the normals of geometries, which actually brings more complexity into the water line dynamics evolution (Liu et al. [2001]).

From the perspective of the designer it is clear that a more accurate eval-

uation of the hydrodynamic pressure field is of great importance, as it allows for accurate loads to be predicted and therefore a more comprehensively structural assessment using either a quasi-dynamic or hydroelasticity analysis. In the quasi- dynamic analysis, the loads on the vessel are estimated solving the rigid body seakeeping problem and are then applied to the vessel structural model (e.g beam or finite element model), the implicit assumption is that fluid structure interaction coupling is reasonably small.

In situations where the fluid structure interaction coupling is not reasonably small, the analysis can be made more consistent by means of the theory of hydroelasticity (Bishop and Price [1979] and Bishop et al. [1986]). In this context, the interaction between the flexible floating structure and the fluid are tackled together, combining the hydrodynamic effects with a dynamic structural analysis (e.g using beam or FE models). The hydroelastic approach has the main advantage of being more general and capable of tackling the coupling between seakeeping and global strength analysis. This is accomplished by accounting for the flexible nature of the structure (as opposed to the rigid body conditions) in the boundary conditions of the hydrodynamic problem.

Obviously either in the quasi-dynamic analysis or in the hydroelastic one, the hydrodynamic pressure field plays a paramount role. In order to incorporate different degrees of non linearity in the evaluation of the hydrodynamic forces, several extensions have been developed. In the context of seakeeping analysis, the partly linear method of Ballard et al. [2003] is probably the most natural extension of the linear frequency domain analysis. Under the partly non linear framework, the frequency domain results of linear analysis are mapped to time domain by the use of Impulsive Response Functions (IRFs). These, although still in a linear sense, provide a suitable way to estimate memory effects and the influence of non-periodic forces in time domain by means of inverse Fourier transforms and convolution integrals. This way, hydrostatics and incident wave actions (Froude -Krylov forces) are calculated on the instantaneous wetted surface and the hydrodynamic forces are estimated by their corresponding IRFs calculated on the mean wetted surface.

The limitations of the partly nonlinear approach is that, although arguably pitch and heave motions are dominated by nonlinear hydrostatic and inertia

(Zhang et al. [2007]), the nonlinear effects on the radiation and diffraction potentials are being neglected. In order to incorporate the non linear effects associated with radiation, the body non linear approach has been formulated in time domain. Under this framework, the hydrodynamic problem is solved on the instantaneous wetted surface, so that the changes in the submerged part of the body are accounted for in both hydrostatics and hydrodynamic forces. Although simple in theory, the extension from partly non linear to body non linear requires considerable efforts, and several avenues of implementations can be pursued. In this method, the free surface boundary conditions are linearized, but interestingly Bernoulli's equation can be used exactly on the body surface, showing that the quadratic term is responsible for higher frequency force. However, the fact the body wetted surface now changes bring considerable numerical challenges in the evalution of potential time derivative, especially when the amplitude of the motion is large.

The fully non linear potential flow problem has also been tackled in order to evaluate the non linear effects under several different problems. These methods are usually built upon the Mixed Eulerian Lagrange scheme, or MEL for short. Within this numerical framework, several non linear effects have been investigated, but numerical challenges and the need for computational algorithms means that more investigations are required in this context.

It is also worth to point out that, in the context of potential flow, even if simulations are carried out using the fully non linear free surface boundary conditions, some of the problems are likely to be be poorly modeled. For instance, it can be argued that during violent slamming flow separation occurs. Therefore, the pressure field and its corresponding hydrodynamic forces need to be modeled more precisely by Navier Stokes equations. Moreover, the wave breaking problem is a natural limitation on fully non linear potential flow simulations and at, the same time, a physical phenomenon that needs to be dealt with. One alternative is to couple potential flow and volume of fluid simulations, so that the dynamics of the breaking waves can be taken into account (Lachaume et al. [2003]) .

1.2 Aims and Objectives

The aim of the present work is to try to address the effects, in the context of potential flow, of relaxing some of the assumptions made by linear theory, focusing on the solution of the radiation problem. Concretely, the efforts have focused on the development of a methodology that is capable of tackling problems of forced oscillations in either rigid or flexible modes and problems related to the evolution of the free surface in time, using either the linear (linear and body non linear simulations) and the non linear free surface boundary conditions. This way, the problem of free motions in waves (which accounts for both the incident wave and diffraction problems) is left out of the present scope.

That said, a numerical tool of this kind, not only generalizes the linear theory predictions, but also allows the analysis of the variations of the amplitude of the oscillatory motion, so that the so called large amplitude added mass and damping coefficients can be investigated. These effects can be analysed in the context of rigid bodies oscillations as well as elastic bodies with relatively small deflections, so that the hydroelastic analysis of the radiation effects of the flexible modes can also be investigated in time domain. The applicability of the current methodology is limited to problems where the viscous effects play a small a role and no separation of the flow is observed.

Therefore, a multi-problem approach is adopted synthesizing and building upon simplified problems. This way, problems with an increasing degree of complexity were tackled, in the following order:

1. Linear Analysis of Rigid Bodies;
2. Linear Hydroelastic Analysis;
3. Body non Linear Analysis;
4. Fully non Linear Analysis.

For all cases described above, the simulations are implemented in time domain with the aid of a Mixed Euler Lagrange (MEL) scheme that is used to march the solution of Boundary Value Problem in time.

The task is by no means easy because problems associated with numerical accuracy, mesh generation and, to a large extent computation time, are daunting when linear theory assumptions start to be relaxed. For instance, a major benefit of linear theory is the frequency domain representation in which the steady state hydrodynamic force can be obtained for several frequencies by solving a linear system once for each frequency of oscillation. On the other hand, the time domain implementation, even in the linear case, calls for a time marching scheme where the free surface boundary conditions are integrated in time and a time history of the hydrodynamic force for each frequency is calculated.

1.3 Achievements and Contributions

The efforts of the present work have been concentrated in basically two fronts, namely: the implementation of a hydrodynamic model capable of incorporating some of the so called non linear potential flow effects and the investigation of suitable meshing techniques that can be applied to mesh (remesh) the evolving free surface as well as the floating body every time step. Note that these two fronts are connected, since a mesh is needed for the implementation of the Euler phase. In order to try to accomplish these tasks several algorithms are proposed throughout the present work. More specifically, in the time domain context, the structure of the MEL simulation, and the place where each developed algorithm fits in, are summarized in figure 1.1.

In the first front, the equations that describe the evolution of the potential flow in time domain are well understood from both mathematical and physical perspectives. However, algorithmic and numerical challenges still remain, limiting the applicability of tackling this problem through numerical simulations. The contributions and achievements of the present work try to address some of these issues.

As pointed out by Yan [2010] the main limitations of three-dimensional potential flow time domain simulations rely in modeling multi scale variations on the velocity potential function. This implies that a larger number of elements per wave lengths are needed to approximate the velocity potential with a reasonable accuracy in regions of steep gradients. On the other hand, for N elements, the

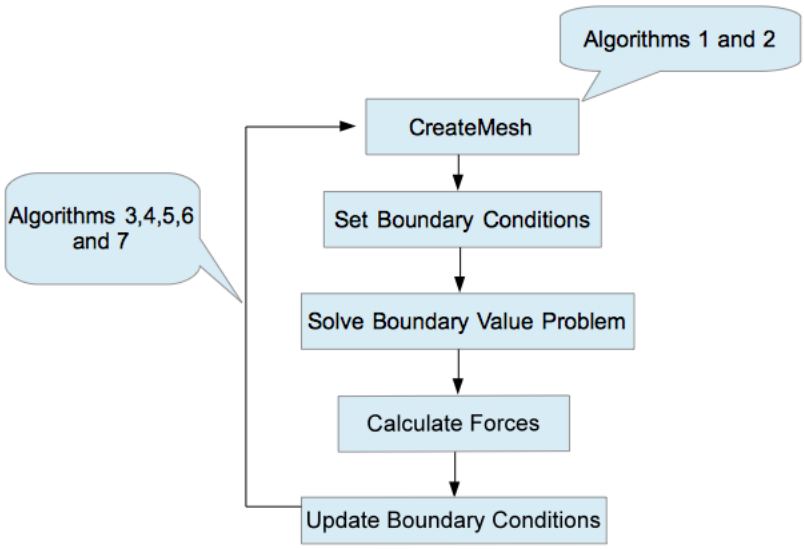

Figure 1.1: Schematic view of the general structure of potential flow simulations in time domain.

running time, for assembling and solving the linear systems that arise in this application, scale as $O(N^2)$, limiting its practical use. In order to tackle this issue, the present work has concentrated its efforts on the use of unstructured triangle meshes, which are usually harder to build (compared to structured meshes) but are able to describe the domain using fewer elements. Moreover, unstructured meshes can be made more dense (have more elements per area) in parts of the domain where the velocity potential has a complex behaviour (near the water line, for instance) and more coarser in other regions. Therefore, one of the achievements of the present work has been in developing a methodology that incorporates the MEL scheme with unstructured meshes, for linear, body non linear and fully non linear problems in the context of forced oscillations. For the linear case, the methodology is summarized in algorithm 3, for rigid body forced motions simulations, and algorithm 4, for the unified hydroelastic simulations.

It is also important to point out that in order to extend the linear time domain constant panel method to account for body non linear and fully non linear effects, several numerical challenges had to be addressed. Among them, three problems stand out, namely:

1. The estimation of the velocity potential time derivative by a finite difference scheme and the solution of a second boundary value problem.

2. The estimation of the spatial derivatives of the velocity potential by introducing an RBF representation;

3. Avoid spurious modes of oscillation on the time series of the hydrodynamic force by introducing a regularization factor on the RBF representation;

The estimation of the velocity potential time derivative is very important (it corresponds to the inertia term in Bernoulli's equation) and, at the same time, its evaluation is not straightforward when the boundary value problem is solved at the instantaneous body surface. In the present work, two algorithms are proposed to estimate it (Algorithms 5 and 6). The results are compared for the case of a sphere undergoing forced oscillations to other numerical procedures.

By the same token, the spatial derivatives of the velocity potential can contribute to second order effects in the hydrodynamic force. Moreover, their approximation is needed as a boundary condition to solve the second boundary value problem for the velocity potential time derivative, which is then solved exactly (Algorithm 6). In this case, once the spatial derivative is available, the boundary condition derived by Battistin and Iafrati [2003] can be imposed on the body surface in a straightforward fashion, still using a constant panel method.

As it will be seen later on, inaccuracies of the constant panel method on the estimation of the normal velocity on the free surface (solution of the Dirichlet problem) can induce spurious modes of oscillations in the hydrodynamic force. In order to deal with this effect, a regularization term is introduced on the radial basis function representation. A parallel with the problem of supervised learning is also briefly explored.

In order to to cope with fully non linear free surface boundary conditions for the case of the sphere undergoing forced motions in heave, algorithm 5 is extended, yielding algorithm 7. In this simulation, a great deal of numerical diffusion is observed. In order to filter these modes, hence the Hilbert-Huang Transform (Huang et al. [1998]) is used and its parallel with the Fourier decomposition is also briefly outlined in the appendix.

The investigation of suitable meshing techniques, to enable the generation of unstructured non uniform grids, was also performed. One of the investigated algorithm was developed by Persson [2005], and builds heavily on the concept of signed distance functions and iterative Delaunay triangulations. For simple geometries (those which the signed distance function is analytic) the use of this algorithm is straightforward. On the other hand, for ship like geometries and for the free surface, the signed distance function needs to be estimated before the meshing scheme is called. In order to estimate the signed distance functions numerically two more algorithms 1 and 2 are proposed. Their suitability for the problem of hydrodynamic simulations is discussed as well.

Alternatively, a second meshing algorithm Geuzaine and Remacle [2009], that is built on a more conventional hierarchical meshing techniques is also analysed in the context of hydrodynamic simulations. Finally, the pros and cons of each methodology (Persson [2005] and Geuzaine and Remacle [2009]) are investigated and highlighted.

In a nutshell, the present methodology can be regarded as hybrid numerical method whereby the solution of a mesh based constant panel method is coupled with a radial basis function representaion, which is meshless. This last step brings differentiability to the CPM solution allowing spatial derivatives to be estimated.

1.4 Thesis Outline

The present work is organized as follows: in chapter 2, the relevant publications, regarding the formulation of the hydrodynamic problem are briefly outlined and discussed for the cases of rigid and flexible floating bodies. In chapter 3, the importance of the modeling the non linear effects is highlighted by investigating the influence of forward speed on the dynamic behaviour of an S175 conteinership under frequency domain and partly non linear methods. The mathematical formulation of the time domain problem is introduced in chapter 4, where departing from Laplace's equation an integral formulation for the problem is derived.

In chapter 5, the investigation of two unstructured meshing libraries for the purpose of hydrodynamic simulations is performed. In this sense, the necessary modifications/inputs needed to each library to account for the change of domain

in time are detailed. In particular, since the input for the meshing technique developed by Persson [2005] is a signed distance function, the problem of estimating signed distance functions for ship like shapes and the free surface evolution was tackled. It is also highlighted how the heuristic techniques used by Persson [2005] to generate high quality meshes can also naturally induce numerical diffusion in the hydrodynamic simulation. The meshing library developed by Geuzaine and Remacle [2009] was also investigated and used to create the meshes of the Wigley hull, for both linear and body non linear simulations.

The linear radiation problem is then solved in chapter 6, for a simple hemisphere and Wigley hull undergoing forced harmonic motions. The linear time domain algorithm is then extended for the unified hydroelastic case, so that the Wigley hull is idealized as an Euler beam. The results for the rigid modes are then compared to analytical solutions (for the hemi sphere) and available experimental data for the case of the Wigley hull. The results for the hydroelastic analysis is compared with 2D strip theory and 3D frequency domain analysis.

The extension of the linear problem for the Body non linear and fully non linear cases is done on chapter 7. For these cases, due to the nodes movement and inaccuracies of the CPM method in estimating the free surface normal velocity, the regularized rbf representation was introduced. Furthermore, the problem of estimating the time derivative of the potential was tackled using two formulations, namely: one based on a backward finite difference scheme and another that solves an auxiliary boundary value problem for the potential time derivative exactly. Results of the body non linear approach for rigid body heave mode are presented for the sphere and Wigley hull and compared to other numerical methods as well as experimental results when available.

Finally, chapter 8 concludes the work, discusses future avenues and extensions of the present numerical method.

Chapter 2

Literature Review

In this chapter, the relevant publications for the current project are presented and discussed. The review is organized in two major sections as follows: the first one covers a review of the fluid-structure interaction problem of rigid bodies, whereas the second section relates to the discussion associated with fluid-structure interaction problems that account for the body flexibility. In addition, the relevant methods available to extend the linear problem of rigid or flexible bodies to account for partial non-linear and fully non linear effects are also discussed.

2.1 Rigid Body

In Inglis [1980] a three dimensional theory of a floating structure traveling in waves is developed. In this work the fluid is regarded as inviscid and the sea-keeping problem is solved in the frequency domain. This way, the free surface boundary conditions are linearized allowing the implementation of the pulsating Green function source distribution. The resulting integral equation is then solved by the constant panel method. Predicted results for a series 60 hull showed better agreement to experimental data than the previous predictions provided by two-dimensional strip theory. In addition, the effect of shallow water and the influence of the forward speed in the motions of ships traveling in waves are also investigated.

In Sclavounos and Huang [1993], the boundary value problem is treated using

a linear potential flow framework (linearized free surface and body boundary conditions are applied) and solved on the frequency domain through the use of Rankine Panel Method (RPM), with quadrilateral panels distributed over the ship hull and free surface. In addition, a bi-quadratic spline variation of the velocity potential over the surface of each panel is assumed and a Kutta type condition to enforce smooth detachment of the steady and unsteady flow at the stern is also applied. The results present the Kelvin wake of a transom stern ship in steady flow, the hydrodynamic coefficients, heave and pitch motions and wave induced structural loads in time harmonic flow for three vessels: SL7, S-175 hulls and an IACC yacht. Heave and pitch motions show good agreement with the experimental data whereas the structural loads (bending moments and vertical shear forces at amidships for the SL7 and S-175) showed great dependence upon the amplitude of heave and pitch motions and the account of waterline terms in the definition of the loads. The major drawback of the RPM is that the far field closure is not satisfied by the corresponding Green function, and, therefore, additional conditions need to be imposed in order to guarantee the uniqueness of the solution of the integral equations in an unbounded domain.

A linear time domain analysis of the seakeeping problem is carried out by Zhang et al. [2010] using double body basis flows. In this approach, the desingularized panel method is used to collocate the sources above the free surface whereas panels with constant strength are distributed over the hull surface. The free surface boundary condition is applied on the calm water, whereas the body boundary condition is applied on the mean wetted hull surface (linear approach). A MEL algorithm is used for the time marching scheme of the free surface. Results for the Wigley Hull and Series 60 show good agreement with experimental data Gerristma et al. [1974] and improvements when compared against the predictions of the following methods: Neuman -Kelvin approximation with simplified m terms, linearized free surface conditions with double-body m terms and time domain body exact strip theory Bandyk [2009]. On the other hand, the method needs to be extended to take into account non linear effects as well as more realistic hull forms.

A large amplitude 3D non linear methodology for the assessment of large amplitude motions and wave loads on a ship traveling on the seaway was developed

by Lin et al. [1994]. Their approach consists of satisfying the body boundary conditions on the instantaneous water line whilst the free surface boundary condition is linearized, thus allowing the use of a time domain transient Green's function. This way, the Froude Krylov forces and the nonlinear hydrostatic restoring actions are calculated accurately, whereas the hydrodynamic radiation and diffraction forces are approximated at each time step. The approximation is done by using the local free surface elevation to transform the body geometry into a computational domain with a deformed body and a flat free surface. Predictions of heave and pitch motions as well as vertical bending moment at midship using the large 3 D non linear method (Large Amplitude Motion Program version 4, LAMP 4) are then compared against measured data and three other models: linear strip theory, the 3D linearized time domain method (LAMP 1) and the approximate large amplitude 3D nonlinear method (LAMP 2). Results are then presented for a series 60 model and for the S175 container ship. The predictions of the LAMP 4 model, for heave and pitch motions of the series 60 model, show better agreement with experimental data than the predictions of LAMP 2 and also predict higher vertical bending moment at midships. Furthermore for the S175 container ship, LAMP 4 predictions for heave motions are in good agreement with experimental data and show a substantial gain from the previous methodology implemented in LAMP 2; however, results for the pitch mode have shown only a reasonable agreement with measured data. Further methods and numerical issues leading forward a fully non linear method are discussed as well.

The partly non linear rigid body problem was also addressed by Bailey et al. [1998] where the authors proposed a general mathematical model to address the problem of manoeuvring and seakeeping for a ship moving in a seaway using three-dimensional potential flow analysis. The equations of motions for both seakeeping and ship manoeuvring problems are formulated with respect to two different frames of reference (equilibrium frame and body fixed frame respectively) and relations between the slow motion and oscillatory derivatives (manoeuvring theory variables) are derived in terms of the hydrodynamic coefficients (seakeeping theory variables). In this approach, the non linear Froude-Krylov and hydrostatic forces are calculated at each time step considering the instantaneous under water portion of the hull, whereas the wave diffraction contributions are estimated by

their respective impulse response function referenced to both equilibrium frame and body fixed frame. Furthermore, within the bounds of linear theory, a convolution integral representation of a general fluid action is also presented allowing the evaluation of either the hydrodynamics coefficients or slow motion and oscillatory derivatives. This way, integro - differential equations of motion can be constructed either using the manoeuvring theory variables or the seakeeping theory variables. The methodology is then validated against the experimental data available for a Mariner ship. At lower frequencies predicted hydrodynamic coefficients show some differences, however, after the introduction of a linear viscous ramp damping effect, a good agreement is then achieved between the theoretical and experimental data over a wide frequency range.

In Bailey et al. [2002], the time domain method on Bailey et al. [1998] is further developed and applied to the prediction of heave and pitch motions in regular waves. The method considers both linear and partly non linear 3D models. In the linear frequency domain model, the fluid forces and moments acting on a ship are evaluated using a pulsating source distribution over the mean wetted surface of the hull (Inglis [1980]). For the partly nonlinear model the methodology proposed by Bailey et al. [1998] was used. Predicted heave and pitch RAOs by both methods, are compared against experimental results for a Series 60 hull and for the S175 container ship and, where available results from the LAMP (Lin et al. [1994]) family programs. In addition, the presented model provides results in line with the predictions of LAMP 2 program.

Methods that, in theory, should be able to account for the non linearities of the free surface exactly have also been developed for three dimensional wave simulations and for fully non linear wave body interactions. These methods basically rely on the Mixed Eulerian Lagrangian (MEL) and the Arbitrary Eulerian Lagrangian (ALE) formulations. Basically, the idea of a MEL scheme is to capture the time domain evolution of the linear or non linear free surface boundary conditions by integrating them in time. Therefore, the problem is usually splitted in a Eulerian and Lagrangian phase. The MEL is often used within the context of potential flow problems, but it can also, in theory, be used to tackle fluid flow being governed by Euler or Navier Stokes equations. The main drawback in the two latter cases is due to the complexity of velocity field Lagrangian nodes move-

ments distorts the domain too much, raising problems related to meshing the fluid domain. One way to overcome the disadvantages of the MEL scheme, but keeping its good features, is to introduce ALE framework; the ALE is, in a sense, a generalization of the MEL scheme (i.e the Lagrangian and Eulerian descriptions can be recovered as particular cases) and its applicability is usually related to solvers of the Navier Stokes Equation for problems where the domain is changing in time. Another way to overcome problems related to mesh distorion is to pursue mesh free formulations, where the Eulerian phase is not necessary anymore, this idea is the starting point of smooth particle hydrodynamics formulations, see for instance Cossins [2010].

The main feature of both MEL and ALE scheme is to try to combine the advantages of using Eulerian and Lagrangian descriptions of flow, in order to minimize mesh distortions so that calculations can still be performed. In the ALE, the governing equations are formulated in an arbitrary domain, this means that a suitable grid velocity is introduced in order to simplify the modeling of convection terms and minimize mesh distortions; its main drawback is the introduction of the mesh governing equation which also needs to be solved on the fluid domain. MEL schemes formulate the problem in two main phases a Lagrangian and and an Eulerian phase, this way convection terms are avoided and the particles of the fluid are followed throughout their motion. Hence a MEL scheme can be viewed as an ALE scheme where the grid velocity is precisely the same as velocity of the fluid particles.

In Huerta and Liu [1988], the ALE method is applied to model the two dimensional free surface evolution of viscous flow. In this publication, the description of the ALE approach is presented and the governing equations of the fluid motion are developed in this framework. Three methods for mesh rezoning algorithm (Mesh motion described a priori, Lagrange-Euler matrix method and the mixed formulation) are introduced to update the mesh and map the moving domain. Using the mixed formulation, the mesh updating equation is solved by the stream line upwind Petrov-Galerkin finite element method. Results show progress in the modeling of a tsunami wave, large amplitude sloshing example and a dam break problem.

Another application of the ALE to two dimensional free surface flows was

carried out by Masud and Hughes [1997], where a space time Galerkin/least squares FEM formulation of the Navier Stokes equations is implemented for the analysis of deforming fluid structure interfaces. Numerical results are presented for a circular cylinder moving in a stationary viscous flow field, a solitary wave propagation without viscosity and missile launch from a submarine. A complete summary of ALE formulation can be found in Stein et al. [2004].

The foundation of the MEL method was established originally to simulate the dynamics in time domain of steep waves in two dimensions by Longuet-Higgins and Cokelet [1976]. In this work it is shown that under the assumptions of potential and irrotational flow the fully non linear free surface boundary conditions can be integrated explicitly when the Lagrangian description of the flow is used. This way, at each time step, the simulation can be split in two main steps. In the first step (Eulerian phase), the conventional boundary integral equations (BIE) are solved; in this case, given an initial potential for the velocity the Dirichlet problem is solved by the BIE formulation to obtain the normal components the velocity field. In the second step (Lagrangian phase), the kinematic and dynamic boundary condition of the free surface are integrated resulting in a new free surface position and an updated velocity potential . The process is then repeated. Their method was then tested on a free, steady wave of finite amplitude and compared against independent calculations based on Stokes' series, showing good agreement.

In Beck et al. [1994] non linear computations of ship motions are presented for 2 and 3 dimensional cases using the Rankine panel method (RPM). Exciting forces acting on a wedge and the free motions of a box barge are tackled using the two dimensional approach. The added mass and damping coefficients of a Wigley hull, in heave and pitch motions, are calculated for the three dimensional case. MEL was used to solve the mixed boundary value problem at each time step. In addition, a desingularized boundary integral method, in which the solution is constructed by integrating a distribution of fundamental singularities over the integration surface outside the fluid domain, is implemented. The results show good agreement with experimental data, however, the method needs to be extended to more realistic hull forms.

A MEL scheme is combined with a higher order BEM in Liu et al. [2001]

in order to simulate the fully nonlinear wave body interactions for two problems: the generation of three dimensional ship bow waves (for a flared wedge, Wigley and Series 60 hulls) and the prediction of high frequency ringing loads on a vertical cylinder in regular waves. This way, quadratic isoparametric panels are distributed over the domain and a double node technique is developed to treat the confluence of different types of boundary conditions (Dirichlet boundary conditions for the free surface and Neumann type for the body). In addition, a method is developed to update the free surface intersection and cubic splines in both parametric directions are used for grid regeneration purposes. The far field closure problem is tackled by the introduction of a numerical sponge layer on the perimeter of the computational domain. In the first problem, the bow wave profiles obtained from MEL are compared with quasi two dimensional simulations and linearized slender body theory. In addition, results for the Wigley hull and Series 60 bow wave profile are compared with experimental data showing good agreement. Good agreement is also achieved between the results for the predictions of high frequency ringing loads and available experimental data. Some limitations of the MEL such as breaking waves and the consequences of the clustering of Lagrangian particles in regions of high flows gradients are also discussed.

In Zhang et al. [2007] the MEL scheme developed by Liu et al. [2001] is combined in the LAMP program to obtain a three dimensional time domain potential flow solution of the body wave interaction problems using linear free surface boundary conditions. For a flared axisymmetric body, a comparison between the constant panel method (CPM) , available experimental data and the QBEM is presented. Although it is shown that the QBEM is more accurate than the CPM when the same number of panels are used and can represent more accurately edges and corners of complex geometries, results for vertical motions (heave and pitch) have not shown a significant difference. Relevant numerical issues are discussed, in particular, in order to keep the free surface stable, a linearized version of the dynamic boundary condition, taking into account linearized components of the velocity field, is used to update the potential on the free surface.

The work of Battistin and Iafrati [2003] considered the problem of calculating hydrodynamic loads, in two dimensions, during water impact. Interestingly, to

address this problem accurately, two boundary value problems are formulated. On the first one, the potential on the free surface is imposed together with a impervious boundary condition on the floating body. This problem is then solved for the potential on the floating body and normal velocity on the free surface. Next, on the second boundary value problem, the time derivative of the potential is imposed on the free surface and the its normal derivative (i.e the normal derivative of the time derivative of the velocity potential) is imposed on the floating body. The solution of the second boundary value problem yields the normal acceleration on the free surface and the time derivative of the potential on the floating body, so that the pressure can be evaluated directly after the second boundary value problem is solved. Furthermore, using techniques form differential manifolds an approximation is derived for the the normal derivative of the time derivative of the velocity potential on the floating body.

A MEL/BEM scheme was also used by Kara et al. [2007] to solve the steady three dimensional wave generation problem of a ship traveling with constant forward speed in calm water. At each time step, the algorithm solves the boundary value problem in an Eulerian frame by the indirect desingularized boundary integral method. Then, a Lagrangian frame is used to integrate the exact free surface conditions with respect to time by an explicit fourth order Runge Kutta method. In this second step, the kinematic free surface condition integration yields the free surface movement whereas the dynamic free surface condition is used to update the free surface potential. The intersection line between the free surface and body surface (Dirichlet and Neumann boundaries respectively) is described by the panel vertices at the edge of the surfaces. Furthermore, a computational window and a node shifting scheme are also developed to satisfy the far field boundary condition. Numerical results (wave resistance and wave elevation) are compared with existing linear theory, experimental measurements for Series 60 hull and other nonlinear numerical computation.

More recently, the higher order BEM developed by Liu et al. [2001] was extended by Yan [2010]. This implementation is very efficient from a computational perspective as it uses the pre-corrected fast Fourier transform to accelerate the calculation of the far field influences. The computational efficiency of this scheme is comparable to the fast multipole implementations (see for instance Liu [2009]),

in which, for N unknows, the computational time becomes proportional to $NlogN$ (or $O(NlogN)$). Three dimensional fully non linear simulations are then carried out for heaving sphere and to the problem of ringging loads in a vertical cylinder. For ship like forms the wave resistance problem, also solved by Liu et al. [2001], is recasted using the pre-corrected Fourier Transform BEM. Next, two dimensional water entry problems for low Froude numbers and impact problems are addressed. Finally, the three dimensional problem of large spar floating structure (i.e a large vertical cylindrical floating body) is also investigated.

2.2 Flexible Body

The three dimensional linear theory of hydroelasticity in the frequency domain was developed by Bishop et al. [1986]. In their analysis the seakeeping problem of a rigid body moving on irregular waves is generalized, so that distortions (including rigid modes) and their interactions with the fluid are taken into account. The three- dimensional structure is consider to be in vacuo and is represented by a finite element model. The three- dimensional hydrodynamic analysis of the fluid actions is carried out using the linear free surface boundary conditions. Generalized hydrodynamic and hydrostatics forces are then calculated with the aid of the modal analysis of the structure. Comparisons between the results obtained from the three- dimensional theory and the two dimensional hydroelasticity strip-beam theory are presented for a uniform box beam like ship showing good agreement. In addition, a hydroelasticity analysis of a small water-plane area twin hull (SWATH) is performed.

The non linear three dimensional hydroelastic response of a SWATH vessel traveling in regular and irregular waves is investigated using the second order hydroelasticity theory developed by Wu et al. [1997]. The hydrodynamic actions are evaluated using pulsating and translating Green source functions. This way, the influences of the forward speed and the steady wave flow are taken into account on the hydroelastic response of the hull. More specifically, the translating and pulsating Green function source was applied in conjunction with uniform flow, double body flow and the steady Kelvin wave flow. Furthermore, the hydrodynamic actions induced by the rigid body motions and variations of the

instantaneous wetted surface area are also included in the analysis. Comparisons between linear (frequency domain) heave and pitch RAOs against model tests are presented for the pulsating and translating source Green functions. It is found out that the results obtained using the translating and pulsating Green function in conjunction with the Kelvin wave flow agree better with the experimental data. Results for the non linear and linear hydroelastic responses are also compared and presented in time domain for heave and pitch motions, horizontal and vertical deflections and Von Mises stress at relevant points of the structure. These data highlights the increase in the stress predicted by the second order hydroelastic theory especially when the variation of the instantaneous wetted surface area is included.

In Park and Temarel [2007], the nonlinear two dimensional hydroelasticity response in regular head waves is obtained. The main concept lies in separating the principal coordinates into linear and nonlinear parts. In this sense, two methods are used: convolution and direct integration techniques. In the convolution method, linear and nonlinear solutions are combined, meaning that the time domain response is estimated by IRFs (calculated from the frequency domain analysis by inverse Fourier Transforms) convoluted with linear and non linear force components. The second method evaluates hydrostatics and hydrodynamic effects on the instantaneous wetted surface and integrates the equations of motion directly in time domain. Results of nonlinear symmetric responses, heave and pitch motions as well as bending moments and shear forces, are presented for a range of speeds and wave length and steepness values for the S175 container ship moving in regular head waves. Comparisons between linear theory and the presented results are made, pointing out the significance of non linear effects in the prediction of sagging and hogging bending moments. In addition, the presented results are in agreement with available experimental data of the bending moment loads of the S175 container ship.

The fluid structure interaction of a nonlinear / non-periodic incident wave over a vertical elastic plate is studied by He and Kashiwagi [2009]. Two-dimensional simulations are carried out in time domain. The free surface flow is modeled by a MEL scheme which is solved by a higher order BEM. On the other hand, FEM is used to address the structural problem. The coupled motions are then solved

as single system in a monolithic way using a fourth order uniform time step with Rungge Kutta integrator. Comparisons of the results showed that the hydroelasticity behaviour depends, as should be expected, on the plate stiffness and on the edge conditions of the plate. Linear analytical solutions of the wave elevation are also compared with nonlinear calculations showing a similar behaviour but flatter troughs.

2.3 Conclusive Remarks

From the above, it is clear that up to now the afore mentioned drawbacks of the MEL scheme have, to a certain extent, limited its applicability to the fully non linear seakeeping problem of more realistic hull forms. For a fully nonlinear computation it seems that the major problems to overcome are related to wave breaking and the mesh distortions caused by the clustering of Lagrangian particles in regions of high velocity gradients (Longuet-Higgins and Cokelet [1976]); both problems leads to a simulation break up. Alternatives are currently being tried and evaluated. For instance, in Zhang et al. [2007] it is argued that the clustering of Lagrangian particles can be circumvented by the desingularized boundary element method, placing the sources above the free surface and keeping them fixed throughout the simulation.They also use a linear form of the free surface boundary conditions , that in theory , should prevent or at least delay the breaking wave phenomenon.

However, some developments did take place, especially in what concerns the run time of the algorithms. For instance, Liu et al. [2001] used a generalized minimum residual algorithm (GMRES) and a symmetric successive over relaxation (SSOR) pre-conditioning;tin this method the computational effort required was at most $O(N^{2.3})$. On the other hand, iterative methods for the calculation of far field influences, such as the Fast Multipole Method Boundary Element Method Liu [2009] or the pre-corrected fast Fourier transform can reduce the computational effort to at most $O(NlogN)$, hence allowing large scale problems to be tackled at the cost of daunting numerical implementation.

Chapter 3

Frequency Domain and partly non linear Seakeeping Analysis

The aim of this chapter is to compare the heave and pitch motions for the S175 containership, travelling in head regular waves, obtained from existing frequency domain linear and time domain partly nonlinear potential flow analyses. The frequency domain methods comprise the pulsating and the translating, pulsating Greens function methods, with the relevant source distribution over the mean wetted surface of the hull. The time domain method uses the radiation and diffraction potentials related to the mean wetted surface, implemented using Impulse Response Functions (IRF), whilst the incident wave and restoring actions are evaluated on the instantaneous wetted surface. The calculations are carried out for a range of Froude numbers, and in the case of the partly nonlinear method for different wave steepness values. Comparisons are made with available experimental measurements. The analysis of the results highlights the necessity of a more accurate nonlinear approach for predicting the radiation potential.

3.1 Linear Analysis in Frequency Domain

In this section a brief description of the main features of linear frequency domain theory is given. A more detailed description can be found in Inglis [1980]. The aim of linear frequency domain analysis is to solve Laplace's equation in the fluid

domain, subject to the so called linearised boundary conditions. In the boundary element context this gives rise to an exterior Neumann problem, where the singularities (in this case the pulsating or translating pulsating Green's function) are distributed on the wetted mean surface of the hull, satisfying both free surface boundary conditions and the radiation condition at infinity. The boundary value problem is then solved for the potential on the hull surface, which is then used to estimate the hydrodynamic coefficients and the exciting forces acting on the ship. Subsequently the equations of motion, for each encounter frequency, are solved yielding transfer functions, or Response Amplitude Operators (RAOs) over the whole frequency range.

In this approach the velocity potential is assumed to decouple into two parts namely, steady and unsteady. In addition, the unsteady potential is also decomposed into components relating to incident wave excitation, diffraction and radiation. Furthermore, if the ship is in the presence of plane progressive waves, both fluid and rigid body motions can be considered to be time harmonic Newman [1977]. Hence, denoting $\hat{\phi}$, ϕ_0 and ϕ_7 the steady, incident wave and diffraction potentials respectively. In addition, letting ϕ_j , j=1,..,6 , be the radiation potentials and ξ_j, j=1, ...,6 be the amplitude of the motions that body experiences in surge, sway, heave, roll, pitch and yaw respectively, the total velocity potential can be written in the following form Newman [1977]:

$$\Phi(\vec{x},t) = U\hat{\phi} + \Re(\exp(i\omega_e t)(\phi_0 + \phi_7 + \sum_{j=1}^{6} \xi_j \phi_j)). \tag{3.1}$$

In equation 3.1, $\vec{x}$ is expressed at the equilibrium axis along the ship, with the equilibrium axis system typically being right handed, situated at the mean water line with its origin aligned with the longitudinal position of the center of gravit and pointing upwards. U denotes forward speed and ω_e is the encounter frequency, evaluated in deep water, i.e:

$$\omega_e = \omega + Ukcos(\chi), \tag{3.2}$$

where, ω is the wave frequency, and in deep water, $k = \omega^2/g$. χ is incident wave angle, measured from the bow, counterclockwise.

Denoting the normal direction of the mean wetted surface of the hull by $\vec{n}$, the boundary conditions for the incident wave and diffraction potentials, i.e the impervious boundary condition on the hull (or Neumann boundary conditions) are imposed on the mean wetted surface, S, of the hull, namely:

$$\frac{\partial(\phi_0 + \phi_7)}{\partial n} = 0. \tag{3.3}$$

Phisically, the radiation boundary condition states that the normal velocity of the fluid is the same as the normal velocity of the hull on its (mean) wetted surface. Its treatment is more subtle because, in the presence of forward speed, it accounts for contributions not only of the radiation potentials but also the steady potential. It is in order to simplify the treatment of the radiation boundary condition that some simplifications in the form of the steady flow are made. Neglecting second order terms the steady flow velocity, in the equilibrium axis system, is expressed as $\vec{W} = U\nabla(\phi - x_1)$. The boundary condition for the radiation potentials, on the mean surface S, then becomes Olgilvie and Tuck [1969]:

$$\frac{\partial \phi_j}{\partial n} = i\omega_e n_j + U m_j, \tag{3.4}$$

where n_j denote the components of the normal vector and the terms m_j involve the influence of the steady flow Inglis [1980]. If it is assumed that the perturbation of the flow due to steady forward motion can be neglected, then the m_j terms can be further simplified to m_j=0 for j=1,2,3,4 and $m_5 = n_3$, $m_6 = -n_2$ by uncoupling steady and unsteady flow effects, namely $\vec{W} = (-U, 0, 0)$.

Under these considerations, the free surface can be linearised Newman [1977]. Therefore, the boundary conditions for the unsteady potentials are given by:

$$\frac{\partial \phi^2}{\partial t^2} - 2U\frac{\partial \phi^2}{\partial t \partial x} + U^2\frac{\partial \phi^2}{\partial x^2} + g\frac{\partial \phi^2}{\partial x^2} = 0. \tag{3.5}$$

Equation 3.5 further simplifies for simple harmonic variation with time, with the pulsating source satisfying the zero forward speed and the translating, pulsating source the forward speed dependent free surface condition, respectively Newman [1977]. The remaining far field boundary condition is satisfied by both the pulsating and translating, pulsating Green's functions. Therefore, Laplace's

equation together with the boundary conditions specified by equations 3.3, 3.4, 3.5 and the far field radiation condition constitutes an exterior Neumann problem, which is solved for the potential on the hull.

It is also important to point out that since the potential 3.1 is harmonic in time, the value of its time derivative (needed to calculate the pressure acting on the hull) can be easily derived from the potential value itself analytically.

Once the incident wave potential is given and the radiation and diffraction potentials are known one can estimate exciting forces and hydrodynamic coefficients at each encounter frequency. Therefore, the equations of motion for the ship in regular waves can be written as Salvensen et al. [1970]:

$$\sum_{j=1}^{6} \xi_j(-\omega_e^2(M_{ij} + A_{ij}) + i\omega_e B_{ij} + C_{ij} = aF_i \tag{3.6}$$

Equation 3.6 is a system of six simultaneous linear equations which are solved for the ship motions ξ_j. The coefficients M_{ij} refer to the mass and inertia properties of the ship. A_{ij} and B_{ij} are hydrodynamic added mass and damping coefficients obtained from the radiation potentials Inglis [1980]. C_{ij} are the hydrostatic restoring coefficients, a is the wave amplitude of the regular wave and F_i, i=1 to 3, corresponds to the forces in surge, sway, heave and moments (i=4 to 6) in roll, pitch and yaw, respectively. The quantities of interest in the present analysis are the heave and pitch motions, namely ξ_3 and ξ_5.

3.2 Time domain Partly non Linear Method

In this section a summary of the main features of the partly nonlinear method, Bailey et al. [1998] and Ballard et al. [2003], is provided. The main goal is not to explain the method in detail, but rather describe the basic equations and link the impulse response functions to the estimation of the coefficients for the system of differential equations to be solved.

In this chapter when using the partly nonlinear method the ship motions are referenced to the body (fixed) axes. The body axes comprise an upright right handed coordinate axes Cxyz with the origin C at the centre of gravity of the hull, and Cxz in its longitudinal plane of symmetry.

In the case of symmetric motions, ignoring the effects of surge, it can be shown that heave and pitch accelerations, $\dot{w}$ and $\dot{q}$ (adopting the conventional manoeuvring nomenclature) , can be written as a function of the heave and pitch velocities, w and q, the displacement of the ship centre of gravity, z_C, the Euler pitch angle, θ and time t. That is to say:

$$\begin{pmatrix} f_w(w,q,z_C,\theta,t) \\ f_q(w,q,z_C,\theta,t) \end{pmatrix} = \begin{pmatrix} m - \tilde{Z}_{\dot{w}}(\infty) & -\tilde{Z}_{\dot{q}}(\infty) \\ -\tilde{M}_{\dot{w}}(\infty) & I_{yy} - \tilde{M}_{\dot{q}}(\infty) \end{pmatrix} \begin{pmatrix} \dot{w}(t) \\ \dot{q}(t), \end{pmatrix} \tag{3.7}$$

where the matrix in the right hand side of equation 3.7 contains the ship mass, m, the pitch moment of inertia I_{yy}, as well the infinite frequency value of the acceleration oscillatory coefficients. It is interesting to point out the analogy between $\tilde{Z}_w$ and A_{33}, $\tilde{Z}_q$ and A_{35},$\tilde{M}_w$ and A_{53} and $\tilde{M}_q$ and A_{55}, namely the acceleration oscillatory coefficients in the body axes and the added mass coefficients in the equilibrium axes. The relationships between these coefficients are given in Bailey et al. [1998].

The functions f_w and f_q physically represent the forces (for heave) and moments (for pitch) acting on the ship . For the heave mode, it can be written as Bailey et al. [1998]:

$$f_w = Z_\tau + Z_{\alpha r} + \tilde{Z}_w(\infty)w + \tilde{Z}_q(\infty)q + mqU, \tag{3.8}$$

and for pitch as:

$$f_q = M_\tau + M_{\alpha r} + \tilde{M}_w(\infty)w + \tilde{M}_q(\infty)q. \tag{3.9}$$

In equations 3.8 and 3.9 the terms $\tilde{Z}_w$, $\tilde{Z}_q$,$\tilde{M}_w$ and $\tilde{M}_q$ contain the infinite values of the velocity oscillatory coefficients. These are analogous to the damping coefficients B_{33}, B_{35}, B_{53} and B_{55} used in the conventional seakeeping analysis and relationships between them and the oscillatory coefficients are given byBailey et al. [1998]. The main difference is that the former are defined with reference to the body axes whereas the latter are, by definition, expressed in the equilibrium axes. In equations 3.8 and 3.9, Z_τ and M_τ are the forces and moments due to

radiation potentials. These are expressed in terms of convolution integrals, ie:

$$Z_\tau = \int_0^t z_w * (\tau) w(t-\tau) d\tau + \int_0^t z_q * (\tau) q(t-\tau) d\tau, \tag{3.10}$$

$$M_\tau = \int_0^t m_w * (\tau) w(t-\tau) d\tau + \int_0^t m_q * (\tau) q(t-\tau) d\tau, \tag{3.11}$$

where z_w^* and z_q^* represent the heave- heave and heave-pitch IRFs, whereas m_w^* and m_q^* are the pitch-heave and pitch-pitch IRFs. In the present work these IRFs are obtained from the frequency domain hydrodynamic data (i.e. hydrodynamic damping coefficients) through the use of discrete Fourier transforms. Thus, it can be seen that these hydrodynamic forces and moments are with reference to the mean wetted surface.

The terms $Z_{\alpha r}$ and $M_{\alpha r}$ in equations 3.8 and 3.9 account for the wave disturbance (incident and diffraction) and restoring actions. The Froude-Krylov (incident wave) and restoring actions are evaluated over the instantaneous wetted surface. This requires discretisation (i.e. panelling) of the entire surface of the ship, up to the main deck, and identification of the instantaneous attitude of the ship with respect to the incident wave. Subsequently the pressures over the instantaneous underwater portion of the hull are summed up to provide relevant forces and moments. On the other hand the diffraction actions are evaluated in a manner similar to equation 3.10 or 3.11. That is to say the frequency domain diffraction force (or moment) provides an IRF, through discrete Fourier transform, and the diffraction actions (with respect to the mean wetted surface) are expressed as convolution integrals Ballard et al. [2003].

Finally, the time domain evaluation of the vessel's motions is carried out using a fourth order Runge-Kutta method in which the velocities are calculated for a set of time steps of fixed increments, i.e solving equation 3.7 . At the start of a simulation, the calm water equilibrium position of the vessel is determined. The subsequent motions are then calculated with reference to this initial position Ballard et al. [2003].

3.3 Results

The methods outlined in sections 3.1 and 3.2 are applied to the prediction of the motions of the S175 container ship travelling in regular head waves. The main particulars of the containership are shown in table 3.1. The body plan of the S175 container ship is shown in Figure 3.1.

Table 3.1: Main particulars of the S175 container ship

Length between perpendiculars(m), L	175
Beam(m)	25.4
Depth (m)	15.4
Draught (m)	9.5
Displacement (tonnes)	24860

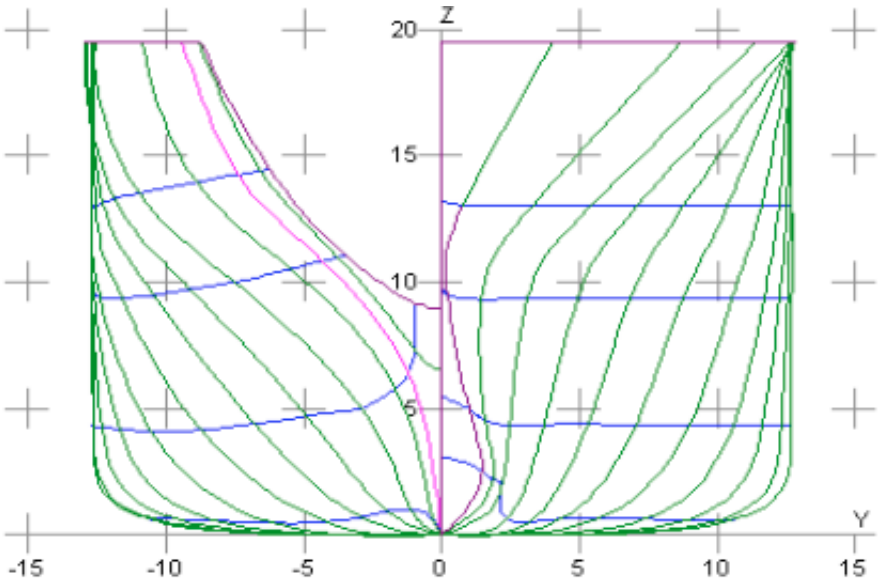

Figure 3.1: Body plan of the S175 container ship.

The first step is to identify a suitable idealization of the mean wetted surface, in terms of obtaining a converged solution with the number of panels used. To this end panel numbers between 288 and 2358 were used to idealise the mean wetted surface, ensuring an adequate panel aspect ratio of 2:1 Bailey et al. [2002]. The crudest and finest mean wetted surface idealizations are shown in figure 3.2.

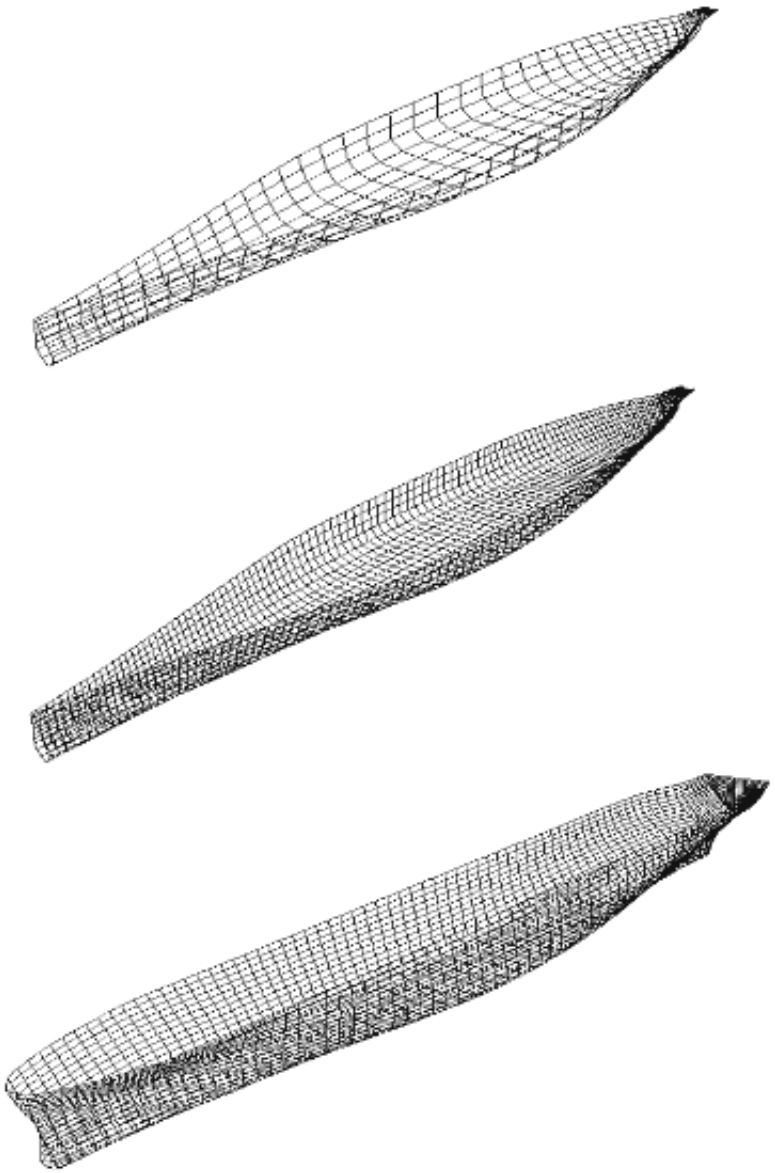

Figure 3.2: Idealization of the surface of the S175 containership; top 588 and middle 2358 panel idealizations of mean wetted surface; bottom 2880 panel idealization of the whole surface up to deck for the partly nonlinear method.

As an example the variation of heave and pitch non-dimensional damping coefficients, obtained from the pulsating source method, for different mean wetted surface idealizations are shown in figure 3.3 for Fn=0.2.

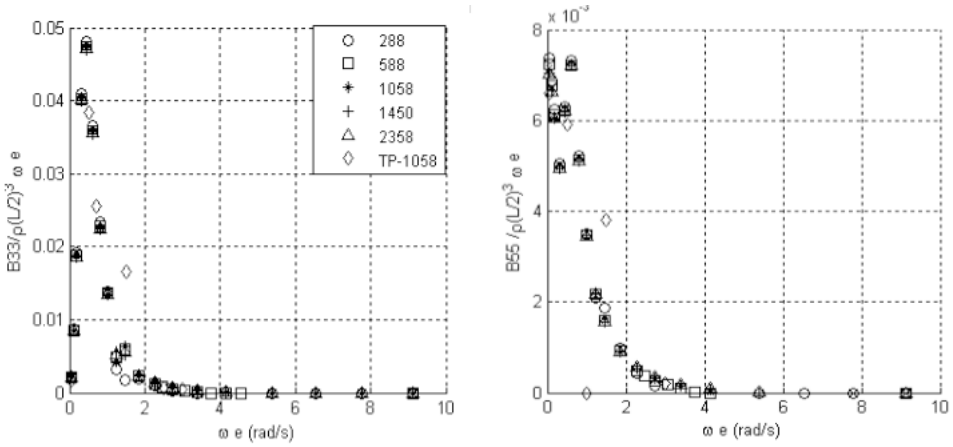

Figure 3.3: Non-dimensional heave and pitch damping coefficients (Fn=0.2) obtained using the pulsating source (various panel numbers on the mean wetted surface) and the translating, pulsating source (TP-1058 panels on mean wetted surface).

Examining the dependence of all the hydrodynamic coefficients on number of panels used, it was concluded that use of 288 panels showed large differences compared to other idealizations. Furthermore, the results using 1058, 1450 and 2358 panels showed negligible differences, indicating that convergence has been achieved. This is confirmed by the heave (heave/wave amplitude) and pitch (pitch/wave amplitude) RAOs shown in figure 3.4 for Fn=0.2. Based on this results the mesh with 1058 panels was selected to perform the remainder of the linear seakeeping analysis.

In addition, for the mesh up to the deck used for the partly non linear method, the panel size was held as close as possible to the panel size of the mean wetted surface idealization with 1058 panels. This resulted in a mesh of the S175 model up to deck line with 2880 panels, shown in figure 3.2. It should be noted that although the range of encounter frequencies shown in figure 3.3 is limited, when the pulsating source frequency domain method was used, the hydrodynamic coefficients were evaluated for a larger range of encounter frequencies, so that an

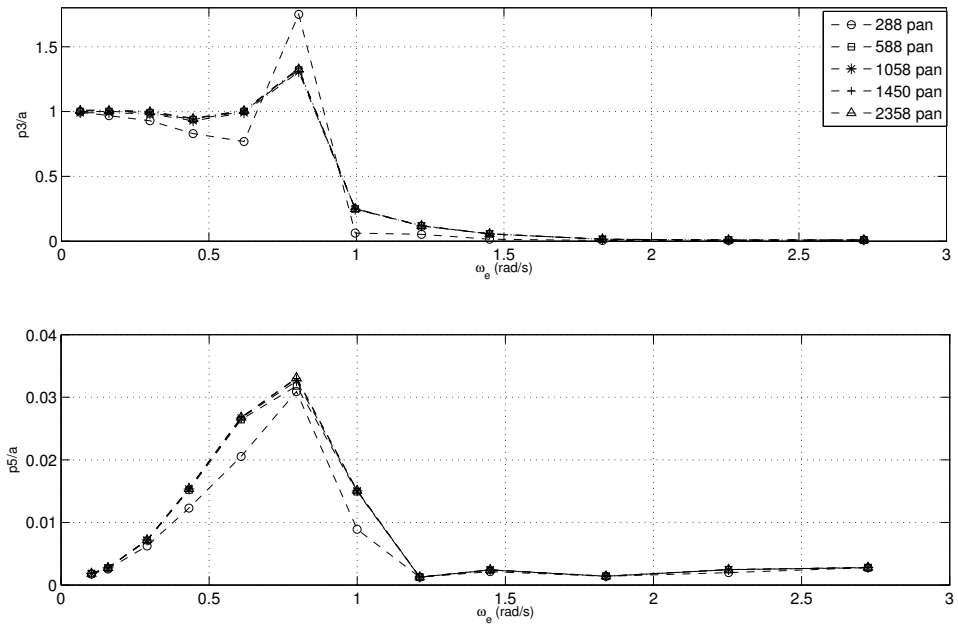

Figure 3.4: Illustration of convergence for the heave and pitch RAOs, with various panel numbers on the mean wetted surface, obtained using the pulsating source method for the S175 containership travelling in head regular waves, Fn=0.2.

accurate discrete Fourier transform could be used to estimate the IRFs Ballard et al. [2003].

There are two sets of results. The first set comprises variation of heave and pitch RAOs with encounter frequency for a range of Froude numbers; Fn=0.2, 0.25 and 0.275 when using the pulsating source and partly nonlinear methods, Fn=0.2 and 0.275 when using the translating, pulsating source method. In the case of the partly nonlinear analysis three wave amplitudes are investigated, i.e. a=1, 3 and 5 m. These results are shown in figures 3.5, 3.6 and 3.7 for Froude numbers Fn= 0.2, 0.25 and 0.275, respectively. Note that p_3 and p_5 denote xi_3 and xi_5, respectively. It should be noted that the pitch RAO is in the form of pitch amplitude (rads)/wave amplitude.

First let us focus on the trends of the predictions obtained by the partly nonlinear method. The differences in predicted RAOs due to different wave amplitudes become notable in the vicinities of the peaks. For both heave and pitch RAOs and all Froude numbers investigated a decrease is observed, in general, in the RAO with increasing wave amplitude. A notable exception to this trend relates to the heave RAOs at $\omega_e = 1$ rad/s for all Fn values. In fact for Fn=0.275 the heave RAO predicted in 5m amplitude waves is nearly zero and out of line with the general trends observed. It should be noted that a wave amplitude a=5m corresponds to a rather steep wave, i.e. wave steepness values ka in excess of 0.12, as can be seen from Table 3.1. The predicted pitch RAO, at the same frequency also shows mixed trends with the pitch RAO for a=3m being larger or same as that for a=1m, at Fn=0.25 and 0.275, respectively. The rate of decreases in the heave RAOs with increasing wave amplitude remains more or less unchanged with increasing Froude number. On the other hand this rate increases with increasing Froude number for the pitch RAOs, as can be seen by comparing figures 3.5, 3.6 and 3.7. In general the rate of change in the RAOs is larger from 1m to 3m wave amplitude and smaller from 3m to 5m wave amplitude. The question that is arising here requires further investigation to establish whether it is a real trend or due to the partly nonlinear method reaching the limits of its validity.

It is important to compare the differences between the RAOs predicted by the linear pulsating source method and the partly nonlinear method. For the lowest of forward speeds (Fn=0.2) the linear heave RAO is smaller than the

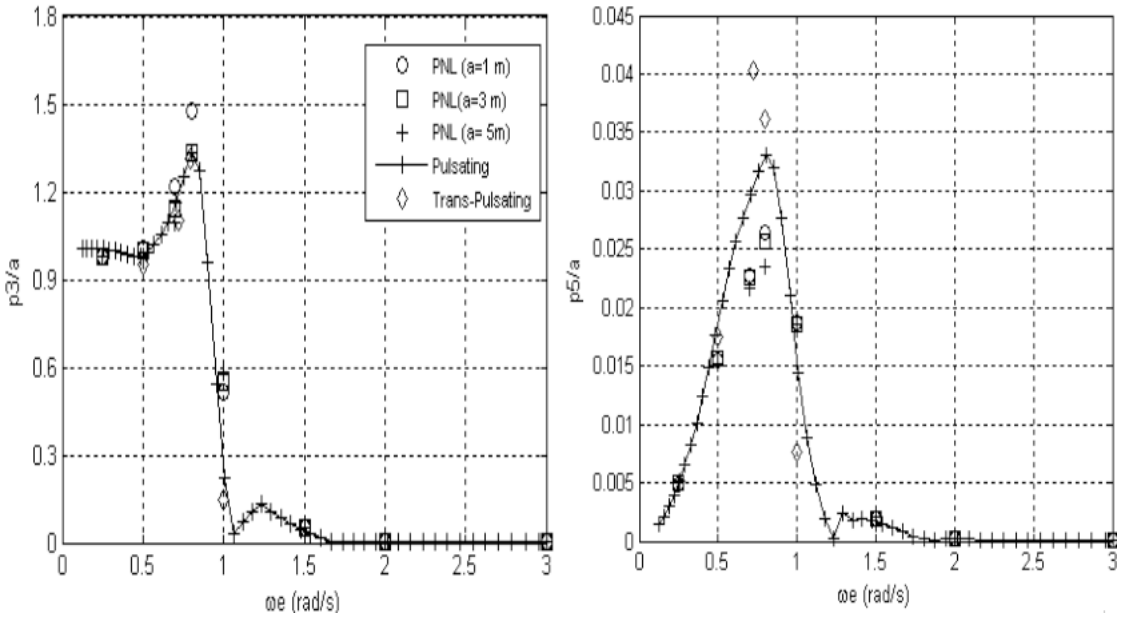

Figure 3.5: Heave and pitch transfer functions for the S175 containership travelling in head regular waves, Fn=0.2; comparison of linear (pulsating and translating, pulsating source) and partly nonlinear (PNL) methods.

partly nonlinear prediction for a=1m. The heave RAOs predicted by the partly nonlinear method for a=1m are the same and smaller than the linear predictions for Fn=0.25 and 0.275, respectively. The trend observed for Fn=0.2 is contrary to expectations of the behaviour of nonlinear methods. As this effect seems to be more pronounced at low speeds it may be linked to the differences in the hydrostatic restoring actions between the linear method based on the mean wetted surface and the partly nonlinear method using the instantaneous wetted surface. Thus it may be possible to argue that at higher Froude numbers the hydrodynamic actions have a more pronounced effect, hence decreasing the influence of the differences in the hydrostatic restoring coefficient. On the other hand the pitch RAOs predicted by the pulsating source method are, in general, larger than the partly nonlinear predictions for all Froude numbers. Nevertheless for Fn=0.275 the pitch RAO predicted by the partly nonlinear method for a=1m is very close to the linear (pulsating source) prediction. The aforementioned reasoning on the differences of the hydrostatic coefficients may also explain the trends observed when comparing linear and partly nonlinear pitch predictions.

The RAO predictions obtained from the translating pulsating source method are shown in figures 3.5 and 3.7, for Fn=0.2 and 0.275, respectively. The heave RAOs predicted by the pulsating and the translating, pulsating source methods are comparable for both Froude numbers. At the highest speed (Fn=0.275) the pitch RAOs predicted by the translating, pulsating source are much higher than the pulsating source predictions, peak values approximately 3.5 times higher. Examining the pitch damping coefficient B_{55}, shown in figure 3.3, it can be seen that the value predicted by the translating, pulsating source method is much lower than that of the pulsating source method in the frequency range where the pitch RAO peaks. Similar trends between pulsating and translating, pulsating source predictions, at relatively high Froude numbers were observed for a NPL hull form Bailey et al. [1999]. This is an important issue in terms of the applicability of the translating, pulsating source method, especially at higher speeds. The influence of the steady flow and its effect on the body boundary conditions (rather than using the simplified conditions given by 3.4) may provide an explanation of the differences observed.

The second set of results compares predicted heave and pitch RAOs against

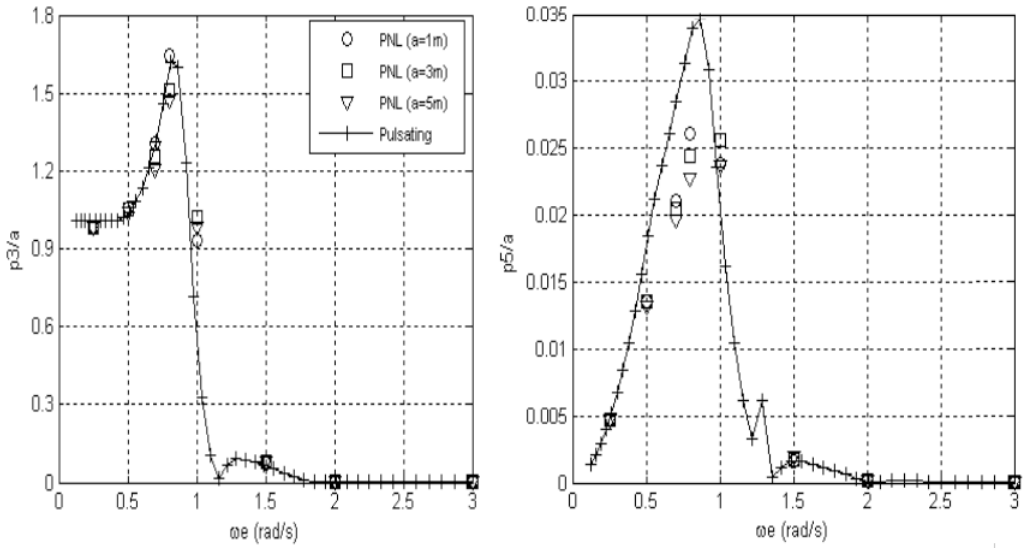

Figure 3.6: Heave and pitch transfer functions for the S175 containership travelling in head regular waves, Fn=0.25; comparison of linear (pulsating source) and partly nonlinear (PNL) methods.

the available experimental data. In this case, due to the limited number of experimental measures available and also bearing in mind the importance of wave steepness fin this particular experiment, the results are presented in a slightly different format, i.e as function of the wave steepness. Moreover, the pitch amplitude p_5, is now normalized by the wave steepness, ka, as well.

That said, the RAOs in heave and pitch, for three different wave to ship length ratios, a range of wave steepness values ka and two Froude numbers Fn=0.2 and 0.275 are shown in figure 3.8. The results predicted by the partly nonlinear method are compared with the experimental measurements of Powers and Zselecsky [1992]. The corresponding linear pulsating source predictions are also shown, in the form of constant lines for each λ/L value. The relationships between various wave properties for this second set of results are shown in table 3.2.

The basic trend displayed by the experimental results, namely a decrease in RAOs with increasing wave steepness ka is observed in all predictions by the partly nonlinear method, except for $\lambda/L = 1.0$ and Fn=0.275 where the predictions show a small increase with increasing ka values. It can be seen from table

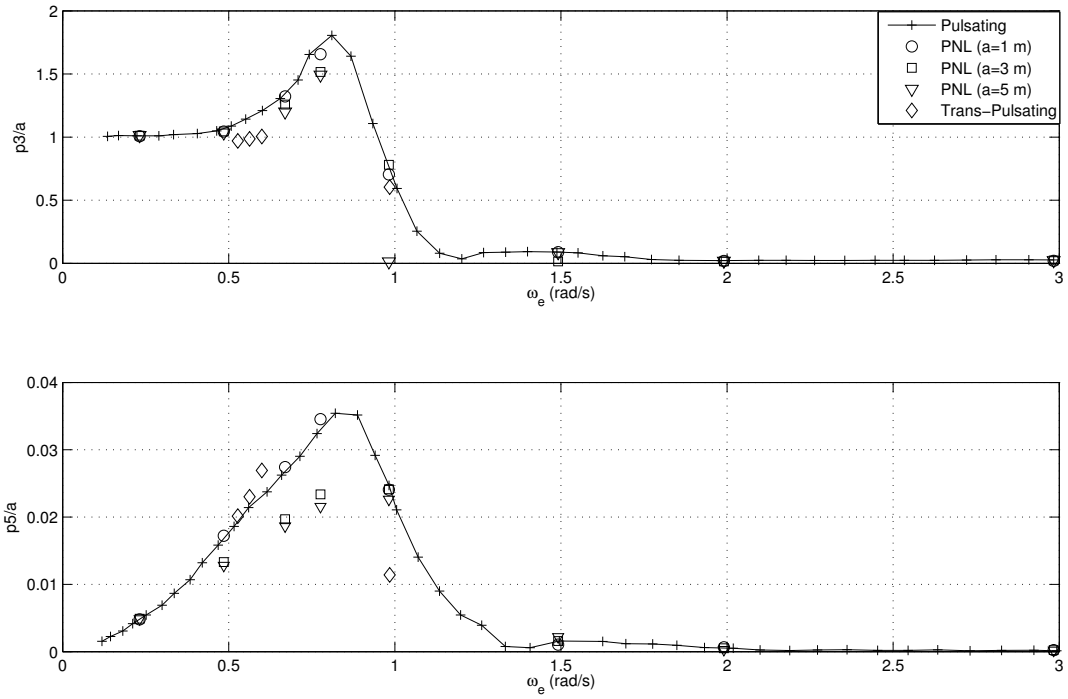

Figure 3.7: Heave and pitch transfer functions for the S175 containership travelling in head regular waves, Fn=0.275; comparison of linear (pulsating and translating, pulsating source) and partly nonlinear (PNL) methods.

Table 3.2: Relationship between wave length, wave frequency and wave slope; encounter frequency in regular head waves

	$\frac{\lambda}{L} = 1.4$	$\frac{\lambda}{L} = 1.2$	$\frac{\lambda}{L} = 1.0$
ω (rad/s)	0.5	0.54	0.59
ω_e (rad/s) and Fn=0.20	0.71	0.79	0.89
ω_e (rad/s) and Fn=0.275	0.79	0.88	1.01
k (1/m)	0.025	0.030	0.036

3.2 that this corresponds to $\omega_e = 1$ in figure 3.7 and was discussed above. It is interesting to note that both heave and pitch RAOs in figure 3.7 show a decrease when a=5m, tying up with the experimental trends for ka values in excess of 0.12. Heave RAOs predicted by the partly nonlinear method are higher than the experimental measurements, as well as the linear predictions by the pulsating source method, for Fn=0.2. Pitch RAOs predicted by the partly nonlinear method are a little higher than the experimental measurements, and the pulsating source prediction, for$\lambda/L = 1.0$ and Fn=0.2. For the same Fn=0.2, pitch RAOs predicted by the partly nonlinear method are lower than the experimental measurements, and closer to these measurements than the linear prediction, for $\lambda/L = 1.2$ and $\lambda/L = 1.4$. Heave RAOs predicted by the partly nonlinear method are closer to the experimental measurements, though a little higher, than the linear pulsating source prediction for $\lambda/L = 1.2$ and $\lambda/L = 1.4$ and Fn=0.275. Pitch RAOs predicted by the partly nonlinear method for Fn=0.275 and for $\lambda/L = 1.2$ and $\lambda/L = 1.4$ are close to each other, as are the linear predictions, and close to the experimental measurements for $\lambda/L = 1.4$, but higher than the measurements for $\lambda/L = 1.2$. Overall it can be said that the partly nonlinear method offers improvement in predictions with reference to trends with increasing wave steepness. The quantitative agreement, based on the limited set of measurements used here, is reasonably good, although it can be patchy on occasion.

In the context of non linear effects, the reasonably good qualitative agreement pointed out in figure 3.8 can be explained by the ability of the partly nonlinear method in accounting for the changes in the submerged geometry of the body and the effects of the water line dynamics. Although their contribution is approximated, since only Froude Krylov and hydrostatic forces are being calculated

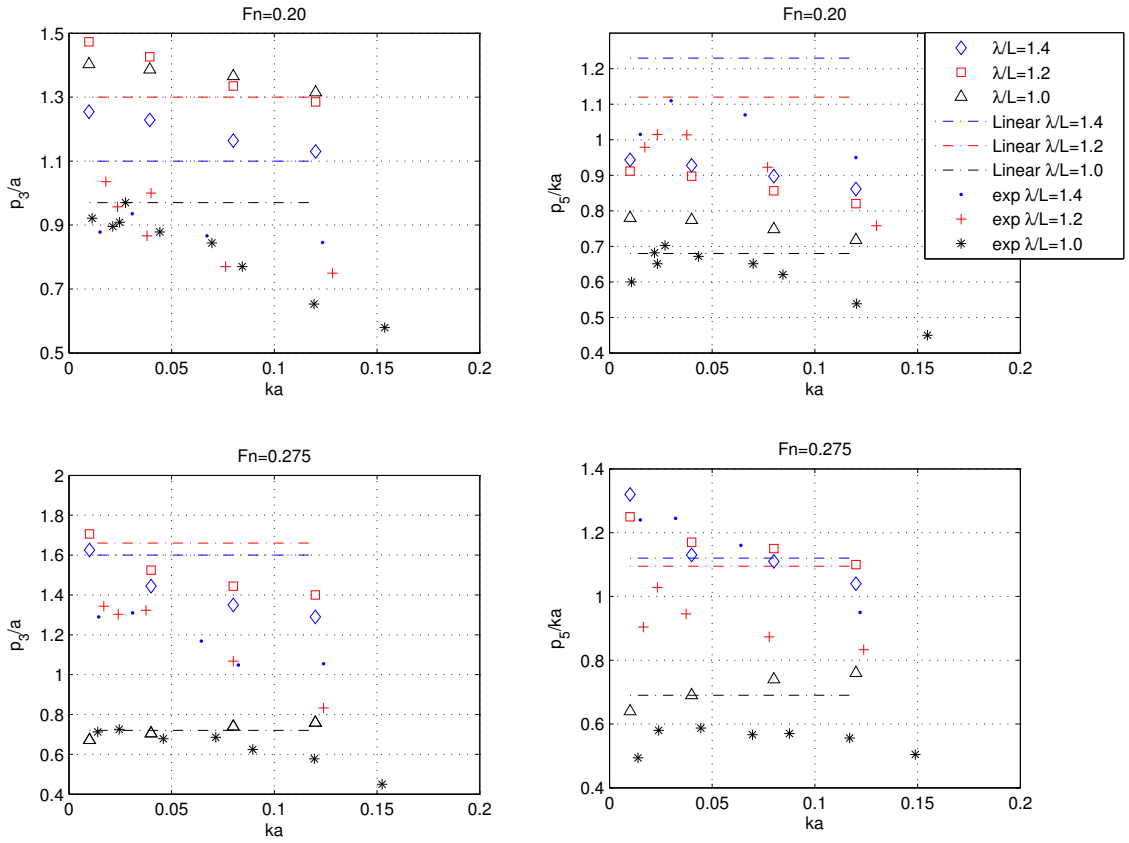

Figure 3.8: Comparison between numerical (partly nonlinear and linear) and experimental heave and pitch RAOs for the containership travelling in head regular waves, Fn=0.2 and Fn=0.25.

exactly, the incorporation of these effects deviates the results considerably from the predictions of linear theory as a function of the wave steepness. In fact, this suggests that modelling these two sources more accurately can yield a better qualitative agreement against experimental data (say a time domain body non linear approach for instance). That said, there is still non linear contributions that can come from the exact free surface boundary conditions whose effects cannot be addressed in the partly non linear analysis.

3.4 Conclusive Remarks

An investigation has been carried out comparing predictions obtained from three-dimensional linear, pulsating and translating, pulsating source, and partly non-linear methods, together with comparisons with available experimental measurements. The S175 containership, travelling regular head waves at a range of Froude numbers and wave amplitudes, was used as an example for this investigation.

Based on this limited investigation it can be concluded that the partly nonlinear method offers, in general, improvements in predicting heave and pitch RAOs. Nevertheless, more comparisons with experimental measurements are necessary in order to establish the range of validity of this method.

In the case of linear methods, the pulsating source method produces better predictions, by comparison to the translating, pulsating source method at reasonably high Froude numbers. The influence of steady flow on the translating, pulsating source method needs further investigation.

The quality of the agreement with experimental measurements tends to emphasize the need for development of nonlinear methods, still within the potential flow domain, accounting for nonlinearities in radiation and diffraction potentials. In what follows of the present work, efforts will be concentrating in the problem of addressing the non linear effects related to the radiation potential. In order to address this issue, the boundary value problem needs to be formulated in time domain and the time harmonic representation of the potential (equation 3.1), does not hold true anymore. In particular, instead of solving a exterior Neumann boundary value problem, a mixed interior boundary value problem formulation will be derived.

In this context, the linear time domain problem will be addressed first, for both rigid and flexible forced oscillations motions. Subsequently, the non linear effects will be introduced in chapter 7.

Chapter 4

Problem Formulation in Time Domain

The Mixed Eulerian Lagrange description of the fluid flow has essentially two stages: in the first one for a potential given on the Dirichlet boundary (free surface) and a given normal velocity on Neumann boundaries (floating body or fixed walls), the mixed boundary value problem is solved yielding the the normal velocity on the free surface and the potential on the floating body, this is the Eulerian phase. In the second step, Lagrangian phase, the kinematic and dynamic boundary conditions are integrated in time so that the the position of the free surface and its potential are updated. The process is then repeated in time. In the first section of this chapter, the integral equations of the boundary value problem (Eulerian phase) are derived. Next, the boundary value problem is combined with the kinematic and dynamic boundary conditions on the free surface so that the MEL scheme is completed. Finally, the time marching scheme adopted is briefly discussed.

4.1 The Mixed Boundary Value Problem

It is interesting to start, in a slightly more general context, by formulating the weak form of Laplace's equation using the method of weighted residuals and then project the solution using the Dirac measure in order to obtain the collocation

(or conventional) Boundary Element formulation. This approach draws a parallel between the Finite Element and Boundary Element methods. Furthermore this structure allows for the introduction of different types of Boundary Element Methods, like Galerkin Boundary Element Methods, see for instance Sutradhar et al. [2008] and Steinbach [2008].

Hence, in order to describe the flow field a fixed three dimensional orthonormal, right handed, Cartesian system $Oxyz$ is used in the fluid domain Ω at the undisturbed free surface. This way, under the assumptions of ideal and irrotational flow, the equation governing the fluid motion on Ω reduces to the continuity equation, which can be equivalently expressed as the Laplacian of the flow potential:

$$\nabla^2\phi(\vec{x},t) = 0, \quad \vec{x} \in \Omega. \tag{4.1}$$

Consider now a very special weight function $G(\vec{x},\vec{y})$ which, for $\vec{x}$ and $\vec{y}$ in Ω, is fundamental solution of Poisson's equation, that is to say:

$$\nabla^2 G = -\delta(\vec{x}-\vec{y}), \quad \forall \vec{x},\vec{y} \in R^3. \tag{4.2}$$

If the weak form of equation 4.1 is multiplied by the weight function $G(\vec{x},\vec{y})$ and integrated over the domain, one has from Gauss' theorem and the properties of the divergence operator (see Apostol [1969] p. 446) that :

$$\int_\Omega \nabla^2\phi \cdot G d\Omega = \int_{\partial\Omega} G\nabla\phi \cdot \vec{n} d\Gamma - \int_\Omega \nabla\phi \cdot \nabla G d\Omega = 0. \tag{4.3}$$

Regarding the notation, note that the surface integrals evaluated on the domain boundary, $\partial\Omega$, are represented by $d\Gamma$ whereas $d\Omega$ is used for the evaluation of volume integrals.

Using Gauss theorem again on the last integral of 4.3 and equation 4.2 the weak form of Laplace equation using the fundamental solution as weight function becomes:

$$\int_{\partial\Omega} G\nabla\phi \cdot \vec{n} d\Gamma - \int_{\partial\Omega} \phi\nabla G \cdot \vec{n} d\Gamma - \int_\Omega \delta(\vec{x}-\vec{y})\phi d\Omega = 0. \tag{4.4}$$

Using the Dirac Delta function definition one has that:

$$\phi(\vec{x}) = \int_{\partial\Omega} G(\vec{x},\vec{y})\nabla\phi(\vec{y})\cdot\vec{n}d\Gamma - \int_{\partial\Omega}\phi(\vec{y})\nabla G(\vec{x},\vec{y})\cdot\vec{n}d\Gamma. \tag{4.5}$$

Equation 4.5 is valid in Ω and it can be extended to boundary ($\partial\Omega$) by taking the limit to yield the following boundary integral equation Liu [2009]:

$$c(\vec{x})\phi(\vec{x}) = \int_{\partial\Omega} G(\vec{x},\vec{y})\nabla\phi(\vec{y})\cdot\vec{n}d\Gamma - \int_{\partial\Omega}\phi(\vec{y})\nabla G(\vec{x},\vec{y})\cdot\vec{n}d\Gamma; \tag{4.6}$$

where $c(\vec{x})$ is the interior solid angle at $\vec{x}$. By its definition, $c(\vec{x})$ is equal to the area of the projection of the domain surface, $\partial\Omega$, onto a unit sphere centred at $\vec{x}$. Physically this equation reflects the mass conservation in the region enclosed by $\partial\Omega$ and the unit sphere centered at $\vec{x}$ Liu et al. [2001].

In addition, the boundary $\partial\Omega$ can be decomposed into N piecewise elements such that, $\partial\Omega = \bigcup_{j=1}^{N} E_j$. This leads to:

$$c(\vec{x})\phi(\vec{x}) = \sum_{j=1}^{N}\int_{E_j} G(\vec{x},\vec{y_j})\nabla\phi(\vec{y_j})\cdot\vec{n}dE_j - \sum_{j=1}^{N}\int_{E_j}\phi(\vec{y_j})\nabla G(\vec{x},\vec{y_j})\cdot\vec{n}dE_j. \tag{4.7}$$

In the context of the method of weighted residuals, the collocation method can be used to obtain the discrete version of the integral equation 4.7. The main idea of the collocation method is to take the projection of 4.7 using the Dirac measure and impose that at the collocation points, (or source points, E_i). The approximate solution has the same value as the unknown potential Karniadakis and Sherwin [2005]. In order to do this, in a non rigorous framework, one can define an integral operator $L(\vec{x})$ as:

$$L(\vec{x}) = -c(\vec{x})\phi(\vec{x}) + \sum_{j=1}^{N}\int_{E_j} G(\vec{x},\vec{y_j})\nabla\phi(\vec{y_j})\cdot\vec{n}dE_j - \sum_{j=1}^{N}\int_{E_j}\phi(\vec{y_j})\nabla G(\vec{x},\vec{y_j})\cdot\vec{n}dE_j; \tag{4.8}$$

and note that when $L(\vec{x}) = 0$ equation 4.7 is satisfied. Next, in order to impose that at collocation points the approximate solution satisfies equation 4.7, at each source point E_i, using the Dirac measure in a weighted residual sense, one has

that:

$$\int_{Ei} \delta(\vec{x} - \vec{x_i}) L(\vec{x}) dE_i = L(\vec{x_i}) = 0. \tag{4.9}$$

Using equation 4.9 in equation 4.7 for each source point i=1 to N, yields the following discrete version of 4.7:

$$c(\vec{x_i})\phi(\vec{x_i}) = \sum_{j=1}^{N} \int_{E_j} G(\vec{x_i}, \vec{y_j}) \nabla\phi(\vec{y_j}) \cdot \vec{n} dE_j - \sum_{j=1}^{N} \int_{E_j} \phi(\vec{y_j}) \nabla G(\vec{x_i}, \vec{y_j}) \cdot \vec{n} dE_j \tag{4.10}$$

It is worth pointing out that although equations 4.6 and 4.7 are equivalent, equation 4.10 is an approximation which exactly satisfies equation 4.6 (or 4.7) only at collocation points (or source points in the BEM terminology).

Since equation 4.10 holds for every i from 1 to N, it can also be written as linear system whose solution is an approximate solution of the integral equation 4.6 which is equivalent to solving Laplace's equation in a weak sense. In equation 4.10, the function $G(\vec{x_i}, \vec{y_i})$ is the so called single layer potential operator, whereas $\nabla G(\vec{x_i}, \vec{y_j}) \cdot \vec{n}$ is the double layer potential operator. Both of them can be seen as a basis in which the potential $\phi(\vec{x_i})$ is being approximated.

In fact, there are several different formulations that can be ensivaged in light of the Boundary Element theory. The approach used here simply discretize the integral equation 4.6, in the same fashion of Xu [1992]. Furthermore, since the problem is being solved directly for the potential of the fluid flow, the approach is called direct. Still in the context of direct boundary element method other approximations can be obtained. For instance it can be shown Steinbach [2008] that the potential can also be approximated not only by the single layer and the double layer potential operators, but also with the self adjoint and the hypersingular operators. The advantages or disadvantages of pursuing such alternatives formulations in the context of hydrodynamic simulations can be an interesting avenue for future research.

The main advantage of BEM over FEM is that the problem is formulated on the boundary, having a lower dimensionality. However the integrals that arise in BEM formulations are usually singular and often require special numerical treat-

ment for the assembly of the influence matrix. In this work, when the source point and the field point are not on the same element standard Gaussian quadrature are used. For the singular case, i.e when source and field points lie on the same element, the integrand is first desingularized using the polar mapping technique, before being integrated. The details regarding the calculation of the influence matrices and the assemblage of the linear system are detailed in the Appendix A Numerical Techniques. In addition, for the problem to be well posed, a suitable set of boundary conditions need to be applied. These are going to be dealt with in the following section.

4.2 Boundary Conditions

Equation 4.10 admit two kinds of boundary conditions namely: Neumann (or natural) and Dirichlet (or essential) boundary conditions. In the context of potential flow simulations, Neumann boundary conditions are the impervious boundary conditions which are imposed on the surface of the floating body or in other impervious surfaces, whereas Dirichlet boundary conditions are associated with the potential value on the free surface. In addition to the essential and natural boundary conditions, in order to account for the presence of the free surface the kinematic and dynamic boundary conditions need also to be satisfied. At last, a radiation boundary condition also needs to be imposed. The radiation condition physically implies that there is no wave reflection at the boundaries of the free surface, i.e the waves travel to "infinity".

More precisely, on the body surface, S_N, the impervious boundary condition states that the normal velocity of the flow should equal the body velocity, $\vec{V}(\vec{x},t)$; this can be written as:

$$\nabla\phi(\vec{x},t)\cdot\vec{n} = \vec{V}(\vec{x},t)\cdot\vec{n}. \tag{4.11}$$

At the free surface, S_D, the kinematic boundary conditions states that the velocity of a particle equals the gradient of the velocity potential. Hence if $\vec{x}(t)$ denotes the position of a fluid particle in R^3 its velocity can be expressed as

Longuet-Higgins and Cokelet [1976]:

$$\frac{D\vec{x}(t)}{Dt} = \nabla\phi, \tag{4.12}$$

where $\frac{D\vec{x}(t)}{Dt}$ is the material derivative (or Lagrangian derivative) and denotes differentiation following a given particle.

The dynamic boundary condition is derived from Bernoulli's equation. In Lagrangian coordinates Bernoulli equation is written as Newman [1977]:

$$\frac{D\phi}{Dt} = \frac{1}{2}\nabla\phi \cdot \nabla\phi - gz \tag{4.13}$$

It should be clear that boundary conditions 4.12 and 4.13 are the so called fully non linear free surface boundary conditions. For instance, in the context of linear analysis it was shown by Newman [1977] that equations 4.12 and 4.13 can be simplified, respectively, to:

$$\frac{\partial z}{\partial t} = \frac{\partial \phi}{\partial z}; \tag{4.14}$$

$$z = -\frac{1}{g}\frac{\partial \phi}{\partial t}. \tag{4.15}$$

Therefore, in order to perform time domain simulations using linearized free surface boundary conditions, equations 4.14 and 4.15 can be imposed on the exact free surface, which differs from the frequency domain approach, and the mixed boundary value problem is solved on the undisturbed mean free surface ($z = 0$). This approximation is resonable as long as $kA << 1$.

On the other hand, if non linear free surface boundary conditions are going to be imposed to time march the simulation, then equations 4.12 and 4.13 need to be used. In fact, it is also possible to formulate equations 4.12 and 4.13 to a semi-Lagragian version Beck et al. [1994], that tries to minimize the distortions on the mesh. An example would be to allow free surface movement only on the vertical direction, more details of which can be found in Chapter 7.

In order to satisfy the radiation boundary condition, i.e neglect the contribution from the far field boundaries of the free surface, the approach used by Liu

[2010] is adopted. Therefore, a strip of sponge layer is added near the boundaries to absorb all wave disturbances which travelled to the boundary. This scheme relies on adding artificial damping terms to the free surface boundary conditions, requiring a damping function to be defined.

The damping rate function, $\nu(\omega, r, r_L, r_D)$ depends on the frequency of the wave to be damped, ω, the distance from the origin where the damping zone starts r_D and the distance where the zone ends, r_L. Therefore, the actual size of the damping zone is given by $r_L - r_D$. In addition, a couple of function forms can be chosen (quadratic, polynomial etc); Nevertheless, still according to Liu [2010] a simple and efficient damping zone can be defined by:

$$\nu(\omega, r, r_L, r_D) = \begin{cases} 0 & \text{if } r < r_D \\ \omega(\frac{r - r_D}{r_L - r_D})^2 & \text{if } r_D < r < r_L. \end{cases} \tag{4.16}$$

Hence, the damping rate function defined in 4.16 can be used on the free surface boundary conditions. This way the potential satisfies the radiation condition at infinity and wave reflections are hopefully avoided. For the case of linear time domain simulations, equations 4.14 and 4.15 can be rewritten as:

$$\frac{\partial z}{\partial t} = \frac{\partial \phi}{\partial z} - \nu z \tag{4.17}$$

$$\frac{\partial \phi}{\partial t} = -gz - \nu \phi. \tag{4.18}$$

The case of non linear free surface boundary conditions can be dealt in the same fashion, if the free surface boundary conditions are used on Lagrangian coordinates (i.e equations 4.12 and 4.13). For the case tackled in this work, the full formulation of the non linear free surface boundary conditions can be found in chapter 7.

4.3 Time Marching Scheme

The main idea of the MEL scheme is to solve equation 4.10, and update the potential value on the free surface using the kinematic and dynamic boundary conditions, taking into account the presence of damping zone at a suitable dis-

tance of the body.

An initial potential value, ϕ_0, is usually applied on the free surface, this can be an undisturbed free surface condition (initial potential is zero) or an incident wave potential; an initial velocity $\vec{V}(\vec{x}, 0)$ is also prescribed on the floating body. This way equation 4.10 can be solved for unknown potentials on the body and the unknown normal velocity on the free surface (Eulerian phase). In the second phase (Lagrangian phase), an explicit integration of equation 4.17 (or 4.12 in the general case) updates the free surface position and another explicit integration of equation 4.18 (or 4.13 for fully nonlinear simulations) updates the free surface position and the potential value. Depending on the problem, the body velocity will either be prescribed (forced motion problem) or calculated from the equations of motion. Therefore equation 4.10 can be solved again with updated boundary conditions. The process is then repeated in time. This way, both the initial boundary value (IVP) problem for the evolution of the free surface potential and the BVP problem that governs the derivative of the IVP are coupled. At this point it is also interesting to highlight that although the process is simple, the BVP-IVP coupling implies that if there are inaccuracies, say on the free surface elevation for instance, it will corrupt the solution of the boundary value problem and so on.

From a numerical perspective, in order to integrate the free surface boundary conditions two methods have been used: a simple Euler method and second order Runge-Kutta method. Both are described in the Appendix A Numerical Techniques.

It is worth pointing out that the flexibility provided by the MEL scheme comes at the cost that the domain is moved (in the sense that the nodes of the free surface are displaced according to the velocity field). In linear analysis, because the wave stepness is small, $ka << 1$, the free surface boundary conditions are applied on the free surface but equation 4.10 is computed on the undisturbed free surface, allowing the same mesh to be used every time step. From a numerical/implementation point of view this is a great simplification. Furthermore, since the domain does not change, the influence matrices of the system are kept the same in linear analysis. However, in order to tackle nonlinearities in the free surface boundary conditions it is necessary to update the free surface and remesh

it every time step. The methods used to tackle this problem are described in chapter 7.

Chapter 5

The coupling of meshing schemes and hydrodynamics simulations

This chapter tackles a couple of practical implementations issues that will allow a link between the generation of unstructured mesh grids and its applications to hydrodynamic simulations in time domain. The main feature that differ the present approach from the current practice lies in the need to generate an unstructured mesh at every time step, for the case of body non linear and fully non linear simulations, taking into account the instantaneous changes on the floating body wetted surface. To the best of our knowledge, there is no well defined current practice for this problem in the potential flow context in time domain and the meshing scheme employed is usually structured and intimately associated to the BEM solver used in the problem (Xu [1992], Xue [1997] and Liu et al. [2001]). On the other hand, recent developments of viscous fluid flow simulations have focused on algorithms capable of simulating the 2 phase fluid flow problem (air and water) by means of convecting the free surface on an Eulerian mesh (so no remeshing is actually required) using, for instance, a coupling between volume of fluid formulations and the level set methods, see Lachaume et al. [2003] and Sethian [1999].

In order to tackle this issue, two unstructured mesh frameworks were investigated: the framework developed by Persson [2005] and the framework developed by Geuzaine and Remacle [2009]. Both approaches can generate unstructured triangle meshes, although the algorithms are different. Signed distance functions representations of the geometry (or geometries) that compose the fluid domain

are the key inputs of the algorithm developed by Persson [2005]. Once signed distance functions are available, they can be manipulated by simple operations such as intersections, differences and unions, allowing for the construction of more complex geometries. In the context of hydrodynamic simulations, natural questions arise, such as: Can a signed distance function can be estimated accurately to mesh ship like forms and the free surface ? Furthermore, could this representation be evolved in time in order to tackle the evolution of the free surface and the movements (forced or freely floating) of the ship ? On the other hand the framework developed by Geuzaine and Remacle [2009] is built on hierarchical geometry entities, i.e points, lines, surfaces and volumes and the meshing scheme is heuristic. In this context, the problem of representing an underwater geometry that changes in time and needs to be remeshed at every time step is not straigthforward as well.

In this chapter, both frameworks are going to be surveyed and the pros/cons will be highlighted in the context of the present MEL simulation scheme. Section 5.1 highlights the main reasons on the choice of an unstructured mesh. In sections 5.2 and 5.3 both algorithms (distmesh from Persson [2005] and Gmsh from Geuzaine and Remacle [2009]) are presented together with applications of interest from a hydrodynamic perspective. Finally section 5.4, highlights the advantages and disadvantages of each approach from both a numerical stability and implementation perspective.

5.1 The choice of the mesh type

In this section, the importance of choosing an unstructured grid to keep the size of the boundary value problem practical is highlighted in the context of potential flow simulations. When a solution of Laplace equation is sought, it can be shown Cordaro and Kawano [2002], by means of a Fourier transformation, that the solution of equation 4.2 is formally the free space Green's function. This way, denoting the Euclidean distance between a source point, $\vec{x}$, and a field point, $\vec{y}$

by r, the free space Green's function is:

$$G(\vec{x}, \vec{y}) = \frac{1}{4\pi r}. \tag{5.1}$$

Equation 5.1 is the simplest form of the Green's function that can be envisaged. On the other hand, it has the major drawback that when it is used in the integral equation 4.10 it does not allow any simplification on the boundaries. So there is clear trade off here: on the one hand a more complicated form of Green's function will allow for a great reduction in the domain size; however, it will be much more time consuming to evaluate and calculate the influence matrix. Therefore different approaches have been pursued, for instance: in the context of free surface flows, Xu [1992] made use of the doubly periodic Green's function which allowed for the discretization of only the free surface (Dirichlet boundary condition), the remainder boundaries (Neumann boundaries) actually vanished from equation 4.10, reducing the computational size of the problem significantly but, at the cost of a more complex Green's function which is more expensive to evaluate, approximately 12 times slower than 5.1 still according to Xu [1992].

In the present, the option to work with the free space Green's function was made due to its flexibility to handle free surface boundary conditions with several degrees of linearity/non linearity. This implies, from a numerical perspective, that the whole domain boundary needs to be represented by a mesh (or meshed). The simplest mesh that can be built is a structured mesh. The major drawback of structured meshes is that too many elements may be needed in order to achieve a good representation of the domain boundary data.

More concretely, one of the main attractiveness of BEM lies on the fact that only $O(N^{d-1})$ unknowns are sought (where d is the dimension of the domain), because only a discretization of the boundary is needed; whereas on numerical methods that require a discretization of the whole domain (e.g FEM) the problem size is of the order $O(N^d)$. However, there are also some disadvantages, specifically in the context of the mixed boundary value problem, namely:

- in BEM the influence Matrix computation involves integrals that are singular, hence more costly to evaluate;

- the linear system that arises from BEM is usually neither symmetric nor sparse.

In addition, recall that for hydrodynamic problems the waves lengths generated by an oscillating body, λ, with circular frequency, ω, are of the order $\lambda = \frac{2\pi g}{\omega^2}$. Hence, the use of structured meshes is actually restricted to higher frequencies (i.e shorter wave lengths). In lower frequency range, the computational cost of structured meshes could become be too high introducing the need for more powerful numerical techniques like the Fast Multipole Boundary Element Method Liu [2009].

Combining these facts with the need of large domains, which usually have different scale, since the wave length dimension can differ, by orders of magnitude, of the dimensions of the floating body, the application of standard BEM in the context of practical ship hydrodynamics problems is still limited, in the sense that domain sizes needed are still too big Yan [2010].

One way to try to alleviate these issues is to adopt an unstructured mesh representation of the domain boundary. In particular, for its relative user simplicity and good mesh quality, two approaches have been tested in the context of the present work: the algorithm developed by Persson [2005], called distmesh, and mesh -visualization library, Gmsh from Geuzaine and Remacle [2009]. Both meshing methods have their pros/cons, for instance:

- Gmsh adopts an heuristic/classical approach to meshing. Its data structure is hierarchical, composed of points, lines, surfaces and volumes. To mesh surfaces it uses Delaunay triangulations and parametric based mapping schemes; it is efficient, runs fast, memory usage is light and mesh quality is good. Compared to distmesh it is not straightforward to evolve the domain in time (in the distmesh framework the signed distance functions can be made time dependent, or evolved as will be seen in the next sections), whereas in gmsh an heuristic approach is needed.

- Distmesh does not have a data structure representation which yields a simple implementation and shorter , easier to understand, code. The mesh generation is an iterative force-based procedure which is built upon the

concept of signed distance functions and Delaunay triangulations. The core update of the algorithm is very closely related to the gradient ascent optimization algorithms. Compared to Gmsh, the memory usage is more intense due to the background grid, hence its runtime is slower, since Delaunay triangulations are iteratively performed. On the other hand, the fact that the background grid is already in place makes distmesh integration to level set and fast marching methods straightforward. In particular in order to perform BEM-VoF coupled simulations (see for instance Lachaume et al. [2003]) the approach is appealing. The quality of the mesh elements is also very good.

In the present work, as a general rule, the distmesh algorithm has been used for the simulation of the hemisphere and sphere presented in chapters 6 and 7, using the linear, body non linear and fully non linear methods. On the other hand, the Gmsh library was used for the simulations presented for the Wigley hull. In case of any exception, the context shall make clear which meshing algorithm was used.

5.2 DistMesh-MEL coupling

In particular, methodology from Persson [2005] makes extensive use of distance functions to represent the computational domain which can be an alternative way to locate nodes on the floating body, on the free surface or on the outer boundary of the domain to set the corresponding boundary conditions as this surfaces evolve in time. Furthermore, a distance function representation of the free surface can be used to model their evolution in time, which in turn can be used to mesh the domain on the subsequent time step. In this context, the domain one is interested in meshing (obtain a triangulation and a connectivity matrix) is embedded in a larger grid, the background grid. This allows for a description of the domain to be meshed, in the present case the fluid domain Ω and its boundary $\partial\Omega$, by means of a signed distance function representation.

More formally, denoting the three-dimensional Euclidean norm by $||.||$ the signed distance function, $d(\vec{x}_g, \vec{x})$, from a fixed point on the background grid $\vec{x}_g$

to a point $\vec{x}$ is defined as:

$$d(\vec{x}_g, \vec{x}) = \begin{cases} ||\vec{x}_g - \vec{x}|| & \text{if } \vec{x} \notin \Omega \\ -||\vec{x}_g - \vec{x}|| & \text{if } \vec{x} \in \Omega \\ 0 & \text{if } \vec{x} \in \partial\Omega \end{cases} \tag{5.2}$$

From the above defintion it also follows that $|\nabla_{x_g} d(\vec{x}_g, \vec{x})| = 1$ which is an important property of distance functions and is intimately associated with the mesh generation algorithm.

Typical inputs to create a mesh are the following:

- the distance function $d(\vec{x}_g, \vec{x})$ for the domain Ω;
- a relative element size function $h(\vec{x})$;
- a desired triangle edge size h_0.

5.2.1 Analytical Signed Distance Functions

As an example, the distance functions of two spheres with radii equal to 0.25 (inner) and 4.0 (outer) units are combined in order to generate the mesh in figure 5.1. In this case since the distance function is prescribed analitically it becomes a function only of the background grid points. Both spheres are centered at the origin so that their distance functions can be simplified to $d_1(\vec{x}_g) = \sqrt{x_g^2 + y_g^2 + z_g^2} - 0.25$ and $d_2(\vec{x}_g) = \sqrt{x_g^2 + y_g^2 + z_g^2} - 4.00$. The mesh in figure 5.1 is then obtained by taking the difference, d_3, between d_1 and d_2, $d_3 = max(d_2, -d_1)$, and then intersecting d_3 with the plane $z = 0$, so that, $d_4 = max(-z, d_3)$, is actually the final distance function. The relative element size function used in this case is given by $h(\vec{x}_g) = 0.08 + 0.1 d_1(\vec{x}_g)$ which increases neighbour element edges by a factor 1.1 moving away from the smaller sphere. In addition, in this case $h_0 = 0.07$ units. The meshing scheme developed by Persson [2005] uses a background grid in which the signed distance functions are calculated. In fact, the background grid is just a collection of nodes and there is some freedom in its choice. For instance: uniform, octree or Delaunay based grids are in theory all allowed. In this example, a uniform background grid was chosen, with a size of a bounding

box with dimensions [-4.5 -4.5 -4.5] x [4.5 4.5 0.5] units in the x, y and z directions respectively.

One of the typical metrics to investigate mesh quality is measured by twice the ratio of the radii of inscribed to circumscribed circles of the triangles, see figure 5.2. Ideally this ratio should be as close as possible to one, meaning that the triangles are as close as possible to equilateral triangles. In the present application, mesh quality is important because the singular integrals in equation 4.6 are numerically evaluated (see Appendix A Numerical Techniques for more details), using either the polar desingularization Pozrikidis [2002] or the triangle mapping technique Zhang and Xu [1989] so it is important that the elements have a good quality in order to avoid a vanishing Jacobian.

Once the boundary mesh is available, it is possible to solve the hydrodynamic problem developed in chapter 3 for the case of forced motions using linear boundary conditions. In this case, since the free surface boundary conditions are linearized and the boundary value problem is solved at the mean undisturbed water level, then the process of mesh creation is performed only once, at the beginning of the simulation. The results of these simulations, for the case of the linear radiation problem were presented in chapter 6.

On the other hand, for non linear or body non linear formulations the meshing scheme needs to be extended. The extension to both realistic ship forms, as well as to the time domain remeshing problem (this is needed in a situation where the underwater profile of the floating body changes in time) is going to be detailed in the sections that follow, which comprise but are not limited to the remeshing schemes used in chapter 7.

5.2.2 Simple Geometries undergoing prescribed movements

For the case of simple geometries undergoing forced oscillations, it is actually straightforward to generate unstructured meshes for different positions of the floating. For the case of the heaving sphere tackled in the body non linear simulations, two distance functions are considered: one to represent the geometry of the cylinder and another to represent the geometry of sphere. The distance function of the cylinder of height, h_c, and of radiis r_c, is constructed by intersecting

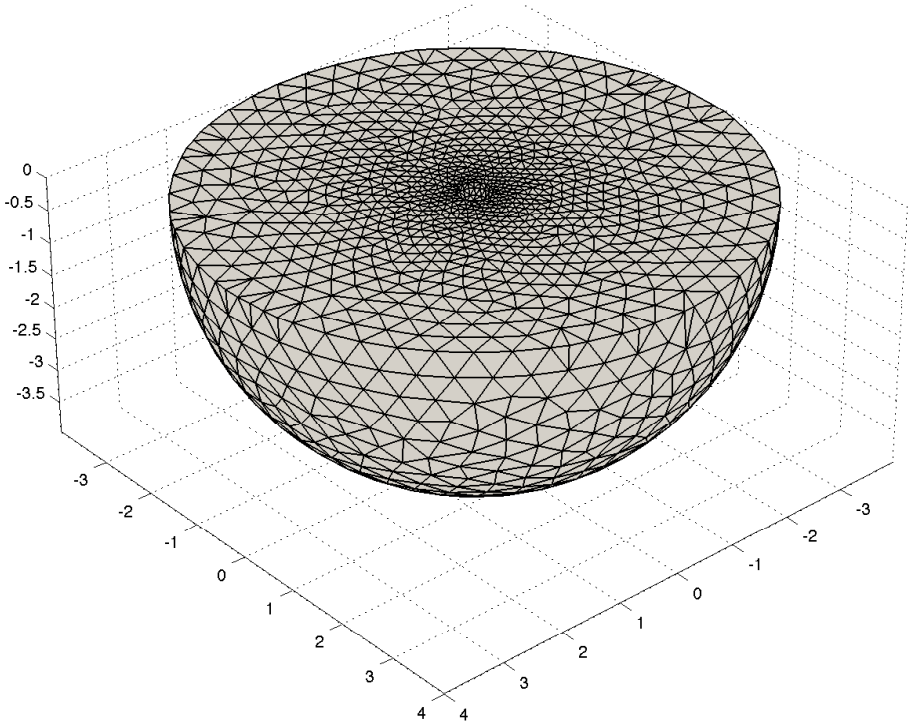

Figure 5.1: Mesh Generated for linear simulation (2758 triangles) using the distance function of two spheres.

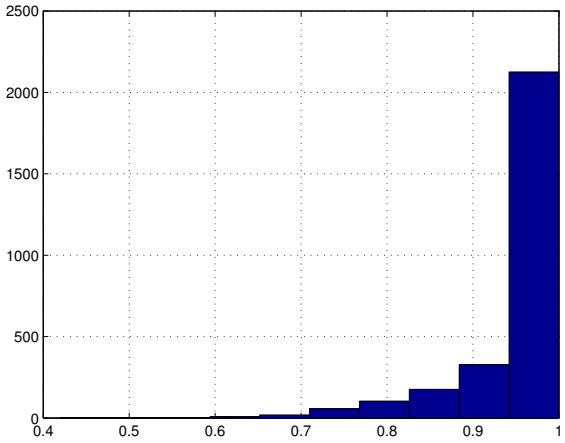

Figure 5.2: Element quality of the mesh with 2758 triangles

the lower and upper plane with an infinite cylinder. So if d_5, d_6 and d_7 represent signed distance functions, respectively, for the cylinder, lower plane and upper plane (free surface), one can write that:

$$\begin{aligned} d_5(\vec{x}_g) &= \sqrt{x_g^2 + y_g^2} - rc, \\ d_6(\vec{x}_g) &= -z_g - h_c, \\ d_7(\vec{x}_g) &= z_g. \end{aligned} \tag{5.3}$$

Next the in order to incorporate the forced oscillation of the sphere in the heave mode, the distance function $d_1(\vec{x}_g) = \sqrt{x_g^2 + y_g^2 + z_g^2} - 0.25$ is extended to $d_1(\vec{x}_g, t) = \sqrt{x_g^2 + y_g^2 + (z_g - z_c(t))^2} - 0.25$, where $z_c = Asin(\omega t)$. Note first that d_1 assumes that sphere is centered at $(0, 0, z_c(t))$. This way as $z_c(t)$ changes the center of sphere changes and the movement implies a new distance function $d_1(\vec{x}_g, t)$. The new distance function is then fed to the distmesh algorithm, generating a mesh at every time step. Figure 5.3 shows a sequence of plots of the sphere for $\omega t = 0, \pi/2 and 3\pi/2$, as well as a typical mesh discretization used on the body non linear simulations. For this mesh the size function, h, prescribed is given by $h = 1.5 + 5d_1(\vec{x}_g, t)$, so that for grid points away from the sphere geometry the edge size increases isotropically on all directions.

5.2.3 Estimating Distance Signed Functions for Ship like shapes

Using the distmesh library, once signed distance functions are available analitically an unstructured mesh could be created. However, for most ship like forms the signed distance function that correspond to their geometry is not known a priori, i.e in closed form. In this section a simple algorithm is proposed to estimate the signed distance function of more general ship like forms and is used to mesh a Wigley hull. The input that is required for the algorithm is a triangulated representation of the ship surface geometry (i.e its nodes and a connectivity matrix), the mesh representation of the surface geometry is usually available from commercial CAD based systems, like Rhinoceros, Delfship, Maxsurf etc.

Before the algorithm is presented, let's try to understand it from an intuitive

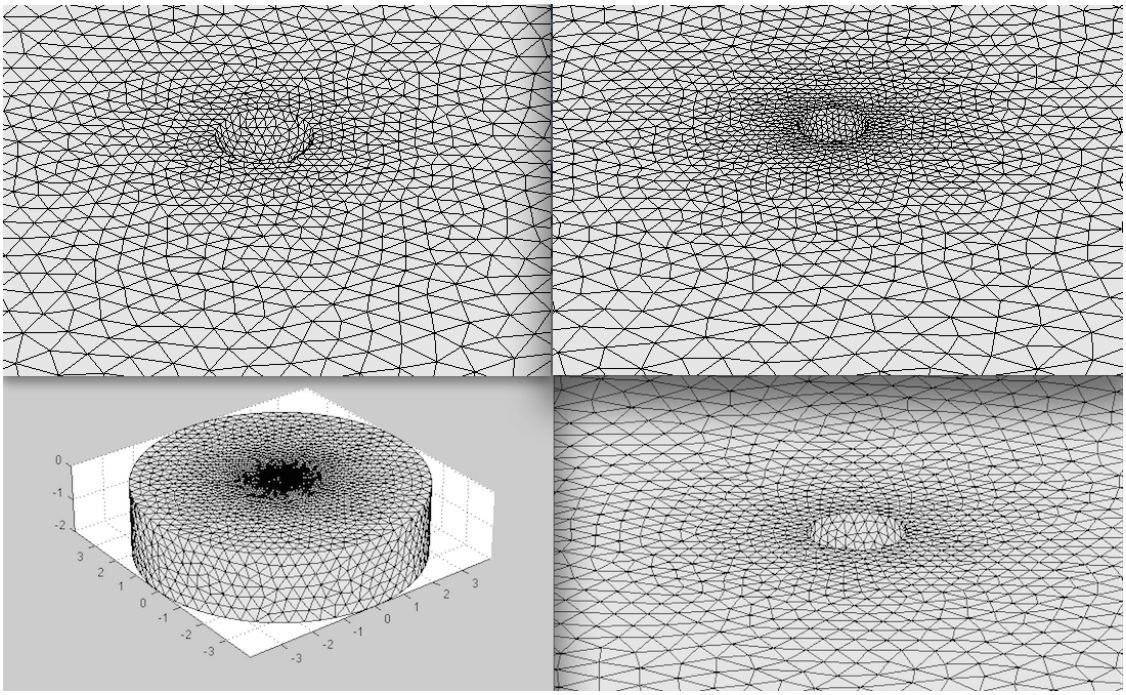

Figure 5.3: Sequence of sphere meshes for A=0.375 R. On the top left is the sphere at its lowest draught $zc = 0.375R$; on the top right the sphere is at its mean waterline, i.e $zc = 0$; bottom left is a typical mesh with $h = 1.5 + 5d_1$ with 5826 triangles; bottom right is the sphere at its highest draught $zc = -0.375R$.

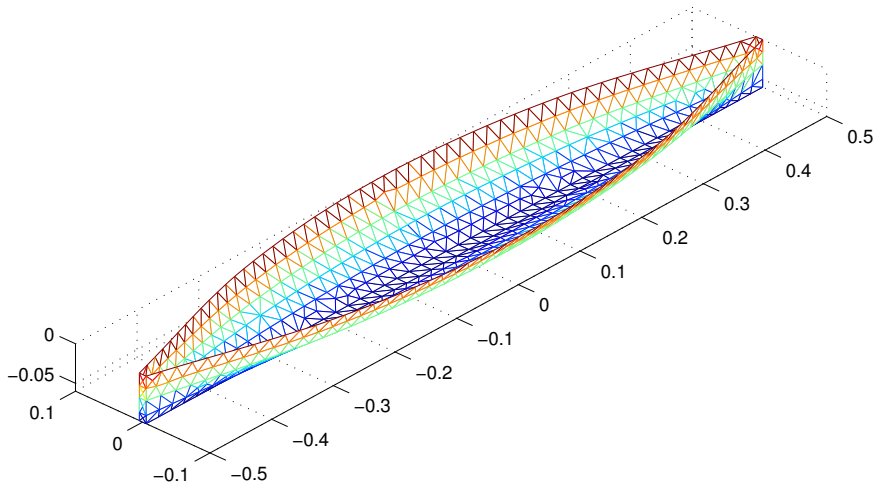

Figure 5.4: Wigley hull triangulation used as input to create the signed distance function, 1232 elements.

perspective. Recall that by its definition a signed distance function (equation 5.3) measures the distance between grid points $\vec{x}_g$ and the points that describe the geometry, $\vec{x}$. This distance is then multiplied by a sign (+1 or -1) corresponding to whether the grid point, $\vec{x}_g$, lies outside or inside the domain respectively. Multiplying by the sign guarantees a key property for the gradient of the distance function, i.e $|\nabla_{x_g} d(\vec{x}_g, \vec{x})| = 1$, which the meshing scheme is build upon.

So, once the representation of figure 5.4 is available and a grid point is given, the distance from the grid point to all triangles on the surface is calculated and the closest point on the surface to that grid point is found. Then in order to find the value of the signed distance function between those two points, $\vec{x_g}$ and $\vec{x}$, the normal direction on the surface is then used. Summarizing what has been said, an algorithm that estimates the distance function from a generic triangulated surface is described on Algorithm 1.

It is worth noting that for each grid point Algorithm 1 needs to pass through all the points of the triangulated surface, therefore is runtime is of $O(mn)$, m and n being the number of points on the background grid and the size of triangulated

Algorithm 1 Signed Distance Function Estimation from triangulated Geometry

1: **procedure** FUNCTION($d_{tri} = signdist(\vec{x}_g)$)
2: distmin:=inf;
3: p:=nodes; ▷ Load nodes and connectivity.
4: t:=conectivity;
5: **while** t =!EOF **do** ▷ Loop on the triangulated surface.
6: triangle:=t(i);
7: [distaux,$\vec{x}$]:=pointTriDist(trip,$\vec{x}_g$); ▷ Distance of $\vec{x}_g$ to triangle.
8: **if** $distaux < distmin$ **then** ▷ Save closest point to $\vec{x}_g$.
9: distmin:=distaux;
10: dotp:=$(\vec{x}_g - \vec{x}) \cdot \vec{n}$ ▷ Use ortogonal projection to determine the sign.
11: $d_{tri} := sign(dotp)||\vec{x}_g - \vec{x}||$ ▷ Signed distance function estimation.
12: **end if**
13: **end while**
14: **end procedure**

surface respectively. So the evaluation, although straightforward, can be time consuming and often limit the applicability of the method when tackling problems where a signed distance function needs to be evaluated at every time step (free floating bodies for instance). In order to make the approach applicable, a couple of alternatives are available, e.g: one can define a small band on the background grid where the triangulated geometry is embedded (this tries to keep m small) and run Algorithm 1 on this band. Next, the value of the signed distance function can be extrapolated to the other points on the background grid using the fast marching method of Sethian [1999].

It is also important to mention that, for some hydrodynamics simulations, i.e forced motions problems in time domain, it can be the case that the distance function of the hull needs to be evaluated only once, which can make the approach interesting. For instance, the distance function of the floating body can be specified with respect to its body fixed axis, then the forced oscillations can be prescribed on the remainder of the domain, which can be built upon analytical signed distance functions. In this context, for the case of body non linear simulations all the available signed distance functions would be readly available. For the non linear case, however, the signed distance function of the free surface, with respect to the body fixed axes would need to calculated by Algorithm 1.

This was not explored in the present work, but is indeed an interesting area for future research.

The implemention in this work also tries to keep m small on the background grid, but does not make use of the fast marching method. Instead, Algorithm 1 is run on a box shaped background grid, in which the triangulated surface is embedded. The size of the box shaped background grid is chosen to be very close to the dimensions of the triangulated surface, again to keep m as small as possible. Once this run is completed the signed distance function is defined on the small box shaped background grid. However, this not sufficient, as in order to build a suitable mesh for hydrodynamic applications a larger domain, hence a much larger background grid is required. Therefore, in order to extend the value of the signed distance function, f_d, on the larger background grid, a simple scheme is introduced, namely: if the point on the larger background grid lies inside the box shaped domain (say the boundaries of the smaller background grid where Algorithm 1 was run) the signed distance function calculated by Algorithm 1 is linearly interpolated, otherwise a simple, analytically prescribed, form of signed distance is used, which is faster to evaluate. Note that in fact, the signed distance function estimated in Algorithm 1, d_{tri}, is actually an input to Algorithm 2.

In particular, turning to the problem of meshing the wigley hull, the signed distance function f_d is generated by algorithm 2. At this point, f_d can be called by the distmesh algorithm of Persson [2005] and the mesh can be created. As a preliminar step, i.e , to check if algorithms 1 and 2 are working as expected, it is useful to check the zero level set contour of the signed distance function f_d, because it corresponds to the boundary of the domain. Its isosurface level set is plotted in figure5.5 and the result of this approach is the mesh created in figure 5.6.

Another point of interest is to ask under what conditions Algorithm 1 fails to converge to the signed distance function representation of the geometry. Not very surprising, issues arise when the curvature of the triangulated body is too pronounced. More specifically, in the cases when the normal vector is orthogonal to distance between the $\vec{x}_g$ and $\vec{x}$ (sharp corners), the dot product is zero. In this pathological cases Algorithm 1 is prone to problems [1]. In order to avoid this

[1]In fact, it should be possible, although out of the scope of the present work, to formulate

Algorithm 2 Signed Distance Function Estimation Assembly

procedure FUNCTION($d = signdistAssembly(\vec{p}, \vec{x}_g, d_{tri})$)
    desf:=$\sqrt{p_1^2 + p_2^2 + p_3^2} - 1.75$; ▷ Sphere signed dist function.
    daux:=$max(besf, p_3)$; ▷ Intersect with z=0.
    d:=daux; ▷ In case p is far from the box shaped background grid, the job is done.
    if $|p_1| < 0.7$ and $|p_2| < 0.15$ and $|p_3| < 0.10$ **then** ▷ Does the point p lie inside the smaller the background grid?
        dwig:=interp($\vec{x}_g$,d_{tri},$\vec{p}$); ▷ Linear Interpolation.
        d:=$max(-dwig, d1)$ ▷ Take the difference between d1 and dwig.
    end if
end procedure

behaviour, the triangulated surface representation needs to be refined in points where the curvature is pronounced.

Instead of using algorithm 1, an alternative approach to estimate the signed distance function of ship like forms would be to start from the zero level set contour of the surface. Since the geometry is defined on R^3, the coordinates of its points, say $\vec{x}_j$, j=1 to m, are all known. Because those points lie on the surface, it follows that the signed distance function, $d_w(\vec{x}_j) = 0$ for all of them. In addition, if on every point $\vec{x}_j$ there is a corresponding normal vector $\vec{n}_j$, an additional set of points located at $\vec{x}_j + \epsilon\vec{n}_j$, j=m+1 to 2m, can also be gathered. At these particular set of points, one can set $d_w(x_j + \epsilon\vec{n}_j) = \epsilon$ McCallum and Evans [2001], so that the value of the signed distance function are also known as well. The last step is then to build a global functional approximation for $d_w(\vec{x}_j)$, this can be done with the aid of radial basis functions, so that $d_w(\vec{x})$ is expanded as Buhmann [2004] :

$$d_w(\vec{x}) = \sum_{j=1}^{2m} c_j f(r_j) + r_0, \tag{5.4}$$

where $r_j = \sqrt{(x - x_j)^2 + (y - y_j)^2 + (z - z_j)^2}$, $f(r_j)$ is the RBF centered at the point $\vec{x}_j = (x_j, y_j, z_j)$, r_0 is a constant and c_j are constant coefficients. By

more precisely under what conditions the signed distance function from 1 converges to the true signed distance function that describes the geometry.

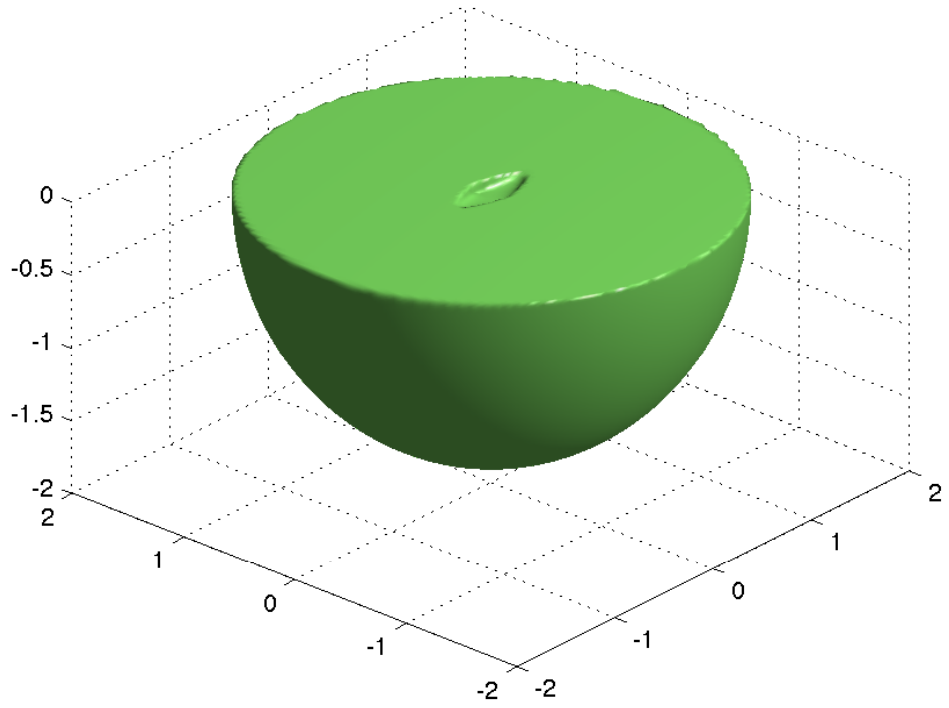

Figure 5.5: Isosurface of f_d created using algorithms 1 and 2.

imposing $d_w(\vec{x}_j) = 0$, for j=1 to m and $d_w(x_j + \epsilon\vec{n}_j) = \epsilon$, this scheme leads to a symmetric linear system which is solved by LU decomposition in the present implementation.

Once the signed distance function is available, the meshing scheme is called and the mesh can be generated. Figure 5.7 shows the resulting mesh obtained by approximating the distance function of the Wigley hull by a family of RBFs. A quick inspection of figure 5.7 reveals the development of kinks, not surprisingly in the regions of high curvature of the Wigley hull.

A possible reason for this poor estimation lies in the fact that the meshing algorithm Persson [2005] uses a force equilibrium approach to move the nodes of the mesh iteratively. After the nodes are moved, some of them are naturally moved outside the boundaries (i.e zero-level iso-contour of the signed distance function). In order, to project these nodes back to boundary the key property

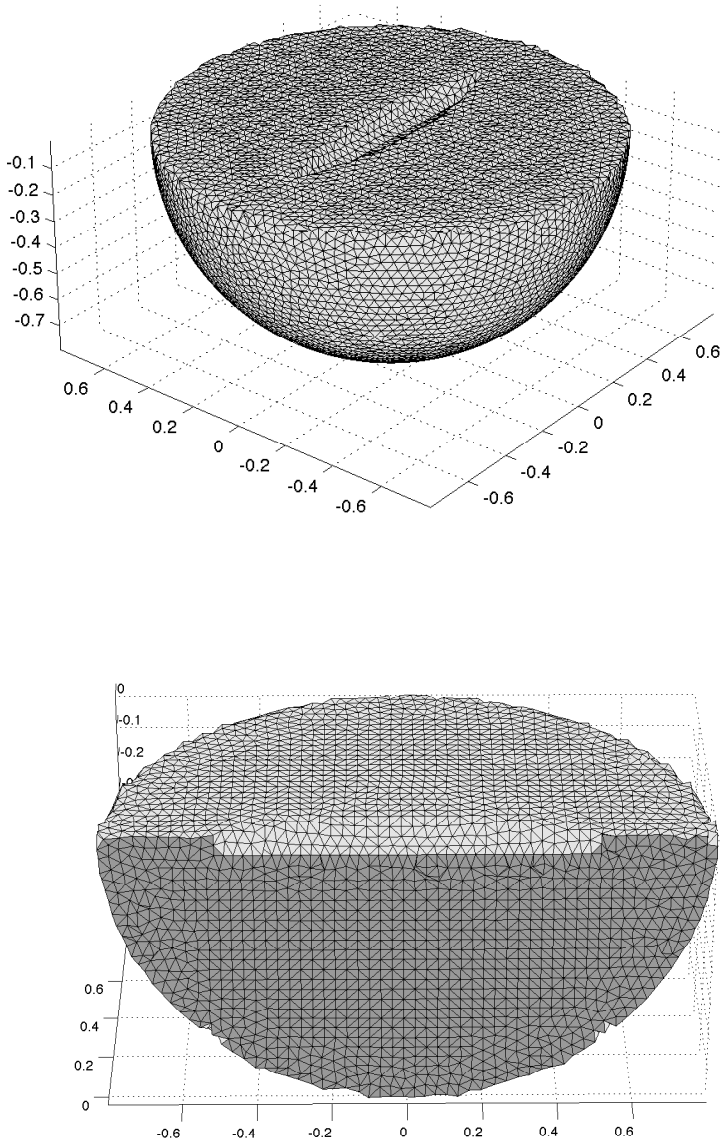

Figure 5.6: Wigley hull mesh created from using the distance function estimation from Algorithm 2. Perspective view on top and half side view on the bottom.

of signed distance functions is explored, $||\nabla f_d|| = 1$, so that the projection $\vec{x} := \vec{x} - \nabla f_d f_d(\vec{x}_g, \vec{x})$, brings the points outside the boundary exactly to the boundary. However, if the radial basis approximation of equation 5.4 violates this property,

the projected nodes will not lie on the boundary anymore, and therefore, the mesh will not describe the geometry accurately. This suggests that it is very likely that the radial basis function approximation has not converged to the true signed distance function of the Wigley hull, which although not very efficient, algorithm 1 calculates more accurately.

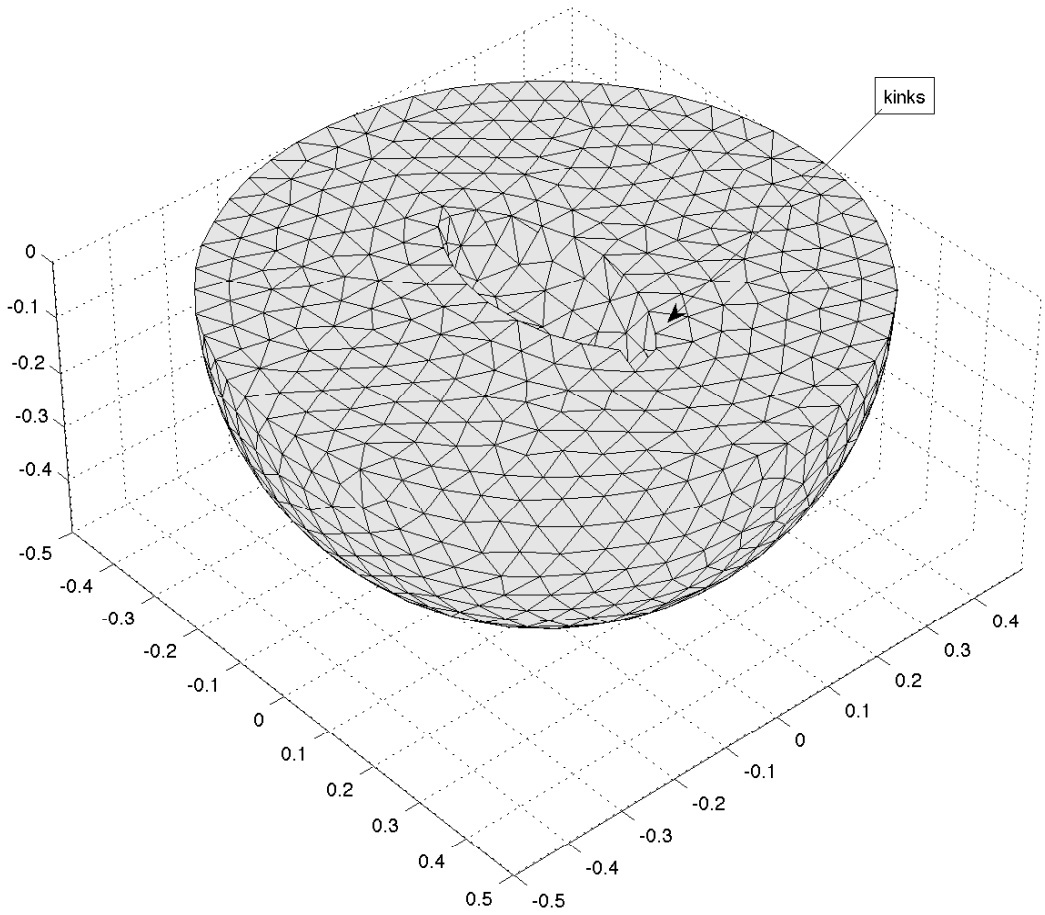

Figure 5.7: Domain mesh using a signed distance function of the Wigley hull (L=0.5, B=0.10 and T=0.0625 units) estimated by RBF intersected with a hemisphere of radius 0.5 units.

5.2.4 Free Surface Evolution

A direct approach to update the free surface position is to move the nodes explicitly using the Lagrangian formulation or a "quasi Lagrangian" free surface boundary condition. This actually means to integrate the kinematic boundary condition, equation 4.12, in time updating the nodes position. Explicit time integration is a simple method to evolve the free surface since it does not involve convection. Once the integration is done the updated signed distance function needs to be recalculated after the free surface is moved.

One way to accomplish this, is to interpolate the new free surface elevation on a pre triangulated mesh and then calculate the signed distance function explicitly by finding the closest point on the background grid to the triangles, using Algorithm 1.

In this context, once the new position of the nodes of the free surface are known from the integration step the wave elevation at a given point $\zeta(x, y, t)$ is approximated in terms of a family of two dimensional radial basis function (RBF) as:

$$\zeta(x, y, t) = \sum_{i=1}^{n} c_i f(\rho_i) + r_0. \tag{5.5}$$

In equation 5.5 ρ_i is the two dimensional euclidean distance function, namely

$$\rho_i = \sqrt{(x - x_i)^2 + (y - y_i)^2}, \tag{5.6}$$

$f(\rho_i)$ is the RBF centered at the point (x_i, y_i), r_0 is a constant and c_i are constant coefficients which are calculated by imposing $\zeta(x_j, y_j, t) = \zeta_j$ for j=1 to n; ζ_j is the current elevation of the free surface, which in a test case can be prescribed or, ideally, calculated from the integration of the kinematic boundary condition. This procedure leads to a linear system which is solved by LU decomposition. The wave elevation, ζ, is then interpolated on a given triangular mesh (this step is important because it brings orientation to the free surface) and the signed distance function is then explicitly calculated by Algorithm 1.

In order to ilustrate the current methodology, assume a cloud of points in three dimensional represent the free surface position (in this ilustration case

$\zeta(x, y, t) = 0.1 \cdot sin(2\pi x)$). These are shown in the upper part of figure 5.8. Next, interpolate their elevation on a triangulated grid (lower part of figure 5.8). Use the triangulated surface to estimate the signed distance function representing the free surface and compute the union of this signed function with the signed distance function corresponding to the intersection of 5 planes ($z_g = -2, x_g = 2, x_g = -2, y_g = 2, y_g = -2$ units, for the example presented) , that is to say:

$$d_\Omega(\vec{x}_g, \vec{x}, t) = Max(d(\vec{x}_g, \vec{x}, t), d_{Box}), \tag{5.7}$$

where d_{Box} is the uncapped box, without the plane $z = 0$ on its top, given by:

$$d_{Box}(\vec{x}_g) = -Min(2 + z_g; 2 + x_g; -2 + x_g, 2 + y_g; -2 + y_g). \tag{5.8}$$

It is worth point out that both d_{Box} and d_Ω are defined on the whole background grid, not only on the boundary of the fluid domain $\partial\Omega$ or in the fluid domain itself Ω.

The final mesh, resulting from the distance function in equation 5.8 is shown on figure 5.9.

To investigate the quality of the mesh generated in figure 5.9, $\partial\Omega$ is decomposed into Neumann and Dirichlet boundaries, the free surface nodes are then projected as function of only x and z and compared with the prescribed free surface elevation $\zeta(x, y, t) = 0.1 \cdot sin(2\pi x)$, as shown in figure 5.10.

Hence, looking at comparison between the obtained free surface profile on the mesh and $\zeta(x, y, t)$ on the right side of figure 5.10, it turns out that the calculation of signed distance function using Algorithm 1 yields a good approximation of the geometry one wants to represent. In addition, a strong point of this mesh is that element quality is very high as can be seen in figure 7.32. On the other hand, a major drawback of this simple approach is that the calculation of the signed distance function of the free surface it is not efficient from a run time point of view.

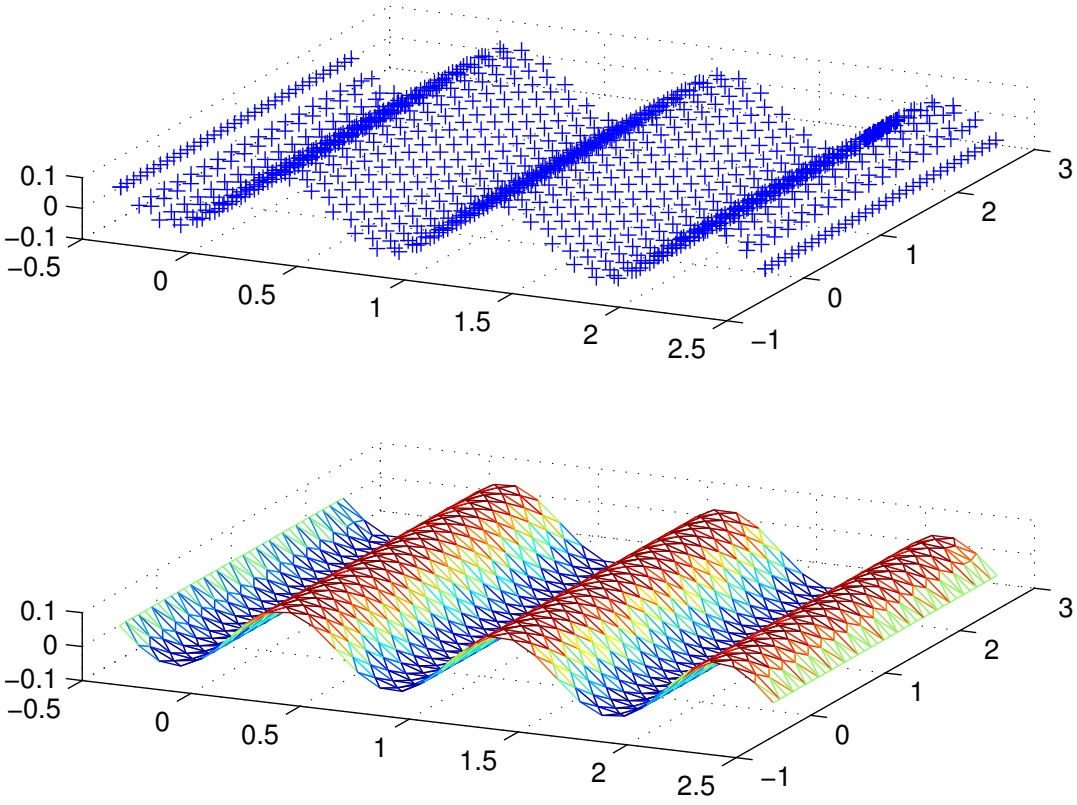

Figure 5.8: Interpolating the free surface position given by a cloud of points (upper part) in a prescribed triangulated mesh (lower part) using the RBF representation of $\zeta(x, y, t)$.

5.3 Gmsh-MEL coupling

In the previous section a couple of approaches were proposed in order to apply the concept of signed distance functions to the present MEL simulations. In particular, armed with the distmesh algorithm, from a signed distance function representation of the domain it is possible to generate a reasonably good mesh. Even for the cases of more ship shaped forms, Algorithm 1 can estimate signed distance functions with an acceptable degree of accuracy. There is however a couple of drawbacks on the distmesh framework that are important to bear in

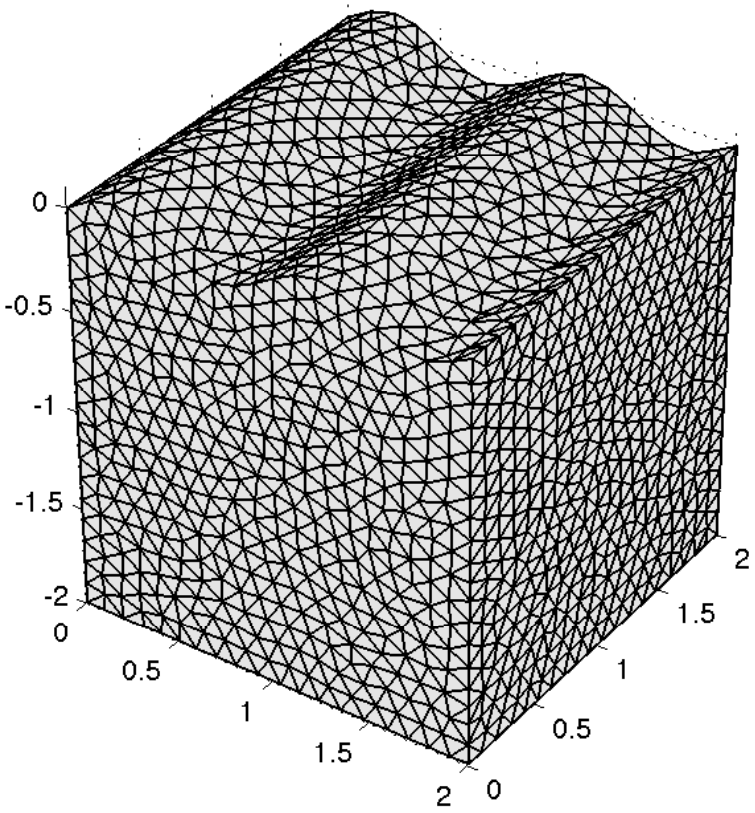

Figure 5.9: Mesh of the fluid domain boundary, $\partial\Omega$, with 4336 triangles resulting from the distance function d_Ω using a uniform element size function, $h_0 = 0.08$.

mind. First, the estimation of signed distance functions has runtime problem, i.e Algorithm 1 can be too slow for a time domain application (this can be overcome by using a parallel architecture in the future applications). Second, and perhaps most importantly, the meshing algorithm of distmesh tends to induce numerical diffusion into the system; interestingly the main reason for this lies on the fact that at each iteration, distmesh moves the points according to an heuristic update rule, which is prescribed at the mesh nodes, $\vec{p}$, as: $\vec{p} := \vec{p} : +\alpha F(\vec{p})$ (see Persson [2005] for more details). The problem that is faced at the implementation is that the nodes displacement, for a meshes at different time instants, can induce

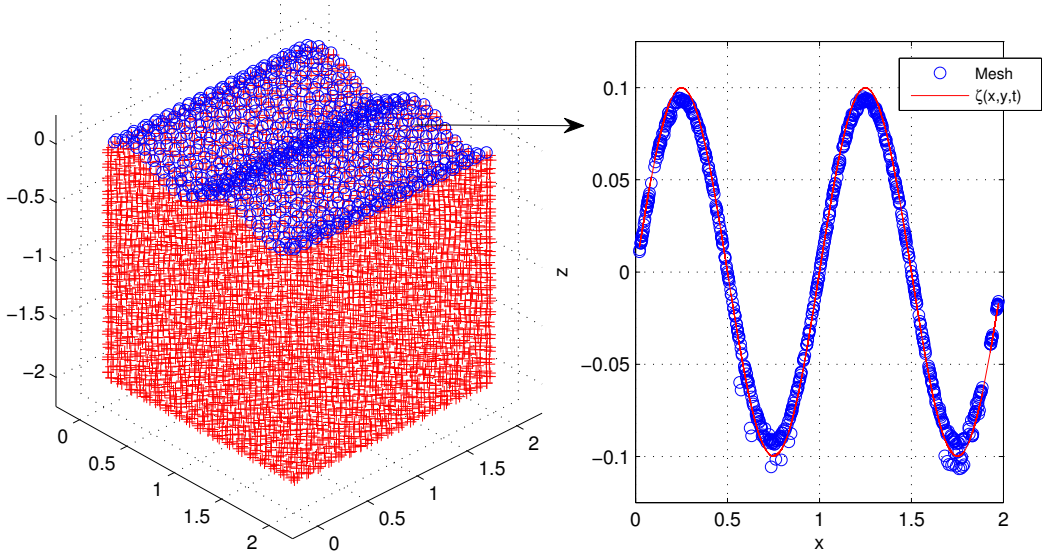

Figure 5.10: Decomposition of $\partial\Omega$ in Dirichlet (free surface) and Neumann boundaries (impervious boundaries) on the left and, on the right, comparison of the obtained free surface profile between the mesh (blue) and the imposed elevation (red).

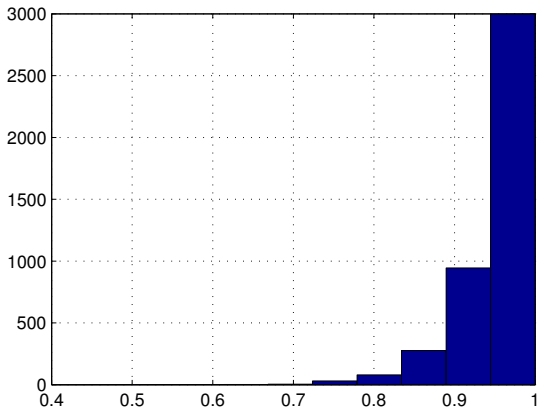

Figure 5.11: Element quality of the mesh representing $\partial\Omega$ measured by twice the ratio of the radii of inscribed to circumscribed circles of the triangles.

spurious numerical diffusion on the simulation.

These two reasons, for the case of Wigley hull simulations, turned out to be daunting obstacles to couple the distmesh framework with the current MEL scheme. As an alternative, the gmsh library (Geuzaine and Remacle [2009]) capabilities were investigated. Gmsh relies on more conventional meshing techniques for the generation of unstructured meshes (Delaunay triagulations and parametric mappings) and it represents the domain entities on a hierarchical level, i.e points, lines, surfaces and volumes. This allows for either surface meshing or volume meshing (in contrast, distmesh only allowed for volume meshing, hence memory usage turned out to be a problem too). This way, the domain of interest for the hydrodynamic simulations is now expressed as geometric entities, whose unions and intersections form the the respective Neumann and Dirichlet surfaces.

In order to perform linear simulations, the Wigley hull points corresponding to three water lines ($z = -0.0625$, $z = -0.03125$ and $z = 0$ units) are inserted and interpolated in the longitudinal direction using splines. Next, the splines are used to describe the hull surface, which is finally meshed. The resulting Wigley hull mesh was shown in chapter 6, in figure 6.8, while the corresponding domain mesh, a box like domain of dimensions [-4 -4 -1] x [4 4 0] units containing the Wigley hull, was also shown in figure **??**. For those two meshes, their element quality is given in figures 5.12 and 5.13.

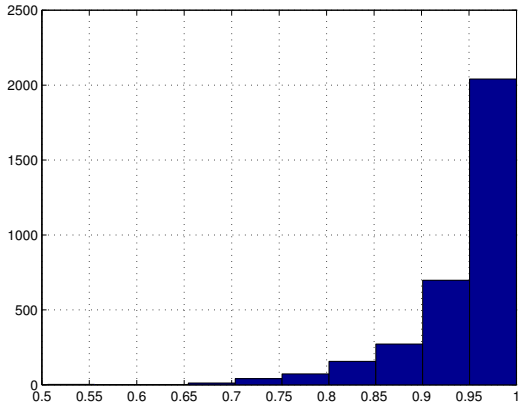

Figure 5.12: Element quality of the mesh of the whole boundary (Wigley hull, free surface and boundaries) with 3298 triangles.

For the case of body non linear analysis investigated n chapter 7 the position

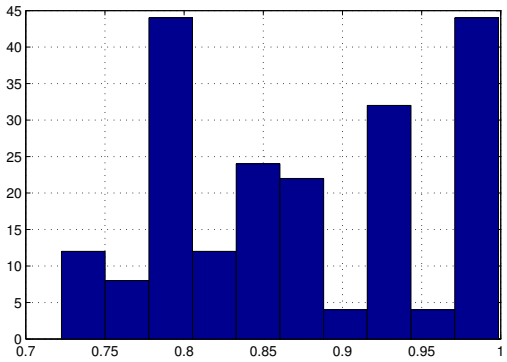

Figure 5.13: Element quality of the mesh of the Wigley hull with 206 triangles.

of the points in the domain are updated. This implies a different position for the lines and surfaces, which are remeshed at every time step. Note that the choice of working with the points (the most basic geometry entities of gmsh) avoids typical cirurgical meshing operations, e.g the problem of which panel (or triangle) is coming in or out of the water as well as possible changes in the connectivity matrix.

For the case of the Wigley hull, undergoing forced oscillations in heave it is relatively straightforward to prescribe a heave velocity on the nodes of the keel and from there imply changes on the underwater surface of the hull. In order to accomplish this, it is useful to consider two coordinate systems: O_{bf} is a body fixed system, placed at the midship of the Wigley hull; O_{FS} is fixed coordinate system, placed on the undisturbed free surface, $z_{FS} = 0$. The systems coincide when the Wigley hull draught is exactly equal to T [1]. So if the body fixed axis is undergoing prescribed motions in the heave mode, with a displacement, $dz(t) = A + Asin(\omega t)$, the points of the system O_{FS} can be expressed in the system O_{bf} by a translation in the z direction, therefore:

$$\begin{pmatrix} x_{FS} \\ y_{FS} \\ z_{FS} \end{pmatrix} = \begin{pmatrix} x_{bf} \\ y_{bf} \\ z_{bf} \end{pmatrix} + \begin{pmatrix} 0 \\ 0 \\ dz(t) \end{pmatrix}. \tag{5.9}$$

[1] In the general case, for motions in the 6 degrees of freedom the translations are taken ino account in the same fashion whereas the rotations can be modeled using the Euler angles.

After a displacement is imposed on the system O_{bf}, the undisturbed water line is still fixed at $z_{FS} = 0$, so $z_{bf} = -dz(t)$. Note that x_{bf} is not only fixed a priori but is also equal to x_{FS}. Thus, the corresponding beam of the Wigley hull is given by:

$$y_{bf} = \pm\frac{B}{2}\big(1 - (\frac{2x_{bf}}{L})^2\big)\big(1 - (\frac{z_{bf}}{T})^2\big). \tag{5.10}$$

This way, as the points on keel are oscillated by $z^K_{bf} = T + dz(t)$, the intersection between the points on the undisturbed free surface and the Wigley hull changes. For the points on the second waterline, a similar approach to equation 5.10 is applied, with the value of z_{bf} substituted by $z^M_{bf} := z^K_{bf}/2$ (i.e the second water line is placed between the free surface intersection and the keel, in the middle point). The results of the procedure described above are shown in the figure 5.14.

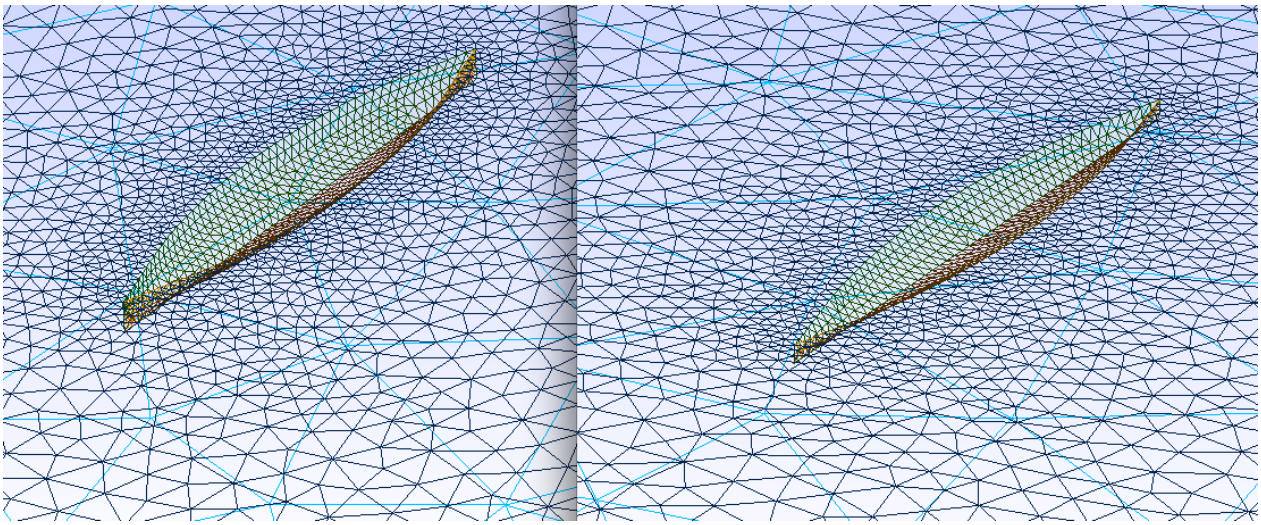

Figure 5.14: Left hand side: mesh of wigley hull at draught T=-0.0625 units , .i.e $dz(t) = 0$. Right hand side: mesh of wigley hull at T=- 0.0292 (i.e $dz(t) = 2A$ where $A = 0.27T$).

The procedure described in this section is then encoded on a simple script. For the body non linear simulations of the Wigley hull, this script is called by the function $CreateMesh(.)$, in line 3 of Algorithm 6. Hence, the problem of

estimating signed distance functions for the Wigley hull is avoided.

5.4 Conclusions

In the context of hydrodynamics simulations, two meshing libraries were investigated to (re)mesh the domain. The distance function approach (distmesh algorithm from Persson [2005]) is able to create meshes with very good quality. The key input for this algorithm is a signed distance function representation of the domain and for geometries that are well defined mathematically, like the sphere, the results obtained were reasonable. In order to extend this approach to the wigley hull, the first step lies in estimating its signed distance function. In this context, given a surface mesh of the hull geometry, algorithm 1 estimates signed distance function numerically. The estimated the signed distance function is then used as input in algorithm 2, which combines individual signed distance functions into one signed distance function that represents the whole domain. This final distance function is the used by distmesh to create the simulation mesh. Although algorithm 1 can approximate signed distance functions for the free surface and the Wigley hull, its use, on the present implementation, is not viable due to runtime constraints. In fact, both distmesh and algorithm 1 have runtime issues when it comes to hydrodynamic simulations, since it needs to mesh the whole fluid domain and extract the boundary. This operation is costly when the size of the domain is large. in addition, a tendency to induce spurrious modes on the numerical stability was also identified with the distmesh algorithm. The reasons related to this issue can be linked to the node movement update prescribed by distmesh algorithm, which needs further investigations.

As an alternative, for the case of ship shaped geometries, the gmsh library developed by Geuzaine and Remacle [2009] was investigated. Its algorithm is based on heuristic meshing strategies. Compared to distmesh, gmsh runtime and implementation are more efficient. On the other hand, the fact that the domain is not described by signed distance functions requires a strategy to find the intersection between the floating body and the free surface. For the case of the Wigley hull undergoing forced oscillations in the heave mode, a simple script,

based on coordinate changes between the body fixed system and the earth fixed system, was implemented to perform this task.

Chapter 6

Linear Time Domain Analysis

In this chapter, the numerical implementation of the theoretical framework developed in chapter 4 is combined with the meshing techniques explained in chapter 5 to tackle the radiation problem, using constant boundary element solver. The main feature of this problem is to perform forced oscillations of the floating body in a initially undisturbed free surface. In this context, the kinematic and dynamic boundary conditions are imposed on the exact free surface (equations 4.17 and 4.18), hence updating the free surface position and potential respectively. The mixed boundary value problem is solved, at each time step, on the mean undisturbed water level ($z = 0$). From its solution (namely, the potential on the Neumann boundaries and the normal velocity on the Dirichlet boundaries) the hydrodynamic pressure on the body surface and, hence the hydrodynamic force can be estimated. In order to translate the results from time domain to the frequency domain, a Fourier decomposition of the hydrodynamic force is performed, giving the corresponding added mass and damping coefficients. The numerical implementation assumes the domain is discretized into a number of small elements (a mesh, with nodes and connectivities) so that in the limit, as the size of the elements tend to zero, the representation of domain becomes, hopefully, exact. In the present work, triangles are used to approximate the domain, so that a mesh with triangular elements is constructed. Once the mesh is available a method to locate nodes on the boundary is developed. This way, Neumann or

Dirichlet boundary conditions are imposed at the center node of each triangle. Next, the boundary value problem is solved, so that both the hydrodynamic force acting on the floating body and the new position/potential on the free surface are calculated. Comprehensive discussion on the mesh generation algorithms used in the present work can be found in chapter 5.

6.1 Forced Motions

In order to test the numerical implementation of the current methodology, two forced motions problems are tackled namely: the heaving and swaying body (hemisphere and Wigley hull) on the free surface. In addition, in the context of potential flow using linear free surface boundary conditions, both of these problems have been solved analytically for the hemisphere by Hulme [1982] and, therefore, added mass and damping coefficients are available for comparison. For the case of the Wigley hull the calculated results are compared against the experimental data from Journée [1992].

For heave, the forced oscilation with amplitude, A, and circular frequency, ω, is prescribed as:

$$z(t) = A\sin(\omega t); \tag{6.1}$$

and for sway it is written as:

$$y(t) = A\sin(\omega t). \tag{6.2}$$

From Equations 6.1 and 6.2, the velocity of oscilation of the floating body can be derived and used in equation 4.11 yielding, therefore, the impervious boundary conditions on the body.

In the radiation problem the free surface is initially undisturbed hence, its initial potential, $\phi(\vec{x}, t_0) = 0$. Schematically, in pseudo-code language, the algorithm that summarizes the steps of the linear time domain simulation is described below as algorithm 3. The procedure is simple and the points worth pointing out

are the following:

1. Line 1 creates the mesh on which the simulation is going to be carried out, that is to say that the function CreateMesh(fd,fh,h0) returns the nodes matrix p and connectivity matrix t, where fd is the distance function, fh relative edge function and h0 is scalar, the edge size. For the linear time domain problem this mesh is created only once either using the algorithm from Persson [2005] or Geuzaine and Remacle [2009].

2. Since the mesh is created for the whole domain, the boundary is extracted using the function FindBoundaryNodes(p,t). This function basically finds surface triangles from the tetrahedra mesh.

3. Line 5: impose the potential at time t (it is set to zero at t=0) on the free surface, this is a Dirichlet Boundary condition, which is imposed after the integration of 4.15.

4. Impose the impervious boundary condition using equation 4.11 (Neumann Boundary condition) on the floating body (line 6) and on the other Neumann boundaries (line 7).

5. Solve equation 4.10 (a linear system) on the undisturbed water surface for the normal velocity on the free surface and for the potential values on the floating body. The assembling of the linear system is described in the appdx A.

6. From the potential on the body surface calculate the hydrodynamic pressure and the corresponding force on the body according to 6.15. This is done in line 9; the time derivative of the potential, in this case, is calculated by a simple backward first order difference scheme.

7. Lines 10 and 11 update the instantaneous free surface vertical position and the free surface potential by integrating equations 4.17 and 4.18. The update is shown schematically as first order numerical scheme, however, both Euler scheme and second order schemes (Rungee Kutta method) have been used depending on the context.

Algorithm 3 Linear Time Domain Simulation

procedure MAIN( )
  [p,t]=CreateMesh(fd,fh,h0); ▷ Create a mesh of the domain
  $[x_{FS}, y_{FS}, x_B, y_B, z_B]$:=FindBoundaryNodes(p,t);
  while $t < T$ **do**
    ϕ_{FS}:=$\Phi_i(x_{FS}$,y_{FS},t) ▷ Set BC Value on the of the FS triangles
    $\nabla\phi \cdot \vec{n}_B := \vec{v}(t)_B \cdot \vec{n}_B$ ▷ Set BC Value on the Floating Body
    $\nabla\phi \cdot \vec{n}_B := 0$ ▷ Set BC Value on other Neumann Boundaries
    $[\phi_B; \nabla\phi \cdot \vec{n}_{FS}] := [G_{FS}; Gn_B]^{-1}[\nabla\phi \cdot \vec{n}_B; \phi_{FS}]$ ▷ Solve the BVP at $z_{FS} = 0$
    $\vec{F} := -\rho \int_{\partial B} \frac{\partial\phi}{\partial t}\vec{n}_B dS$ ▷ Calculate the force on B
    $z_{FS} := z_{FS} + (\frac{\partial\phi}{\partial z} - \nu z_{FS})dt$ ▷ Update the FS elevation
    $\phi_{FS} := \phi_{FS} + (-z_{FS}g - \nu\phi_{FS})dt$ ▷ Update the FS potential
    $t := t + dt$
  end while
end procedure

6.2 Hydrodynamic Coefficients

In the case of forced oscillation in a single degree of freedom, neglecting the hydrostatic restoring force (i.e assuming the oscillations are sufficiently small so that the draught of the floating body can be considered constant), the hydrodynamic force [1] has basically two main components: one proportional to the acceleration of the body, added mass, and one component proportional to the normal velocity which the body oscillates, damping. The coefficients, A_{ij} and B_{ij}, refer to the added mass and damping respectively on jth degree of freedom induced by a motion in the ith degree of freedom.

That said, the heave hydrodynamic force in the heave mode one can be written as:

$$F_h(t) = A_{33}\ddot{z} - B_{33}\dot{z}. \tag{6.3}$$

Using equation 6.1 in 6.3 it follows that:

$$F_h(t) = -\omega^2 A A_{33}\sin(\omega t) + \omega A B_{33}\cos(\omega t). \tag{6.4}$$

[1] Because the interest rely on the hydrodynamic force component, the hydrostatic force was neglected throughout this chapter, i.e the pressure was calculated by: $p = -\rho\frac{\partial\phi}{\partial t}$.

Multiplying equation 6.4 by $\sin(\omega t)$ and integrating this equation over one period, T, the added mass coefficient A_{33} is given by:

$$A_{33} = \frac{1}{\pi A \omega} \int_{t-\frac{T}{2}}^{t+\frac{T}{2}} F_h \sin(\omega t)\, dt. \tag{6.5}$$

By the same token, multiplying 6.4 by $\cos(\omega t)$ and integrating yields the damping coefficient, B_{33}:

$$B_{33} = \frac{1}{\pi A} \int_{t-\frac{T}{2}}^{t+\frac{T}{2}} F_h \cos(\omega t)\, dt. \tag{6.6}$$

Once the time series of the hydrodynamic force is available, equations 6.5 and 6.6 are used to calculate the hydrodynamic coefficients for a given time instant, t. This way, the time window of the Fourier Transform is moved by $\frac{T}{2}$ before and after each time step (taking into account a period T of the force), producing a time series of the hydrodynamic coefficients. These corresponding values of A_{33} and B_{33} for each t are then averaged to obtain the final values. It is also worth pointing out that equations 6.5 and 6.6 can only be applied once the hydrodynamic force has reached its steady state. For forced motions in sway mode, the decomposition is performed in the same fashion, using the sway force $F_S(t)$, as the hydrodynamic force in equations 6.5 and 6.6.

6.3 Rigid Body Analysis

In this section the results obtained for the radiation problem are presented. The radiation problem plays a paramount role in seakeeping analysis. In addition, a numerical solution of the radiation problem in time domain, opens a door to investigate body non linear and fully non linear radiation effects in both rigid and elastic modes settings. This way, forced motion problems are of particular interest.

On one hand, they allow for the estimation of the hydrodynamic coefficients and on the other they keep the problem numerically simple, so that the there is no incident wave potential, nor diffraction potential to be accounted for. Moreover,

in order to try estimate how the hydrodynamic coefficients change as a function of the amplitude of oscillation (this problem is tackled in the next chapter), it can be helpful to solve a second boundary value problem for the time derivative of the potential. In this case, the body boundary condition to be imposed is also a function of the acceleration of the body, which is known for the case of forced motions.

Conversely, for the case of free floating bodies, the estimation of the body boundary condition is more difficult, it requires knowledge of the pressure field (or say, the time derivative of the potential) which in turn requires an estimation of the body acceleration itself. The solution of this problem leads either to an iterating scheme (this is costly from a computational perspective) or to the approach of Wu and Eatock Taylor [1996], which lies outside the scope of the present work.

For the half submerged hemisphere, the heave and sway forced motion problems are simulated and the results are compared against the analytical calculations of Hulme [1982]. In addition, the forced heave radiation problem of a more ship like form, a Wigley hull (model IV of Journée [1992]), without forward speed is also simulated and its the analysis is extended to the unified hydroelastic approach, so that forced oscillations in pitch, sway and flexible modes are also addressed.

With respect to the computational time, each of the simulations in this chapter were carried out in one 2.6 GHz Intel Sandybridge processor and the average runtime for each one was 48 hours.

6.3.1 Forced motions of a submerged hemisphere

Once a circular frequency ω is fixed for the forced motion, the wave number k is also fixed. For the numerical simulations two meshes are used, namely a coarse mesh with 3217 (figure 6.1) triangles and a refined mesh with 5380 triangles (figure 6.2).The results of the hydrodynamic vertical forces for heave forced motions of a sphere with radius R can then be compared with the calculations made by Hulme [1982], using equation 6.4. These are shown in figure 6.3, for the circular frequencies corresponding to kR=0.5,1,2,3,4 and 5.

In figure 6.3, the time series of the heave hydrodynamic force is plotted against time, note that one oscillation cycle is usually enough for the system to reach steady state. In addition, it can be seen that as domain representation is refined the numerical hydrodynamic force approaches the analytical forces predicted by Hulme [1982], which is an indication of convergence in h-sense Karniadakis and Sherwin [2005].

For forced motions in sway the scheme is the same as the one outlined for forced heave oscillations (i.e algo 3). In fact the only change is the boundary conditions imposed on the floating body, which, for sway, is given by equation 6.2. In addition, only the more refined mesh (5380 triangles) is used to carry out the sway simulations for $kR = 0.5, 1.0, 2.0, 3.0, 4.0$ and 5.0. The time series of the hydrodynamic sway force, $F_S(t)$, is presented in figure 6.4.

In order to express the results obtained in the time domain to the frequency domain, equations 6.5 and 6.6 are used to estimate the added mass and damping coefficients respectively, which are shown in figures 6.5 and 6.6 for heave and sway respectively. An interesting point can be drawn from the data in figure 6.5 . Although the numerical values of A_{33}, calculated using the refined the mesh, are a closer to the analytical values, B_{33} does not have the same agreement. In fact, the values of B_{33} obtained for the coarser mesh are sometimes in better agreement than the ones obtained by the refined mesh. The numerical limitations of the CPM (constant panel method) when applied to mixed boundary value problems have been extensively described by Xu [1992], Yan [2010] and Xue [1997]. The error is more pronounced in solving Dirichlet problems, that is estimating the normal velocity of the free surface when an initial potential is prescribed. In this case, the potential value on the free surface is marched in time with an error which is going to affect the solution of the problem in the next time step and probably propagate by numerical diffusion. Due to this effect, a time domain approach usually needs to rely on a more accurate solver than the frequency domain approach. This point is well investigated by Karniadakis and Sherwin [2005] in the context of the numerical simulation of transient flow, highlighting the importance of higher order methods in time domain simulations of fluid flow, in order to avoid error propagation as time is marched. It is also worth pointing out that, although a CPM method can fail to converge (or converge very slowly) to the solution of

a mixed boundary value problem, simple modifications, like linear extrapolation schemes near the the intersection of Neumann and Dirichlet boundaries, can actually improve the convergence of a crude CPM implementation in the estimation of the normal velocity Xue [1997].

That said, the primary aim of the present work is to demonstrate that the relatively simple numerical method provides a good qualitative agreement with analytical (numerical or experimental data, when available) in situations where the hypothesis of potential flow holds true. The accuracy of the predictions can be improved by refining the numerical approximations (i.e using higher order BEM, desingularised CPM or Galerkin based BEM). This way, the implementation is more on the lines of trying to increase the accuracy of the CPM when needed, rather than implementing a higher order numerical solver . For instance, by extrapolating the numerical solution at collocation points to intersection points by means of a radial basis function interpolation (see chapter 7).

By this token, it is interesting to compare the results obtained here, for the hemisphere undergoing small amplitude forced oscillations motions, against the ones from Lin and Yue [1991], where a transient Green function function was used. More specifically, the hydrodynamic coefficients obtained by the SAMP code (Small Motion Amplitude Program), show a tendency to oscillate around the analytical values predicted by Hulme [1982]. There is an indication that, as the number of panels on the floating body increases, the oscillations tend to vanish. In the present work, using a simpler form of Green function, but at the cost of discretizing the whole domain and solving the problem in time domain, such oscillations did not occur, either for heave or sway. In addition, the qualitative agreement of the results calculated in the present work against the analytical results from Hulme [1982] is reasonably good.

Therefore, despite the aforementioned drawbacks of the present methodology, figures 6.5 and 6.6 also show that a good qualitative behaviour can be achieved using a CPM solver in linear time domain analysis of the radiation problem. Furthermore, the use of unstructured meshes allows for an efficient discretization of the whole boundary, so that the size of problem can be kept suitable for simple numerical techniques, such as the conventional BEM used in this work, to be applied.

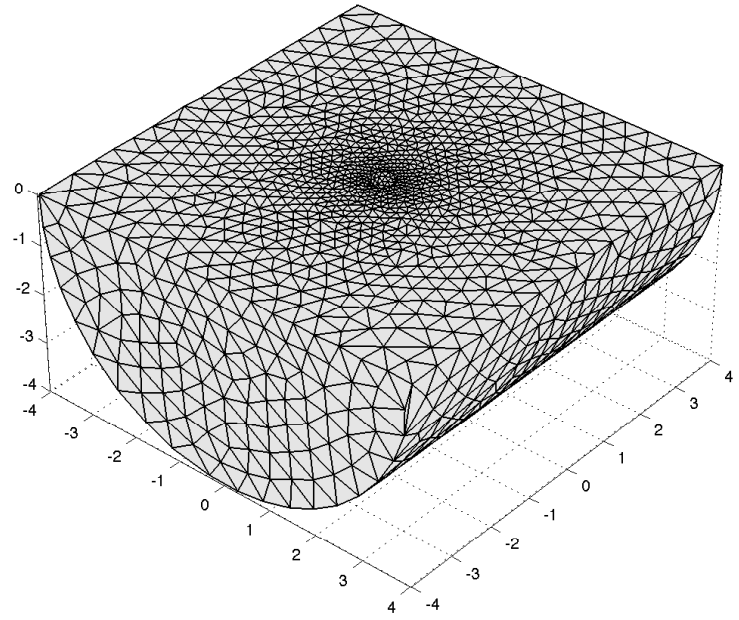

Figure 6.1: Crude mesh 3127 triangles

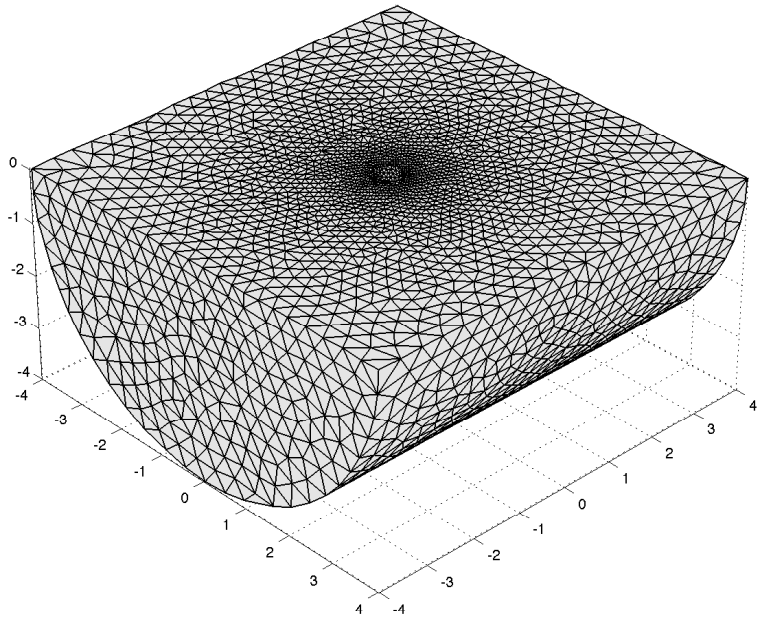

Figure 6.2: Refined Mesh 5380 triangles

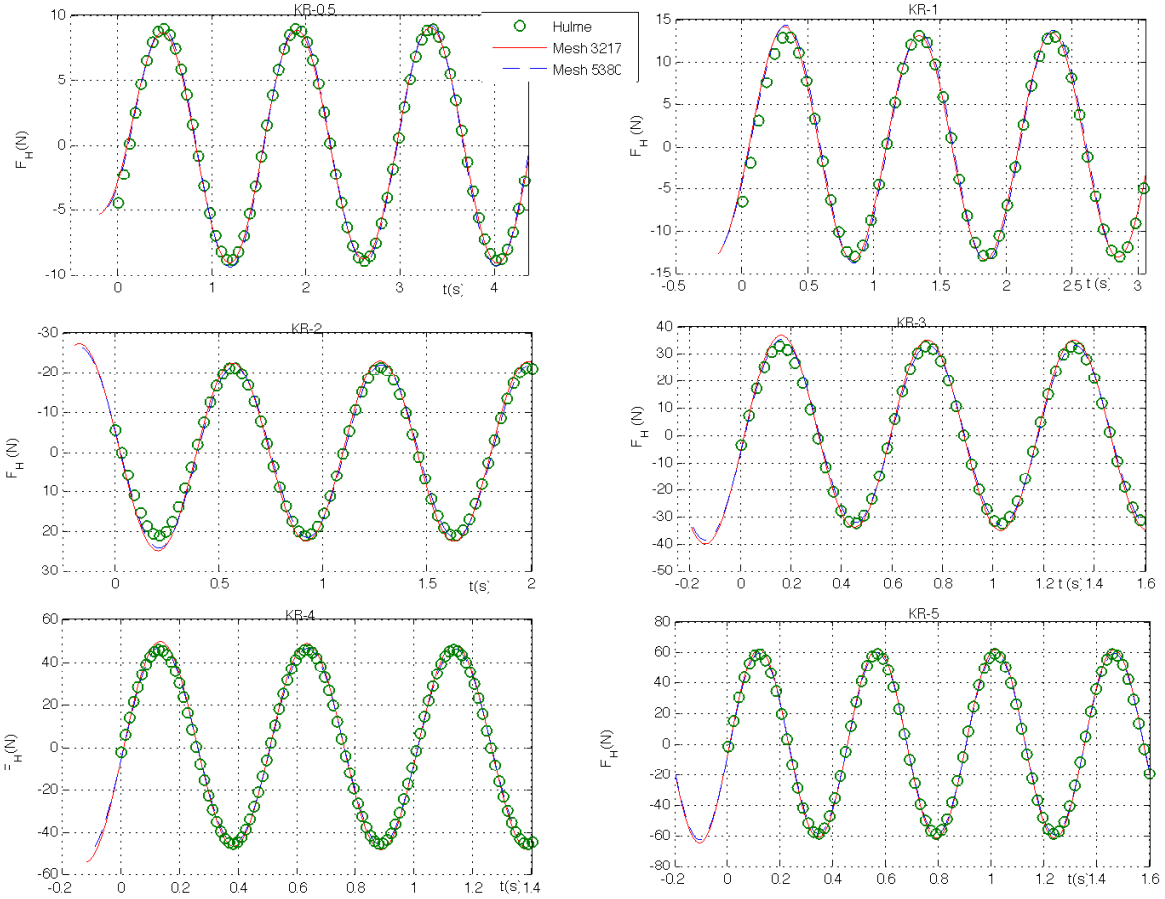

Figure 6.3: Comparison of the heave hydrodynamic force for the hemisphere for KR=0.5,1,2,3,4 and 5 against numerical calculations for a coarse and a refined mesh.

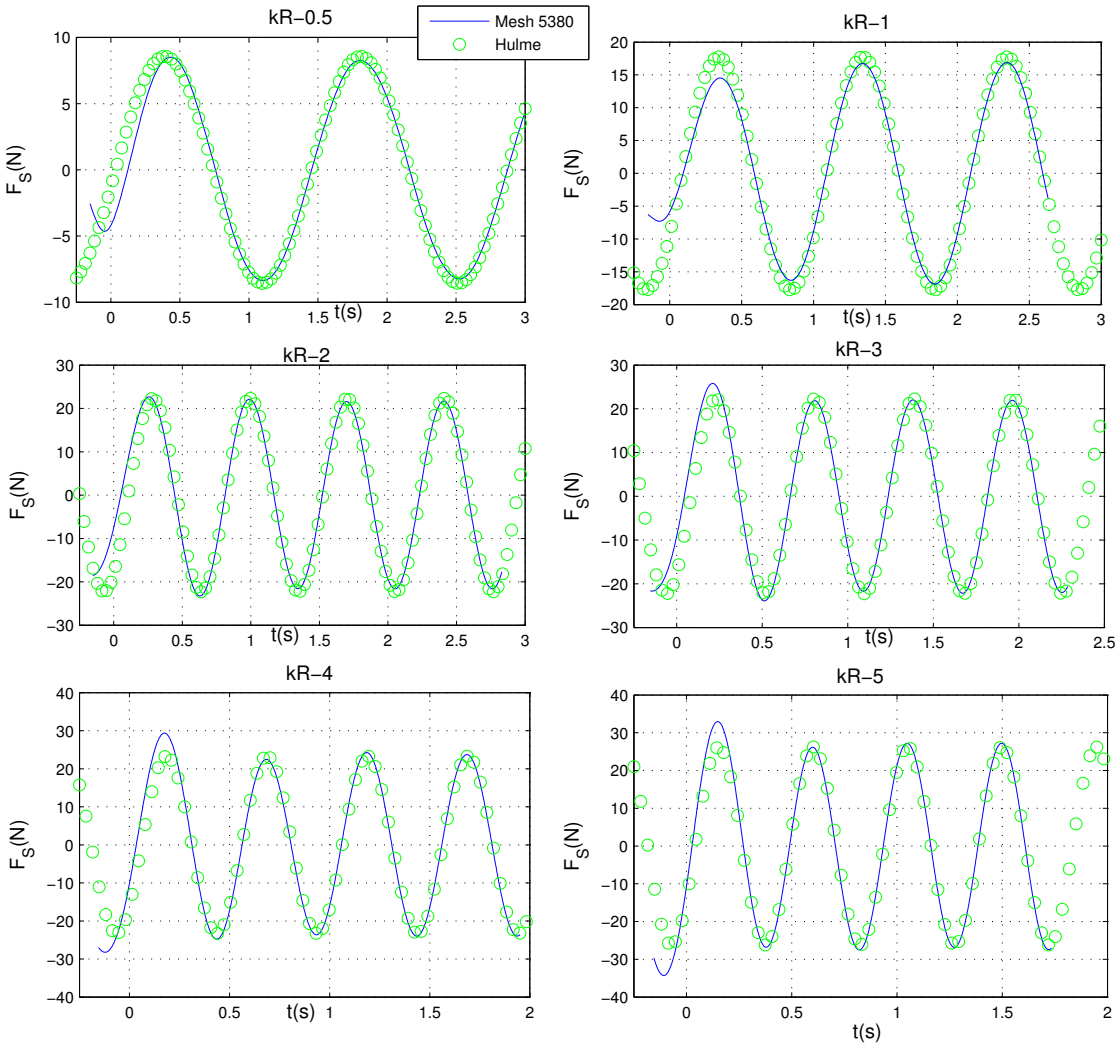

Figure 6.4: Time series of the sway force, $F_S(t)$, compared with the analitycal results for the swaying hemisphere, for kR=0.5, 1, 2, 3, 4 and 5.

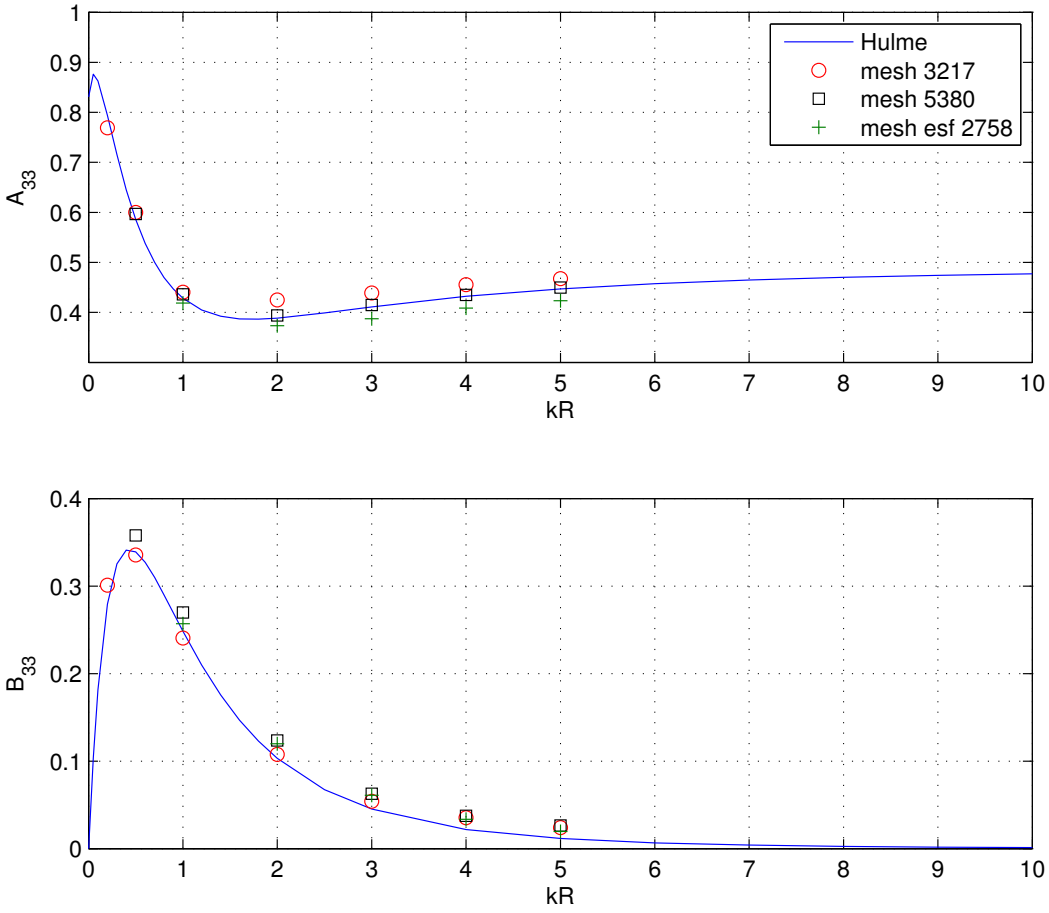

Figure 6.5: Comparison of the heave hydrodynamic coefficients for the hemisphere for kR=0.5,1,2,3,4 and 5 against numerical calculations using different mesh refinements .

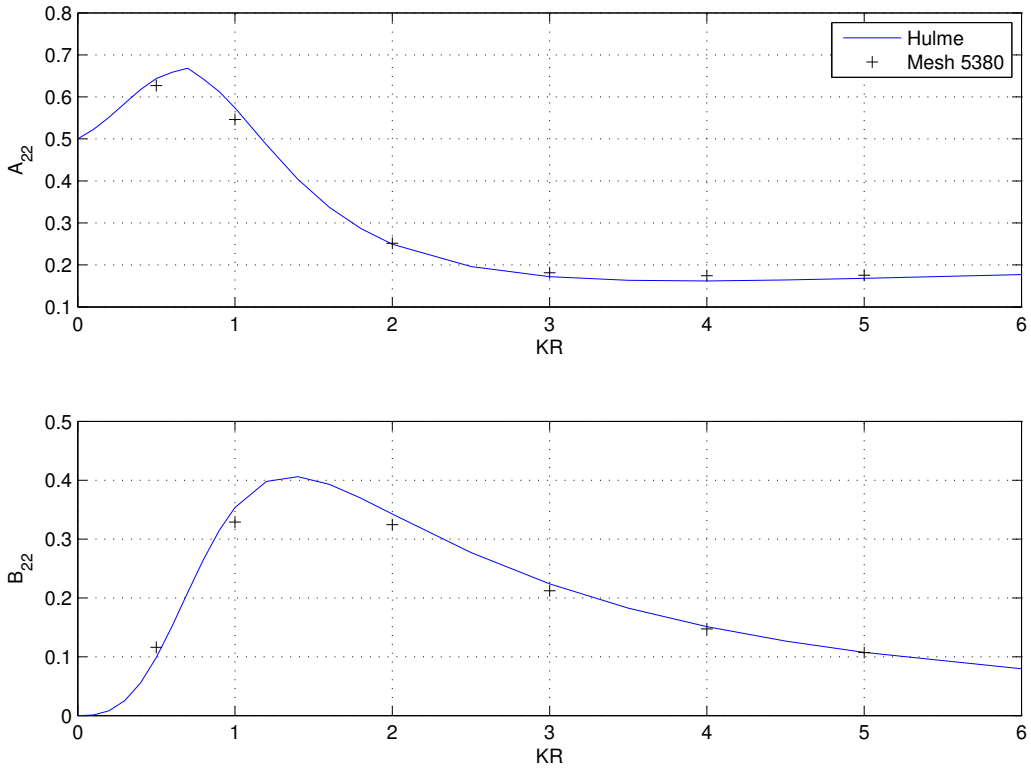

Figure 6.6: Comparison of the sway hydrodynamic coefficients force for the sphere for kR=0.5,1,2,3,4 and 5 agaisnt numerical calculations using the mesh with 5380 triangles.

6.3.2 Heave forced motions of a Wigley Hull form

In this section, the problem of forced oscillations in heave of a Wigley hull form is tackled. In this context, the Wigley hull model IV of Journée [1992] is chosen. The length,L in units, of the Wigley Hull as well as its non dimensional main data and block coefficient, C_b, are summarized in the Table 6.1. As it will be discussed in later chapters, the problem of estimating a signed distance function for ship like forms can be numerically daunting due to the different scales and curvature of ship like geometries. Consequently, for the simulation of the forced oscillation problem in this section, the Wigley hull is meshed using the algorithm developed by Geuzaine and Remacle [2009]. Therefore, points corresponding to three water lines ($z = -0.0625$, $z = -0.03125$ and $z = 0$ units) are inserted and interpolated using splines. Next, the splines are used to describe the hull surface, which is finally meshed.

The coarser mesh generated by this procedure and its corresponding domain mesh, a box like domain of dimensions [-4 -4 -1] x [4 4 0] units containing the Wigley hull, are shown in figure 6.8. In addition, element quality of both meshes are given in figures 5.12 and 5.13. Moreover, a refined mesh was also built in order to check the convergence properties of algorithm 3.

In the context of the numerical simulation, the primary concern is on element quality, because bad elements can actually break up the whole numerical scheme. This way, the problem of how close the geometry of the mesh fits the original geometry is left as secondary issue. However, in order to estimate the goodness of the fit to the original geometry, the still water displacements of both coarser and refined meshes (∇_1 and ∇_2 respectively) are compared against the exact value of the still water displacement of the original geometry (∇_{Model}), in units^3, in table 6.2.

Table 6.1: Wigley Hull Data

L	1.0
$\frac{L}{B}$	5.0
$\frac{B}{T}$	3.2
C_b	0.46

Table 6.2: Still Water Displacement

∇_{Model}	0.0058
∇_1	0.0051
∇_2	0.0051

Once a mesh is available for the Wigley hull, the problem of forced oscillations in heave can be solved using the formulation described in sections 6.1 and 6.2, for the zero forward speed case. The time series of the hydrodynamic force is shown on the figure 6.9 for different frequencies of oscillations, showing that the steady state is reached quickly. The usual Fourier decomposition, equations 6.5 and 6.6, is then used to calculate the added mass and damping coefficients.

The results obtained for the hydrodynamic coefficients are then compared with the experimental data of Journée [1992] in table 6.10, for the case with the lowest Froude number, i.e $F_n = 0.2$. At ranges of frequency where the assumptions of linear theory holds this comparison makes sense, because, in this case, the hydrodynamic coefficients are a function of only the frequency of oscillation Newman [1977] [1]. In addition, in the lower frequency range, the experimental data obtained showed a considerable velocity dependence. It can be argued, that this sort of effect is probably associated with viscous phenomena where the low speed of oscillation allows for a thick boundary layer to be formed around the floating body. Unfortunately, this sort of behaviour can be only be addressed by either tackling Navier-Stokes equations or by adding viscous corrections to the present code.

It is important to note that the data in figure 6.10 is non dimensionalized in following fashion:

$$\hat{\omega} = \frac{\omega}{\sqrt{g/L}} \tag{6.7}$$

$$\hat{A_{33}} = \frac{A_{33}}{\rho\nabla} \tag{6.8}$$

[1] In fact, effects due to the forward speed will also change the hydrodynamic coefficients. However, if the coupling between heave and pitch motions is small, the changes due to foward speed can also be shown to be small Newman [1977].

$$\hat{B_{33}} = \frac{B_{33}}{\rho \nabla \sqrt{g/L}} \tag{6.9}$$

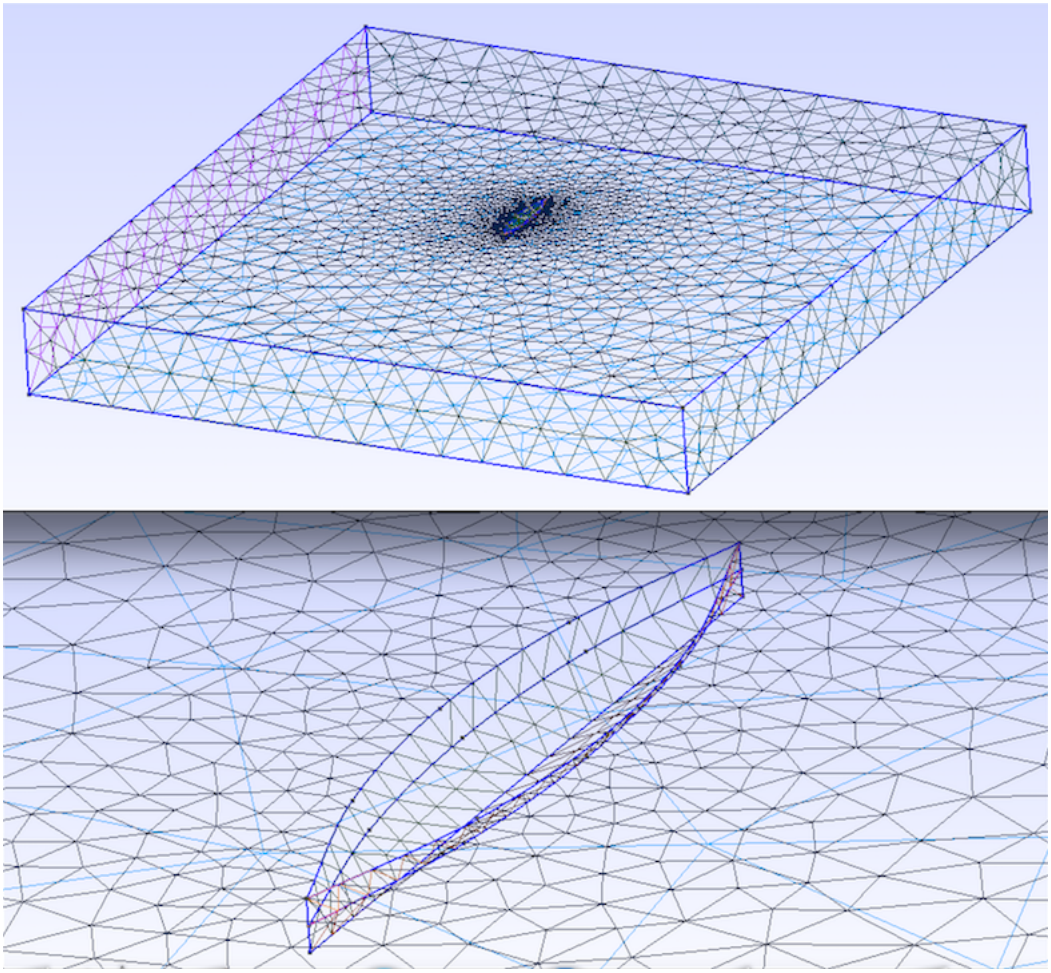

Figure 6.7: Top: Coarser mesh of the whole domain (box like domain) used to carry out forced heave oscilations of the wigley hull, 3298 triangles. Bottom: Wigley hull (L=1 unit, L/B=5 and B/T=3.20) mesh used to perform forced heave motions with 206 triangles.

The results in figure 6.10 indicate a reasonable agreement, for $\hat{w} > 1.63$, with the experimental results, for both the coarser and the refined meshes. In particular, algorithm 3 seems to have a small tendency to overestimate the damping coefficient and to underestimate the added mass coefficients, still the qualitative behaviour is reasonably good.

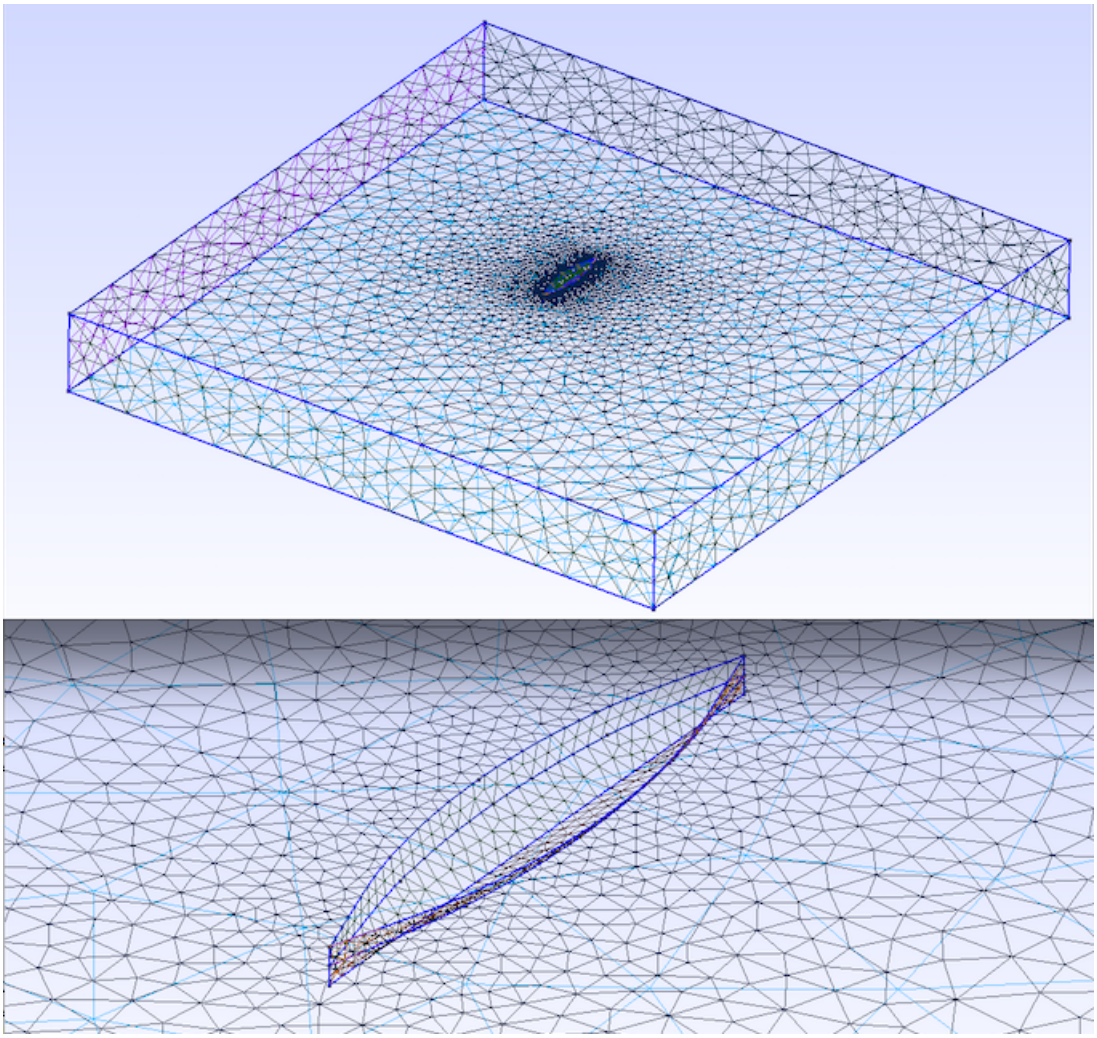

Figure 6.8: Top: Refined mesh of the whole domain (box like domain) used to carry out forced heave oscilations of the wigley hull, 6684 triangles. Bottom: Wigley hull (L=1 unit, L/B=5 and B/T=3.20) mesh used to perform forced heave motions with 796 triangles.

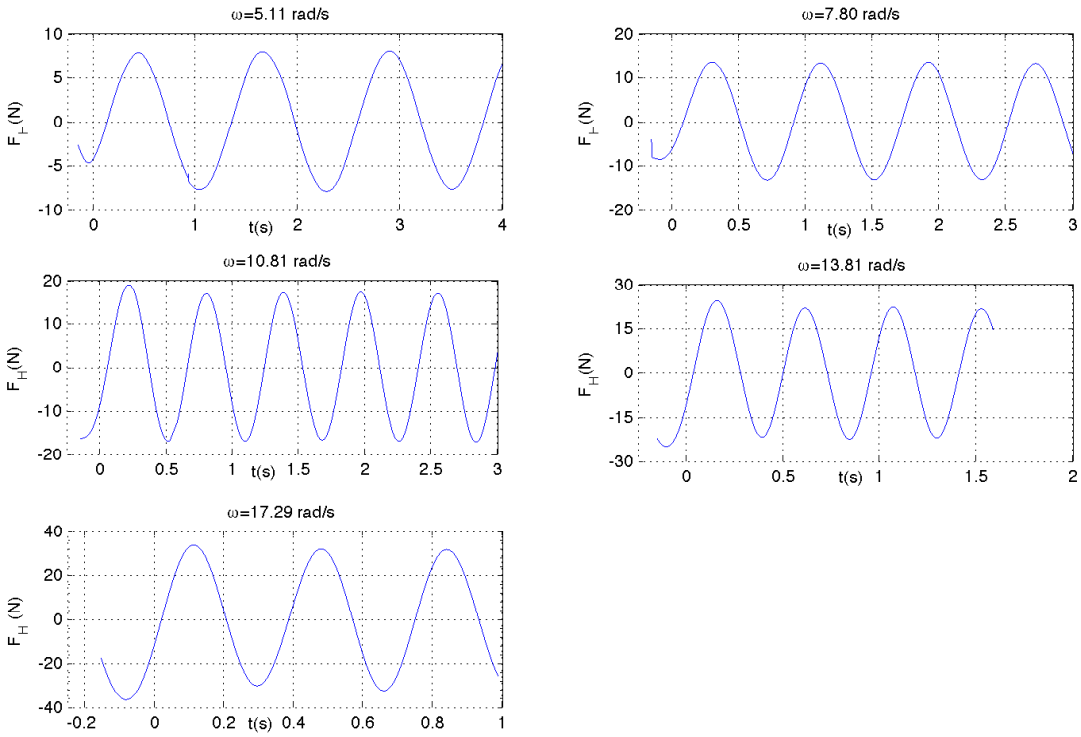

Figure 6.9: Time series of the Wigley hull heave force $F_H(t)$ for ω=5.11, 7.80, 10.81, 13.81 and 17.29 rad/s .

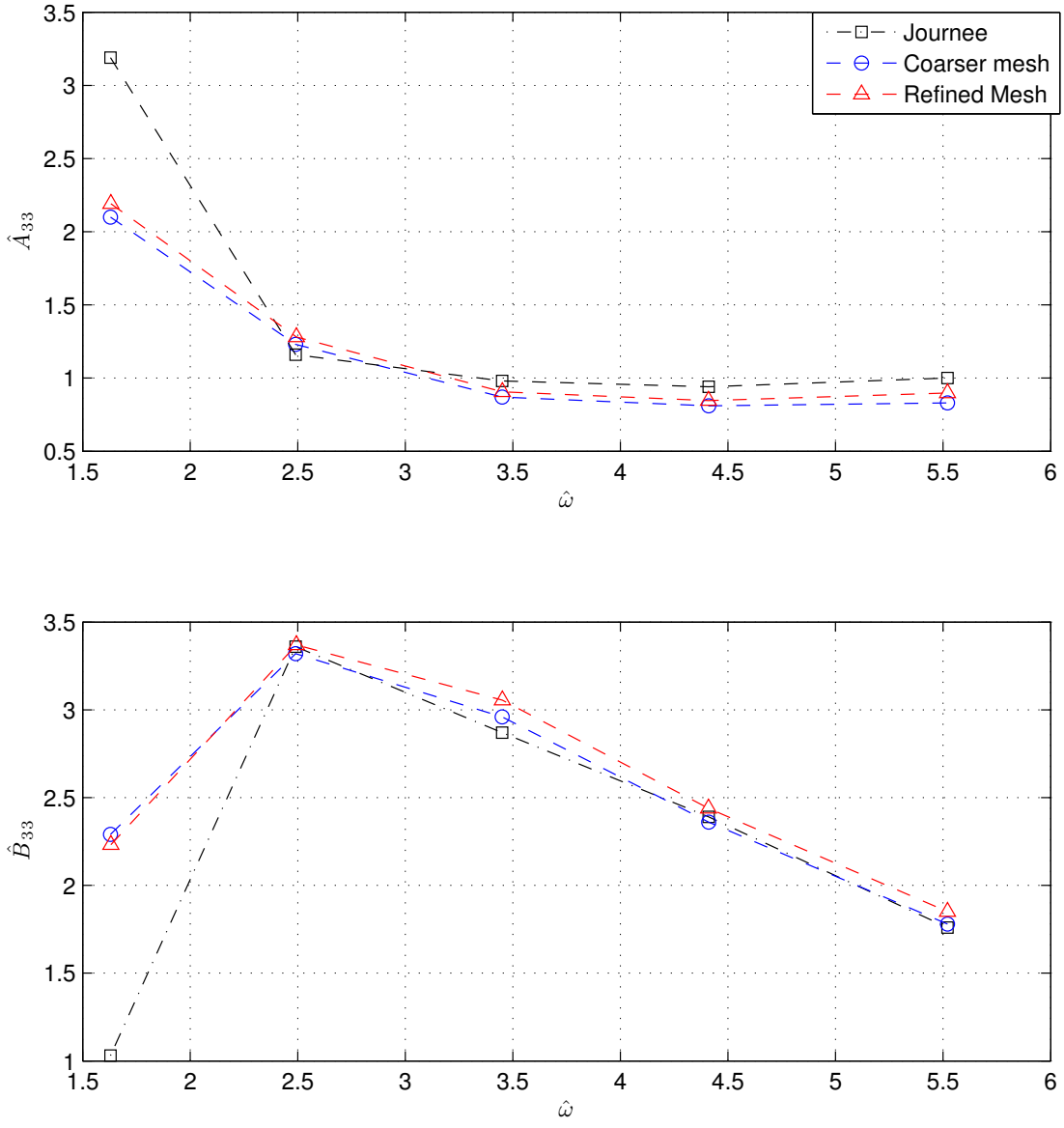

Figure 6.10: Comparison between the results obtained using algorithm 3 for the coarser and refined meshes and the experimental data from Journée [1992] for the Wigley hull undergoing forced oscillations in heave.

In order to go beyond the qualitative agreement two avenues could be pursued. First, note that the hydrodynamic coefficients are intimately associated with the actual geometry of the body and table 6.2 suggests that there is room to improve the fit to the original geometry, since the deviation of the volume estimated from the meshes to the original geometry is of the order of 0.13 per cent. Secondly, the accuracy of the BEM solver can certainly be improved, by the use of higher order methods or Garlekin based approaches. On the other hand, the cost of such improvements are higher from a computational runtime perspective, in the sense that they can easily lead to the fast multipole influence computation, GPU based linear system solvers and curved elements representations (see Xu [1992], Yan [2010] and Liu [2009]).

However, in the context of the present work, one of the main objectives lies in the development of a methodology that is capable of tackling problems of forced oscillations (radiation problems) in either rigid or flexible modes and problems related to the evolution of the free surface in time. This way, qualitative agreement is sought and improvements in either the numerical accuracy of the algorithms or in the geometry representation of the floating body are going to be discussed in the context of future work. By this token, in the next section algorithm 3 is extended to tackle the unified problem which takes into account rigid and flexible modes. Furthermore, since the qualitative behaviour of both coarser and refined meshes of the Wigley hull are reasonable, the coarser mesh will be used in the unified framework unless mentioned otherwise.

6.4 Hydroelasticity Analysis

In this section the formulation of the unified problem Bishop et al. [1986] is used to extend the problem of forced oscillations of rigid bodies to the case of flexible bodies. Essentially, in the MEL framework, in order to extend the analysis to tackle flexible floating structures undergoing forced oscillations, the crucial step is to formulate a structural model of the floating structure, so that distortion modes and their respective mode shapes are known. To this end, the Wigley hull is modeled as uniform Euler beam that undergoes forced rigid motions and dis-

tortions. In the boundary element context, a consequence of the unified approach is that the Neumann boundary conditions, imposed on the floating structure, are generalized, allowing to the introduction of the mode shapes of the beam model. The remainder of the boundary conditions remain unchanged, as in the rigid body problem. Once the boundary conditions are imposed, the problem is solved in time domain using the previous MEL scheme.

6.4.1 Boundary Conditions for the Flexible Case

For the unified 3D hydroelasticity radiation problem the forced motions of the floating structure are defined using the approach developed by Bishop et al. [1986]. Therefore, the forced oscillation motion with amplitude A, and circular frequency ω, imposed in the i^{th} mode of the structure, is written as follows:

$$\vec{u}_i(t) = p_i(t)\vec{W}_i(\vec{x}) = A\sin(\omega t)\vec{W}_i(\vec{x}); \tag{6.10}$$

where $\vec{W}_i(\vec{x})$ is the displacement vector associated with the mode shape corresponding to the i^{th} distortion mode. Therefore, if the six conventional rigid body motions (surge, sway, heave, roll, pitch and yaw) are denoted by the indexes i=1,2,3,4,5,6 respectively, then for translations (i=1 to 3) $\vec{W}_i(\vec{x})$ is actually equal to the unit vector and the oscillation is performed in the corresponding direction (x,y,z respectively). In addition, for rigid rotations about the origin of the reference system (i=4 to 6) the mode shape is calculated by the vector product $\vec{W}_i(\vec{x}) = \vec{W}_{i-3}(\vec{x}) \times \vec{x}$. For the flexible modes ($i > 6$), a subtle simplification is introduced which is reasonable if the deflections are assumed to be small. That is to say, it is assumed that the flexible mode shapes, in the vertical direction, are given by $\vec{W}_i(\vec{x}) = W_i(\vec{x})\vec{k}$, where $\vec{k}$ is unit vector along the vertical (z) direction. By the same token, in the horizontal direction, it is assumed that the flexible mode shapes are given by $\vec{W}_i(\vec{x}) = W_i(\vec{x})\vec{j}$, where $\vec{j}$ is unit vector along the horizontal direction, pointing to starboard. These approximations can take into account both vertical and horizontal bending, but they cannot be applied for the case of twisting.

In addition, assuming that the structure can be idealized as an Euler beam

leads to a simple expression for the displacement vector $\vec{W}_i(\vec{x})$:

$$W_i(x) = R_i(\cosh(q_i\frac{x}{L}) + \cos(q_i\frac{x}{L})) + (\sinh(q_i\frac{x}{L}) + \sin(q_i\frac{x}{L})). \tag{6.11}$$

The $q_i s$ are the constants eigen-solutions of the Euler beam. L is the length of the floating body and:

$$R_i = \frac{\sinh(q_i) - \sin(q_i)}{\cos(q_i) - \cosh(q_i)}. \tag{6.12}$$

Given this framework, from 6.10 it is straightforward to derive the impervious boundary condition on the floating body surface. Therefore the generalized version of 4.11 can be expressed, for motions in the vertical direction, as:

$$\nabla\phi(\vec{x}, t) \cdot \vec{n} = \dot{u}_i(t)\vec{k} \cdot \vec{n}; \tag{6.13}$$

likewise, for motions in the horizontal direction, the generalized version of 4.11 can be expressed as:

$$\nabla\phi(\vec{x}, t) \cdot \vec{n} = \dot{u}_i(t)\vec{j} \cdot \vec{n}. \tag{6.14}$$

Note that equations 6.13 and 6.14 are approximate versions of the impervious boundary condition for flexible modes. In fact, they neglect terms of the order A^2 and higher once the normal vector of the floating structure is assumed not to change when the body is subject to oscillations defined by the distortion modes (Bishop et al. [1986] actually derives a more general condition correct up to terms of order A^2). However, this boundary condition does make sense for small deflections of the flexible body and turns out to be a good approximation for the current purposes (i.e linearized free surface assumptions).

Once equation 4.10 is solved and under the assumptions of linear theory, the pressure acting on the floating body oscillating in the i^{th} mode can be greatly simplified. Therefore, the hydrodynamic force in the j^{th} direction is calculated for a rigid body, according to Newman [1977], by integrating the time derivative

of the potential on the floating body surface, ∂B; that is to say:

$$F_{ij}(t) = -\rho \int_{\partial B} \frac{\partial \phi}{\partial t} n_i dB. \tag{6.15}$$

Although equation 6.15 is valid only for rigid modes, it can be extended to account for unified mode shapes Bishop and Price [1979], yielding a generalized expression for the hydrodynamic force, as follows:

$$F_{ij}(t) = -\rho \int_{\partial B} W_j(\vec{x}) \frac{\partial \phi}{\partial t} n_i dB. \tag{6.16}$$

From the hydrodynamic force the added mass and damping coefficients are calculated by performing a Fourier decomposition of the force in the usual fashion, which leads to an estimation of hydrodynamic coefficients corresponding to both rigid and flexible modes.

Algorithm 4 summarizes the time domain simulation, under the assumptions of the unified hydroelastic theory applied to the problem of forced oscillations.

Algorithm 4 Unified Linear Time Domain Simulation

1: **procedure** MAIN( )
2: [p,t]=CreateMesh(fd,fh,h0); ▷ Create a mesh of the domain
3: $[x_{FS}, y_{FS}, x_B, y_B, z_B]$:=FindBoundaryNodes(p,t);
4: **while** $t < T$ **do**
5: ϕ_{FS}:=$\Phi_i(x_{FS},y_{FS}$,t) ▷ Set BC Value on the of the FS triangles
6: $\nabla\phi \cdot \vec{n}_B := \vec{u}(t) \cdot \vec{n}_B$ ▷ Set BC Value on the Floating Body
7: $\nabla\phi \cdot \vec{n}_B := 0$ ▷ Set BC Value on other Neumann Boundaries
8: $[\phi_B; \nabla\phi \cdot \vec{n}_{FS}] := [G_{FS}; Gn_B]^{-1}[\nabla\phi \cdot \vec{n}_B; \phi_{FS}]$ ▷ Solve the BVP at $z_{FS} = 0$
9: $F_{ij}(t) := -\rho \int_{\partial B} W_j(\vec{x}) \frac{\partial \phi}{\partial t} n_i dB.$ ▷ Calculate the force on B
10: $z_{FS} := z_{FS} + (\frac{\partial \phi}{\partial z} - \nu z_{FS})dt$ ▷ Update the FS elevation
11: $\phi_{FS} := \phi_{FS} + (-z_{FS}g - \nu\phi_{FS})dt$ ▷ Update the FS potential
12: $t := t + dt$
13: **end while**
14: **end procedure**

At this point, it is interesting to compare both algorithms 3 and 4. In fact, just lines 6 (i.e the boundary condition imposed on the floating body) and line 9 (the integration of the pressure around the body surface) actually change due

to the unified formulation. Using this algorithm results, for both symmetric and antisymmetric modes, were obtained, The next sections presents these results and compare them against other numerical methods.

6.4.2 Results for Symmetric Modes

In this section the problem of forced motions of the Wigley hull model IV, shown in Table 6.1,is investigated. In this context, the symmetric rigid modes of heave (i=3) and pitch (i=5) together with two flexible modes for i=7 (2-node) and 8 (3-node) are considered.

For the Wigley hull, it was found empirically that the size of the damping zone has a more pronounced effect than for the hemisphere, especially in the lower frequency range (higher wavelengths) where reflection has been observed. In order to overcome this problem two meshes were created with different free surface sizes, whereas the mesh on the floating body surface remained the same, i.e. 206 triangles.

The smaller mesh comprised 3298 triangles with a range between [-4, -4, -1] and [4, 4, 0] units, shown in 6.8. The larger mesh 5318 triangles with a range between [-5, -5, -1] and [5, 5, 0] units. The non-dimensional added mass $A_{ii}/(\Delta L^2)$ and and damping $B_{ii}/(\Delta L^2\sqrt{gL})$ coefficients shown in figures 6.11, 6.12, 6.13 and 6.14. These are plotted against non-dimensional frequency $\omega\sqrt{g/L}$. The larger of the meshes is used for the two smaller frequencies, whilst the smaller mesh is used for the remainder. The predicted values are compared with experimental measurements by Journée [1992] (rigid body motions only), 2D hydroelasticity predictions by Bishop and Price [1979] (using 20 sections along the hull, denoted by mars) and 3D hydroelasticity predictions by Bishop et al. [1986] (pulsating source method using 350 panels on the mean wetted surface, denoted by flxbd). The predictions of the current method, i.e algorithm 4 are denoted by time domain.

The non-dimensional (generalized) heave and pitch added mass and damping coefficients (no coupling due to fore-aft symmetry) are shown in figure 6.11. There is good agreement between the current predictions and Journees experimental measurements, except for the relatively small frequencies. The agreement

is also good between the current predictions and the 3D analysis. In some cases the current prediction is closer to the experimental results than the 3D analysis, e.g. for B_{33}. The predictions from the 2D analysis are smaller than all other results. The non-dimensional (generalized) added mass and damping coefficients for the distortion modes i=7 and 8 are shown in figure 6.12 The comparison between 3D hydroelasticity and the current predictions show good overall agreement, with the results by the current method in general larger than the 3D frequency domain hydroelasticity. There is poor correlation between the 2D and 3D hydroelasticity results. It should be noted that there is no coupling between i=7 and i=8 modes due to the fore-aft symmetry. The coupled hydrodynamic coefficients are illustrated using i=3 (heave) and i=7, and i=5 (pitch) and i=8, these are shown in figures 6.13 and 6.14. The agreement is good between the 3D frequency and time domain methods, although the latter is larger for the B37 damping coefficient for relatively large frequencies of oscillation. The predictions from the 2D hydroelasticity theory are smaller than either 3D prediction, especially for the added mass A37 and do not show good agreement for the damping coefficient B85.

The experience with the Wigley hull shows the complexities of the problem even when comparing simple geometries, such as the hemisphere and Wigley Hull. Although the domain is relatively large, the body or mean wetted surface is still relatively crude. Differences were observed for relatively small and large frequencies of oscillation. The former can be dealt with at the expense of a larger domain. The latter is likely to require more refinement on the body, implying a much finer free surface mesh in the vicinity of the body, hence, a much larger overall mesh, which again calls for a parallel linear system solver.

6.4.3 Results for Anti-Symetric Motions

In the context of anti-symmetric motions, the problem to be addressed is the one of a floating structure undergoing sway and roll forced oscillations. For sway, in framework currently adopted, the boundary condition, equation 6.14, needs to be imposed on the body surface. By using this impervious boundary condition, the assumptions of Euler beam and its respective mode shape are assumed to hold true, since $\vec{u_i}$ actually depends on the mode shapes of the beam by equation 6.10.

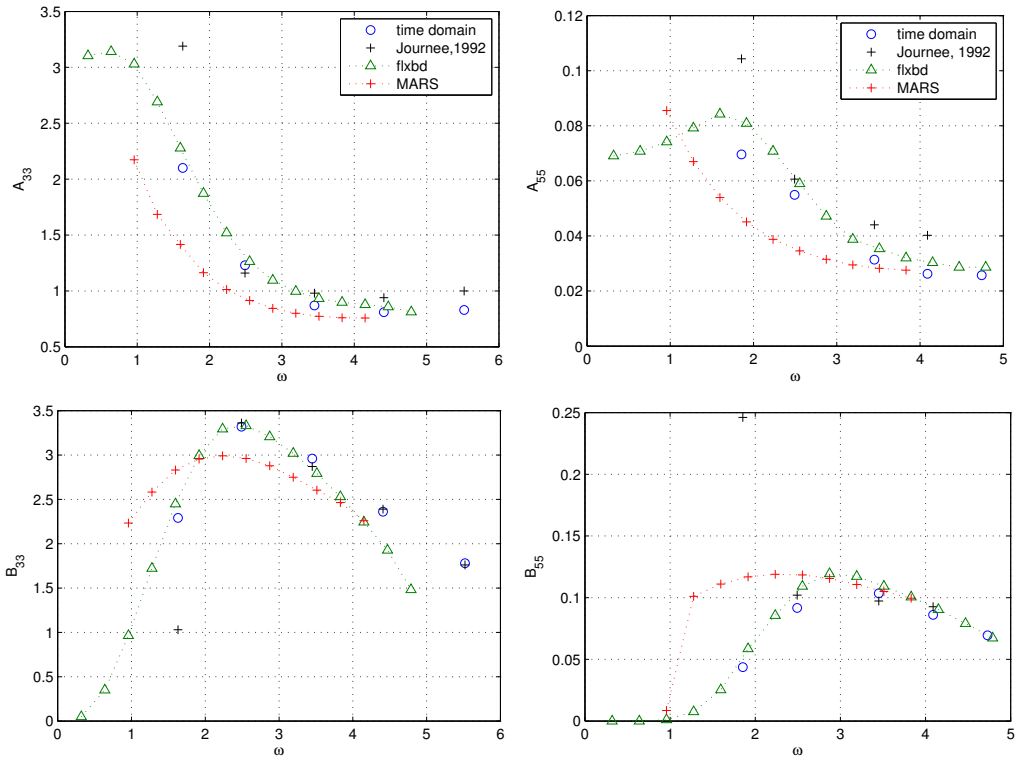

Figure 6.11: Comparison of model test results, MARS (2d strip theory) and the model developed by Bishop et al. [1986] (3d frequency domain model , flxbd) against the current calculations for the wigley hull undergoing forced motions in mode 3 (heave) and 5 (pitch).

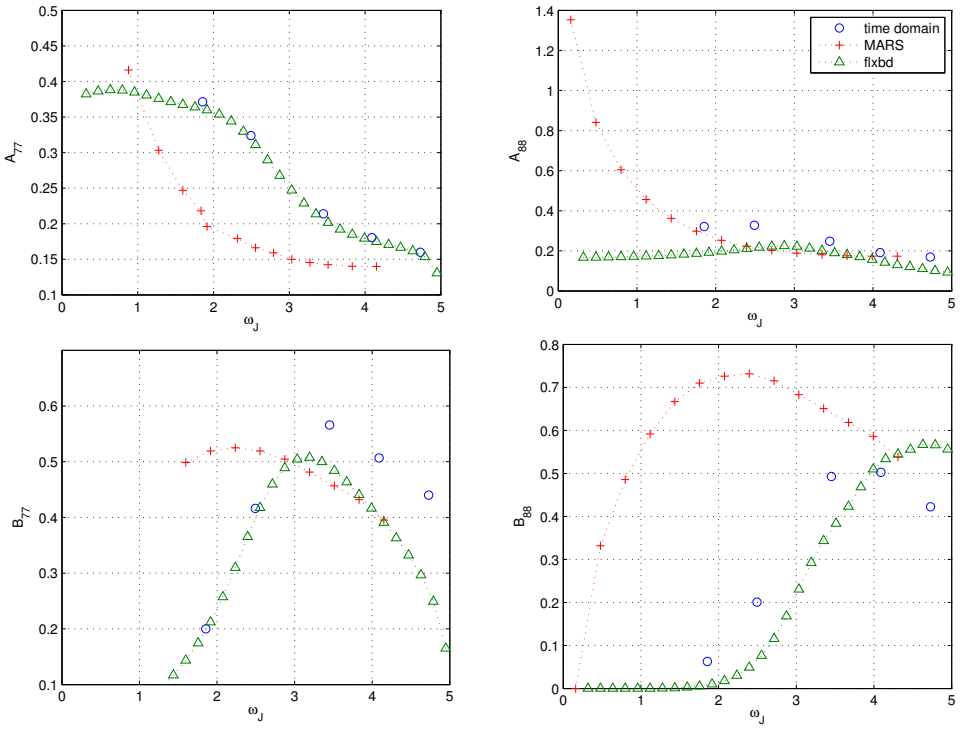

Figure 6.12: Comparison of MARS (2d strip theory) and the model developed by Bishop et al. [1986] (3d frequency domain model , flxbd) against the current calculations for the wigley hull idealised as an Euler Beam model undergoing forced motions in modes 7 (2-node) and 8 (3-node).

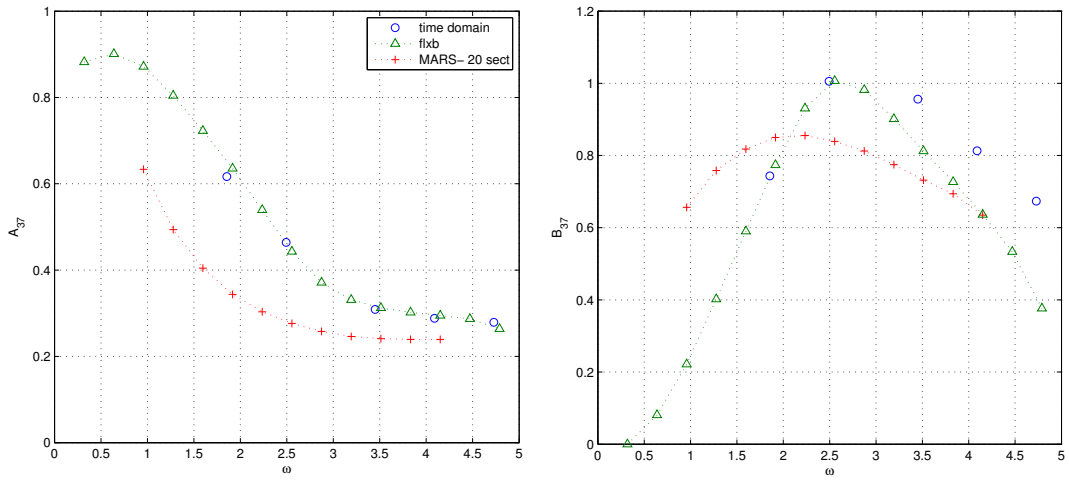

Figure 6.13: Comparison of MARS (2d strip theory) and the model developed by Bishop et al. [1986] (3d frequency domain model , flxbd) against the current calculations for the wigley hull idealised as an Euler Beam model undergoing forced motions for cross couple modes 3 (heave) and 7 (2-node).

Using the same meshes described in the previous section the simulation is then carried on. Note that, since the hull is now being oscillated on the y direction we are interested in three sets of hydrodynamic coefficients, namely: sway into sway, sway into roll and sway in the first distortion mode (i.e 2-node) in the horizontal plane, which is called here mode 7 as well. Unfortunately the notation is overloaded because mode 7 in this section refers to first distortion mode in the horizontal plane, whereas mode 7 in the previous section referred to the first distortion mode in the vertical plane.

The hydrodynamic coefficients obtained are then compared against the numerical calculations from Bishop et al. [1986] , i.e 3d frequency domain analysis (referred as flxbd in the plots). The hydrodynamic coefficients are plotted in figures 6.15, 6.16 and 6.17 for sway into sway, sway into roll and sway into the first distortion in the horizontal plane (2-node , denoted by mode 7 throughout

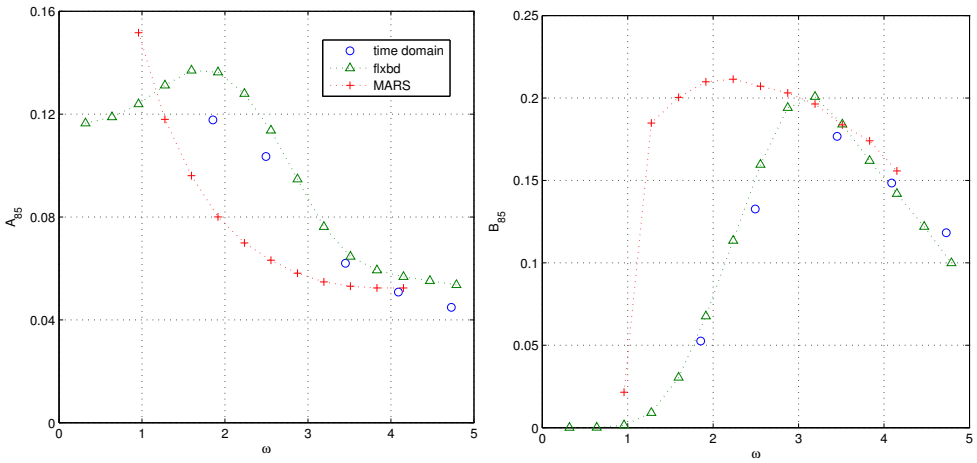

Figure 6.14: Comparison of MARS (2d strip theory) and the model developed by Bishop et al. [1986] (3d frequency domain model , flxbd) against the current calculations for the wigley hull idealised as an Euler Beam model undergoing forced motions for cross couple modes 5 (pitch) and 8 (3-node).

this section).

At this point a couple of remarks can be highlighted. First, it can actually be seen that the agreement, compared to what was obtained in heave and pitch, has worsened, although the overall qualitative behaviour is resonable. In addition, by looking at the cross coupled hydrodynamic coefficients the agreement is somewhat poor.

In a attempt to improve the numerical accuracy of the simulations, the integration method of the free surface boundary condition was refined. This way, a second order Rungee Kutta scheme (RK2) was implemented (its description and implementation are detailed in the Appendix A Numerical Techniques) and some of the frequencies for the sway forced motions were run again and compared to the former results obtained by the Euler scheme (green circles in figures 6.15, 6.16 and 6.17). A comparison between the results suggest that, although the use of

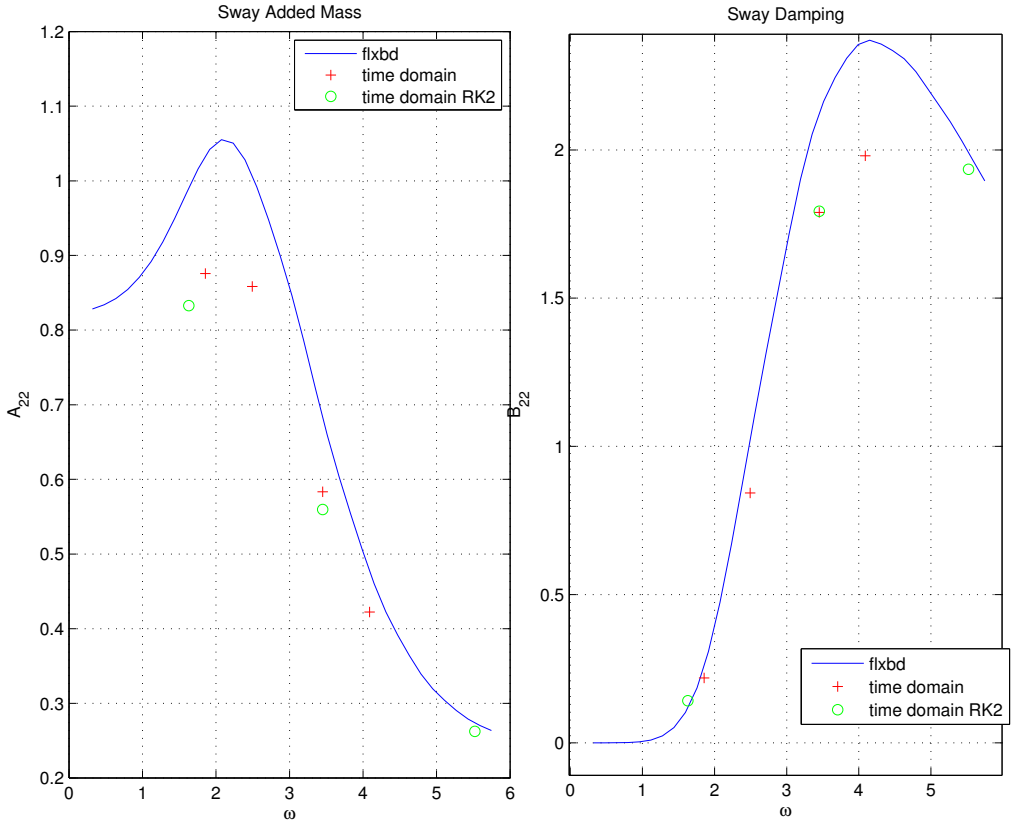

Figure 6.15: Comparison of the model developed by Bishop et al. [1986] (3d frequency domain model , flxbd) against the current calculations for the wigley hull idealised as an Euler Beam model undergoing forced motions of sway into sway.Green circles denote the RK2 scheme, red crosses Euler method.

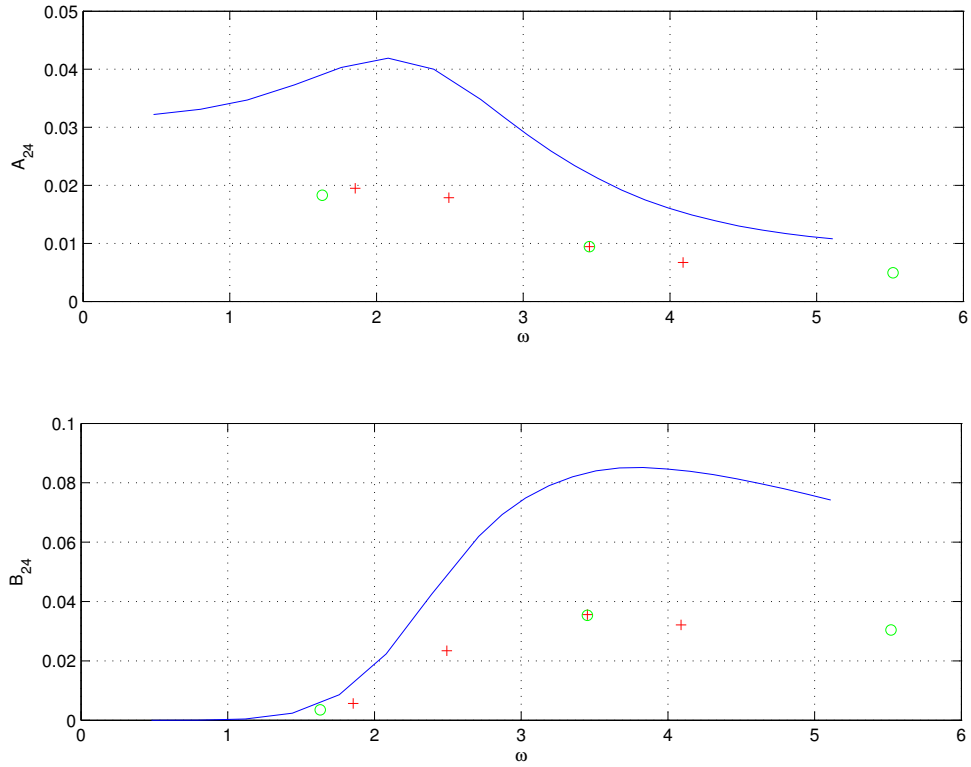

Figure 6.16: Comparison of the model developed by Bishop et al. [1986] (3d frequency domain model , flxbd) against the current calculations for the wigley hull idealised as an Euler Beam model undergoing forced motions of sway into roll. Green circles denote the RK2 scheme, red crosses Euler method.

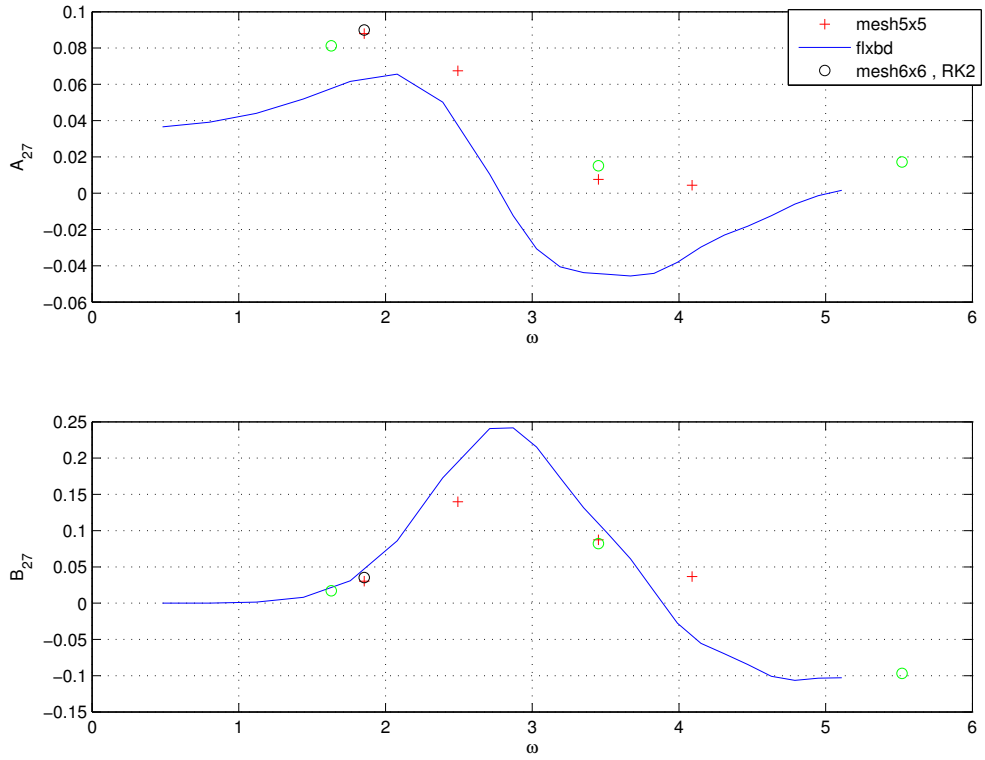

Figure 6.17: Comparison of the model developed by Bishop et al. [1986] (3d frequency domain model , flxbd) against the current calculations for the wigley hull idealised as an Euler Beam model undergoing forced motions of sway into the first distortion mode in the horizontal plane, 7 mode (2-node).Green circles denote the RK2 scheme, red crosses Euler method and black circles are calculated on the mesh with a bigger damping zone [-6,-6,-1] x [-6,6,0] free surface using RK2.

the second order integration scheme allows the simulation to run at larger time steps, the comparison of the hydrodynamic coefficients using an Euler scheme and the second order method, suggest that for the range of time steps where the Euler scheme is stable, the accuracy of both integrators are very close. In addition, to investigate further the occurence of wave reflection in the lower frequency range a third mesh [-6,-6,-1] x [-6,6,0] was also used together with the RK2 scheme, this result plotted in figure 6.16 as black dots. This results indicates that, for the present purposes, convergence has been achieved with the [-5,-5,-1] x [-5,5,0] mesh, hence, there is no need to use a bigger domain or damping beaches in this case.

Therefore, the bottleneck is not actually in the free surface integration. Other possible reasons rely on relatively crude mesh representation of the geometry (this can be investigated further by a convergence estimation of the numerical algorithm in the h-sense Karniadakis and Sherwin [2005], at the cost of much bigger domain) or in inacuracies relating to the estimation of the potential derivative around the floating body (i.e $\frac{\partial \phi}{\partial t}$), which is actually being estimated by simple backward difference scheme in algorithm 4. For a more comprehensive discussion on the evaluation of $\frac{\partial \phi}{\partial t}$ please refer to the next chapter.

Despite some drawbacks relating to accuracy issues, a methodology that encompasses the simulation of potential flow and gives a qualitative good agreement with other methods based on potential flow theory has been developed and shown to work in the context of the unified linear time domain problem. Once this is achieved, it is possible to then work out refinements, like the accuracy of the Boundary Value problem solver for instance, and improve the methodology further.

6.5 Conclusions

In this chapter, the problem formulated in chapter 4 was implemented numerically. Under the assumptions of linearized potential flow theory, forced oscillations problems for a rigid body were tackled and the results compared against exact potential flow solutions (for the hemisphere) and experimental data (for the

wigley hull, when available), showing a good qualitative behaviour on the rigid modes simulated.

An extension of the boundary conditions for the case of a floating structure undergoing forced distortion motions was also derived and implemented, accomplished by formulating the problem using the unified theory of hydroelasticity. The approach used for the unified problem was then validated through comparisons with 3D and 2D hydroelasticity predictions for symmetric and anti-symmetric (bending) modes. For the symmetric modes the results a good qualitative agreement was obtained. For the case of anti-symmetric modes the hydrodynamic coefficients obtained showed a reasonable qualitative agreement, but the numerical results were not as accurate as the ones obtained for symmetric modes. In order to tackle this issues a RK2 scheme was also implemented and the results were compared with the coefficients obtained using the Euler method. Although RK2 allowed the simulation to march with larger time steps, the hydrodynamic coefficients were basically unchanged. This suggests that the discrete domain (mesh of the geometry) could still be too crude. Finer meshes would require a parallel implementation of a linear system solver, which was left out of the scope of the present work. Nonetheless, this is indeed an avenue for future research.

Issues related to problems of accuracy of the constant panel method solver as well as possible issues related to the accuracy of the geometry representation of the floating body have been outlined. In addition, issues have been identified with reference to the size of the domain, in particular at relatively low frequencies of oscillation. A brief analysis of influence of the free surface size suggests that for the Wigley hull simulations on the lower frequency range, the mesh [-5, 5, 0]x[-5, 5, -1] has a suitable size, whereas, with [-4, 4, 0]x[-4, 4, -1] mesh, wave reflection has been observed.

Despite of the drawbacks mentioned above the results obtained showed a qualitative good/resonable agreement for the present purposes, i.e developing a methodology to simulate three dimensional potential flow structure interactions using an unstructured grid. Accordingly, in the next chapter, an extension of the algorithms presented in this chapter, to include body non linear and non fully linear effects, will be carried out.

Chapter 7

Time Domain Non Linear Analysis

This chapter discusses how the methodology developed in chapters 4 and 5 can be extended to carry out potential flow simulations using the body non linear and fully non linear formulations, still in the context of forced motions. As pointed out earlier, the problem of free motions in waves is out of the scope of the present work and the efforts will focus in trying to model the changes in the hydrodynamic coefficients as a function of the amplitude of the forced oscillation.

Under the assumptions of potential flow theory, in time domain, there are basically three sources of nonlinearities that can change the hydrodynamic coefficients of a floating structure. The first source of non linearity is caused by the changes in the submerged geometry of the floating body. The second source is caused by the time evolution of water line, i.e, as the body enters and exits the water not only its submerged geometry changes, but also, the instantaneous water line evolves in time. In this process, it turns out that not only changes in hydrostatic forces are observed, but also hydrodynamic components, neglected by the linearized theory, arise. The third source of non linearity is the non linear free surface boundary conditions, so that on the free surface, as opposed to the linear case, the Bernoulli equation cannot be linearised anymore, thus a quadratic

term, i.e, the velocity of the fluid, needs to be computed as well. In order to tackle this these issues, a couple of changes in the algorithm that was used in the last chapter are required. In particular, one of the most difficult numerical challenges is that the domain now changes in time, therefore a new mesh and a new influence matrix will have to be computed at each time step. In addition, in the context of the fully non linear theory, the free surface position also changes in time. Therefore a numerical scheme to deal with not only its movements but also with the interpolation of the free surface potential needs to be implemented.

In section 7.1 the body non linear is approach is introduced. The numerical techniques used to estimate the derivatives of the velocity potential are also described and two algorithms are proposed to solve the body non linear problem. Section 7.2 presents the results of the BNL analysis for the case of a sphere undergoing forced oscillations in the heave mode, for a range amplitudes; the results are compared to other numerical predictions. Moreover, the results of the Wigley hull undergoing forced oscillations in heave are computed and compared against available experimental data. Section 7.3.1 formulates the non linear free surface bondary conditions by allowing motions only on the vertical direction.

The results of the non linear analysis are presented in section 7.3.2 and compared to other numerical predictions available. Finally, section 7.4 concludes the analysis developed in this chapter.

7.1 Body Non Linear

The body non linear approach aims to capture effects caused by the changes of the wetted surface of the floating body. From a hydrodynamic perspective, in order to gain some intuition on this behaviour, a parallel to hydrostatics can be helpful, for instance: when a body undergoes small oscillations about its mean free surface position, the variation of its immersed volume can be linearized with respect to its draught (actually this depends on the geometry, but this holds true for small curvatures along the longitudinal and transversal directions); in that sense the hydrostatic force is written as linear function of the draught. As the amplitude of the oscillation increases, this approximation no longer holds true

and the immersed volume has to be calculated by integration. When it comes to hydrodynamic coefficients the behaviour turns out to be similar, but the dependence on the immersed volume is not as straightforward as in the hydrostatic case because the pressure field is more complex.

In order to investigate this dependence, the model used in the last chapter needs to be extended to account for the changes on the wetted surface of the floating body. From an implementation perspective, this brings problems associated with the model used here, namely:

1. Due to the amplitude of the body motions, the distance function of the floating body now varies with time;

2. As the domain changes through time, a new mesh needs to be generated at each time step so that the changes of the position of the floating body are accounted for;

3. The evaluation of the derivative of the potential function with respect to time becomes harder to evaluate (see He and Kashiwagi [2009] for instance) , since now the potential scalar field is defined in a specific mesh at each time step and its temporal derivative needs to be calculated;

4. As pointed out by Lin and Yue [1991] , even when the free surface boundary conditions are linearized, the quadratic term on Bernoulli's equation (i.e the pressure) can have a considerable contribution to the hydrodynamic force on the floating body. Therefore, the potential gradient needs to be estimated as well.

Issues 1 and 2 are straightforward to deal with. Actually, given the correct distance function at a given time step the mesh generator can be called and output a new mesh. This new mesh then represents the idealization of the domain at that given time step. However, in order to accomplish this, one still has to make the signed distance function of the floating body, hence of the whole domain, $fd(t)$, time dependent. Recall that the signed distance function of a sphere, with radius r, centered at a point $\vec{x}_c = (x_c, y_c, z_c)$, can be easily described analytically,

on a grid point $\vec{x}$, by:

$$d_{esf}(\vec{x}, \vec{x}_c) = \sqrt{(x - x_c)^2 + (y - y_c)^2 + (z - z_c)^2} - r. \tag{7.1}$$

So, if the sphere undergoes an oscillatory motion in heave with amplitude A and frequency ω, then $z_c(t) = Asin(\omega t)$ gives the position of its center. Thus, the time dependence of the distance function can be made by a direct substitution on the equation above; more details on how to estimate and propagate signed distance functions in time can be found in the next chapter.

7.1.1 Estimation of the potential time derivative

The estimation of the time derivative of the potential, in the body non linear (and fully non linear) framework, is much more involved than in the linear case. Under the assumptions of linear theory the geometry of the domain does not change, therefore the same mesh can be used every time step. This implies that the total time derivative is equal to partial derivative of the potential at each point (i.e the grid has zero velocity, so the convection terms vanishes). On the other hand, when the submerged geometry of the floating body is changing in time a different approach is needed.

There are two avenues to tackle this problem. The first one, is to adopt a grid tracking scheme, where the nodes on the floating body are tracked at every time step. Since the position of nodes are known in subsequent time steps their velocities can be calculated. This way, the material derivative of the potential can be approximated using a finite difference scheme and, since the velocity of the nodes of the floating body, V_g, is also known, $\frac{\partial \phi}{\partial t}$ can be estimated as Lin and Yue [1991]:

$$\frac{\partial \phi}{\partial t} = \frac{D\phi}{Dt} - V_g \cdot \nabla \phi, \tag{7.2}$$

where $\frac{D\phi}{Dt}$ is evaluated by an upwind scheme, between t=t and t=t-dt, i.e:

$$\frac{D\phi}{Dt} = \frac{\phi(x, y, z, t) - \phi(x, y, z, t - dt)}{dt}, \tag{7.3}$$

and V_g is the grid velocity.

Since the meshes t=t and t=t-dt are not the same, the potential needs to be interpolated at the points of time t=t, but at the instant t=t-dt. In order to accomplish this, at every time step, a radial basis function representation of the potential is found, as follows:

$$\phi(x,y,z,t) = \sum_{i=1}^{n} b_i f(\sqrt{(x-x_i)^2 + (y-y_i)^2 - (z-z_i)^2}) + b_0, \tag{7.4}$$

where a solution of the linear system will lead to the values of the coefficients $b_i's$, see proposition 7.1.2 for case where $\lambda = 0$. In equation 7.2, note that if the grid velocity equals the floating body velocity, the fully Lagrangian particle tracking scheme is recovered.

Once the rbf representations are available, the runtime of encoding equation 7.2 is proportional to the number of nodes on the floating body, so it is computationally efficient (linear run time). In addition, according to Yan [2010] a reasonable estimation of the pressure field for problems with zero or small amplitude body motions can be attained. On the other hand, issues related to non physical oscillations when the body discretization is modified have also been reported by (Battistin and Iafrati [2003] and Wu and Eatock Taylor [1996]). In fact, the results obtained by the body non linear approach suggest that these non physical oscillations are associated with interpolation innacuracies. This happens because as the domain is remeshed the points on the new mesh are not same as the ones on the old mesh, so if the interpolation has a lower accuracy it induces spurious oscillations.

Alternatively, the boundary value problem can be solved directly for $\frac{\partial \phi}{\partial t}$, in theory avoiding the instabilities inherent from the finite difference scheme. This can be achived by taking partial derivatives with respect to time of equation 4.10, i.e:

$$c(\vec{x_i})\phi_t(\vec{x_i},t) = \sum_{j=1}^{N} \int_{E_j} G(\vec{x_i},\vec{y_j}) \frac{\partial(\nabla\phi(\vec{y_j},t)\cdot\vec{n})}{\partial t} dE_j - \sum_{j=1}^{N} \int_{E_j} \phi_t(\vec{y_j}) \nabla G(\vec{x_i},\vec{y_j})\cdot\vec{n} dE_j. \tag{7.5}$$

In this second BVP, equation 7.5 is solved for ϕ_t on the floating body and for $\frac{\partial^2\phi}{\partial t\partial n}$ (the normal acceleration) on the free surface.

This way, on the free surface, the Dirichlet boundary condition is prescribed on ϕ_t, which is actually the dynamic boundary condition of the free surface. In the context of body non linear simulations it is written simply as:

$$\frac{\partial\phi}{\partial t} = -gz. \tag{7.6}$$

The Neumann boundary condition imposed on the floating body is the time derivative of the impervious boundary condition, i.e $\frac{\partial^2\phi}{\partial t\partial n}$. For a rigid body with no heel angle, it can shown (Wu and Eatock Taylor [1996], Battistin and Iafrati [2003]) that it is given by :

$$\frac{\partial^2\phi}{\partial t\partial n} = \vec{n}_B \cdot \vec{a}_B - \vec{n}_B \cdot (\vec{v}_B \cdot \nabla)\nabla\phi, \tag{7.7}$$

where $\vec{n}_B$ is normal vector of the floating body, $\vec{a}_B$ its acceleration and $\vec{v}_B$ its velocity.

Under this framework, it is worth pointing out the dependence of the first and second BVPs. On the first one the potential on the floating body ϕ is found. Once ϕ is known its spatial gradient $\nabla\phi$ can be calculated at the corresponding time step to enter the last term in equation 7.7. Actually, the terms in equation 7.7 can be difficult to evaluate, specially in the context of free floating bodies when the body acceleration $\vec{a}_B$ is not known a priori, but instead depends on the pressure field itself, in this situation, an iterative scheme is needed. Furthermore, under free motions, the velocity potential is more complex since it now has also components corresponding to the diffraction problem, making its estimation numerically daunting.

On the other hand, in the context of forced oscillations problems both $\vec{a}_B$ and $\vec{v}_B$ are known a priori, making equation 7.7 more straightforward to apply.

More concretely, when we are concerned with forced oscillations in the heave mode, $\vec{v}_b = (0, 0, A\omega cos(\omega t))$ and $\vec{a}_b = (0, 0, -A\omega^2 sin(\omega t))$. Furthermore, it can be shown (see Appendix A Numerical Techniques), that for the case of heave

forced motions equation 7.7 reduces to:

$$\frac{\partial^2 \phi}{\partial t \partial n} = \vec{n}_B \cdot \vec{a}_B - v_3 \vec{n}_B \cdot \nabla \frac{\partial \phi}{\partial z}, \tag{7.8}$$

v_3 being the velocity on the vertical direction, i.e $v_3 = A\omega cos(\omega t))$.

The major drawback of this method is that instead of solving one boundary value problem, two boundary value problems need to be solved so that the solution of the first is the boundary condition for the second one (i.e $\nabla \frac{\partial \phi}{\partial z}$ term in equation 7.8). At this point it is important to point out that before estimating $\nabla \frac{\partial \phi}{\partial z}$, one needs to estimate the spatial derivatives of the velocity potential, this problem is tackled in the next section.

7.1.2 Estimation of the Potential Spatial Derivatives

From what was presented in the last section, the question of how to calculate $\nabla \frac{\partial \phi}{\partial z}$, when the value of ϕ is known only on the body surface still needs to be addressed. In fact, in the context of constant panel methods even the estimation of $\frac{\partial \phi}{\partial z}$ is not straightfoward. Since the potential is calculated at the element centers and assumed to be constant over them, it is not continuous (therefore not differentiable) from element to element (or panel to panel), therefore it is not possible to estimate $\frac{\partial \phi}{\partial z}$ directly.

One option is to treat the body surface on the element (panel) level, work out the derivatives on the local coordinates and map them back to the global coordinate system. In order to achieve this, higher order boundary element methods have been developed and the so called double node boundary conditions have also been introduced to remove the singularity on the water line (intersection of Dirichlet and Neumann surfaces) Liu et al. [2001]. Under this framework the spatial derivatives are calculated on the element basis and then mapped back to the global coordinate system Xu [1992].

In this work, another path, novel to the best of our knowledge in the context of hydrodynamic simulations, is pursued. The motivation to introduce this method comes from the problem of interpolating scatter data, which is a useful tool in the context of unstructured grids. However, one seeks here not only interpolation but

to impose the conditions in order to obtain a good approximation, in the sense that it captures the "essence" or "learns" [1] the function been modeled, even in the presence of noise or inaccuracies (say from the CPM for instance). In this context a couple of properties are important, namely:

1. the interpolation needs to "generalize well" (in a sense that if the test error is small then the generalization error will also be small Vapnik [2000]) for points other than the ones for which the interpolator was fit (say, training data, features or examples) ; otherwise once the grid is remeshed and the centers of the new triangles are in different positions the interpolation error can become high. As it will be seen in the next section, this was precisely the main reason in the body non linear simulations for the spurious picks in the hydrodynamic force of the heaving sphere.

2. Since the spatial derivatives are sought, the interpolator needs to be differentiable at least up to second order.

3. Once a global approximation is being pursed, it is important to have some guarantee about its ability approximate complex functions.

Due its suitability on scatter data sets, radial basis function were chosen as functions approximators in the present context. They are used to obtain representations for the velocity potential on the floating body and on the free surface, as well as for the free surface elevation when needed. Moreover, radial basis function are differentiable and can be used to calculate the spatial derivatives, in fact, the problem of solving a partial differential equation can be formulated in a meshless manner using radial basis functions Buhmann [2004]. Furthermore, the universal approximation theorem for radial basis functions networks from Park and Sandberg [1991] states the following:

[1] The idea of capturing the essence of the model is being used here in the sense of statistical learning theory, i.e small generalization error. Intuitively, in the present context, small generalization error means that in a neighborhood of point where the interpolation was fit the difference betwwen the true value and the prediction is kept small (i.e there are no spurious oscillations)

Theorem 7.1.1 Universal Approximation Theorem for Radial Basis Functions Networks Park and Sandberg [1991]: *Let* $f(x) : R^n \rightarrow R$ *be an integrable bounded continous function and assume that*

$$\int_{R^n} f(x) \neq 0. \tag{7.9}$$

Then for any continuous function $g(x)$, $\epsilon > 0$ *and* $a > 0$ *there is an RBF Network with* N *neurons a set of centers* $C_{i=1}^N$, *and a common width* $\sigma > 0$

$$\hat{g}(x) = \sum_{i=1}^{N} w_i f(\frac{x - C_i}{\sigma}) \tag{7.10}$$

such that

$$\int_{||x|| \leq a} (g(x) - \hat{g}(x))^2 dx \leq \epsilon = O(N^{\frac{-1}{n}})$$

Theorem 7.1.1 implies that the rate of an approximation of an RBF network is $O(N^{\frac{-1}{2n}})$. For instance if one wants to approximate the free surface elevation, $\zeta(x, y, t)$ at a fixed time instant, on a region where $||\vec{x}|| \leq a$, then $n = 2$ (two dimensions), with a precision $\epsilon = 10^{-3}$, the number of RBF centers is of the order of 10^6. Moreover, if one wants to approximate the potential the potential, then $n = 3$, and the number of centers required, for the same precision grows by a factor of 1.5, i.e 10^9. Hence, the number of centers required for the rbf network to generalize well is clearly not feasible for the present purposes. In order to try to overcome this difficult the idea of a regularized rbf network regression will be explored with the hope that one can achieve generalization with less training data. Actually the results for the free surface elevation, presented in the next section, confirm the fact that the regularization term allows for the rbf network to generalize better in points that are not the same as the rbf centers, $C_i's$.

More generally, the problem of finding a function approximator (or a hypothesis) can be recast as supervised learning problem, as follows: given a set of input vectors (or features) $\vec{x}_1$, $\vec{x}_2$,.., $\vec{x}_m$ in R^d (d=2 or 3 for the present purposes) and

a set of scalar labels y_1, y_2 ,.., y_m one searches for a map $h(\vec{x} : R^N \rightarrow R)$ that is "close" to y for any given $\vec{x}$ and y. Since the radial basis functions representations were chosen the approximator $h(\vec{x})$ is parameterized by weights w_i, i.e $h_w(\vec{x})$, and is given by:

$$h_w(\vec{x}) = \sum_{i=1}^{m} w_i f(||\vec{x} - \vec{x}_i||) + w_0, \tag{7.11}$$

where $||.||$ refers to the Euclidian metric and f is the radial basis function centered at $\vec{x}_i$.

There are several possible choices for f. For instance, denoting the Euclidian distance by r typical choices of radial basis function, parametrized by σ, include Buhmann [2004]:

- Gaussian: $f = \exp(-\frac{r^2}{\sigma^2})$,
- Mutiquadratic: $f = \sqrt{\sigma^2 + r^2}$,
- Inverse multiquadratic: $f = \frac{1}{\sqrt{\sigma^2+r^2}}$.

Motivated by the results presented in Chinchapatnam [2006], a multiquadratic rbf was selected.

Once the radial basis function f is chosen and both the features, $\vec{x}_i$, and scalar labels y_i are given, the parameters of rbf, w_i need to be found. If the idea is to set an rbf interpolator, one could impose on equation 7.11, that $h_w(\vec{x_j}) = y_j$, for all j=1 to m. This procedure will yield a linear system of equations, whose influence matrix is $A(i, j) = f(||\vec{x}_j - \vec{x}_i||)$, which is solved for the unknowns w_i. This scheme ensures that the interpolation is exact on the $\vec{x}_j$ points. However, the solution can present spurious oscillations on the vicinities of the points $\vec{x}_i$ (unless there is enough centers available so that theorem 7.1.1 can be applied). In other words, it can be easily to "memorize" the inputs $\vec{x}_i$ leading to overfitting and possible inaccuracies, specially when dealing with noisy observations.

In order to make the interpolator more robust or, to put it in another way, make its generalization error smaller, a regularization is introduced in the radial basis function interpolator. More specifically, the regularization is imposed on the l_2 norm (i.e the sum of squares of the vector components), but other norms,

like l_1 (i.e the absolute value) are also possible Murphy [2012]. In this work this carried out by seeking $w*$ that minimize the regularized mean square deviation between $h_w(\vec{x_i})$ and y_i, that is to say:

$$w* = \underset{w}{\operatorname{argmin}} \frac{1}{2} \sum_{i=1}^{m} (h_w(\vec{x_i}) - y_i)^2 + \frac{\lambda}{2} ||w^2||. \tag{7.12}$$

Equation 7.12 can be recast as a quadratic optimization problem where $w*$, its solution, are given by a simple closed form expression. A simple way to do this is to write the objective function, F_{obj}, in a vector form, as follows:

$$F_{Obj} = \frac{1}{2}(Aw - y)^T(Aw - y) + \frac{\lambda}{2} w^T w. \tag{7.13}$$

Therefore, the problem of finding $w*$, is equivalent to minimize equation 7.13. Since it is a convex function, all that is needed is to calculate the gradient of F_{Obj} with respect to the vector w, $\nabla_w F_{Obj}$, and set it to zero.

Proposition 7.1.2 *Let F_{Obj} be a convex function given by equation 7.13, then the vector $w*$ that minimizes F_{Obj} is given by:*

$$w* = (A^T A + \lambda I)^{-1} A^T y. \tag{7.14}$$

Proof Due to the convexity property, to find $w*$, it suffices to calculate $\nabla_w F_{Obj}$ and set it to zero, this yields:

$$\begin{aligned} \nabla_w F_{Obj} &= \frac{1}{2} \nabla_w (w^T A^T A w - y^T A w - w^T A^T y + y^T y + \lambda w^T w) \\ &= \frac{1}{2}(2A^T A w - 2A^T y + 2\lambda w) \\ &= (A^T A w - A^T y + \lambda I w) \end{aligned}$$

So, setting $\nabla_w F_{Obj} = 0$ and solving for w, yields:

$$w* = (A^T A + \lambda I)^{-1} A^T y. \quad \blacksquare$$

Moreover, from a probabilistic perspective, equation 7.14 has an interesting Bayesian interpretation. It corresponds to the maximum a posteriori (MAP) estimation Bishop [2007], where instead of finding w by maximizing the likehood probability function, w is found as the vector that maximizes the posterior probability density function.

Once the coefficients of the radial basis functions are found, it is straightfoward to calculate its spatial derivates. Specifically, let $\vec{x} = (x, y, z)$, then one can write:

$$\begin{aligned}
\frac{\partial h_w(\vec{x})}{\partial x} &= \sum_{i=1}^{m} w_i \frac{\partial f(||\vec{x} - \vec{x}_i||)}{\partial x}, \\
\frac{\partial h_w(\vec{x}}{\partial y}) &= \sum_{i=1}^{m} w_i \frac{\partial f(||\vec{x} - \vec{x}_i||)}{\partial y}, \\
\frac{\partial h_w(\vec{x}}{\partial z}) &= \sum_{i=1}^{m} w_i \frac{\partial f(||\vec{x} - \vec{x}_i||)}{\partial z},
\end{aligned} \tag{7.15}$$

in particular, chosing f as a multiquadratic function yields the following:

$$\begin{aligned}
\frac{\partial f(||\vec{x} - \vec{x}_i||)}{\partial x} &= \frac{x - x_i}{\sqrt{\sigma^2 + r^2}}; \\
\frac{\partial f(||\vec{y} - \vec{y}_i||)}{\partial y} &= \frac{y - y_i}{\sqrt{\sigma^2 + r^2}}; \\
\frac{\partial f(||\vec{z} - \vec{z}_i||)}{\partial z} &= \frac{z - z_i}{\sqrt{\sigma^2 + r^2}}.
\end{aligned} \tag{7.16}$$

This way the spatial derivatives can be estimated, both with the aid of the radial basis function and their respective coefficients given by equation 7.14. Moreover, with the aid of the rbf approximation some innacuracies and possibly noise of the constant panel method can be reduced, hopefully making it applicable to problems where only higher order methods have been employed. From a learning

theory perspective one can interpret the coupling between rbf representations and the constant panel method as solution reconstruction problem, whereby the CPM provides labels that are then used to build the solution by the rbf approximator; hence, the method is in way a hybrid numerical tool somewhere in between meshfree methods and Eulerian based solvers.

7.1.3 Body Non Linear Model

In the last two sections, it was highlighted that the move from linear time domain analysis to body non linear analysis, requires spatial and time derivatives of the potential to be evaluated. In order to estimate the time derivatives two approaches were proposed: one based on equation 7.2, i.e a finite difference scheme and a second approach is based on the solution of a second boundary value problem. The spatial derivatives are estimated with the aid of a regularized radial basis function representation according to equations 7.15, 7.15 and 7.16. Once spatial derivatives of the velocity potential are estimated, the contribution of the square of the velocity gradient can be accounted for in Bernoulli's equation, i.e:

$$p = \frac{\partial \phi}{\partial t} + \nabla \phi^2. \tag{7.17}$$

The force contribution of $\nabla \phi^2$ is typically a second order harmonic contribution to the time series of hydrodynamic force. The results of this contribution are shown in the next section.

Armed with these new tools the linear time domain algorithm can be extended to the body non linear case. In fact, the structure of the algorithm used to simulate the body non linear problem is similar to the one presented in the last chapter, i.e Algorithm 3 . The main differences are related to the changes of the influence matrix of the boundary value problem as time is evolved and with the estimations of the spatial and time derivatives of the potential function. In what follows, both Body Non Linear algorithms are going to be presented and their differences highlighted.

The Body Non Linear Algorithm based on the finite difference approximation

for the potential time derivative, equation 7.2, is summarized in Algorithm 5.

Algorithm 5 Finite Difference Body Non Linear

1: **procedure** MAIN( )
2: **while** $t < T$ **do**
3: [p,t]=CreateMesh(fd(t),fh,h0); ▷ Create a mesh of the domain
4: $[x_{FS}, y_{FS}, x_B, y_B, z_B]$:=FindBoundaryNodes(p,t);
5: ϕ_{FS}:=$\Phi_i(x_{FS}$,y_{FS},t) ▷ Set BC Value on the of the FS triangles
6: $\nabla\phi \cdot \vec{n}_B := \vec{v}(t)_B \cdot \vec{n}_B$ ▷ Set BC Value on the Floating Body
7: $\nabla\phi \cdot \vec{n}_B := 0$ ▷ Set BC Value on other Neumann Boundaries
8: $[\phi_B; \nabla\phi \cdot \vec{n}_{FS}] := [G_{FS}; Gn_B]^{-1}[\nabla\phi \cdot \vec{n}_B; \phi_{FS}]$ ▷ Solve the BVP at $z_{FS} = 0$
9: $\nabla\phi = (\nabla\phi \cdot \vec{t}_b)\vec{t}_b + (\nabla\phi \cdot \vec{n}_b)\vec{n}_b$ ▷ Compose $\nabla\phi$ on the body surface
10: $p := \frac{\partial\phi}{\partial t} + \frac{\nabla\phi^2}{2}$ ▷ Equation 7.2 is used for $\frac{\partial\phi}{\partial t}$
11: $\vec{F} := -\rho \int_{\partial B(t)} p\vec{n}_B(t)dS$ ▷ Calculate the force on B(t)
12: $z_{FS} := z_{FS} + (\frac{\partial\phi}{\partial z} - \nu z_{FS})dt$ ▷ Update the FS elevation
13: $\phi_{FS} := \phi_{FS} + (-z_{FS}g - \nu\phi_{FS})dt$ ▷ Update the FS potential
14: $t := t + dt$
15: **end while**
16: **end procedure**

Comparing Algorithms 3 and 5, note that the lines 2 and 3 of Algorithm 3 have come into the while loop because the domain is meshed every time step. Furthermore the integral of the force at line 9 of Algorithm 5 is now evaluated at the instantanous body surface, $\partial B(t)$ instead of the mean body surface ∂B, and the pressure now takes into account the full form of Bernoulli's equation. The BVP is still solved on the mean free surface, which is the essence of the Body Non Linear approach.

Different from Algorithm 5, Algorithm 6 evaluate the time derivative of the potential exactly. As mentioned before, this is accomplished by solving a second boundary value problem (line 12). It is worth pointing out that the influence matrix of the first and second boundary value problems is the same, and what changes in fact are only the boundary conditions.

Algorithm 6 ϕ_t Exact Body Non Linear

procedure MAIN( )
  while $t < T$ **do**
    [p,t]:=CreateMesh(fd(t),fh,h0); ▷ Create a mesh of the domain
    $[x_{FS}, y_{FS}, x_B, y_B, z_B]$:=FindBoundaryNodes(p,t);
    ϕ_{FS}:=$\Phi_i(x_{FS}$,y_{FS},t) ▷ Set 1st BC Value on the of the FS triangles
    $\nabla\phi \cdot \vec{n}_B := \vec{v}(t)_B \cdot \vec{n}_B$ ▷ Set 1st BC Value on the Floating Body
    $\nabla\phi \cdot \vec{n}_B := 0$ ▷ Set 1st BC Value on other Neumann Boundaries
    $[\phi_B; \nabla\phi \cdot \vec{n}_{FS}] := [G_{FS}; Gn_B]^{-1}[\nabla\phi \cdot \vec{n}_B; \phi_{FS}]$ ▷ Solve the BVP at $z_{FS} = 0$
    $\frac{\partial\phi}{\partial t}_{FS} := -z_{FS}g$ ▷ Set BC Value on the FS for the 2ond BVP
    $\frac{\partial^2\phi}{\partial t\partial n}_B := \vec{n}_B \cdot \vec{a}_B - v_3\vec{n}_B \cdot \nabla\frac{\partial\phi}{\partial z}$ ▷ Set BC on Body for the 2ond BVP
    $\frac{\partial^2\phi}{\partial t\partial n} := 0$ ▷ Set BC on other Neumann Boundaries
    $[\frac{\partial\phi}{\partial t}; \frac{\partial^2\phi}{\partial t\partial n}] := [G_{FS}; Gn_B]^{-1}][\frac{\partial^2\phi}{\partial t\partial n}_B; \frac{\partial\phi}{\partial t}_{FS}]$ ▷ Solve the 2ond BVP at $z_{FS} = 0$
    $\nabla\phi = (\nabla\phi \cdot \vec{t_b})\vec{t_b} + (\nabla\phi \cdot \vec{n}_b)\vec{n}_b$ ▷ Compose $\nabla\phi$ on the body surface
    $p := \frac{\partial\phi}{\partial t} + \frac{\nabla\phi^2}{2}$ ▷ 2ond BVP is solved for $\frac{\partial\phi}{\partial t}$
    $\vec{F} := -\rho\int_{\partial B(t)} p\vec{n}_B(t)dS$ ▷ Calculate the force on B(t)
    $z_{FS} := z_{FS} + (\frac{\partial\phi}{\partial z} - \nu z_{FS})dt$ ▷ Update the FS elevation
    $\phi_{FS} := \phi_{FS} + (-z_{FS}g - \nu\phi_{FS})dt$ ▷ Update the FS potential
    $t := t + dt$
  end while
end procedure

7.2 Results of the Body Non Linear Analysis

7.2.1 Forced oscillations of a Sphere

In this section the body non linear problem of a sphere undergoing forced motions in the heave mode will be considered. As it was highlighted in the previous section, the key point in this simulation lies on the estimation of the time derivative of the potential function around the floating body; for this purpose, two algorithms were presented, namely: Algorithm 5 approximates $\frac{\partial \phi}{\partial t}$ by an up wind scheme, whereas Algorithm 6 solves for $\frac{\partial \phi}{\partial t}$ exactly. The approximation of the spatial gradient of ϕ is done using the radial basis functions approach described in the previous section.

More specifically, in either the body non linear or non linear analysis, new terms arise when the time series of the hydrodynamic force is decomposed in the frequency domain. This means that by performing a Fourier decomposition of the hydrodynamic time series not only component proportional to the first harmonic are relevant (say, frequency of oscillation), but also components proportional to higher order harmonics, as well as a mean term, should be taken into account Lin and Yue [1991]. In the context of forced oscillatory motions in the heave mode, $A(t) = Asin(\omega t)$, the hydrodynamic force can be decomposed, by means of a Fourier decomposition, as follows:

$$\hat{f}_0 = \frac{1}{T}\int_{t-T/2}^{t+T/2} F_h(t)dt; \tag{7.18}$$

$$A_{33} = \frac{2}{T}\int_{t-T/2}^{t+T/2} F_h(t)sin(\omega t)dt; \tag{7.19}$$

$$B_{33} = \frac{2}{T}\int_{t-T/2}^{t+T/2} F_h(t)cos(\omega t)dt; \tag{7.20}$$

$$A_{33}^{(2)} = \frac{2}{T}\int_{t-T/2}^{t+T/2} F_h(t)sin(2\omega t)dt; \tag{7.21}$$

$$B_{33}^{(2)} = \frac{2}{T}\int_{t-T/2}^{t+T/2} F_h(t)cos(2\omega t)dt; \tag{7.22}$$

where $F_h(t)$ is the time series of the hydrodynamic force in the heave mode. From equations 7.19 and 7.20, the norm of first harmonic,$\hat{f}_1$ is calculated as $\|\hat{f}_1\| = \sqrt{(A_{33})^2 + (B_{33})^2}$. The norm of the second harmonic, $\hat{f}_2$, is calculated in the same fashion from the values of $A_{33}^{(2)}$ and $B_{33}^{(2)}$.

In the context of the BNL simulations a mesh is created each time step. The mesh topology, and the size functions used are described in figure 7.1. The damping zone, in this simulation, is kept circular and its dimesion is a strip of length 1.0 (i.e in equation 4.16, $r_D = 3.0$ and $r_L = 4.0$).

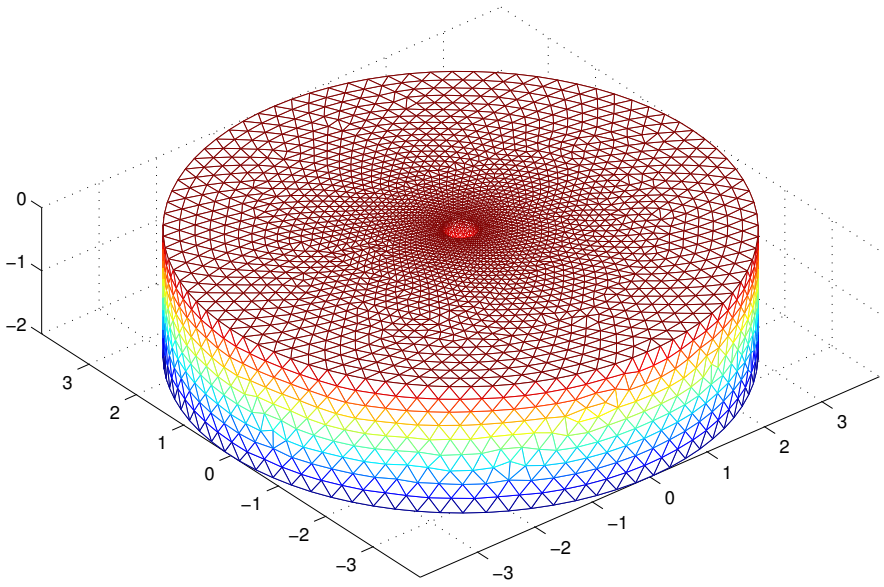

Figure 7.1: Mesh topology used on the BNL simulations: on average a total of 8926 triangles of which 300 are on the floating body. The distance function is the difference of the cylinder and sphere, the relative size distribution is given by: $f_h = 1 + 5\sqrt{x^2 + y^2 + z^2}$ and $h_0 = 0.04$.

In figure 7.2, the hydrodynamics term obtained from the Fourier decomposition of the hydrodynamic force time series are plotted as a function of the amplitude of oscillation in heave. These harmonics are non dimensionalised as

follows:

$$f_0 = \frac{\hat{f}_0}{\rho g \pi R A^2}; \tag{7.23}$$

$$f_1 = \frac{|\hat{f}_1|}{\rho g \pi R^2 A}; \tag{7.24}$$

$$f_2 = \frac{|\hat{f}_2|}{\rho g \pi R A^2}. \tag{7.25}$$

In addition in figure 7.2, an analysis of the effect of different terms in pressure evaluation was carried out. The blue dot line is the pressure field resulting only from $\partial\phi_t$, so that $\nabla\phi^2$ is considered to be negligible. The red line evaluates $\nabla\phi$ using only the tangential velocity components to the floating body; finally the green line calculate $\nabla\phi$ by combining both tangential and normal velocities components (i.e the Neumann data prescribed as a boundary condition on the floating body $\nabla\phi \cdot \vec{n}$ is combined with the tangential derivate of ϕ, calculated using the rbf representation, i.e equations 7.16). Interestingly, the effect of the $\nabla\phi^2$ term is more pronounced on the evaluation of f_0 and $|f_2|$. The results suggest that the magnitude of the normal gradient component is of great importance in comparison with the tangential potential component, since it changes the values of both f_0 and $|f_2|$ when it is accounted for. In fact, compared to the results obtained by Lin and Yue [1991], there is some indication that the value of f_0 is being overestimated by time the present simulation [1]. That said, there is also evidence that, the tangential gradient has not a considerable contribution to the pressure field, once its addition does not change significantly the values of f_0 and $|f_2|$ across the amplitudes range. In addition, when comparing the harmonics calculated by algorithm 5 (FD BNL) against the body non linear results from Lin and Yue [1991], it can be seen that the trends are qualitatively in line, but algorithm 5 has a tendency to over/underestimate the harmonics. More concretely, looking at the components of $|f_1|$ in phase with velocity and

[1] Since the sphere is undergoing forced oscillations, the normal velocity is given by the impervious boundary condition, which is exact. However, the values of f_0 are consistently below the ones obtained by Lin and Yue [1991].

acceleration (damping and added mass respectively), one can see from figure 7.4, that the values of the the BNL case, even for small amplitudes of oscillations, are far from the linear prediction when it comes to the added mass coefficients. On the other hand, the agreement for damping is reasonably good, as compared to the QBEM results from Yan [2010]. The exact reason for this particular behaviour is something that needs further investigation as it could be linked to the accuracy of the approximation of the time derivative of the potential by the finite difference scheme of equation 7.3.

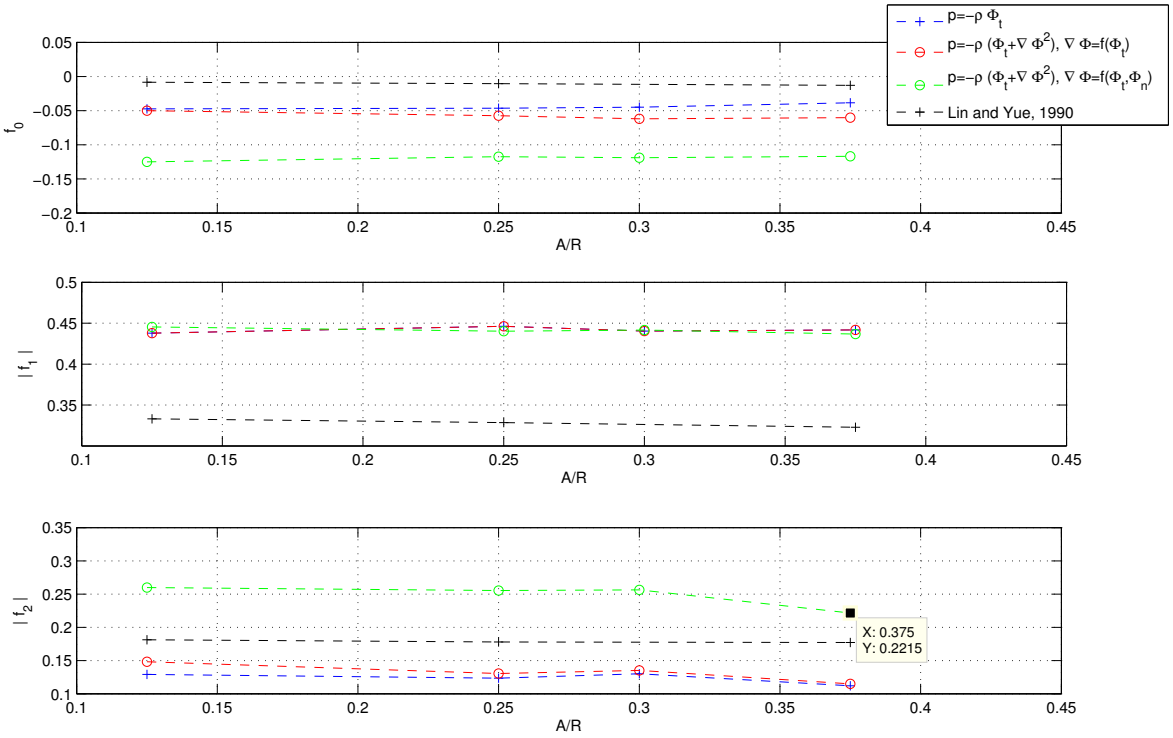

Figure 7.2: Harmonics obtained from a Fourier decomposition of the force time series using the BNL approach described in Algorithm 5 .

In order to investigate this further, algorithm 6 (ϕ_t Exact BNL) is used to solve the same forced oscillation problem. A comparison of the force time series generated from ϕ_t Exact BNL and FDBNL are plotted in figure 7.5 for the amplitudes of oscillations $A = 0.30R$ and $A = 0.25R$. Note how the results from

FDBNL overshoots when compared to ϕ_t and this is more pronounced on the troughs, which correspond to the phase where more than half of the sphere is submerged. Coming to the harmonics extracted from the ϕ_t Exact BNL (figure 7.3), the quantitative agreement is more in line as compared to the results of Lin and Yue [1991]. Specifically, the trend for $|f_1|$ is in line, although its value decay faster with the amplitude than the values obtained by Lin and Yue [1991]. This can be seen in more detail in figure 7.4, which shows that the step decline of $|f_1|$ is linked to the damping coefficient and the agreement of added mass coefficient is reasonably good, except for the higher amplitude, where more investigations are needed. In fact, the agreement of added mass has been better compared to the linear simulations. It is also interesting to highlight that there is no jump of the hydrodynamic coefficients in smaller amplitude range, which is actually expected and suggests a reasonable behaviour of algorithm 6. In addition, there is also tendency in overestimating the value of $|f_2|$ as compared to Lin and Yue [1991].

That said, turning back to figure 7.5, it can be seen that the there are some spurious high frequency oscillations on both force time series, but they are more pronounced on the red line (i.e ϕ_t Exact BNL) and have a tendency to increase as with the amplitude. In particular, these oscillations are more pronounced when the sphere is on its way down whereas the flow speed on the free surface is still on its way up. This effect turns out to be related with the jagged free surface profile that is created by inaccurate normal velocity calculation of the constant panel method.

What happens is that on the ϕ_t Exact BNL approach, the free surface elevation is the boundary condition applied on the free surface (the time derivative of the potential on the free surface in this context is $-g * z$). Once the boundary value problem is solved, this spurrious fluctuations are then being propagated to $\partial\phi/\partial t$ on the body surface. Here, the introduction of the regularization parameter on the rbf approximation (λ) plays a key role, since it allows for a more accurate approximation of the free surface position. This effect, although between different time instants, can be seen in figure 7.8 where the jagged profile of the free surface can be seen on the left hand side part of the figure and the resulting free surface approximation using ($\lambda = 0.1$) is shown on the right hand side.

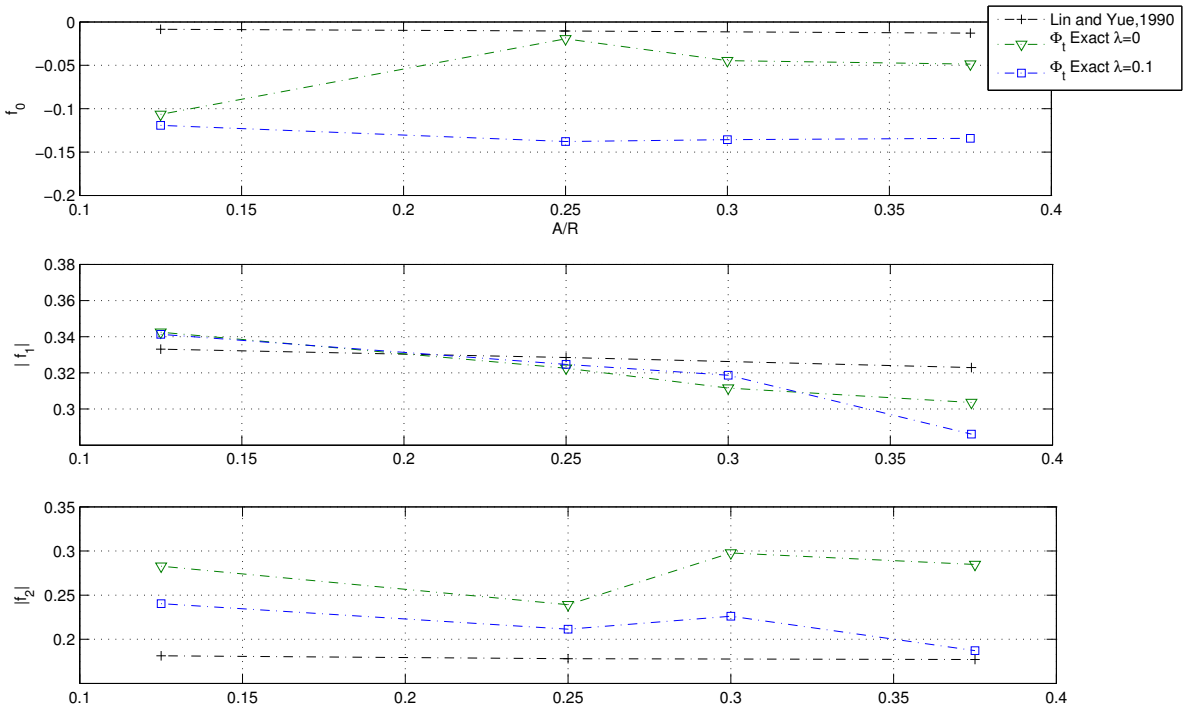

Figure 7.3: Harmonics obtained from a Fourier decomposition of the force time series using the BNL approach described in Algorithm 6 .

The effect of the regularization term also influences the hydrodynamic coefficients. Figure 7.3, compares the harmonics obtained by the ϕ_t Exact BNL, with and without regularization. The results suggest improvements on the estimation $|f_2|$, as compared to Lin and Yue [1991]. However, the agreement for $|f_0|$ is worse in the presence of the regularization term. The precise effect that is causing this issue is something that needs future investigations. The agreement for the first harmonic, $|f_1|$, is reasonable, but as the amplitude increases some deterioration of the accuracy is observed. Looking at the time force series of the ϕ_t Exact BNL, with $\lambda = 0.1$, i.e figure 7.7, the force time series for $A = 0.375R$ suggests that the effects of the quadratic pressure term are starting to cancel out the component of the potential derivative. This could be either linked to a inaccuracies in the estimation of the potential gradient around the body or with inaccuracies associated with the body boundary condition for the second boundary value problem. The evidence points to the latter, since the agreement for the second harmonic, for the case of $A = 0.375R$, is in line with the results of Lin and Yue [1991]. This is also a subject that needs further exploitation.

Looking at the added mass and damping coefficients, the ϕ_t Exact BNL, with $\lambda = 0.1$, produces an overall better agreement, specifically on the prediction of the damping coefficient. These results, together with a comparison of other numerical predictions for the same problem are shown in figure 7.4.

7.2.2 Forced oscillations of the Wigley hull

Encouraged by the results obtained for the sphere undergoing forced motions in the heave mode, Algorithm 6 is used in this section to tackle the problem of a Wigley hull undergoing forced oscillations in the heave mode. Due to numerical issues of generating a signed distance function for the Wigley hull, the gmsh (Geuzaine and Remacle [2009]) library was linked against the BEM solver, more details of the implementation as well as on the numerical issues that were faced can be found in the next chapter.

The dimensions of the Wigley hull are the same as in chapter 5 (table 6.1). The initial domain is also similar to the one used in chapter 5, i.e a box like domain, extended on the free surface, [-5 -5 0] x [5 5 -1] units, in order to mitigate issues

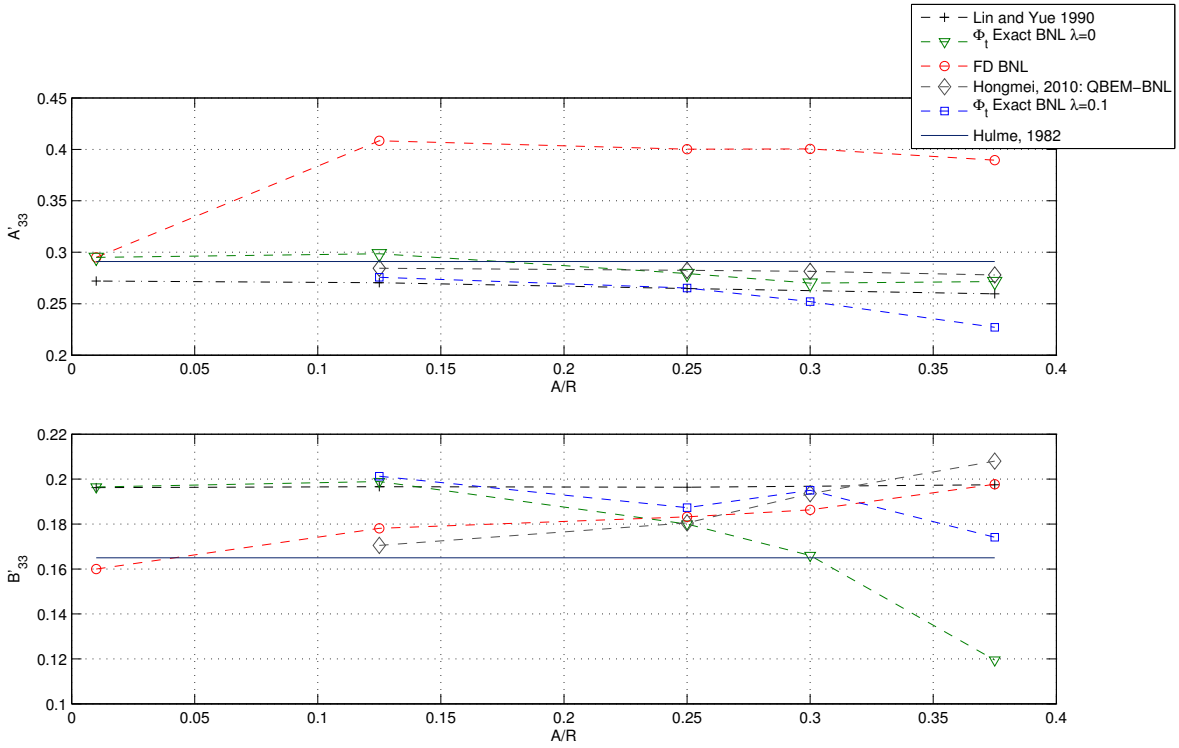

Figure 7.4: Comparison of the components of $|f_1|$ using the two body non linear algorithms, Lin and Yue [1991] and Yan [2010]. Φ_t Exact is obtained from algorithm 6 whreas FD BNL is obtained from algorithm 5.

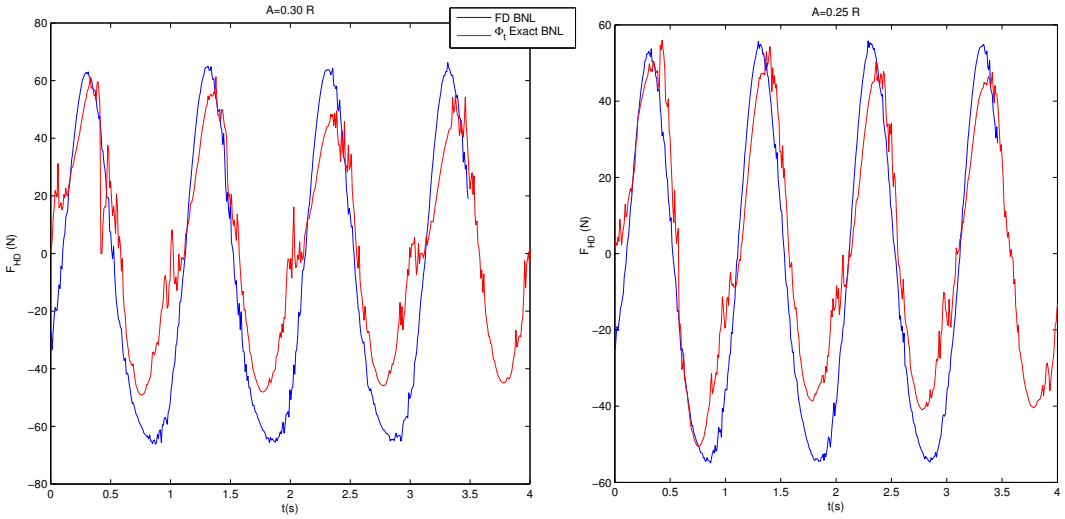

Figure 7.5: Comparison of the force time series between FD BNL and and Φ_t Exact for amplitudes A=0.25 R and A=0.30 R.

related to wave reflexion.

The numerical analysis performed consists of two amplitudes $A = 0.053T$ and $A = 0.27T$ and three frequencies, $\hat{\omega} = 2.49$, 3.45 and 4.41. For the lower amplitude a single mesh, named mesh 1 (figure 7.9), was used for all the frequencies. This case can be seen as sanity check of algorithm 6, since, for small amplitudes, one would actually expects the body non linear solution to be reduced to the linear solution.

The higher amplitude case, i.e $A = 0.27T$, turned out to be more delicate from a numerical perspective. For this numerical analysis, four meshes, mesh 1, mesh 2, mesh 3 and mesh 4 were used. These meshes are shown in figures 7.9, 7.10, 7.11 and 7.12 respectively. In addition, the comparison between the still water displacements of these meshes and the exact value of the model is essentially the same as the one presented in table 6.2.

For the lower frequency, $\hat{\omega} = 2.49$, Meshes 1 and 2 were used. Mesh 2 was obtained by halving the edge size of the triangles on the surface of the Wigley hull. The edge size of the elements on the walls remained the same while the

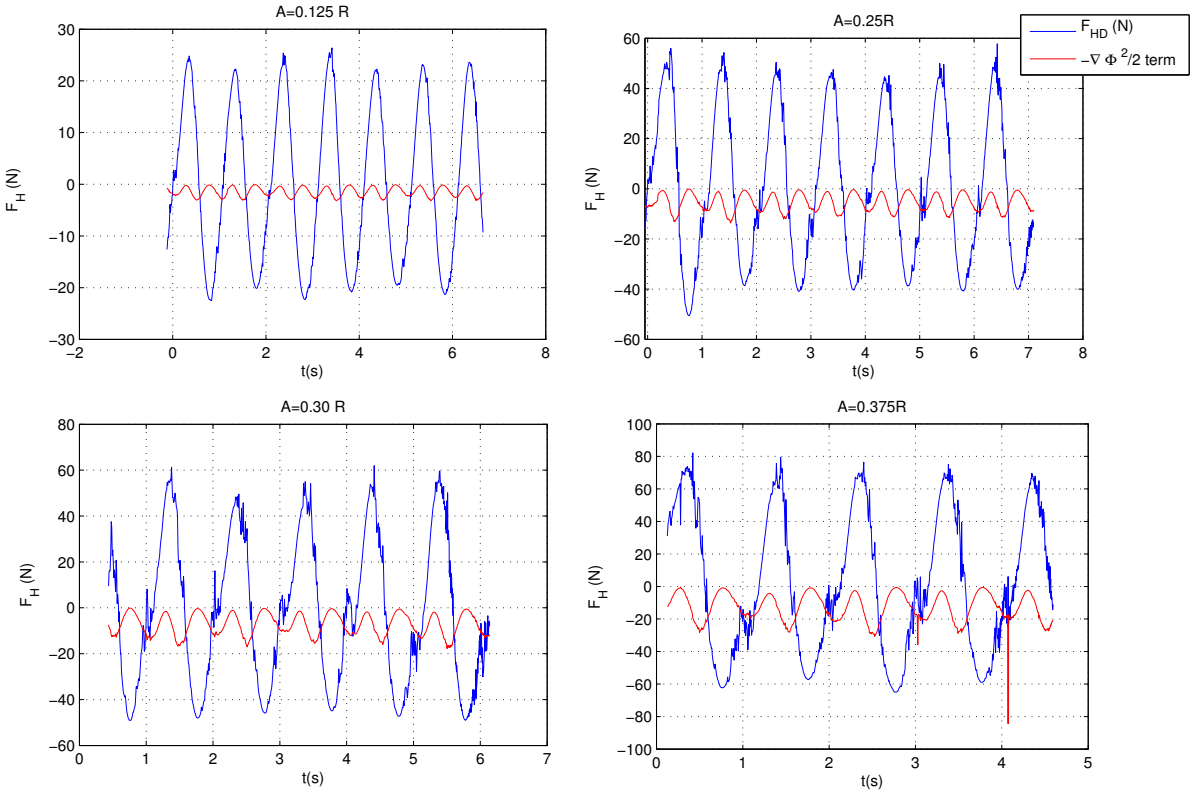

Figure 7.6: Hydrodynamic force time series obtained from Algorithm 6 . In blue the total force and in red the contribution from the gradient squared term of Bernoulli's equation with $\lambda = 0$.

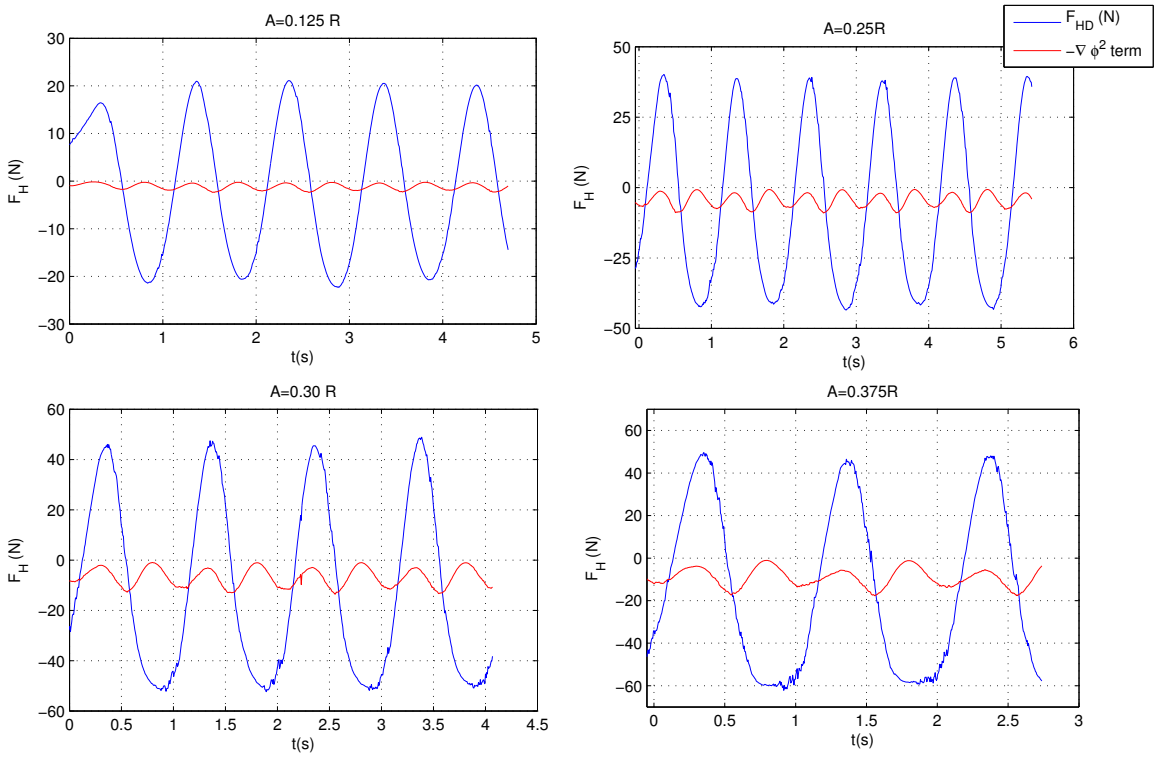

Figure 7.7: Hydrodynamic force time series obtained from Algorithm 6 . In blue the total force and in red the contribution from the gradient squared term of Bernoulli's equation with $\lambda = 0.1$.

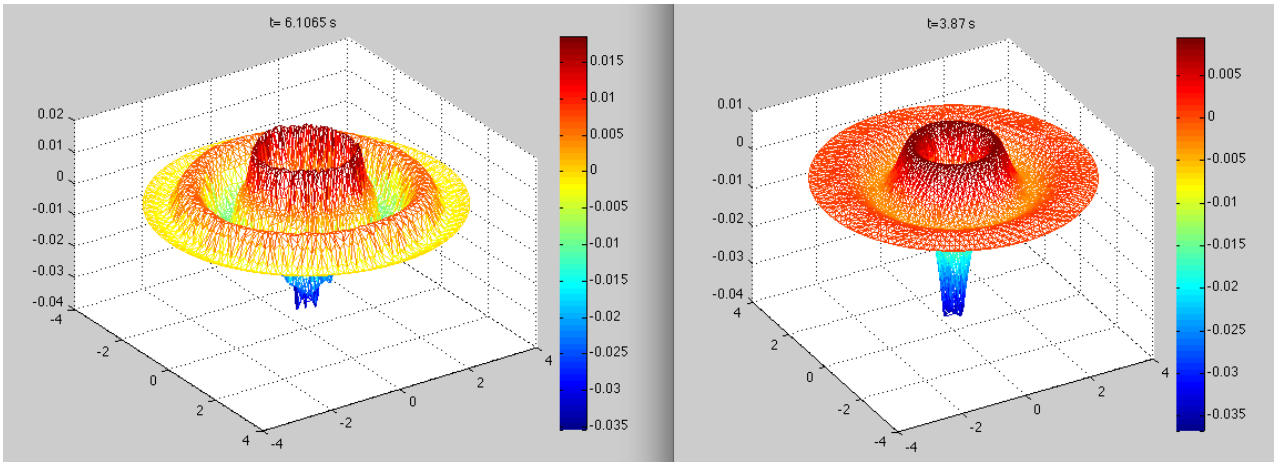

Figure 7.8: The left hand side shows the free surface profile when $\lambda = 0$ whereas the right hand side shows the free surface profile for $\lambda = 0.1$.

edge size of the elements between the Wigley hull and the walls were linearly interpolated. Thus, the refinement is locally placed on the Wigley hull and on the free surface in its vicinity [1].

The force time series for $\hat{\omega} = 2.49$ (or $\omega = 7.81$ rad/s) are shown in figure 7.13 using both meshes 1 and 2 and the respective value of the hydrodynamic coefficients are shown in table 7.1 . In this context, both force time series are close to each other, suggesting that for this frequency the method has converged (or is very close to converge). Note, however, that there is a tendency for the force time series simulated by mesh 2 to peak before the one generated by mesh 1. In addition, mesh 1 has also a snall tendency to overestimate the quadratic component.

For $\hat{\omega} = 3.45$, three meshes were used, namely mesh 1, mesh 2 and mesh 3. For meshes 1 and 2, it can be seen in figure 7.14 that the issues are more pronounced . The force time series peak predicted by mesh 1 is delayed in comparison to the peak predicted by mesh 2. In addition, the difference between the quadratic terms is also pronounced, close to a factor of 2. The free surface profile brings more insight on why a more refined mesh is needed for the case of $\hat{\omega} = 3.45$.

[1] In fact, this flexibility of the unstructured grid reduces the consequences of the so called curse of dimensionality, since, on structured grids, halving the edge size in two dimensions would result in a mesh four times larger.

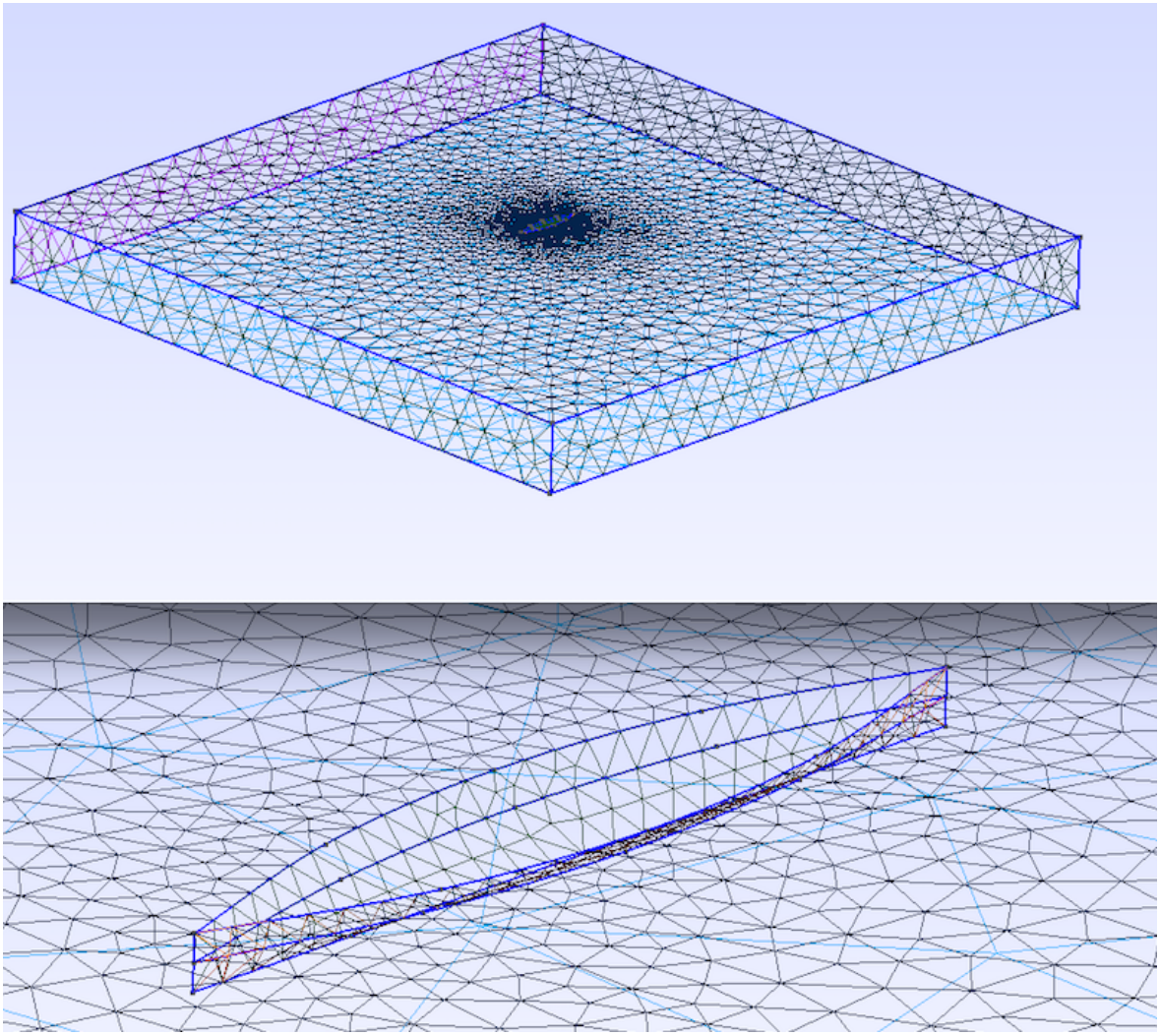

Figure 7.9: Mesh topology 1 (Mesh 1) used for the Wigley Hull forced oscillations in heave. On average the mesh has a total of 4300 triangles of which 300 are on the floating body surface.

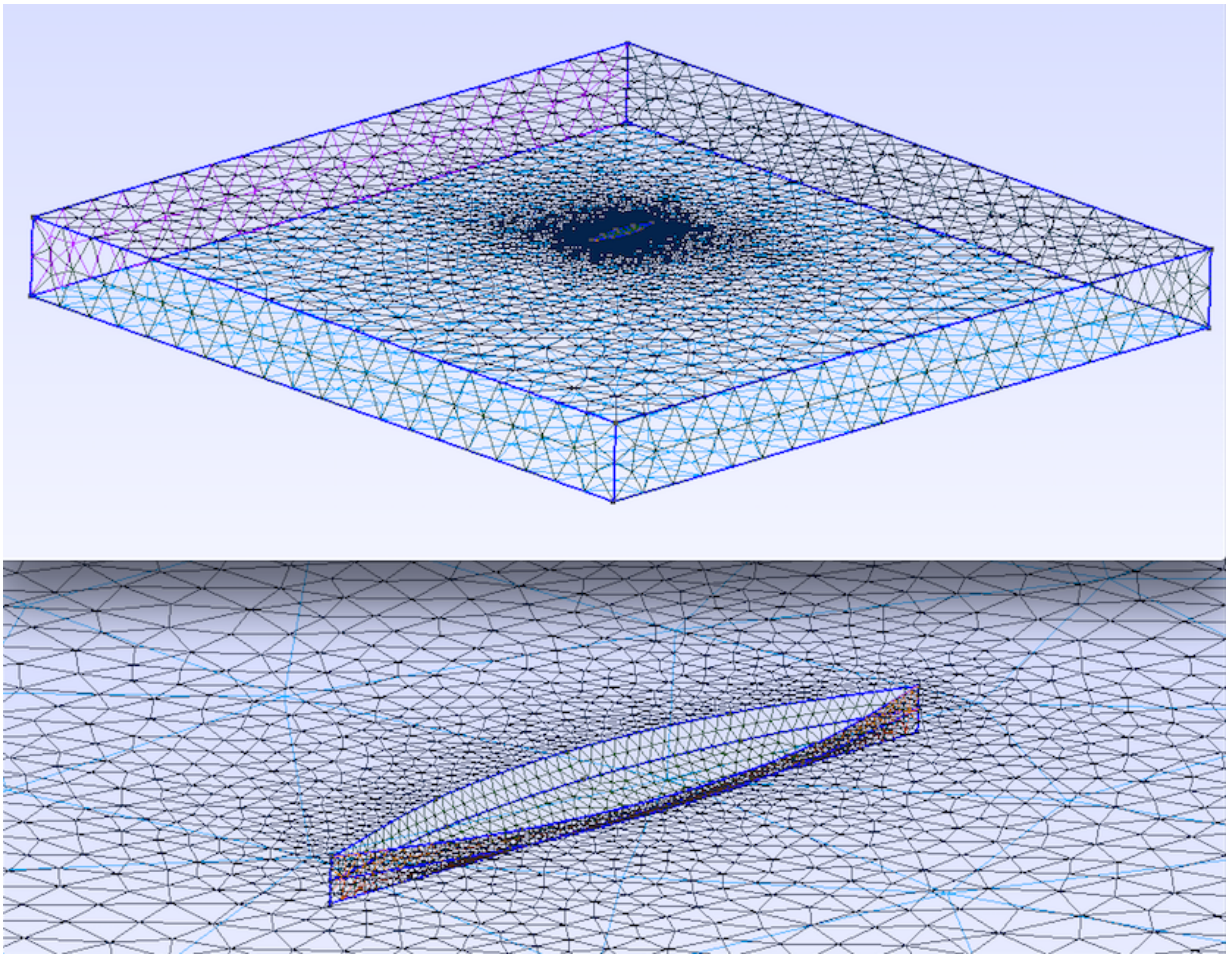

Figure 7.10: Mesh topology 2 (Mesh 2) used for the Wigley Hull forced oscillations in heave. On average the mesh has a total of 6800 triangles of which 600 are on the floating body surface.

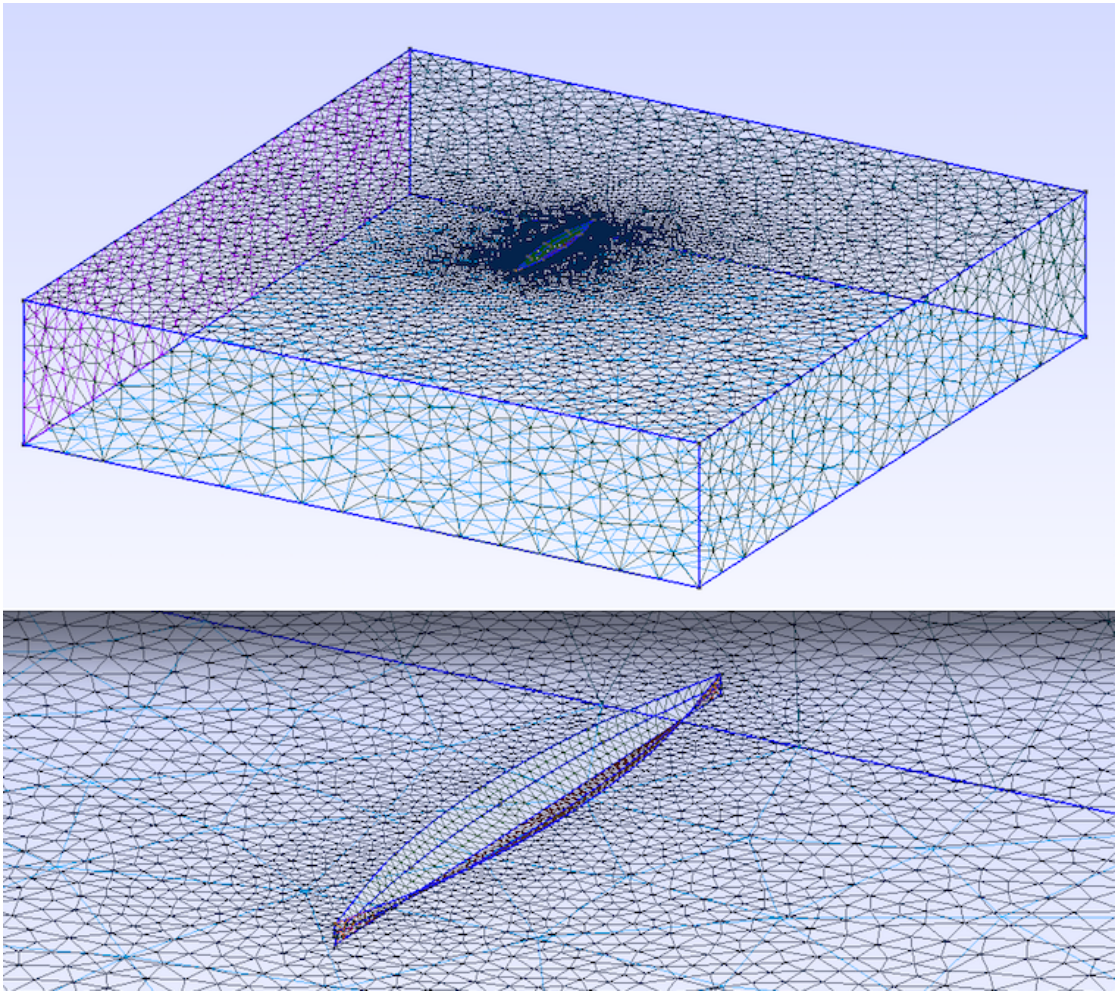

Figure 7.11: Mesh topology 3 (Mesh 3) used for the Wigley Hull forced oscillations in heave when $\hat{\omega} = 3.45$. On average the mesh has a total of 10800 triangles, of which 1000 are on the floating body surface.

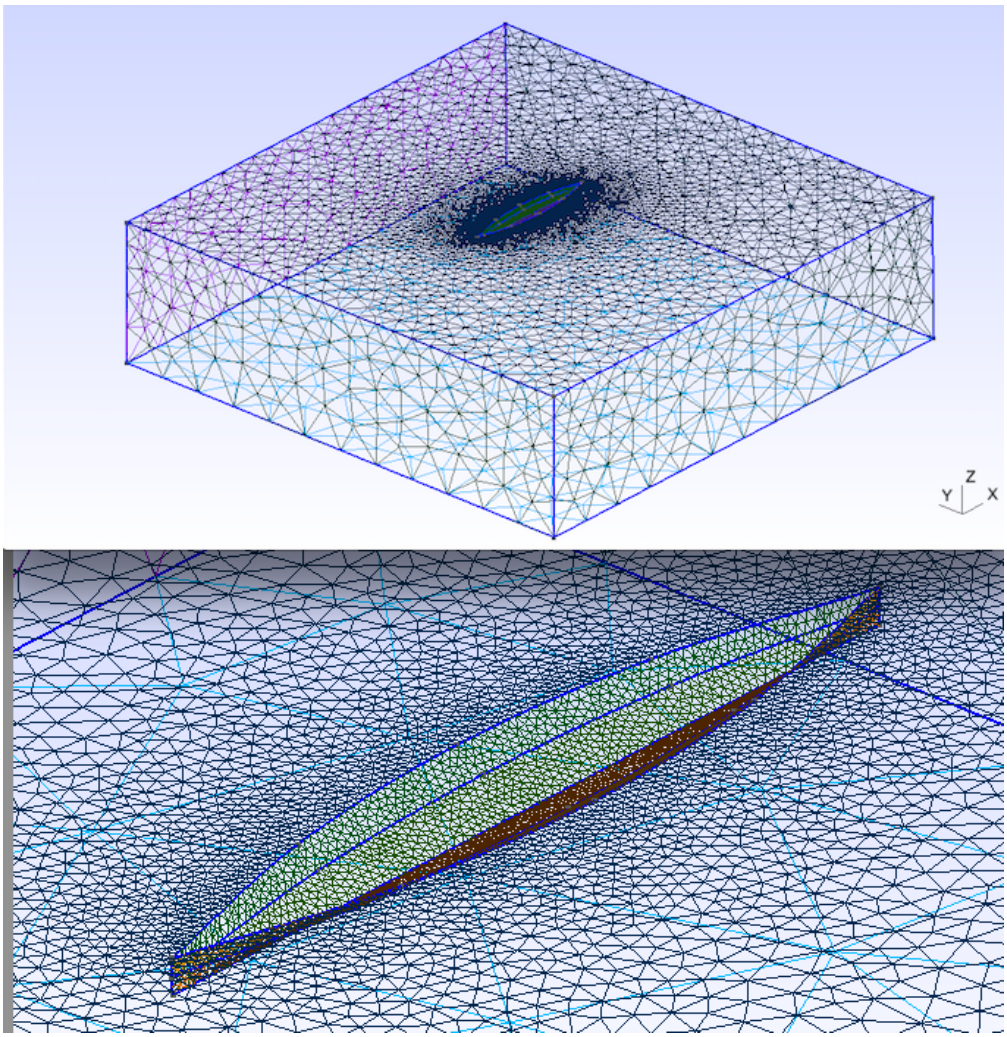

Figure 7.12: Mesh topology 4 (Mesh 4) used for the Wigley Hull forced oscillations in heave when $\hat{\omega} = 4.41$. On average the mesh has a total of 11484 triangles, of which 3216 are on the floating body surface.

The profile for both frequencies are given in figure 7.19. Note that the higher frequency induces a more pronounced gradient of the free surface elevation near the Wigley hull, so, in order to model this more accurately, smaller edges would be needed. So in order to check for convergence, mesh 2 is refined further. The resulting mesh, mesh 3, is shown in figure 7.11.

Mesh 3 is created by adjusting the edges of the elements of mesh 2 by the corresponding wave length of the higher frequency, i.e the ratio edge/λ [1] is kept constant on the vicinity of the Wigley hull. The damping zone and free surface dimensions are also adjusted accordingly. More concretely, since $\lambda = \frac{2\pi g}{\omega^2}$, the edge size of mesh 3, l_3, is $l_3 = l_2/1.7$, say two times smaller for implementation purposes. Note that the domain dimensions were scaled in the same fashion, mesh 2 domain size is [-5.0 -5.0 -1.0] x [5.0 5.0 0.0] , whereas mesh 3 domain size is [-2.5 -2.5 -1.0] x [2.5 2.5 0.0]. The damping and undamped zone free surface sizes were also rescaled in terms of wave lengths, kept at 1.8λ and 3.25λ respectively, approximately same dimensions used on mesh 2. The results obtained by the three meshes are presented in table 7.2 and compared to the experimental data. As the refinement is carried out, there more improvement in going from mesh 1 to mesh 2 , than from mesh 2 to mesh 3. This suggests convergence has been achieved.

In order to investigate the behaviour on the higher frequency, i.e $\hat{\omega} = 4.41$, Mesh 4 was created using the same rational of mesh 3. Since the frequency is higher, the wave lengths are shorter. Rescaling according to the corresponding wavelength, the box domain was reduced to [-1.8 -1.8 0] x [1.8 1.8 -1] units and the edge length on hull, l_4, was further refined, yielding $l_4 = (2/3)l_3$. The free surface damped/undamped zones were kept in the same size, with respect to the wave length generated, i.e 1.8λ and 3.25λ respectively. It is interesting to point out that the simulation using mesh 3 leads to an overestimation of the quadratic force contribution. As it can be seen in figure 7.18 the effect of refining from mesh 3 to mesh 4 has an important effect on the behaviour of the hydrodynamic force time series. The hydrodynamic coefficients obtained from figure 7.18 are

[1] Unfortunately the notation is overloaded as λ here denotes the wave length. In contrast, λ was also used to denote the rbf regularization parameter. These quantities are by no means related, and the context shall make clear what λ refers to.

shown in table 7.3. The set of results presented in tables 7.1, 7.2 and 7.3 is also summarized in figure 7.17 .

Concerning the hydrodynamic coefficients in heave, the results obtained in the present simulations, as well as the results of linear analysis performed in the last chapter, are compared against the experimental data from Journée [1992] in figure 7.20. For the lower amplitude ($A = 0.053T$), the results from Algorithms 4 (Linear) and 6 (Φ_t BNL), compare relatively well. In fact, the agreement of the added mass is good, whereas for damping, Φ_t BNL, despite the good qualitative agreement, shows a tendency to overestimate it, even for small amplitudes. For the higher amplitude ($A = 0.27T$) the agreement of Φ_t BNL against experimental data is good on the lower frequency, but deteriorates as kA increases. The deterioration is more pronounced in the damping coefficient as it increases with the frequency of forced oscillation. For the added mass the effect of increasing the amplitude of oscillation is less pronounced. This effect reduces the magnitude of the added mass coefficients as a function of the amplitude of oscillation.

The deterioration on the predictions of the damping coefficients (as compared to Linear analysis and experimental data) as kA increases is a point that clearly needs further investigation. It can be linked to inaccuracies either on the rbf approximation of $\nabla\frac{\partial\phi}{\partial z}$ or in the estimation of $\nabla\phi^2$ on the Wigley hull surface, which alters the pressure field. In particular, the use of rbfs in the so called finite difference mode can be an alternative approach Chinchapatnam [2006], since it tries to approximate the derivatives of the function locally instead of seeking a global approximator.

Moreover, on a overall basis, as the amplitude increases the experimental measures imply a slightly higher added mass in the lower and higher frequency range with no appreciable change in the mid frequency range. The variations on the damping coefficient implied by the experimental measures is similar to the added mass behaviour on the lower and higher frequencies, but in the mid frequency range the damping coefficient decreases with the amplitude of oscillation.

From a hydroelastic perspective, the behaviour of the coupling coefficients, heave into to the first distortion mode (2-node) turns out be very similar to the predictions for the heave hydrodynamic coefficients. Figure 7.15 shows the force time series of heave into the first distortion mode, for two frequencies, $\hat{\omega} = 2.49$

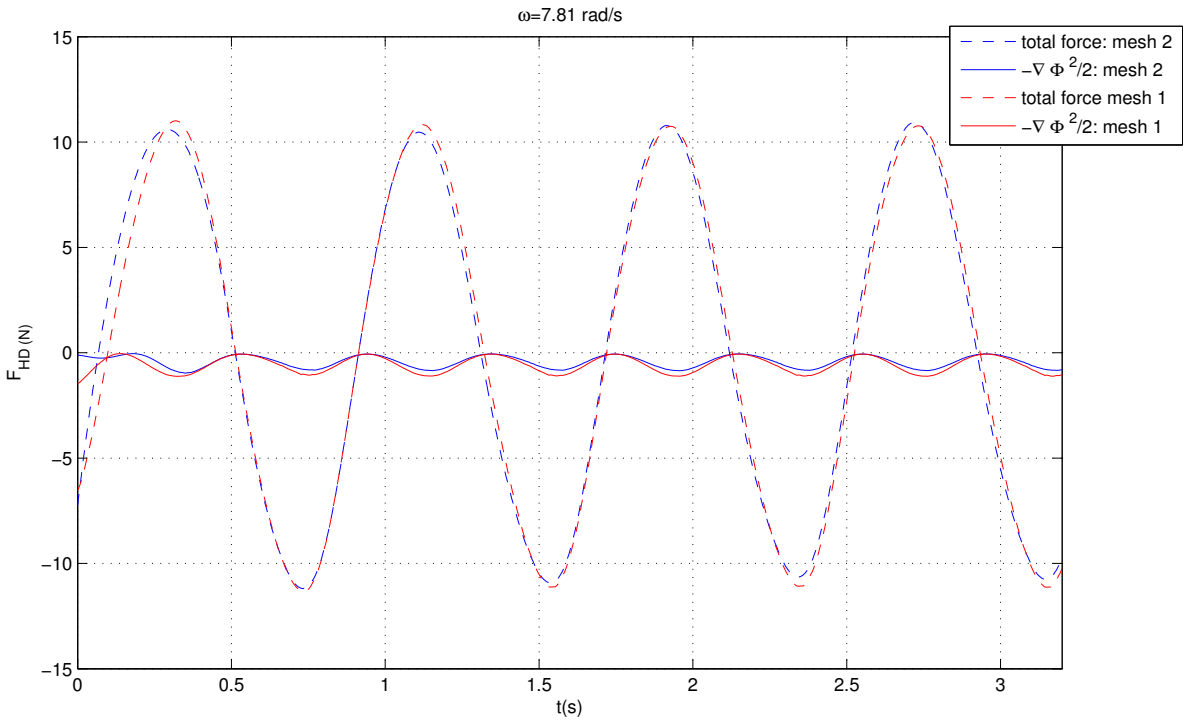

Figure 7.13: Forces of the Wigley hull undergoing forced heave oscillations, $\hat{\omega} = 2.49$, $A = 0.27T$ and $\lambda = 0.01$. The total force and the force corresponding to square of the gradient are shown for meshes 1 and 2.

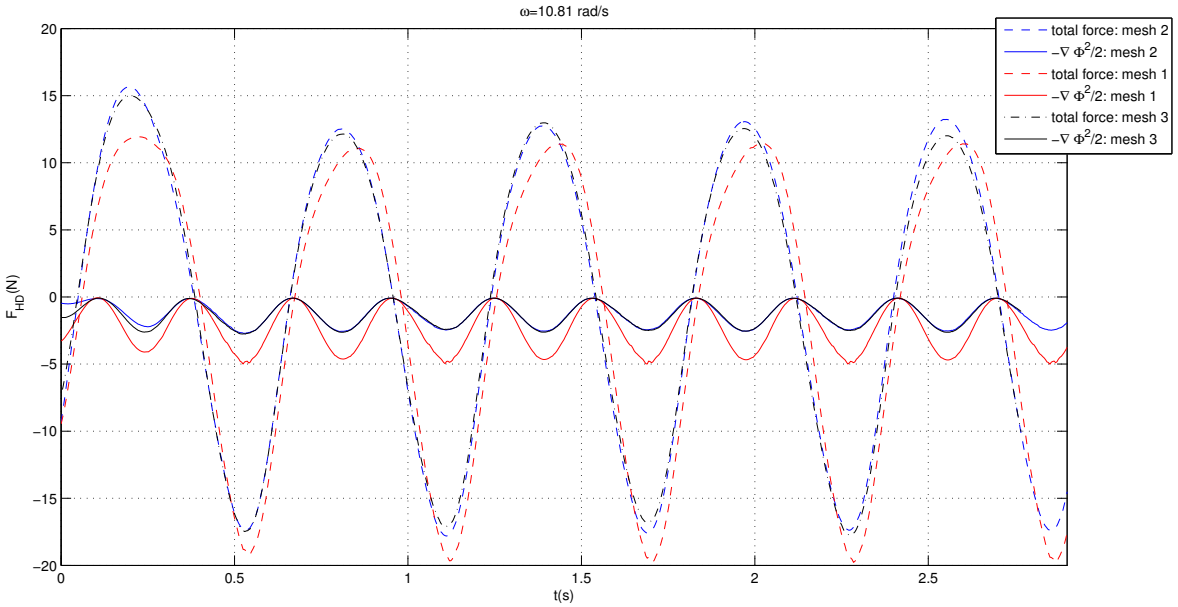

Figure 7.14: Forces of the Wigley hull undergoing forced heave oscillations, $\hat{\omega} = 3.45$, $A = 0.27T$ and $\lambda = 0.01$. The total force and the force corresponding to square of the gradient are shown for meshes 1 and 2.

($\omega = 7.81$ rad/s) and $\hat{\omega} = 3.45$ ($\omega = 10.81$ rad/s), for meshes and 1 and 2. The effects of refinement are the same as the ones metioned before, for the case of heave into heave. Figure 7.16 compares the value of the cross coupled coefficients obtained from the body non linear analysis to the ones obtained from the linear analysis of chapter 6.

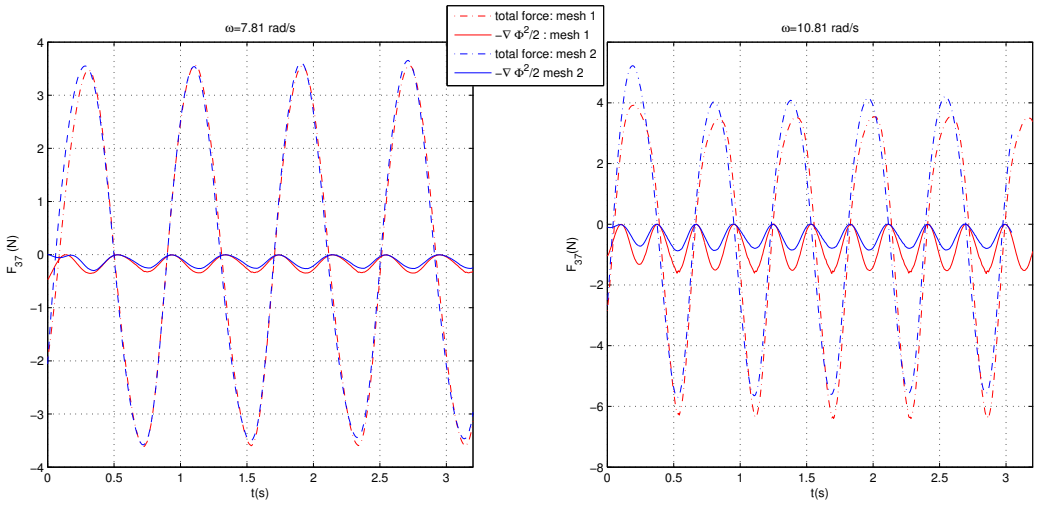

Figure 7.15: The left hand side shows the hydrodynamic force component of heave into the first distortion mode (2 node) for the lower frequency whereas the right hand side shows the hydrodynamic force for the higher frequency for meshes 1 and 2.

Table 7.1: Wigley Hull Hydrodynamic coefficients in heave calculated by Algorithm 6, for $\hat{\omega} = 2.49$, compared against the experimental data obtained by Journée [1992].

Mesh	$\hat{A}_{33}$	$\hat{B}_{33}$
mesh 1	1.10	3.55
mesh 2	1.17	3.34
experiment	1.23	3.21

Another point worth pointing out is that the force time series obtained in this section are less prone to numerical diffusion as compared to the sphere simulations of the last section. As it will be seen in chapter 7, there are indications that,

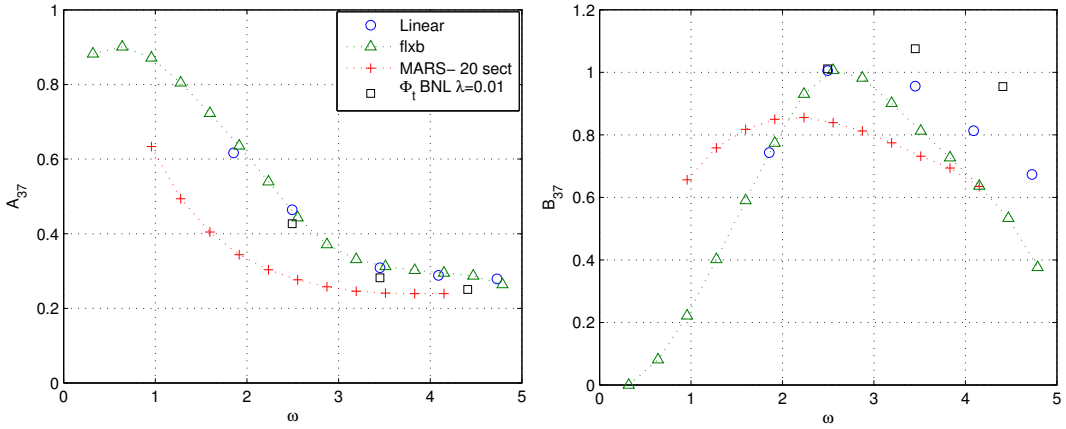

Figure 7.16: Comparison of the cross coupled coefficients of the heave mode into the 2-node distortion mode. The green triangles were obtained from frequency domain analysis; the blue dots are the results calculated by algorithm 4 from chapter 6; the red crosses are obtained from 2D strip theory and the black squares were calculated by 6.

under some circumstances, the node displacement updates used by Persson [2005] meshing algorithm can increase the numerical diffusion of the simulation. In this sense, the meshing library from Geuzaine and Remacle [2009] seems to be less prone to this sort of effect.

7.3 Fully Non Linear Analysis

The body non linear model can be extended to take into account the fully non linear nature of the free surface boundary conditions. This can be done by extending algorithms 5 or 6, depending on the way the pressure is going to be evaulated at the floating body. In order to achieve this, the formulation of the free surface boundary condition needs to be taken into account exactly. Accordingly, the free surface movement also needs to be taken into account, so that the boundary value problem is solved on the exact free surface. In contrast, in the body non linear analysis, the BVP is solved at the mean undisturbed free surface, i.e $\zeta = 0$.

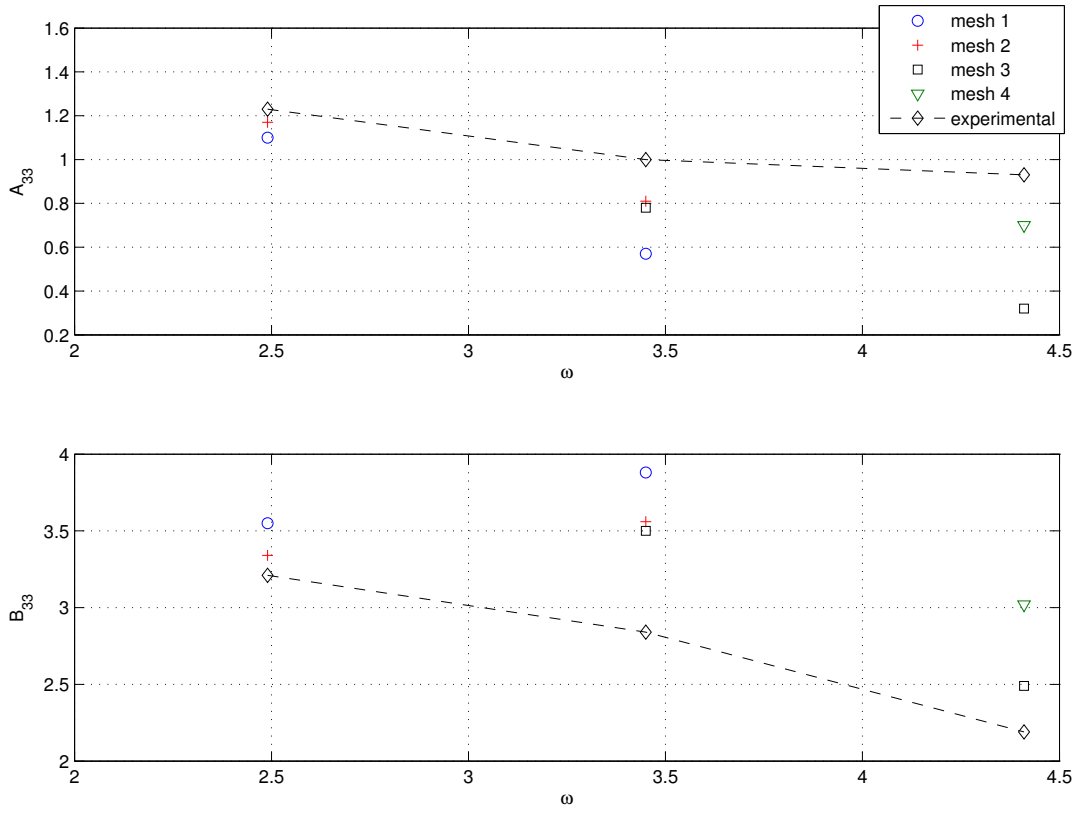

Figure 7.17: A comparison between the results presented in tables 7.1, 7.2 and 7.3 and the experimental measures of Journée [1992].

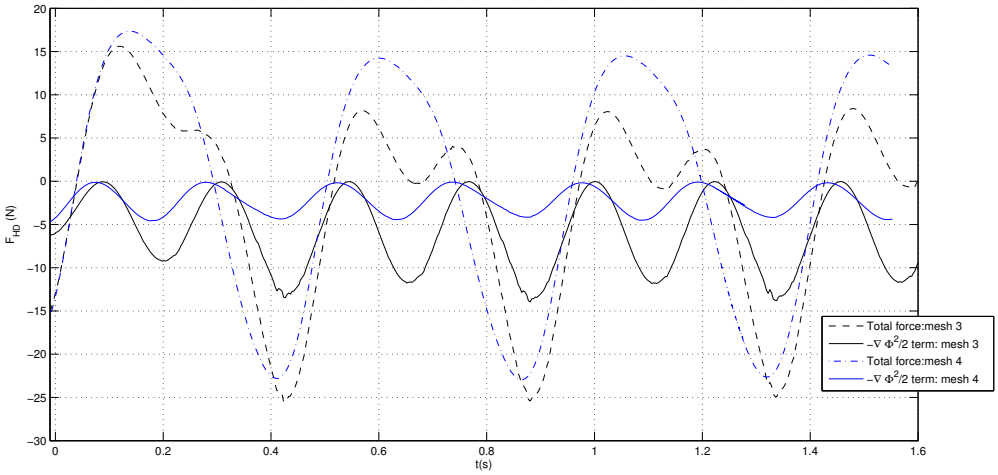

Figure 7.18: Forces of the Wigley hull undergoing forced heave oscillations, $\hat{\omega} = 4.41$, $A = 0.27T$ and $\lambda = 0.01$. The total force and the force corresponding to square of the gradient are shown for meshes 3 and 4.

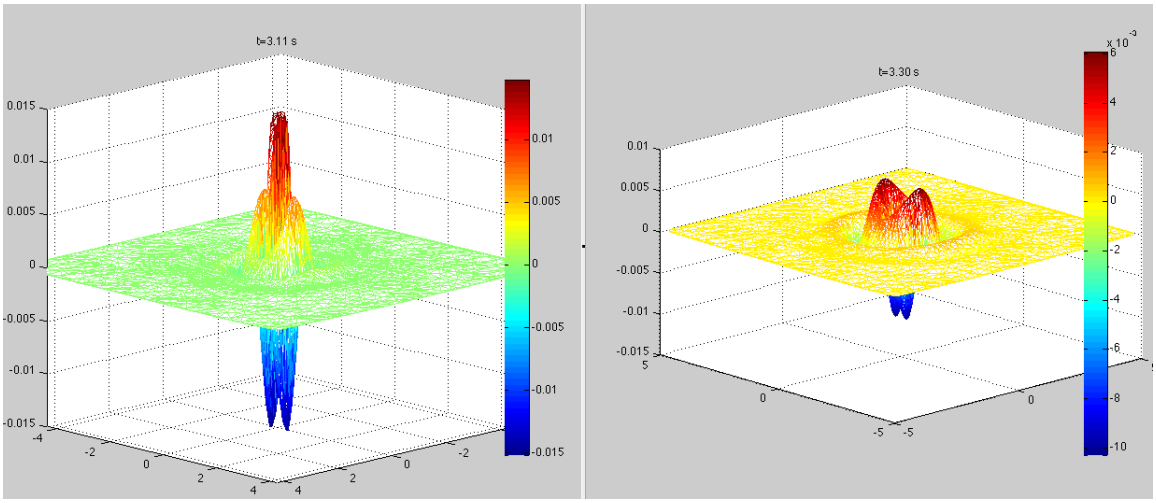

Figure 7.19: Free surface profile of Wigley hull body non linear simulations: left hand side $\hat{\omega} = 3.45$ and right hand side $\hat{\omega} = 2.49$.

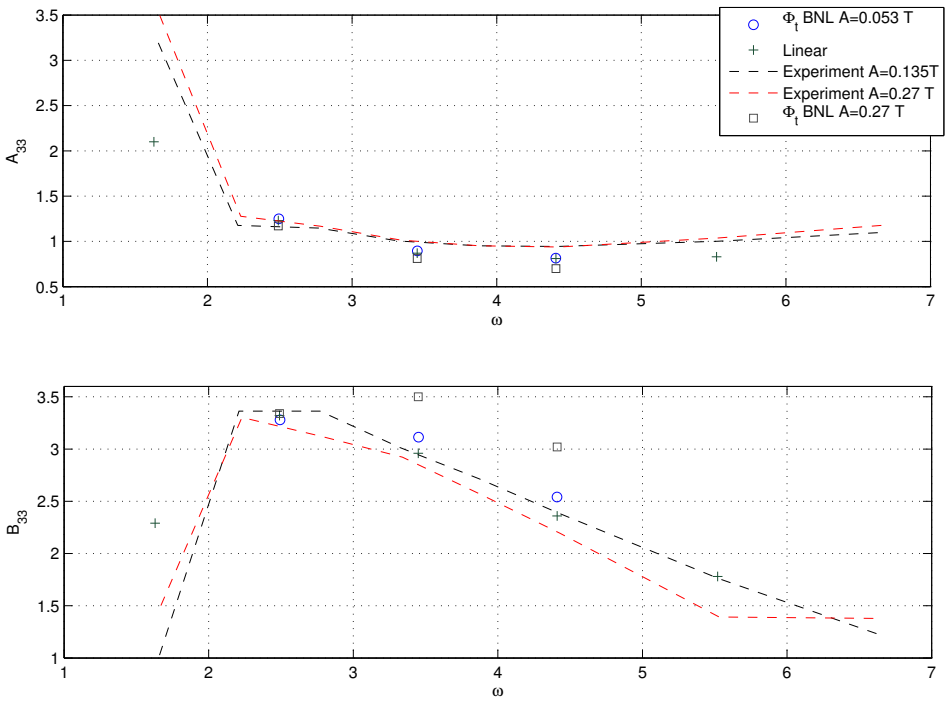

Figure 7.20: Comparison of heave hydrodynamic coefficients using Algorithms 4 (Linear), 6 (BNL) and experimental data, for a different ranges of frequencies and amplitudes.

Table 7.2: Wigley Hull Hydrodynamic coefficients in heave calculated by Algorithm 6, for $\hat{\omega} = 3.45$, compared against the experimental data obtained by Journée [1992].

Mesh	$\hat{A}_{33}$	$\hat{B}_{33}$
mesh 1	0.57	3.88
mesh 2	0.81	3.56
mesh 3	0.78	3.50
experiment	1.00	2.84

Table 7.3: Wigley Hull Hydrodynamic coefficients in heave calculated by Algorithm 6, for $\hat{\omega} = 4.41$, compared against the experimental data obtained by Journée [1992].

Mesh	$\hat{A}_{33}$	$\hat{B}_{33}$
mesh 3	0.32	2.49
mesh 4	0.70	3.02
experiment	0.93	2.19

7.3.1 Free Surface Boundary Conditions

In order to account for nonlinear effects, the linear assumption on the free surface boundary conditions need to be relaxed. This means that instead of using equations 4.14 and 4.15, equations 4.12 and 4.13 are going to be used. This brings new numerical problems because, since equation 4.12 is written in Lagrangian coordinates, it is implied that fluid particles are being followed along their motion. Moreover, the motion of the fluid particles change the fluid domain (i.e the distance between collocation and field points change) so that a new mesh needs to be constructed every time step in order to calculate the influence matrix and solve the Eulerian phase. There are a couple of different formulations of the free surface boundary conditions that can be explored to tackle this issue see for instance Liu et al. [2001], Kara et al. [2007] and Yan [2010]. In the present work, the free surface boundary conditions are modified from the fully Lagrangian description of the fluid flow to a pseudo Eulerian description, where the grid points are allowed to move only on the vertical direction. The intuition that motivated this idea is that a a good mesh with a flat free surface is still a good mesh after

the points on free surface are mapped to their actual $z = \zeta(x, y)$ position [1]. The derivation details are on the appendix 8.2, the final form of the kinematic free surface boundary conditions can then be written as:

$$\frac{\delta\zeta}{\delta t} + \frac{\partial\phi}{\partial x}\frac{\partial\zeta}{\partial x} + \frac{\partial\phi}{\partial y}\frac{\partial\zeta}{\partial y} = \frac{\partial\phi}{\partial z}, \tag{7.26}$$

whereas the dynamic free surface conditions is given by:

$$\frac{d\phi}{dt} - \frac{\partial\phi}{\partial z}\frac{\partial\zeta}{\partial t} + \frac{1}{2}\nabla\phi^2 + gz = 0. \tag{7.27}$$

As in chapter 4 , the damping zone described by equation 4.16 is used so that the radiation condition at infinity can be met on both dynamic and kinematic boundary conditions, i.e:

$$\frac{\delta\zeta}{\delta t} + \frac{\partial\phi}{\partial x}\frac{\partial\zeta}{\partial x} + \frac{\partial\phi}{\partial y}\frac{\partial\zeta}{\partial y} = \frac{\partial\phi}{\partial z} - \nu\zeta, \tag{7.28}$$

$$\frac{d\phi}{dt} - \frac{\partial\phi}{\partial z}\frac{\partial\zeta}{\partial t} + \frac{1}{2}\nabla\phi^2 + gz = -\nu\phi. \tag{7.29}$$

Equations 7.28, 7.29 and 4.10 form the core of the nonlinear hydrodynamic solver developed so far. In order to implement them numerically, account for the changes in boundary domain and calculate the time derivatives of the fluid potential on the surface of the floating body some numerical techiniques were introduced. These numerical techniques, together with the algorithm that was implemented are described in the next section.

7.3.2 Fully Non Linear Model

Once the boundary conditions of the free surface are formulated, algorithm 5 can be extended to perform non linear simulations. Besides the free surface boundary condition, the mesh is now deformed on the vertical direction to take into account the exact position of the free surface. Thus, the boundary value

[1] More precisely this "intuition" assumes that: 1- the free surface is single valued in x and y; 2-the elevation is "reasonably" small in the z direction so that a triangle with vertices on the plane $z = 0$, will still be a good triangle at $z = \zeta(x, y)$.

problem is solved at the exact free surface position. In addition, at this point, there is no special treatment for the water line dynamics, i.e , it is assumed that the rbf representation of the free surface generalizes well enough to extrapolate the position of the water line given the position of the nodes in its vicinity. That said, the finite difference non linear algorithm, FDNL, is shown below.

Algorithm 7 Finite Difference Non Linear

1: **procedure** MAIN( )
2: **while** $t < T$ **do**
3: [p,t]=CreateMesh(fd(t),fh,h0); ▷ Create a mesh of the domain
4: $[x_{FS}, y_{FS}, x_B, y_B, z_B]$:=FindBoundaryNodes(p,t);
5: ϕ_{FS}:=$\Phi_i(x_{FS},y_{FS},t)$ ▷ Set BC Value on the of the FS triangles
6: $\nabla\phi \cdot \vec{n}_B := \vec{v}(t)_B \cdot \vec{n}_B$ ▷ Set BC Value on the Floating Body
7: $\nabla\phi \cdot \vec{n}_B := 0$ ▷ Set BC Value on other Neumann Boundaries
8: z_{FS}:=$\zeta(x_{FS}, y_{FS})$ ▷ Move the free surface on the z direction.
9: $[\phi_B; \nabla\phi \cdot \vec{n}_{FS}] := [G_{FS}; Gn_B]^{-1}[\nabla\phi \cdot \vec{n}_B; \phi_{FS}]$ ▷ Solve the BVP at $z_{FS} = \zeta$
10: $\nabla\phi := (\nabla\phi \cdot \vec{t}_b)\vec{t}_b + (\nabla\phi \cdot \vec{n}_b)\vec{n}_b$ ▷ Compose $\nabla\phi$ on the body surface
11: $p := \frac{\partial\phi}{\partial t} + \frac{\nabla\phi^2}{2}$ ▷ Equation 7.2 is used for $\frac{\partial\phi}{\partial t}$
12: $\vec{F} := -\rho \int_{\partial B(t)} p\vec{n}_B(t)dS$ ▷ Calculate the force on B(t)
13: $\zeta_t := \zeta_{t-1} + dt(-\frac{\partial\phi}{\partial x}\frac{\partial\zeta}{\partial x} - \frac{\partial\phi}{\partial y}\frac{\partial\zeta}{\partial y} + \frac{\partial\phi}{\partial z} - \nu\zeta)$ ▷ Update the FS elevation
14: $\phi_t := \phi_{t-1} + dt(\frac{\partial\phi}{\partial z}\frac{\partial\zeta}{\partial t} - \frac{1}{2}\nabla\phi^2 - gz - \nu\phi)$ ▷ Update the FS potential
15: $t := t + dt$
16: **end while**
17: **end procedure**

As compared to Algorithm 5, note that the changes are in line 8, where the mesh is deformed and in lines 14 and 15, where the exact free surface boundary conditions replace the linearized versions.

7.3.3 Analysis of the Rigid Body Results

In this section the analysis of the hydrodynamics coefficients presented in section 6.2 is revisited and extended to the purpose of non-linear analysis.

A natural question that arises when applying Fourier decomposition is how many harmonics one should use to approximate "well" the signal that is being de-

composed. In addition, in the presence of noisy data [1] , there is only an heuristic framework (up to our knowledge) of investigating the significance of each harmonic component. Thus, it is not entirely clear which harmonic component is more likely to be noise or not. Lastly, although the problem at hand is in theory stationary [2], the numerical results from the simulations turn out to present localized numerical diffusion effects, questioning the assumption of stationarity. In addition, other problems of great interest from a hydrodynamic perspective (such as water impact problems and transient phenomena) don't share the stationary property.

In order to overcome some of these issues, the Empirical Mode Decomposition and the Hilbert Huang transform developed by Huang et al. [1998] is a valuable tool. Furthermore, its filtering properties yield an empirical framework where noisy components of the data can be filtered out Wu and Huang [2004]. In fact, since Hilbert Huang transform generalizes the Fourier transform to non stationary data. This new tool turns out to so powerful that even an alternative definition of hydrodynamic coefficients (in the time-frequency-energy distribution as opposed to the frequency-energy distribution from Fourier analysis) can be envisaged. This is an embrionary idea that is very briefly discussed in the Appendix B.

As it will be seen in due course, the results of the non linear simulations have a great deal of noise, so the properties of the EMD, as filter, become very handy. Therefore, they are going to be used to filter the time series of the hydrodynamic forces before performing the usual Fourier decomposition. Actually, there is no harm in using the Hilbert Huang Transform, since it can seen as a generalization of the Fourier decomposition Huang et al. [1998].

The filtering scheme employed to analyse the time series of the hydrodynamic force is the same as the one proposed by Wu and Huang [2004]. The basic idea is to decompose the the time series in its intrisic mode functions (IMFs, which are defined in Appendix B) and then apply the empirical statistical test in order to

[1] Noise can come from variety of sources, the focus on this work is on noise generated from numerical instabilities and inaccuracies associated with CPM.

[2] By definition stationary means that the properties of the signal do not change when they are shifted in time. More precisely, a signal X_t is strongly stationary if its cumulative probability function is invariant in time. Let $F_x(X_{t_1}, X_{t_2}, ..., X_{t_n})$ be the cumulative probability density function of X_t, then X_t is stationary if, for all τ, $F_x(X_{t_1+\tau}, X_{t_2+\tau}, ..., X_{t_n+\tau}) = F_x(X_{t_1}, X_{t_2}, ..., X_{t_n})$.

select which IMFs are different from white noise. The filtered time series is then reconstructed as the sum of the relevant IMFs plus the residual term. This is done for the three cases of the sphere undergoing forced motions in heave mode, at a frequency corresponding to $KR = 1$, and amplitudes A equal to $0.04R$, $0.25R$ and $0.375R$.

Figures 7.21 , 7.25 and 7.28 show how the original time series is decomposed into series of IMFs, $C_i's$ and a residual term R_1. The IMFs are then compared to white noise by plotting the logarithm of its energy density, $log(E)$, against the logarithm of its period, $log(T)$. For white noise this relation was investigated by Wu and Huang [2004] and the the results therein, for 0.95 confidence level, are summarized on the solid blue lines in figures 7.22, 7.26 and 7.29. Interestingly, the IMFs that are the most relevant are usually the 4th,5th and 6th depending on the time series. These IMFs are then used to reconstruct a filtered version of the signal and compared against the original time series of the hydrodynamic forces (figures 7.23 , 7.27 and 7.30. By doing so, it is clear that some higher frequency components on the time series of the hydrodynamic force are removed, these components don't have a physical meaning wih high probability. In fact, these non physical oscillations could be linked to the numerical innacuracies and numerical diffusion of the CPM, i.e body discretization and the poor estimation of the time derivative of the potential field (Yan [2010] and Battistin and Iafrati [2003]).

Once the filtered time series of the hydrodynamic force is available, equations 7.23 to 7.20 can be applied and the components of interest, from hydrodynamic perspective, can all be evaluated. Tables 7.4 and 7.5 compare, as function of the amplitude of oscillations, these components, for both filtered and raw time series of hydrodynamic force. The results obtained by Yan [2010] are shown in table 7.6.

The corresponding force time series of the two higher amplitudes ($A = 0.25R$ and $A = 0.375R$) tackled by algorithm 7 are shown in figures 7.27 and 7.30. In these plots, both raw force and filtered versions are shown.

Figures 7.31 and 7.32 compare both added mass and damping coefficients calculated by Algorithm 7 against the fully non linear simulations of Yan [2010] and the body non linear results of Lin and Yue [1991]. At this point, it is worth

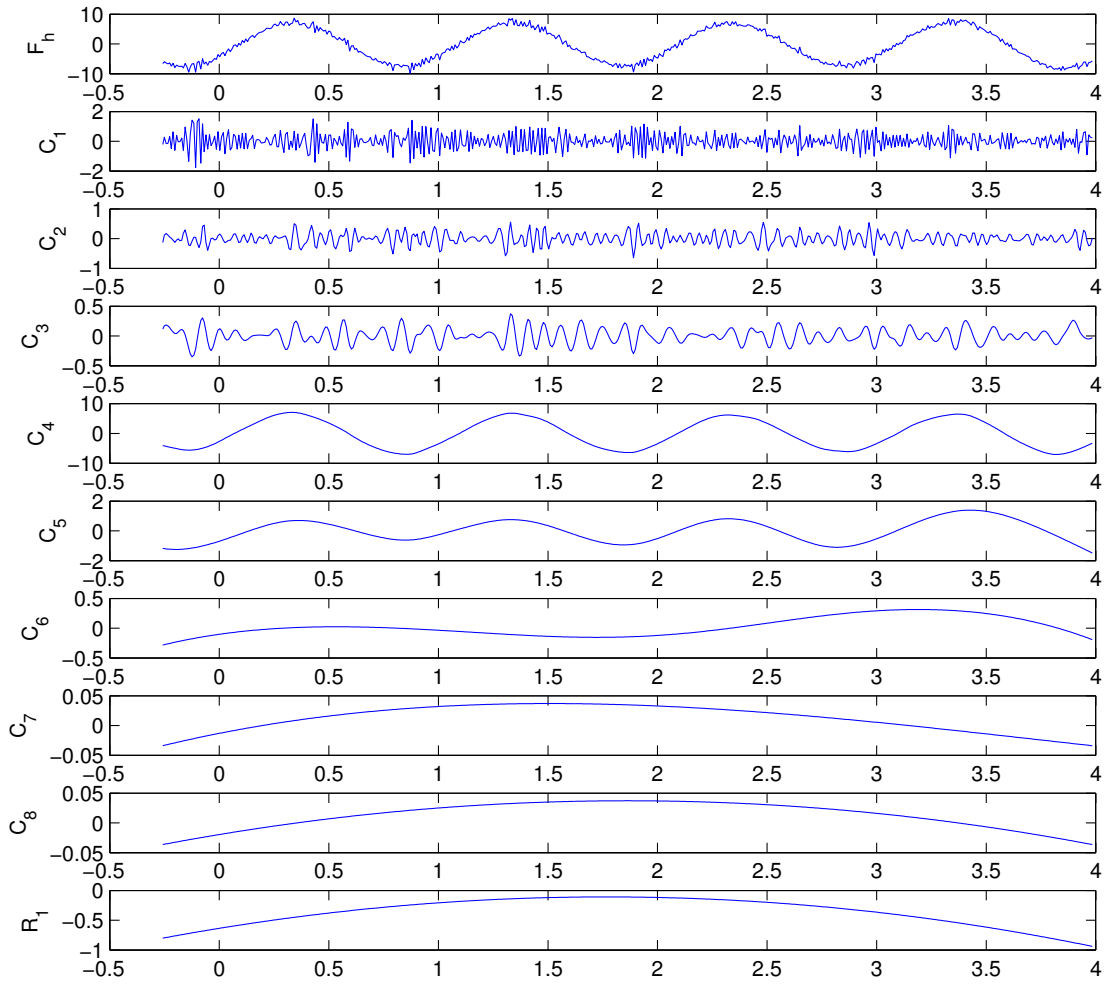

Figure 7.21: Decomposition of the force time series into IMFs using the EMD method for $A = 0.04R$. The top plot shows the original time series of the hydrodynamic force. C_1 to C_8 are the IMFs obtained from the decomposition and R_1 is the residual term.

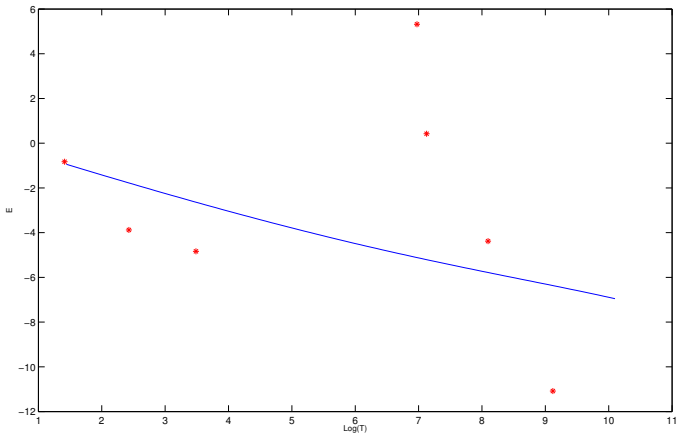

Figure 7.22: IMFs Statistical Test for $A = 0.04R$: the blue line displays the 0.95 confidence interval threshold of white noise energy density $log(E)$ as a function of its period $log(T)$. IMFs whose energy are above this line are keept in the filtering process.

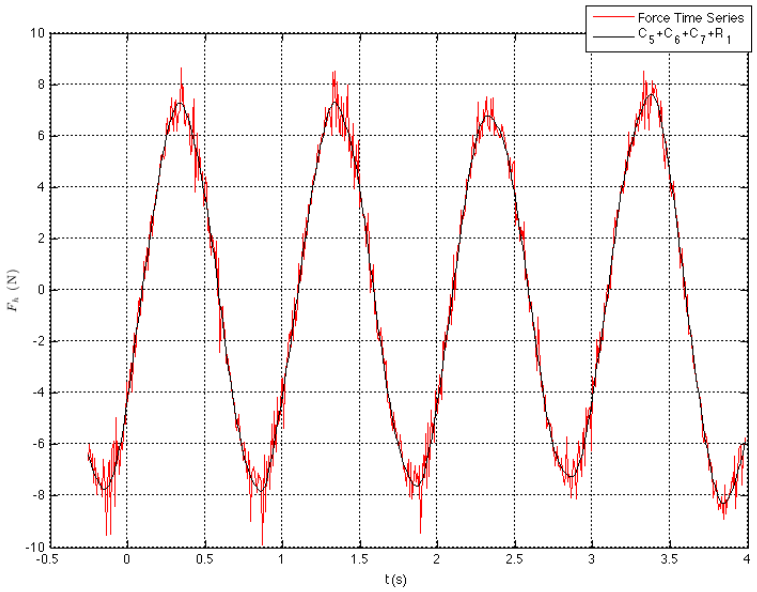

Figure 7.23: Time series of the sphere undergoing heave oscillations with $A = 0.04R$ and the filtered version of the series, i.e the sum of the relevant IMFs (in this case 4, 5 and 6) from figure 7.21 plus the residual term.

Table 7.4: Harmonics of the non filtered time series of hydrodynamic forces

$\frac{A}{R}$	$\frac{f_0}{\rho\pi g R A^2}$	$\frac{f_1}{\rho\pi g R^2 A}$	$\frac{f_2}{\rho\pi g R A^2}$
Linear (analytical)	0.0	0.3298	0.0
Linear (calculated)	$-5.4 \cdot 10^{-6}$	0.3340	$-3.95 \cdot 10^{-6}$
0.04	-0.0147	0.365	0.046
0.25	-0.1145	0.375	0.127
0.375	-0.0844	0.3899	0.126

Table 7.5: Harmonics of the filtered time series of hydrodynamic forces using EMD.

$\frac{A}{R}$	$\frac{f_0}{\rho\pi g R A^2}$	$\frac{f_1}{\rho\pi g R^2 A}$	$\frac{f_2}{\rho\pi g R A^2}$
Linear (calculated)	$-5.4 \cdot 10^{-6}$	0.3340	$-3.95 \cdot 10^{-6}$
0.04	-0.137	0.366	0.079
0.25	-0.110	0.375	0.128
0.375	-0.117	0.3877	0.142

highlighting the resonable qualitative agreement of the harmonics, as compared to the QBEM method of Yan [2010]. Theae resuts are showns in tables 7.4, 7.5 and 7.6 and are also summarized in figure 7.24. In fact, for the three harmonics one can spot a jump in small amplitude range. This behaviour is actually linked to the innacuracy of algorithm 7 when it comes to the estimation of the time derivative of the velocity potential. That said, the qualitative behaviour of the $\hat{f}_0$, $\hat{f}_1$ and $\hat{f}_2$ are resonable from a qualitative perspective.

Besides that, the agreement between the hydrodynamics coefficients is rather poor. It is hard to identify an agreement in the qualitative behaviour of the hydrodynamic coefficients. There is a similar trend as the one observed in section 6.2 of overestimating the added mass coefficients. Furthermore, for $A = 0.25R$, the algorithm 7 overshoots the added mass and underestimates the damping coefficient, basically breaking the qualitative agreement between the lowest amplitude $A = 0.04R$ and the higher amplitude $A = 0.375R$. This issues are clearly related to the low accuracy of the numerical simulations of the constant panel method. In particular, an accurate solution of the Dirichlet problem, which yields the normal velocity on the free surface in the present work, is an important building block to depart and develop a more accurate BEM solver.

Table 7.6: Results from Yan [2010], obtained using the quadratic boundary element method.

$\frac{A}{R}$	$\frac{f_0}{\rho\pi g R A^2}$	$\frac{f_1}{\rho\pi g R^2 A}$	$\frac{f_2}{\rho\pi g R A^2}$
0.125	-0.0864	0.3328	0.174
0.25	-0.0808	0.3338	0.179
0.30	-0.0789	0.3392	0.187
0.375	-0.0768	0.3449	0.193

In this context, the extension to fully non linear problems is a subject that needs future investigations. In particular, based on the results obtained by Yan [2010], the use of Higher Order Boundary Element Methods (HOBEM) and higher order Galerkin BEM approaches are promising avenues of future research.

7.4 Conclusions

In this chapter, the hypothesis of linear theory were relaxed progressively. First, the body non linear problem was addressed for the sphere and for the Wigley hull undergoing forced oscillations in the heave mode. The results were compared to other numerical techniques and experimental data when available. For the sphere simulations, the results from the FDBNL algorithm suggests a reasonable agreement for the estimation of the damping coefficient and overestimation of the added mass coefficient, as compared to the body non linear results obtained by Yan [2010]. The Φ_t Exact BNL algorithm, in contrast, suggest a better agreement for added mass coefficient and f_2. The agreement obtained in the damping coefficient is good, without taking into account the higher amplitude of oscillation $A = 0.375R$. At this amplitude, there are issues that need further investigations. These issues are probably linked with a poor estimation of the boundary condition of the second boundary value problem (i.e the normal derivative of the time derivative of the velocity potential). This quantity is intimately associated with m_3, see appendix A, and its numerical estimation is usually cumbersome.

The body nonlinear results of the Wigley hull under heave forced oscillations brought more insight on the behaviour of the Φ_t Exact BNL algorithm. For a

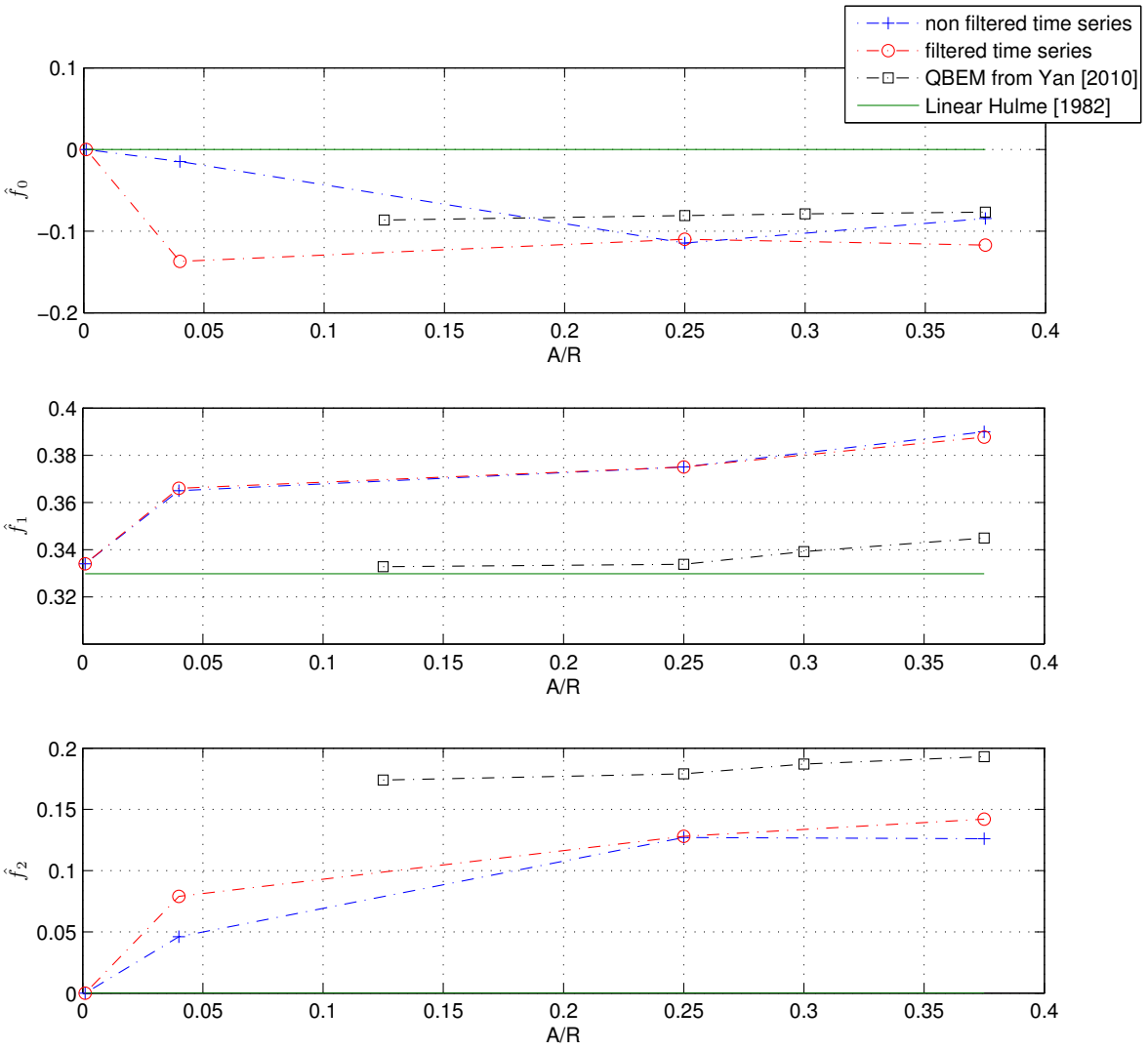

Figure 7.24: Comparison between harmonics, $\hat{f}_0$, $\hat{f}_1$ and $\hat{f}_2$, obtained from the unfiltered/filtered time series, the results obtained by Yan [2010] and the analytical values from Linear analysis.

low amplitude, the agreement is in line with the predictions made by the linear algorithm. On the other hand, using a higher amplitude, $A = 0.27T$, the results showed considerable deterioration as the frequency is increased, as compared to

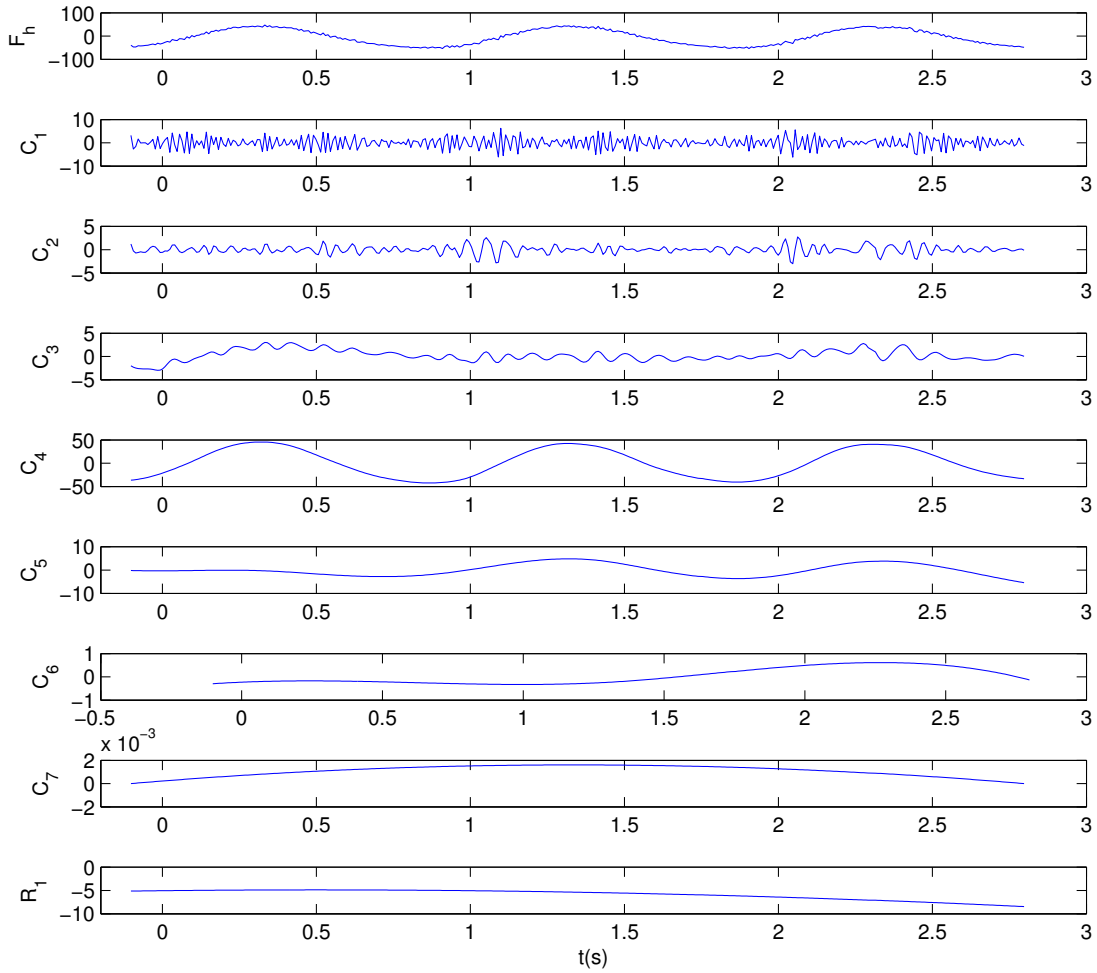

Figure 7.25: Decomposition of the force time series into IMFs using the EMD method for $A = 0.25R$. The top plot shows the original time series of the hydrodynamic force. C_1 to C_7 are the IMFs obtained from the decomposition and R_1 is the residual term.

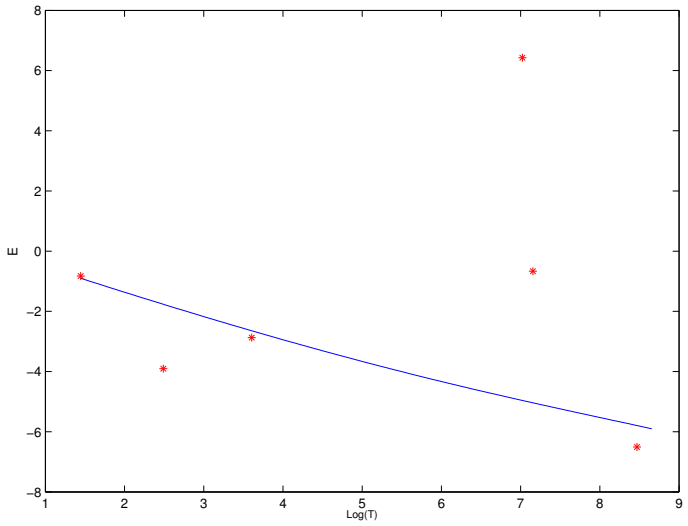

Figure 7.26: IMFs Statistical Test for $A = 0.25R$: the blue line displays the 0.95 confidence interval threshold of white noise energy density $log(E)$ as a function of its period $log(T)$. IMFs whose energy are above this line are keept in the filtering process.

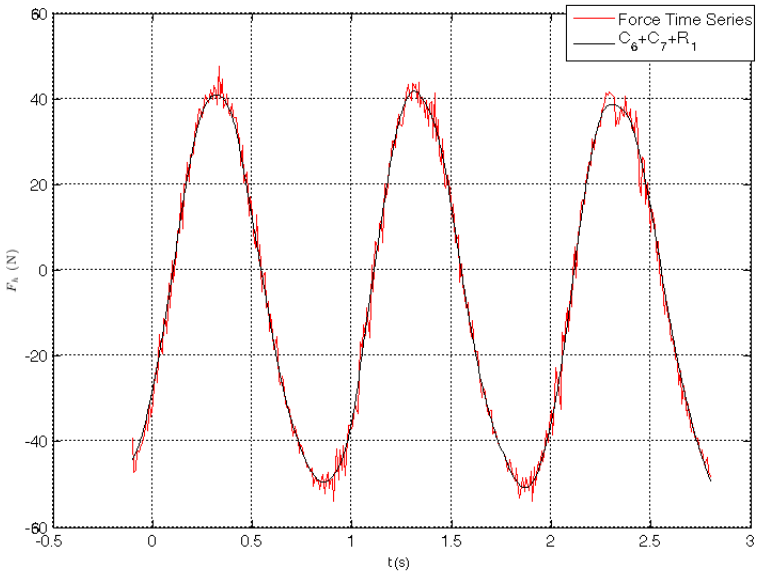

Figure 7.27: Time series of the sphere undergoing heave oscillations with $A = 0.25R$ and the filtered version of the series, i.e the sum of the relevant IMFs (in this case 4 and 5) plus the residual term from figure 7.25 .

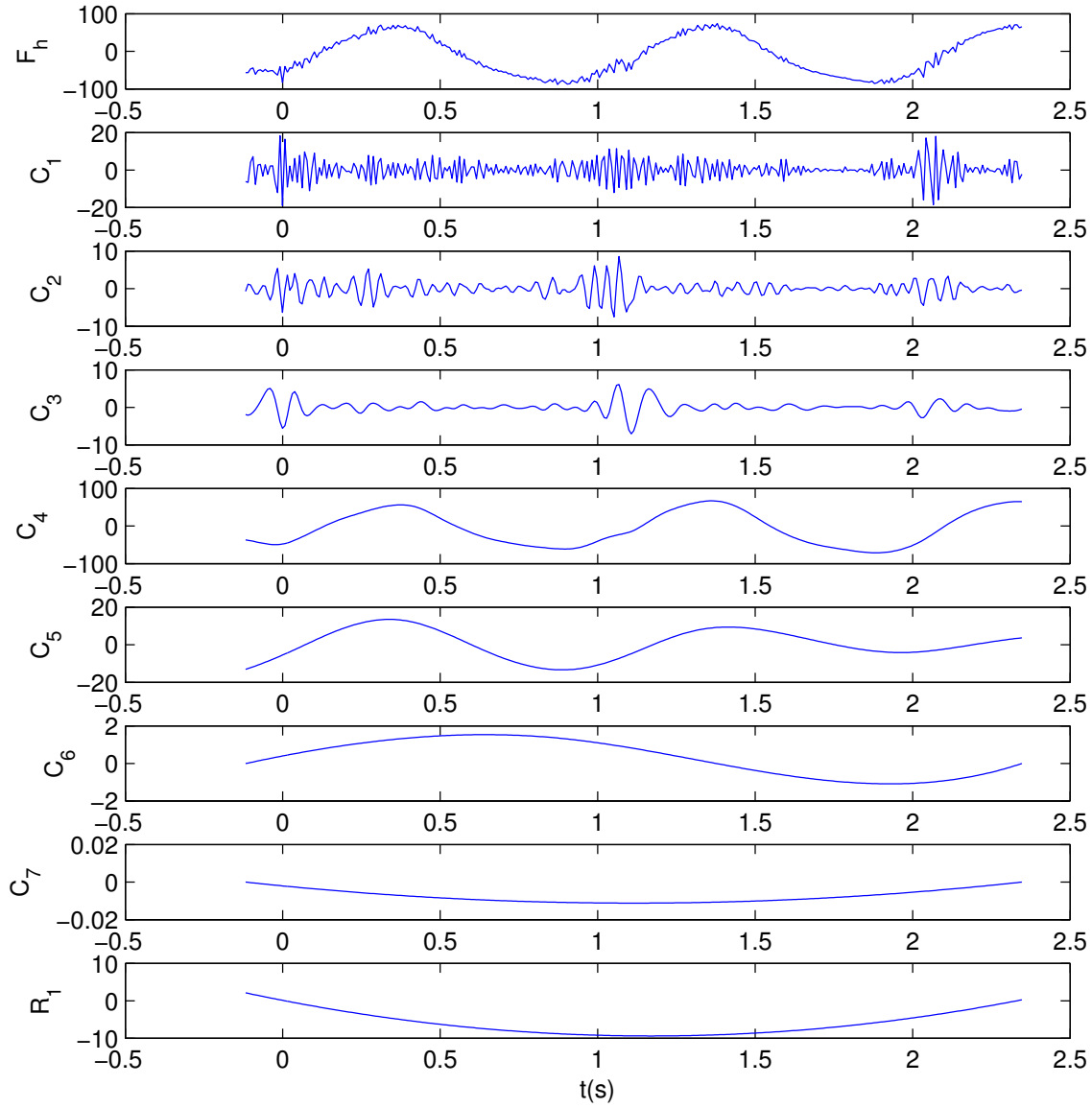

Figure 7.28: Decomposition of the force time series into IMFs using the EMD method for $A = 0.375R$. The top plot shows the original time series of the hydrodynamic force. C_1 to C_7 are the IMFs obtained from the decomposition and R_1 is the residual term.

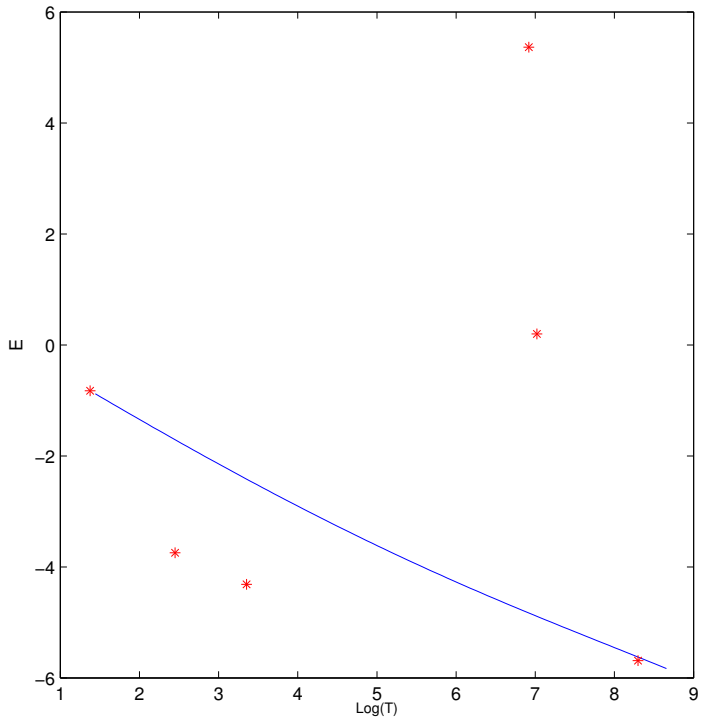

Figure 7.29: IMFs Statistical Test for $A = 0.375R$: the blue line displays the 0.95 confidence interval threshold of white noise energy density $log(E)$ as a function of its period $log(T)$. IMFs whose energy are above this line are keept in the filtering process.

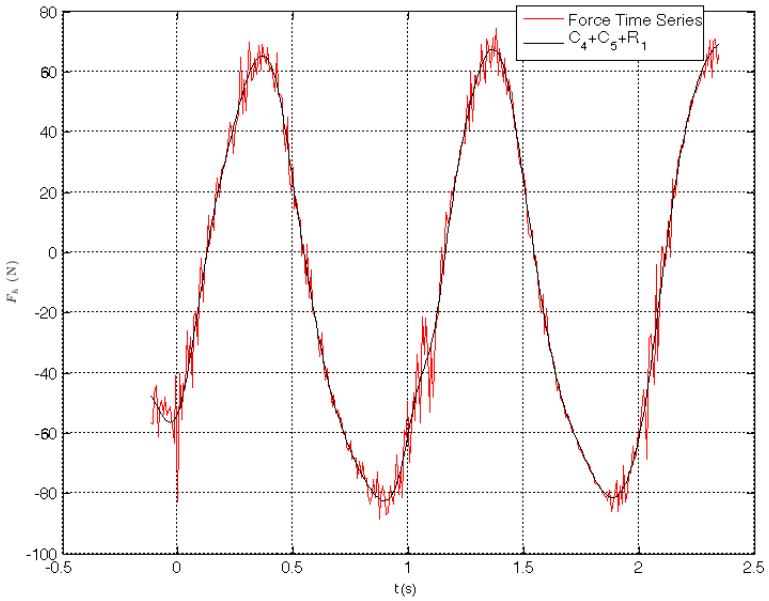

Figure 7.30: Time series of the sphere undergoing heave oscillations with $A = 0.375R$ and the filtered version of the series, i.e the sum of the relevant IMFs (in this case 4 and 5) plus the residual term.

both linear and experimental results. Yet, the general behaviour of body non linear predictions, i.e lower added masses and higher damping coefficients as the amplitude of oscillation increases, was observed. This raises an interesting point regarding the applicability of the Body non Linear analysis, namely that it can improve the results from linear theory only in a region where the wave steepness, kA, is kept small.

On the fully non linear front, the results for sphere undergoing forced oscillations in heave achieved a reasonable agreement in terms of f_1 and f_2, after the time series was filtered using the EMD algorithm. However, a deeper analysis of the components of f_1, the added mass and damping coefficients, indicates that more investigations are needed in this front. More specifically, the spurious modes observed in the force time series, indicates that a more robust boundary element solver (higher order boundary element methods, or HOBEM) could be beneficial and improve the predictions made by the algorithm.

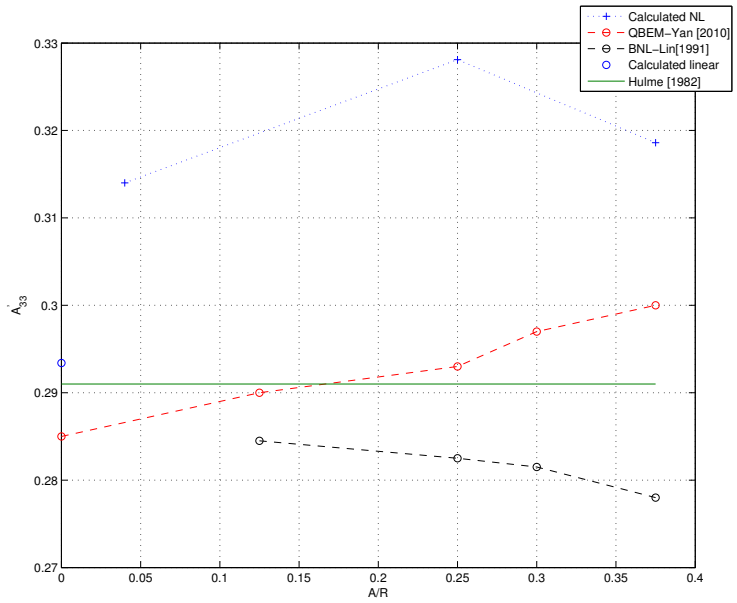

Figure 7.31: Comparison of the added mass coefficients for the sphere under forced oscillations motions , $kR = 1$, where the added mass is non dimensionalized as $A'_{33} = \frac{A_{33}}{\pi\rho R^2 A}$.

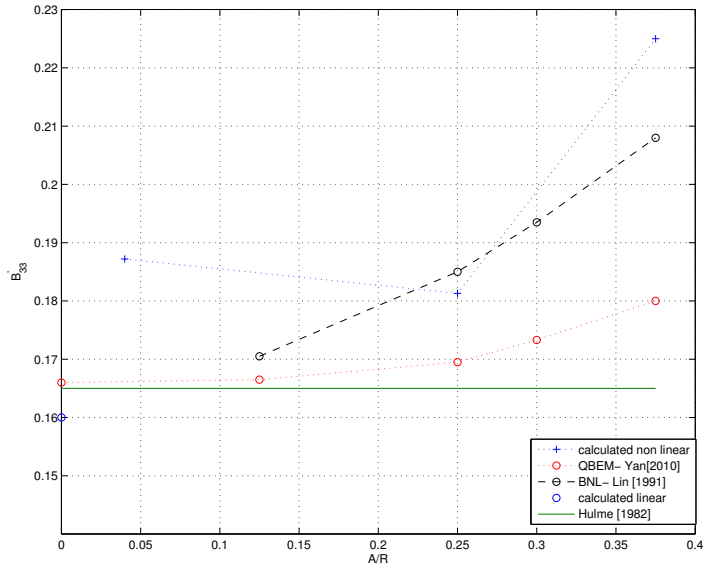

Figure 7.32: Comparison of the added mass coefficients for the sphere under forced oscillations motions , $kR = 1$, where the damping coefficient is non dimensionalized as $B'_{33} = \frac{B_{33}}{\pi\rho RA^2\sqrt{kR}}$.

Chapter 8

Conclusions and Future Work

8.1 Conclusions

The main feature of the present work has focused on the modeling of the three dimensional radiation problem in time domain using an unstructured mesh by means of the constant direct Rankine panel method (or direct Boundary Element Method) . In that context, algorithms have been proposed to solve the following problems in time domain: (i) the linear radiation problem of a hemisphere undergoing forced heave and sway oscillations. (ii) The unified hydroelastic problem of a Wigley hull undergoing forced rigid, symmetric and anti-symmetric bending distortion motions. (iii) The body non linear problem of a sphere and Wigley hull undergoing large amplitude of oscillations in the heave mode. (iv) The fully nonlinear problem of a sphere undergoing forced oscillations in the heave mode. In addition, the coupling between meshing libraries and hydrodynamic simulations was also investigated. In this context, two algorithms were proposed in order to estimate signed distance functions for the free surface evolution and for ship like shapes. With these algorithms, the meshing scheme based on signed distance functions could be linked against the BEM solver. However, for these algorithms to be used in the context of the present MEL simulation a parallel implementation is needed, otherwise the runtime is still an obstacle to perform the required tests. This implementation was left out of the scope of the present work. Alternatively, a simpler meshing library Geuzaine and Remacle [2009] was linked against the MEL scheme and used to remesh the domain of the body non

linear Wigley hull simulations. Both approaches, as well as their pros/cons were discussed in chapter 5.

The results of the linear time domain analysis agree qualitatively well with analytical predictions for the hemisphere, with available experimental data and with other computational models for the Wigley hull for symmetrical distortion modes. For the motion in the sway mode, the agreement achieved, compared to other numerical methods, was resonable, but a deterioration in the accuracy has been observed. This deterioration was again observed on the coupling of sway into the first horizontal bending distortion mode (2-node).

In the body non linear analysis, two different numerical algorithms have been proposed to evaluate the time derivative of the velocity potential: FDBNL and Φ_t Exact BNL. In addition, the difficulties associated with the estimation of the spatial derivatives in the context of constant panel method solver (i.e a $C^0(\Omega)$ method) were tackled by the introduction of radial basis function representations for both potential and free surface elevations. More concretely, due to inaccuracies in the estimation of the normal velocity, the resulting free surface position was not being estimated accurately enough for the purposes of the numerical simulations. Remeshing combined with a high generalization error of the Radial Basis Functions representation, were bringing even more inaccuracies to the free surface position, resulting in spurious oscillations of the hydrodynamic force time series. Two numerical methods were proposed to deal with these effects, increasing the accuracy of CPM solver, i.e: the first method introduced a regularization parameter on the RBF representations. From a statiscal perspective the regularization parameter reduces the complexity of the hypothesis, in this case the RBF's coefficients, improving the generalization error of the RBF representation, allowing for an accurate estimation of the m_3 term (see Appendix A Numerical Techniques for more details). The second method uses the Ensemble Mode Decomposition (EMD) and its empirical results to represent the time series of the force time series as a sum of intrisic mode functions (IMF's) . Assuming the spurious modes of oscillations of the hydrodynamic force time series are white noise, the IMF's with energy close to white noise are extracted from the hydrodynamic time series. The sum of the IMF's that were not rejected corresponds to the filtered hydrodynamic force. The results of the body non linear analysis

compared the predictions from both FDBNL and Φ_t Exact BNL methods againist other numerical predictions for the sphere with resonable agreement, with the Φ_t Exact BNL method resulting in better overall accuracy. Using the Φ_t Exact BNL method, results for the Wigley hull, undergoing high amplitude forced motions in the heave mode, show good agreement against experimental data on the lower frequency range, but, a deterioration was observed for higher values of kA. Results of the fully non linear simulations for the sphere, using the FDBNL method and EMD decomposition technique, overestimate of the order of 10%, the hydrodynamic coefficients compared to other non linear methods. These comparisons suggest that further research is required to improve the accuracy of this method.

One of the main objectives of the present work was to develop a methodology in time domain capable of tackling problems of forced oscillations in either rigid or flexible modes and problems related to the evolution of the free surface in time, using either the linear (linear and body non linear simulations) and the non linear free surface boundary conditions. To this extent, the objective has been achieved.

However, during this whole process the main limitations of the current methodology and algorithms have also become clear. In a way, this can be seen as good news since it can certainly help in guiding future research and improvements in the present algorithms. More specifically, the major points that have limited the applicability of the present work are: the accuracy of the constant panel method and the accuracy of the geometric definition of the floating body.

Regarding the accuracy of the constant panel method, the indications are that the accuracy of this particular numerical scheme, in the context of mixed boundary value problems in unstructured meshes, can be poor. This has been highlighted in chapters 6 and 7, when performing either linear, body non linear and fully non linear simulations. In particular, the main concern lies in the estimation of the normal velocity on the free surface (i.e the solution of the Dirichlet problem). Since the MEL scheme evolves the free surface boundary conditions in time and its values are used as boundary conditions to the Eulerian phase, it can be the case that errors in the estimation of the normal velocity on the free surface are being propagated in time through the Lagrangian phase. This issue is more pronounced as the free surface distortions increase, i.e higher

amplitude motions of the both the Wigley hull and sphere.

The hydrodynamic coefficients of a floating body are in fact a function of its geometry. Therefore, it is important for the numerical mesh not only to have a good element quality, but also to be close to the geometry of the floating body itself. The problem of element quality was addressed in the present work but the investigation of how accurate the mesh is, as compared to the floating body one is trying to represent was not performed. In fact, because the aim was in the design of a methodology, qualitative agreement was sought. Hence, it can be the case that a more accurate representation the Wigley hull or instance, can yield more accurate results, still using the constant panel method, than the ones obtained in chapters 6 and 7.

In the context of the design of offshore structures and ships, the proposed methodology can be viewed as a small step towards a tool that can be integrated, in the future, to a virtual simulator, whereby the hydrodynamic problem is solved in real time by a three dimensional potential flow method. To this date, from the hydrodynamic side, such virtual environments can be powered by a two dimensional time domain strip theory approach and, in the next few years, the extension to three dimensional potential flow methods will certainly bring more improvements. In fact, it will happen probably much sooner than RANS becomes a feasible tool for this task. The impact of these virtual environments for both industry and researches in naval architecture is promising as it will allow for not only more reliable designs but also open the door to the incorporation of more optimization methods, culminating in a faster evolution from one vessel to another.

8.2 Future Work

In order to extend the present work, the following research topics are suggested:

1. In the context of time domain simulations:

    - The influence of forward speed in the hydrodynamic force can be investigated by changing the impervious boundary condition on the floating

body. In this case, even in the context of forced motions, the effects of the Froude number,F_n, can be investigated further. In particular, the wave resistance problem can also be solved in this context. This problem can be formulated under the three frameworks, i.e: linear, body non linear and fully non linear simulations.

- The boundary conditions can also be modified in order to impose the potential corresponding to a incident sinusoidal wave. In this context, instead of imposing a prescribed forced oscillation motion, the structure is freely floating. The solution of the Euler phase, i.e, the hydrodynamic forces are then integrated in time, together with the free surface boundary conditions, to yield the motions of the floating body. Furthermore, in this case the hydrodynamic force comprises both the diffraction and radiation force components. Because the velocity potential has components due to diffraction and radiation, it needs a more detailed description from the numerical perspective. For the linear case, the superposition principle implies that the radiation and diffraction effects can be modeled separately and then added together, simplifying the numerical analysis. For the case of non linear simulations the numerical analysis is more subtle and probably requires a higher order element representation.

2. As was highlighted in the present work, the extension from linear to body non linear and fully non linear time domain simulations, involve a series of numerical/algorithms challenges, spanning from runtime issues to the accurate approximation of spatial and temporal derivatives of the velocity potential. The numerical problems become more complex, because the domain configuration changes in time as the remesh procedure is performed. In this context a couple of topics arise naturally, namely:

   - Efficient calculations of the influence matrix, ideally performed using a parallel architecture with the aid of a fast multipole method.
   - The use of higher order boundary element methods is an important subject, since, in theory, a more accurate estimation of the solution

of the Dirichlet problem can be achieved. They also allow the spatial derivatives of the velocity potential to be estimated locally, on a element wise basis. This provides an alternative to the radial basis function representation introduced in the present work. Still concerning the solution of the boundary value problem, which sort of boundary element method to use, i.e collocation or Garlekin based, is also an interesting research topic, in the context of hydrodynamic applications.

- The solution of the linear system of the boundary value problem can also be optimized by the use of the generalized minimal residual method (GMRES) or the biconjugate gradient stabilized method (BiCGSTAB), since the linear system is not symmetric, nor sparse. In this context, the solution of the linear system arising from the rbf representation is symmetric, hence, a iterative solution, based on gradient descent (say conjugate gradient method) , is faster and scalable than the current implementation based on LU decomposition.

Appendix A Numerical Techniques

"There is much less practice in theory than in practice."

The relevant numerical techniques associated with the mixed boundary value problem and its corresponding time marching scheme are briefly outlined. These techniques were implemented in the C++,matlab and Python and were used to produce all the results in this work. Once the MEL concept has been adopted, the numerical techniques used in the Eulerian and in the Lagrangian phase are going to be discussed separately, in the first two sections. Next the derivation of the boundary condition, for the second boundary value problem described in chapter 7 is derived. On the last section, the free surface boundary condition used in the simulations of the fully non linear case is also described in detail.

Eulerian Phase

Numerically in the context of the MEL scheme the Eulerian phase consists of solving equation 4.10. Therefore, from a numerical point of view, this phase has the following steps:

1. Calculation of the influence Matrix coefficients for the Green function $G^{ij} = G(\vec{x}_i, \vec{y}_j)$ and the dipole $G_n^{ij} = \nabla G(\vec{x}_i, \vec{y}_j) \cdot \vec{n}$.

2. Assembling the linear system corresponding to equation 4.10.

3. Solution of the linear system.

Influence Matrix Computation

Using a short hand notation, equation 4.10, for i=1 to N, can be written in the following form:

$$c(\vec{x}_i)\phi(\vec{x}_i) = \sum_{j=1}^{N} \int_{E_j} G^{ij}\phi_n(\vec{y})dE_j - \sum_{j=1}^{N} \int_{E_j} G_n^{ij}\phi(\vec{y})dE_j, \tag{1}$$

where $\vec{x}_i$ and $\vec{y}_i$ are, respectively, source and field points, $\phi_n(\vec{y}) = \nabla\phi(\vec{y}) \cdot \vec{n}$ and $\vec{n}$ is the normal on the field point $\vec{y}$ pointing out of the fluid domain.

Furthemore, in the context of the constant Boundary Element Method both $\phi_n(\vec{y})$ and $\phi(\vec{y})$ are assumed to be constant in each element E_j, hence they can be taken out of the integrals, yielding:

$$c(\vec{x}_i)\phi(\vec{x}_i) + \sum_{j=1}^{N} \int_{E_j} G_n^{ij} dE_j \phi^j = \sum_{j=1}^{N} \int_{E_j} G^{ij} dE_j \phi_n^j. \tag{2}$$

Note that the equation above can be written in a matrix form. In fact it is precisely the linear system one solves in the Eulerian phase. Therefore, let $g_{ij} = \int_{E_j} G^{ij} dE_j$ and $d_{ij} = c(\vec{x}_i)\delta_{ij} + \int_{E_j} G_n^{ij} dE_j$ correspond to the influence of a source point i on a field point j, then one can write:

$$\begin{pmatrix} d_{1,1} & d_{1,2} & \cdots & d_{1,N} \\ d_{2,1} & d_{2,2} & \cdots & d_{2,N} \\ \vdots & \vdots & \ddots & \vdots \\ d_{N,1} & d_{N,2} & \cdots & d_{N,N} \end{pmatrix} \begin{pmatrix} \phi^1 \\ \phi^2 \\ \vdots \\ \phi^N \end{pmatrix} = \begin{pmatrix} g_{1,1} & g_{1,2} & \cdots & g_{1,N} \\ g_{2,1} & g_{2,2} & \cdots & g_{2,N} \\ \vdots & \vdots & \ddots & \vdots \\ g_{N,1} & g_{N,2} & \cdots & g_{N,N} \end{pmatrix} \begin{pmatrix} \phi_n^1 \\ \phi_n^2 \\ \vdots \\ \phi_n^N \end{pmatrix} \tag{3}$$

The Kronecker delta, δ_{ij}, was used in the definition of d_{ij} in order to account for the presence of the solid angle in the diagonal of this matrix when $i = j$.

In addition, if $i \neq j$ all the integrands are non singular. In this case, the off-diagonal coefficients are calculated using the element area, A_{rj}, the Euclidean

distance between the source point i and the field point j, $\vec{r}_{ij}$, and the normal vector of the jth field point, $\vec{n}$, hence giving:

$$g_{ij} = \frac{A_{rj}}{4\pi r_{ij}}, \tag{4}$$

$$d_{ij} = \frac{A_{rj}(\vec{r}_{ij} \cdot \vec{n})}{4\pi r_{ij}^3}. \tag{5}$$

In the equations above, $r_{ij} = ||\vec{r}_{ij}||$ is the three dimensional distance between a source point i and a field point j (or equivalently the norm of $\vec{r}_{ij}$) and $\cdot$ denotes the scalar product between two vectors.

In the case where $i = j$, g_{ii} becomes weakly singular and d_{ii} strongly singular Liu [2009]. There are a couple of alternatives for dealing with the weakly singular behaviour of g_{ii}. In this work, the triangle mapping technique is chosen because of its flexibility in dealing with higher order BEM schemes Zhang and Xu [1989].

The basic premise of the mapping is to note that although Green's function is singular when the source and field point are the same, the integral is well defined as long as the integration surface is sufficiently smooth, i.e the Jacobian of the transformation does not vanish. A classic example is the integration of the Green's function over a circle. Thus, after the triangle mapping is performed the integrand is no longer singular and can be evaluated using standard Gaussian quadratures techniques.

Very briefly, the triangle mapping technique works as follows: let $\vec{x}_1$, $\vec{x}_2$ and $\vec{x}_3$ denote the three vertices of the E_j triangle, then the degenerate mapping is introduced by the following transformation:

$$\vec{x}' = (1 - \rho_1)\vec{x}_1 + (1 - \rho_2)(\rho_1)\vec{x}_2 + \rho_1\rho_2\vec{x}_3. \tag{6}$$

Using this change of variables, the weakly singular integrand over an element transforms to a non-singular integrand given by:

$$\int\int_{Ej} \frac{1}{||\vec{r}_{ii}||} dE_j = \frac{1}{2}\int_0^1 \int_0^1 \frac{J(\rho_1, \rho_2)}{\sqrt{R_x^2 + R_y^2 + R_z^2}} d\rho_1 d\rho_2 \tag{7}$$

Where, after some algebra, the Jacobian of the transformation, $J(\rho_1, \rho_2)$, R_x, R_y and R_z are given by:

$$J(\rho_1, \rho_2) = \sqrt{v_1^2 + v_2^2 + v_3^2},$$

$$R_x = (-x_1 + (1 - \rho_2)x_2 + \rho_2 x_3)\rho_1;$$

$$R_y = (-y_1 + (1 - \rho_2)y_2 + \rho_2 y_3)\rho_1;$$

$$R_z = (-z_1 + (1 - \rho_2)z_2 + \rho_2 z_3)\rho_1;$$

where:

$$v_1 = \rho_1((-y_1 + (1-\rho_2)y_2 + \rho_2 y_3)(-z_2 + z_3) - (-y_2 + y_3)(-z_1 + (1-\rho_2)z_2) + \rho_2 z_3);$$

$$v_2 = \rho_1((-z_1 + (1-\rho_2)z_2 + \rho_2 z_3)(-x_2 + x_3) - (-z_2 + z_3)(-x_1 + (1-\rho_2)x_2) + \rho_2 x_3);$$

$$v_3 = \rho_1((-x_1 + (1-\rho_2)x_2 + \rho_2 x_3)(-y_2 + y_3) - (-x_2 + x_3)(-y_1 + (1-\rho_2)y_2) + \rho_2 y_3).$$

Fortunately, in order to calculate the self influence coefficient associated with the dipole matrix, d_{ij}, there is no need to evaluate any integral. It can be shown, Pozrikidis [2002], that when $i = j$ the integral part of $d_{ii} = c(\vec{x}_i) + \int_{E_i} G_n^{ii} dE_i$ vanishes. This way, $d_{ii} = c(\vec{x}_i)$. Furthemore, the solid angle can be calculated by summing the off diagonals elements of the ith row. Hence, for i=1 to N:

$$d_{ii} = \sum_{j=1}^{N} d_{ij}^{i \neq j}. \tag{8}$$

At this point all the coefficients of the matrices in equation 3 are known. The next steps are to assemble and solve the linear system.

Assembling and Solving the Linear System

In order to assemble the linear system, it is worth going back to equation 3 and note that N boundary conditions have to be imposed to obtain its solution. Because the boundary value problem is mixed, the potential ϕ (Dirichlet problem)

will be known at the free surface where ϕ_n is unknown. On the floating body, however, the opposite condition follows ϕ_n is known (Neumann problem) but ϕ is not known. Once these two sets are disjoint and their union comprises the boundary of the whole domain, there are N boundary conditions to be imposed in equation 3. The problem is that the Neumann boundary conditions are imposed on the left hand side, while Dirichlet boundary conditions are placed on right hand side. Therefore the standard linear system, $Ax = b$, is formed by applying the corresponding boundary condition at each node (Neumann or Dirichlet) and switching the columns in the two matrices d_{ij} and g_{ij}. This way, the matrix A is usually dense and is nonsymmetric.

Once assembled the linear system is solved by LU decomposition, to this end a direct solver from the LAPACK library is used.

Lagrangian Phase

Euler Method

This phase consists of the integration of the dynamic and kinematic free surface boundary conditions in time. In the linearized case (say linear and body non linear analysis), these boundary condtions are prescribed by equations 4.17 and 4.18. Usually, for this purpose, a second or fourth order Runge-Kutta scheme (Xu [1992], Kara et al. [2007] and Liu [2010]) is adopted to guarantee the stability of solution in time. The present results were obtained by integrating the kinematic and dynamic boundary conditions using the Euler method and a second order Runge-Kutta scheme (described in the next section). Therefore, the numerical versions of equations 4.17 and 4.18 are, respectively, given by:

$$z^{t+\delta t} = z^t + \delta t(\frac{\partial \phi^t}{\partial z} - \nu z^t) \tag{9}$$

$$\phi^{t+\delta t} = \phi^t + \delta t(-gz^t - \nu \phi^t) \tag{10}$$

For the fully non linear case studied in chapter 7 the corresponding version

of the kinematic and dynamic boundary conditions are given by equations 7.28 and 7.29 respectively. Their respective numerical versions is obtained in the same fashion.

Second Order Runge-Kutta Method

A more accurate numerical approach would be to integrate equations 4.17 and 4.18 in time using a second order Runge-Kutta scheme. In a way, the Euler method can be viewed as particular case of the second order Runge-Kutta scheme. To see this, suppose we have a scalar the function $y(t)$, which is differentiable in the domain of interest to us. Let its derivative dy/dt be given by the function $f(y,t)$. Then the problem is how to evaluate $y(t+\delta)$ at the subsequent time step. A second order Runge-Kutta scheme performs this update as follows:

$$k_1 = \delta f(y,t), \tag{11}$$

$$k_2 = \delta f(y + \beta k_1, t + \alpha\delta), \tag{12}$$

$$y(t+\delta) = y(t) + ak_1 + bk_2. \tag{13}$$

The constants α, β, a and b have to be evaluated in order to guarantee that error is proportional to δ^3, or O(δ^3). In particular , note that if we set $k_2 = 0$ and a=1, we recover the Euler method. Let's now show under what choices of constants α, β, a and b the integration error of O(δ^3). In order to do this, Taylor series is used to expand $y(t)$ in its neighborhood of t correct to O(δ^2). Hence,

$$y(t+\delta) = y(t) + \delta\frac{dy(t,y)}{dt} + \delta^2\frac{d^2y(t,y)}{dt^2} + O(\delta^3). \tag{14}$$

In equation 14, $\frac{d^2y(t,y)}{dt^2}$ can be evaluated in terms of $f(y,t)$, i.e:

$$\frac{d^2y(t,y)}{dt^2} = \frac{\partial f}{\partial t} + \frac{\partial f}{\partial y}\frac{dy}{dt}. \tag{15}$$

From 14 and 15, one has that:

$$y(t+\delta) = y(t) + \delta\frac{dy(t,y)}{dt} + \frac{\delta^2}{2}(\frac{\partial f}{\partial t} + \frac{\partial f}{\partial y}\frac{dy}{dt}). \tag{16}$$

In equation 13, the k_2 term can also be expanded to second order and the result can be given in terms of the constants of interest, since $k1 = hf(y,t)$; hence, after some algebra, this yields :

$$y(t+\delta) = y(t) + (a+b)\delta f(y,t) + b\delta^2(\alpha\frac{\partial f}{\partial t} + \beta\frac{\partial f}{\partial y}f(y,t)). \tag{17}$$

By comparing the respective coefficients of equations 16 and 17, it is straight forward to see that in order to achieve precision of $O(\delta^3)$, the constants α, β, a and b should satisfy:

$$a + b = 1, \tag{18}$$

$$\alpha b = 1, \tag{19}$$

$$\beta b = 1, \tag{20}$$

A classical choice, the one adopted here, is $\alpha = \beta = 1$ and $a = b = \frac{1}{2}$. A second order Runge-Kutta (RK2) implementation in order to integrate the free surface boundary conditions in time, this will comprise the Lagrangian phase of the MEL scheme, is given below. Because the free surface boundary conditions are coupled and there are two differential equations, the RK2 integration comprises 7 equations which can be written as follows:

$$k_1^z = \delta t(\frac{\partial \phi^t}{\partial z} - \nu z^t); \tag{21}$$

$$z^{t+\delta t} = z^t + k_1^z; \tag{22}$$

$$k_1^{\phi} = \delta t(-gz^t - \nu\phi^t); \tag{23}$$

$$k_2^{z} = \delta t(\frac{\partial \phi^{t+\delta}}{\partial z} - \nu z^{t+\delta}); \tag{24}$$

$$z^{t+\delta t} = z^t + (k_1^z + k_2^z)/2; \tag{25}$$

$$k_2^{\phi} = \delta t(-gz^{t+\delta} - \nu\phi^{t+\delta}); \tag{26}$$

$$\phi^{t+\delta t} = \phi^t + (k_1^{\phi} + k_2^{\phi})/2. \tag{27}$$

Equations 21, 22 and 23 comprise the first step of the RK2 scheme and they all rely in solving the Euler phase at time t. Equation 21 calculates the change in the free surface position, equation 22 updates the free surface position and equation 23 calculates the change in free the surface potential. Next, the Euler phase is solved at time $t + \delta$, and the second phase of the RK2 starts; equations 24,25,26 do the same job as in the first phase whereas equation 27 , finally, updates the potential on the free surface.

Boundary Conditons for the Second Boundary value problem

In order to evaluate $\frac{\partial \phi}{\partial t}$ exactly, the time harmonic property of the potential can be explored and a second boundary value problem can be solved on the Neumann surface for $\frac{\partial \phi}{\partial t}$ directly. However, to accomplish this, a boundary condition on the Neumann surface, for $\frac{\partial^2 \phi}{\partial t \partial n}$, needs to be imposed.

In this section, a simple case where a motion is considered only on the heave mode, is going to be tackled, the general case can be found in Wu and Eatock Taylor [1996]. The main assumption that is needed to go through the derivation is

that the potential is C^2, i.e it is differentiable up to order 2, with respect to its field variables (x, y, z). That said, the Neumann condition on the body for second boundary value problem can be written as:

$$\frac{\partial^2 \phi}{\partial t \partial n} = \vec{n}_B \cdot \vec{a}_B - \vec{n}_B \cdot (\vec{v}_B \cdot \nabla)\nabla\phi. \tag{28}$$

Expanding the last term gives:

$$\vec{n}_B \cdot (\vec{v}_B \cdot \nabla)\nabla\phi = \vec{n}_B \cdot (V_1 \frac{\partial}{\partial x} + V_2 \frac{\partial}{\partial y} + V_3 \frac{\partial}{\partial z})\nabla\phi. \tag{29}$$

For forced motions on the heave mode, $V_1 = V_2 = 0$ and $V_3 = Asin(\omega t)$, hence , after some algebra it can be shown that:

$$\vec{n}_B \cdot (\vec{v}_B \cdot \nabla)\nabla\phi = V_3 \vec{n}_B \cdot (\frac{\partial \phi_x}{\partial z}\vec{i} + \frac{\partial \phi_y}{\partial z}\vec{j} + \frac{\partial \phi_z}{\partial z}\vec{k}). \tag{30}$$

The last step is to interchange the order of differentiation with respect to ϕ (i.e its assumed that the velocity potential is twice differentiable, $\phi \in C^2(\Omega)$), resulting in:

$$\vec{n}_B \cdot (\vec{v}_B \cdot \nabla)\nabla\phi = V_3 \vec{n}_B \cdot (\frac{\partial \phi_z}{\partial x}\vec{i} + \frac{\partial \phi_z}{\partial y}\vec{j} + \frac{\partial \phi_z}{\partial z}\vec{k}) = V_3 \vec{n}_B \cdot \nabla \frac{\partial \phi}{\partial z}. \tag{31}$$

It is also interesting to point out that $V_3 \vec{n}_B \cdot \nabla \frac{\partial \phi}{\partial z}$ has actually the same form of the m terms, i.e $-(\vec{n} \cdot \nabla)\nabla\phi$, described in Nakos [1990].

Free Surface Boundary Conditions

Under the potential flow framework, when a MEL scheme is used, the free surface boundary conditions usually take a simpler form (see for instance Longuet-Higgins and Cokelet [1976] or Liu et al. [2001]). However, the fully Lagrangian formulation considers that all fluid particles are moving with the same velocity as the fluid field which leads to computational difficulties. The idea here is twofold: first from the Lagrangian kinematic free surface boundary condition recover the kinematic boundary condition of the free surface with respect to its elevation ζ;

second, formulate both boundary conditions (kinematic and dynamic) when the velocity field imposed on the free surface is not equal to the flow velocity. This last issue is of more practical use since the mesh can be moved in a direction that avoids remeshing but at the same time tries to mitigate the convection terms on the free surface boundary condition. In particular, for the application at hand , imposing a velocity on the mesh on the vertical direction is of interest, since the mesh distortions from this movement are small, the problem of remeshing the free surface at every time step can, hopefully, be avoided.

The Lagrangian kinematic condition states that the velocity of the particles on the free surface are equal to the gradient of the velocity potential. Since the flow is potential, this condition holds throughout the domain , and in particular, on the free surface. Assuming there is a coordinate system O(x,y,z), the kinematic boundary condition is written as:

$$\frac{D(\vec{r})}{Dt} = \nabla\phi. \tag{32}$$

In the equation above $\vec{r} = (x(t), y(t), z(t))$ is the position of the surface node and $\frac{D}{Dt} = \frac{\partial}{\partial t} + \nabla\phi \cdot \nabla$.

What happens, if instead of following the free surface particles, the points x and y are fixed and the free surface elevation is expressed as $\zeta(x, y, t)$? In this case the position vector of the free surface is $\vec{r} = (x, y, \zeta(x, y, t))$. Using the Lagrangian kinematic boundary condition on $\vec{r}$, the equality on x and y are trivial, but on the z direction one has that:

$$\frac{D(\zeta(x, y, t))}{Dt} = \frac{\partial\zeta}{\partial t} + \nabla\phi \cdot (\frac{\partial\zeta}{\partial x}, \frac{\partial\zeta}{\partial y}, 0) = \frac{\partial\phi}{\partial z}. \tag{33}$$

Expanding one can recover another form of the kinematic boundary condition, say an Eulerian representation of the free surface, Newman [1977], as:

$$\frac{\partial\zeta}{\partial t} + \frac{\partial\phi}{\partial x}\frac{\partial\zeta}{\partial x} + \frac{\partial\phi}{\partial y}\frac{\partial\zeta}{\partial y} = \frac{\partial\phi}{\partial z}. \tag{34}$$

Therefore the kinematic boundary condition in the Lagrangian form implies equation 34.

Assume that the free surface nodes are going to be moved along the vertical

direction. So let $\vec{v_p} = (0, 0, v_z)$ be the mesh velocity and $\frac{\delta\zeta}{\delta t}$ the derivative of ζ when its motion is followed in the vertical direction. The derivative of the free surface with respect to time can be calculated as:

$$\frac{\delta\zeta}{\delta t} = \frac{\partial\zeta}{\partial t} + (0, 0, v_z) \cdot (\frac{\partial\zeta}{\partial x}, \frac{\partial\zeta}{\partial x}, 0) = \frac{\partial\zeta}{\partial t}, \tag{35}$$

which does not depend on $\vec{v_p} = (0, 0, v_z)$, simplifying the numerical treatment.

Hence the kinematic boundary condition, equation 34, can be written in terms of $\frac{\delta\zeta}{\delta t}$ as follows:

$$\frac{\delta\zeta}{\delta t} + \frac{\partial\phi}{\partial x}\frac{\partial\zeta}{\partial x} + \frac{\partial\phi}{\partial y}\frac{\partial\zeta}{\partial y} = \frac{\partial\phi}{\partial z}. \tag{36}$$

It is also worth noting that if the steepness of the free surface is small in x and y directions the linearized form of the kinematic boundary condition is recovered.

The dynamic boundary condition on the free surface, under potential flow assumptions, can be derived from Bernoulli's equation which can be written as, Newman [1977]:

$$\frac{\partial\phi}{\partial t} + \frac{1}{2}\nabla\phi^2 + gz = 0 \tag{37}$$

Assuming that x,y are fixed and that the free surface elevation is given by $\zeta(x, y, t)$, the potential can be written as $\phi(x, y, \zeta(x, y, t), t)$. The derivative of the potential with respect to time, by the chain rule, is therefore:

$$\frac{d\phi}{dt} = \frac{\partial\phi}{\partial t} + \frac{\partial\phi}{\partial\zeta}\frac{\partial\zeta}{\partial t}, \tag{38}$$

since $z = \zeta(x, y, t)$, $\frac{\partial\phi}{\partial\zeta} = \frac{\partial\phi}{\partial z}$.

From equation 37 and 38, the dynamic boundary condition becomes:

$$\frac{d\phi}{dt} - \frac{\partial\phi}{\partial z}\frac{\partial\zeta}{\partial t} + \frac{1}{2}\nabla\phi^2 + gz = 0 \tag{39}$$

It is also interesting to note that if the particles are followed in a Lagragian fashion (x,y and z are time dependent) then the fully Lagrangian formulation is recovered . In this case the potential is $\phi(x(t), y(t), z(t), t)$ and its derivative, by

the chain rule, becomes $\frac{D\phi}{Dt} = \frac{\partial \phi}{\partial t} + \nabla \phi^2$.

Appendix B Time Series Analysis of Hydrodynamic Forces

The results obtained in time domain simulations can be recast in the frequency domain by performing a Fourier decomposition of the hydrodynamic force time series. Assuming that the hydrodynamic force, $F_h(t)$ admits a Fourier decomposition (i.e it is square integrable), then its Fourier decomposition can be written as:

$$F_h(t) = \frac{A_0}{2} + \sum_{j=1}^{n} A_j sin(\omega jt) + B_j cos(\omega jt). \tag{40}$$

In addition, in the context of forced oscillations, the Fourier coefficients can be readly identified with the added mass and damping coefficients. For instance, in the heave case, since $z_c(t) = Asin(\omega t)$, A_1 and B_1 corresponds to the definition of added mass (A_{33}) and damping (B_{33}) respectively. Looking at equation 40 the components due to the higher order harmonics (i.e $j > 1$) are also present, in particular the coefficients A_{33}^2 and B_{33}^2 introduced in equations 7.21 and 7.22 respectively can also be identified to A_2 and B_2.

Sometimes it is also useful to write equation 40 in terms of the harmonics instead of the Fourier coefficients. In order to achieve this, the coefficients f_j's are defined as follows:

$$f_j = \begin{cases} A_0/2 & \text{if } j = 0 \\ A_j - iB_j & \text{if } j > 0 \end{cases} \tag{41}$$

where i refers to the imaginary unit in the complex plane.

Using the coefficients defined in equation 41, equation 40 can be rewritten in terms of the harmonics as follows:

$$F_h(t) = \Re(\sum_{j=0}^{n} f_j e^{i\omega jt}), \tag{42}$$

where $\Re(.)$ denotes the real part. In order to see this, one can expand the $f_j e^{i\omega jt}$ term, using Euler's formula and plug in equation 41:

$$\begin{aligned}
\Re(f_j e^{i\omega jt}) &= \Re((A_j - iB_j)(sin(\omega jt) + icos(\omega jt))) \\
&= \Re(A_j sin(\omega jt) + B_j cos(\omega jt) + i(A_j cos(\omega jt) - B_j sin(\omega jt))) \\
&= A_j sin(\omega jt) + B_j cos(\omega jt).
\end{aligned}$$

For the case where $j = 0$, $e^{i\omega jt} = 0$, which gives $f_0 = A_0/2$.

This way, the norm, for instance, of f_1 is $f_1 = \sqrt{A_1^2 + B_1^2}$. In the particular case of heave forced oscillations it then follows that $f_1 = \sqrt{A_{33}^2 + B_{33}^2}$. Therefore, the Fourier decomposition provides a link between frequency domain and time domain analysis.

Note however that equation 40 (or equivalently equation 42) makes sense when the signal (e.g the force time series) is stationary since the temporal information is lost and the spectrum of the signal is a function of only the frequency. For stationary signals, the Fourier representation expand the signal on a orthogonal basis with respect to the dot product defined by $< g(x), h(x) >= \int_{t-T}^{t+T} g(x)h(x)dx$. This follows from the orthogonality relations of $sin(x)$ and $cos(x)$ functions, i.e:

$$\int_{t-T}^{t+T} sin(\omega jt)sin(\omega kt)dt = \begin{cases} \pi & \text{if } j = k \\ 0 & \text{otherwise,} \end{cases} \tag{43}$$

$$\int_{t-T}^{t+T} cos(\omega jt)cos(\omega kt)dt = \begin{cases} \pi & \text{if } j = k \\ 0 & \text{otherwise,} \end{cases} \tag{44}$$

$$\int_{t-T}^{t+T} cos(\omega jt) sin(\omega kt) dt = 0. \tag{45}$$

Since the temporal information lost, transient effects are not straightforward to capture. Moreover, the question of what harmonics should be kept in the expansion is also daunting. One usually drops the higher frequency components but this procedure is rather heuristic.

Recently, an alternative approach to signal analysis, the Hilbert Huang transform, has been developed by Huang et al. [1998]. This framework is comprised of two parts: the empirical mode decomposition (EMD) and the Hilbert transform. The final result of the Hilbert transform can then be represented on an energy-frequency-time distribution (in contrast Fourier analysis results are represented as an energy-frequency distribution), which is called Hilbert spectral analysis.

In fact, the key aspect of the Hilbert Huang transform lies in the observation that, although the Hilbert transform is able to capture the local properties of functions in the L^p class in time domain, its direct application to this class of functions can yield negative frequencies that bear no relationship with the real oscillation of the data Huang et al. [1998]. In order to overcome this issue, the EMD technique is used to decompose the original signal time series into a finite (usually small number) of intrinsic mode functions (IMFs). The IMFs enjoy a well behaved Hilbert transform, and hence their Hilbert spectral analysis provide a energy-frequency-time distribution that brings insight into the oscillatory behaviour of the data.

In chapter 6, the EMD decomposition was used in filtering mode, where the IMFs that were statistically close to white noise were not kept in the force time series decomposition, this approach followed closely the empirical study performed by Wu and Huang [2004] . In what follows the application of the Hilbert Huang transform to the problem of a force time series decomposition is addressed and compared to the conventional Fourier decomposition. To this end, a brief summary of the Hilbert Huang transform will be given. First, the Hilbert transform will be introduced and next the EMD algorithm will be described. After introducing these concepts, a generalization of the Fourier decomposition in equation 42 will be naturally introduced. Next, this result of Huang et al. [1998], is brought

to the context of time domain hydrodynamics as an alternative formulation of the harmonics, now in terms of Hilbert transforms of IMFs.

The motivation behind the development of the Hilbert transform is the following: Given function, X in the L^p class that maps from R to R (i.e t to $X(t)$), is it possible to find an imaginary part $iY(t)$ such that the complex function, $Z(t)$, $Z(t) = X(t) + iY(t)$, can be analytically extended from the real line to the upper half of the complex plane?

The answer is the Hilbert transform (see for instance Hahn [1995]) and Y(t) is given by the Cauchy principal value, PV, of the integral:

$$H(X(t)) = Y(t) = \frac{1}{\pi} PV \int \frac{X(t')}{t - t'} dt'. \tag{46}$$

Since, $Z(t) = X(t) + iY(t)$, is defined on the upper half complex plane, it can also be written using Euler's formula, namely:

$$Z(t) = X(t) + iY(t) = a(t)e^{i\theta(t)}, \tag{47}$$

where:

$$a(t) = \sqrt{X^2(t) + Y^2(t)}, \tag{48}$$

and

$$\theta(t) = tan^{-1} \frac{Y(t)}{X(t)}. \tag{49}$$

Since the phase angle, $\theta(t)$ is time dependent the instantaneous frequency can be defined as:

$$\omega(t) = \frac{d\theta(t)}{dt}. \tag{50}$$

For the case of the Fourier Decomposition defined in equation 42, $\theta_j(t) = \omega_j t$, so the instantaneous frequency is constant for each mode j and given by ω_j. Therefore, in this sense, equation 47 generalizes equation 42, with f_j and ω_j being replaced by their time variants counterparts, $a(t)$ and $\omega(t)$ respectively.

If all the functions in the L^p class enjoyed a well defined Hilbert transform

(in the sense that the transform has a physical relationship with the signal), the problem will be solved and it would suffice to substitute the Fourier decomposition by the Hilbert transform. However, it was pointed out by Huang et al. [1998] that this is not the case. In particular, in order to overcome this issue the Ensemble Mode Decomposition was developed and it is used as pre-processing step.

The EMD is an empirical algorithm that decomposes a signal into its local oscillations. The idea is to express each oscillation scale as separate component, (this yields the Intrinsic Mode Function, or IMF) so that the sum of the IMFs, plus a residual term will reconstruct the original signal. IMFs are functions that satisfy the two following criteria Huang et al. [1998]:

- in the whole data set, the number of extrema and the number of zero-crossings must either be equal or differ at most by one;
- at any point, the mean value of the envelope defined by local maxima and local minima is zero.

That said, the EMD algorithm is summarized in algorithm 8. The output of the algorithm are the IMFs and the residual term. This way, the initial signal, say $X(t)$, is decomposed as follows:

$$X(t) = \sum_{j=1}^{N_{IMFs}} c_j + r, \tag{51}$$

in which, N_{IMFs} is the number of IMFs used to decompose the signal. It depends on the size of the signal as $log_2(size(signal))$ Huang et al. [1998], which is usually much smaller than the Fourier harmonics decomposition. At this point, since IMFs behave well under Hilbert transformations, one can let $X'(t) = X(t) - r$ and use equation 46. This result is summarized on the following proposition.

Proposition .0.1 *Let c_j's be $N_{IMFs} \in N^+$ functions. Let $X(t)$ be a continuous real function mapping from $t \in R^+$ to $X(t) \in R$, such that its corresponding EMD decomposition is given by $X(t) = \sum_{j=1}^{N_{IMFs}} c_j + r$. If $X'(t) = X(t) - r$, then $X'(t)$*

can be represented by :

$$X'(t) = \Re(\sum_{j=1}^{N_{IMFs}} a_j(t)e^{i\int \omega_j(t)dt}). \tag{52}$$

Proof Since $X'(t) = X(t) - r$, it follows from the EMD decomposition (equation 51) that $X'(t) = \sum_{j=1}^{N_{IMFs}} c_j$. Denoting the Hilbert transform of $X'(t)$ by $Y'(t)$, it follows from equation 47 and the fact that the Hilbert transform is a linear operator that:

$$\begin{aligned} Z'(t) &= X'(t) + iY'(t) \\ &= \sum_{j=1}^{N_{IMFs}} c_j + iH(\sum_{j=1}^{N_{IMFs}} c_j) \\ &= \sum_{j=1}^{N_{IMFs}} c_j + i\sum_{j=1}^{N_{IMFs}} H(c_j) \\ &= \sum_{j=1}^{N_{IMFs}} (c_j + iH(c_j)) \\ &= \sum_{j=1}^{N_{IMFs}} a_j(t)e^{i\int \omega_j(t)dt}. \end{aligned}$$

So, taking the real part of Z'(t) yields:

$$X'(t) = \Re(Z'(t)) = \Re(\sum_{j=1}^{N_{IMFs}} a_j e^{i\int \omega_j(t)dt}). \quad \blacksquare$$

Therefore, coming back to the context of analyzing time series of forces, it is interesting to note how equation 52 is closely related to the Fourier harmonics decomposition, equation 42. In fact, in the context of hydrodynamic analysis, all that is needed to extend, the frequency-energy representation of the the harmonics f_j to the time-frequency-energy representation of the Hilbert Huang Transform,

is to associate f_j to $a_j(t)$ and $w_j t$ to $\int \omega_j(t)dt$ in equations 42 and 52 respectively. This way, the Hilbert transform of the jth IMF for instance, c_j, will give rise to "added mass" and "damping coefficients" that vary in time as well as in the frequency domain. Furthermore, their respective phase and amplitude are given by equations 49 and 48, respectively. One of the advantages of this approach is that the IMFs representation is usually smaller than the Fourier expansion, since the number of IMFs is of the order of $log_2(size(signal))$. Moreover, by definition, the IMFs form a base for the signal, which is adaptive, because the spline construction depends of the signal data itself. What is striking is that this base, in practice, turns out to be very close to a orthogonal base, this is actually a topic of active research in adaptive time series analysis.

Algorithm 8 Ensemble Mode Decomposition

procedure FUNCTION(IMFs=EMDecomp(signal))
    aux:=signal; ▷ lnitialize h(0) to be the signal itself.
    $N_{IMFs} = log_2(size(signal)) + 1$
    while $j < N_{IMFs}$ **do**
        h(t):=aux
        while $Iter_{sift} < N_{sift}$ **do**
            $[ext_{up}, ext_{down}] := extrema(signal)$ ▷ Identify the extreme points of the signal.
            $[envelope_{up}, envelope_{down}] := cubicspline(extup, extdown)$ ▷ Fit cubic splines to represent the upper and lower envelopes, respectively.
            $m(t) := median(envelope_{up}, envelope_{down})$ ▷ Compute the local medians.
            h(t):=h(t)-m(t); ▷ Extract the spline mean.
            $Iter_{sift} := Iter_{sift} + 1$
        end while
        aux:=aux-h(t) ▷ After the inner while, h(t) has become an IMF, so its extracted from the aux and the process is reiterated.
        c(j):=h(t) ▷ c(j) saves the jth IMF on jth column of c.
    end while
    $r := aux$ ▷ After the iterations r receives the residual of the last IMF, r.
    $IMFs := [c; r]$ ▷ Output the the IMFs on vector c and the residual term.
end procedure

Appendix C Sensitivity Analysis of Sphere Simulations

In this appendix, a sensitivity analysis of the sphere undergoing forced heave simulations is presented when the Φ_t Exact BNL algorithm is used. During this analysis four parameters were varied on the Φ_t Exact BNL algorithm, namely:

- the regularization parameter, λ;
- the edge size of the element, h;
- the free surface size ;
- the time step dt.

The role that the regularization parameter, λ, plays was discussed in chapter 7. The size of the element tries to measure the convergence in the h sense Karniadakis and Sherwin [2005], since the mesh is unstructured h represents the edge size of elements that are used to mesh the sphere. The domain topology that was considered in chapter 7, i.e a cylindrical domain where the free surface is circular (figure 7.1) , was kept the same during the sensitivity analysis, however the diameter of the free surface was changed. In what follows, the results of the sensitivity analysis are presented in a tabulated form. The first table refers to the value of the parameters used whereas the second table shows the results obtained, in terms f_0, f_1, f_2, A_{33} and B_{33}, all of which were nondimensionalized according to the framework presented in chapter 7. Unfortunately, due to runtime

constraints, the analysis is rather limited and it was not possible to perform an analysis where the value of the parameters were changed on a systematic fashion.

Table 1: First Set of Simulation Parameters Values

Parameter	Value
λ	0.0
h	0.02 units
Free Surface Diameter	8.0 units
dt	0.0045 s

Table 2: Results of the first set

A/R	f_0	f_1	f_2	A_{33}	B_{33}
0.125	-0.0533	0.3425	0.2828	0.293	0.177
0.25 0	-0.0090	0.3226	0.2391	0.2871	0.147
0.300	-0.0225	0.3116	0.2978	0.2660	0.1622
0.375	-0.0243	0.3036	0.2847	0.2715	0.1360

Table 3: Second Set of Simulation Parameters Values

Parameter	Value
λ	0.0
h	0.02 units
Free Surface Diameter	8.0 units
dt	0.00225 s

Table 4: Results of the second set

A/R	f_0	f_1	f_2	A_{33}	B_{33}
0.125	-0.0370	0.3572	0.2883	0.296	0.199
0.250	-0.0010	0.3289	0.2803	0.281	0.170
0.300	-0.0225	0.3193	0.2570	0.269	0.171
0.375	-0.0020	0.3014	0.2373	0.272	0.128

Table 5: Third Set of Simulation Parameters Values

Parameter	Value
λ	0.0
h	0.02 units
Free Surface Diameter	16.0 units
dt	0.0045 s

Table 6: Results of the third set

A/R	f_0	f_1	f_2	A_{33}	B_{33}
0.300	-0.066	0.3134	0.2053	0.267	0.163

Table 7: Fourth Set of Simulation Parameters Values

Parameter	Value
λ	0.0
h	0.02 units
Free Surface Diameter	10.0 units
dt	0.0045 s

Table 8: Results of the fourth set

A/R	f_0	f_1	f_2	A_{33}	B_{33}
0.300	-0.033	0.3122	0.2250	0.266	0.164

Table 9: Fith Set of Simulation Parameters Values

Parameter	Value
λ	0.0
h	0.01 units
Free Surface Diameter	8.0 units
dt	0.0045 s

Table 10: Results of the fith set

A/R	f_0	f_1	f_2	A_{33}	B_{33}
0.300	-0.092	0.350	0.284	0.281	0.209
0.375	-0.096	0.331	0.276	0.280	0.176

Table 11: Sixth Set of Simulation Parameters Values

Parameter	Value
λ	0.01
h	0.02 units
Free Surface Diameter	8.0 units
dt	0.0045 s

Table 12: Results of the sixth set

A/R	f_0	f_1	f_2	A_{33}	B_{33}
0.250	-0.137	0.325	0.211	0.265	0.187
0.300	-0.135	0.318	0.226	0.252	0.195
0.375	-0.134	0.286	0.187	0.227	0.174

References

Apostol, T. (1969). *Calculus*, volume Vol II. John Wiley and Sons. 42

Bailey, P., Hudson, D., Price, W., and Temarel, P. (1998). A unified mathematical model describing the manouvering of a ship travelling in a seaway. In *RINA Transactions*, volume 140. 13, 14, 25, 26

Bailey, P., Hudson, D., Price, W., and Temarel, P. (1999). Theoretical and experimental validation of the seakeeping characteristics of high speed mono- and multi-hulled vessels. In *Proceedings of the 5th International Conference on Fast Sea Transportation*, Washington, USA,. 34

Bailey, P., Hudson, D., Price, W., and Temarel, P. (2002). A simple yet rational approach to the panelling of hull surfaces. In *RINA Transactions*, volume 144. 14, 28

Ballard, E., Hudson, D., Price, W., and Temarel, P. (2003). Time domain simulations of symetric ship motions in waves. In *RINA Transactions*, volume 145. 3, 25, 27, 32

Bandyk, P. (2009). *A body exact strip therory approach to ship motions computations*. PhD thesis, University of Michigan. 12

Battistin, D. and Iafrati, A. (2003). Hydrodynamic loads during water entry of two dimensional and axisymmetric bodies. *Journal of Fluids and Structures*, 17:643–664. 8, 17, 115, 116, 155

Beck, R. F., Cao, Y., Scorpio, S., and Schultz, W. (1994). Nonlinear ship motion computations using the desingularized method. In *20th Symposium on Naval Hydrodynamics*, pages 227–247. 2, 16, 46

Bishop, C. M. (2007). *Pattern Recognition and Machine Learning*. Springer. 122

Bishop, R. and Price, W. (1979). *Hydroelasticity of Ships*. Cambridge University Press. 3, 99, 100

Bishop, R., Price, W., and Wu, Y. (1986). A general linear hydroelasticity theory of floating structures moving in a seaway. *Philosophical Transactions of the Royal Society of London*, Series A:375–426. xiii, xiv, 3, 19, 96, 97, 98, 100, 102, 103, 104, 105, 106, 107, 108

Buhmann, M. (2004). *Radial Basis Functions: Theory and Implementations*. Cambridge University Press. 63, 118, 120

Chinchapatnam, P. P. (2006). *Radial Basis Function Based Meshless Methods for Fluid Flow Problems*. PhD thesis, University of Southampton. 120, 143

Cordaro, P. and Kawano, A. (2002). *O Delta de Dirac*. Instituto de Fisica da Universidade de Sao Paulo. 51

Cossins, P. J. (2010). Smoothed particle hydrodynamics. *http://arxiv.org/abs/1007.1245*. 15

Gerristma, J., Beukelman, W., and Glansdorp, C. (1974). The effect of beam on the hydrodynamic characteristics of ship hulls. In *10 th Symposium on Naval Hydrodynamics*. 12

Geuzaine, C. and Remacle, J.-F. (2009). Gmsh: a three-dimensional finite element mesh generator with built-in pre- and post-processing facilities. *International Journal for Numerical Methods in Engineering*, 79(11):1309–1331. 9, 10, 50, 51, 53, 72, 75, 79, 90, 132, 147, 168

Hahn, S. L. (1995). *Hilbert Transforms in Signal Processing*. Artech House. 189

He, G. and Kashiwagi, M. (2009). Full-nonlinear solution for vibration of vertical elastic plate due to wave impact. In *5 th International Conference on Hydroelasticity*, Southampton, UK. 20, 113

Huang, N. E., Shen, Z., Long, S. R., Wu, M. C., E. H, S., Zheng, Q., Tung, C. C., and Liu, H. H. (1998). The empirical mode decomposition method and the hilbert spectrum for non-stationary time series analysis,. *Proc. Roy, Soc. London*, (A454):903–995. 8, 154, 188, 190

Huerta, A. and Liu, W. (1988). Viscous flow with large free-surface motion. *Comput. Methods Appl. Mech. Eng*, 69(3):227–324. 15

Hulme, A. (1982). The wave forces acting on a floating hemisphere undergoing forced periodic oscilations. *J. Fluid Mech*, 8:22–44. 78, 82, 83, 84

Inglis, R. (1980). *A Three Dimensional Analysis of The Motion of a Rigid Ship in Waves*. PhD thesis, University of London. 11, 14, 22, 24, 25

Journée, J. M. J. (1992). Experiments and calculations on four wigley hull forms. Report 909, Delft. xiii, xvi, xviii, 78, 82, 90, 91, 95, 100, 143, 146, 148, 151

Kara, F., Tang, C., and Vassalos, D. (2007). Time domain three-dimensional fully nonlinear computations of steady body–wave interaction problem. *Ocean Engineering*, 34:776–789. 18, 151, 178

Karniadakis, G. and Sherwin, S. J. (2005). *Spectral/hp Element Methods for Computational Fluid Dynamics*. Oxford University Press. 43, 83, 109, 193

Lachaume, C., Biausser, B., Grilli, S. T., Fraunié, P., and Guignard, S. (2003). Modeling of breaking and post-breaking waves on slopes by coupling of bem and vof methods. *International Offshore and Polar Engineering Conference*. 4, 50, 54

Lin, W., Meinhold, M., Salvesen, N., and Yue, D. (1994). Large-amplitude motions and wave loads for ship design. In *20th Symp. on Naval Hydrodynamics*, pages 205–226. 13, 14

Lin, W. M. and Yue, D. (1991). Numerical solutions for large amplitude ship motions in time domain. In *Eighteenth Symposium on Naval Hydrodynamics*. xiv, 84, 113, 114, 126, 128, 130, 132, 133, 155

Liu, H. Y., editor (2010). *Efficient Computations of Fully Nonlinear Wave Interactions with Floating Structures*, number 20412. OMAE. 46, 47, 178

Liu, Y. (2009). *Fast Multipole Boundary Element Method*. Cambridge University Press. 18, 21, 43, 53, 96, 176

Liu, Y., Xue, M., and Yue, D. K. P. (2001). Computation of fully nonlinear three-dimensional wave-wave and wave-body interactions. *Journal of Fluid Mech*, 438. 2, 16, 17, 18, 19, 21, 43, 50, 117, 151, 182

Longuet-Higgins, M. and Cokelet, C. (1976). The deformation of steep surface waves on water: A numerical method of computation. In *Royal Society of London*, volume A350, pages 1–26. 16, 21, 46, 182

Masud, A. and Hughes, T. J. R. (1997). A space-time galerkin/least squares finite element formulation of the navier -stokes equations for moving domain problems. *Comput. Methods Appl. Mech. Eng*, 146:91–126. 16

McCallum, J. C. C. R. K. B. J. B. C. T. J. M. W. R. F. B. C. and Evans, T. R. (2001). Reconstruction and representation of 3d objects with radial basis functions. In *Computer Graphics ACM SIGGRAPH*, pages 67–76. 63

Murphy, K. P. (2012). *Machine Learning A Probabilistic Perspective*. MIT press. 121

Nakos, D. E. (1990). *Ship Wave Patterns and Motions by a Three Dimensional Panel Method*. PhD thesis, MIT. 182

Newman, J. N. (1977). *Marine Hydrodynamics*. MIT press. 23, 24, 46, 91, 98, 183, 184

Olgilvie, F. and Tuck, E. (1969). A rational strip theory for ship motions. Report 013, University of Michigan. 24

Park, J. and Sandberg, I. W. (1991). Universal approximation using radial-basis-function networks. In *Neural Computation*, volume Vol 3, pages 246–257. 118, 119

Park, J. and Temarel, P. (2007). The influence of nonlinearities on wave-induced motions and loads by two-dimensional hydroelasticity analysis. In of Shipping, A. B., editor, *10 th International Symposium on Practical Design of Ships*. 20

Persson, P. (2005). *Mesh Generation for Implicit Geometries*. PhD thesis, MIT. 9, 10, 50, 51, 53, 54, 55, 62, 64, 70, 75, 79, 147

Powers, J. O. E. and Zselecsky, J. (1992). Theoretical and experimental study of the non linearities in vertical plane ship motions. In *Proceedings of the 19th Symposium on Naval Hydrodynamics*, pages 73–91. 35

Pozrikidis, C. (2002). *A Practical Guide to Boundary Element Methods*. Chapman Hall. 56, 177

Salvensen, N., Tuck, E. O., and Faltinsen, O. (1970). Ship motions and sea loads. *The Society of Naval Architects and Marine Engineers*. 25

Sclavounos, P.D; Nakos, D. and Huang, Y. (1993). Seakeeping and wave induced loads on ships with flare by a rankine panel method. In *Sixth International Conference in Numerical Ship Hydrodynamics*. 11

Sethian, J. A. (1999). *Level Set Methods and Fast Marching Methods*. Cambridge University Press. 50, 61

Stein, E., Borst, R., and Hughes, T. (2004). *Encyclopedia of Computational Mechanics*. John Wiley and Sons. 16

Steinbach, O. (2008). *Numerical Approximation Methods for Elliptic Boundary Value Problems*. Springer Verlag. 42, 44

Sutradhar, A., Paulino, G. H., and Gray, L. J. (2008). *Symmetric Galerkin Boundary Element Method*. Springer. 42

Vapnik, V. (2000). *The Nature of Staistical Learning Theory*. Springer-Verlag. 118

Wu, G.-X. and Eatock Taylor, R. (1996). Transient motion of a floating body in steep water waves. In *11 th Internationl Workshop on Water Waves and Floating Bodies*. 82, 115, 116, 181

Wu, Y., Maeda, H., and Kinoshita, T. (1997). The second order hydrodynamic actions on a flexible body. *Journal of Institute of Industrial Science*, 49(4):8–19. 19

Wu, Z. and Huang, N. E. (2004). A study of the characteristics of white noise using the empirical mode decomposition method. *Proc. Roy. Soc. London*, 460(2046):1597–1611. 154, 155, 188

Xu, H. (1992). *Numerical Study of Fully Nonlinear Water Waves in Three Dimensions*. PhD thesis, MIT. 44, 50, 52, 83, 96, 117, 178

Xue, M. (1997). *Three-dimensional fully-nonlinear simulations of waves and wave body interactions*. PhD thesis, MIT. 50, 83, 84

Yan, H. (2010). *Computation of fully nonlinear three-dimensional wave-body interactions*. PhD thesis, MIT. xiv, xvi, xviii, 6, 18, 53, 83, 96, 115, 129, 133, 151, 155, 158, 159, 160

Zhang, S., Weems, K., Lin, W., Yan, H., and Liu‘, Y. (2007). Application of a quadratic boundary element method to ship hydrodynamic problems. In *27th Int. Conf. on Offshore Mechanics and Arctic Engineering*. 4, 17, 21

Zhang, W. and Xu, H. R. (1989). A general and effective way for evaluating the integrals with various orders of singularity in the direct boundary element method. *Journal of Numerical Methods in Engineering*, 28:2059–2064. 56, 176

Zhang, X., Bandyk, P., and Beck, R. F. (2010). Seakeeping computations using double-body basis flows. *Applied Ocean Research*, 32(4):461–482. 12